UNIVERSIDADE DE LISBOA
FACULDADE DE CIÊNCIAS

Geodynamic modelling of subduction zones: Subduction zone initiation by polarity reversal and main dynamic controls on the stability of single-sided subduction

"Documento Definitivo"

Doutoramento em Geologia

Especialidade em Geodinâmica Interna

Jaime Eduardo Cadeias de Araújo Moreira de Almeida

Tese orientada por:

Filipe Medeiros Rosas

Nicolas Riel

Documento especialmente elaborado para a obtenção do grau de doutor

2021

2021

UNIVERSIDADE DE LISBOA
FACULDADE DE CIÊNCIAS

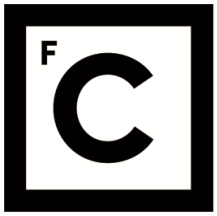

Ciências
ULisboa

Geodynamic modelling of subduction zones: Subduction zone initiation by polarity reversal and main dynamic controls on the stability of single-sided subduction

Doutoramento em Geologia
Especialidade em Geodinâmica Interna

Jaime Eduardo Cadeias de Araújo Moreira de Almeida

Tese orientada por:
Filipe Medeiros Rosas
Nicolas Riel

Júri:
Presidente:

- Doutora Ana Cristina Costa Neves dos Santos Azerêdo, Professora Catedrática, Faculdade de Ciências da Universidade de Lisboa

Vogais:

- Doutor Taras Gerya, Adjunct Professor and Privatdozent do Institute of Geophysics da ETH Zurich (Suíça)
- Doutora Laetitia Le Pourhiet, Titular Professor do Institut des Sciences de la Terre de Paris da Sorbonne Université (França)
- Doutor Rui Manuel Soares Dias, Professor Catedrático da Escola de Ciências e Tecnologia da Universidade de Évora
- Doutor Filipe Medeiros Rosas, Professor Auxiliar com Agregação da Faculdade de Ciências da Universidade de Lisboa

Documento especialmente elaborado para a obtenção do grau de doutor

This research has been supported by the Fundação para a Ciência e a Tecnologia through grant no. UIDB/50019/2021 – Instituto Dom Luiz, grant no. IF/00702/2015, and PhD grant no. PD/BD/135067/2017.

2021

Dedico esta tese ao meu avô
Carlos e à minha avó Isilda, que
partiram antes de verem esta
jornada chegar ao fim.

Dedico também ao meu filho Áureo,
que chega mesmo perto do fim.

Acknowledgements

There are simply too many people to thank for their incredible help and support throughout the immense journey that was this doctoral degree. If someone feels they have been left out from this list, I do humbly apologize.

First and foremost, I would like to thank both my supervisors, Prof. Filipe Rosas and Dr. Nicolas Riel. Their advice and guidance were fundamental for the development of both this work and own as both a scientist and a person. Filipe has been far more than my supervisor over the past few years. He was and is not only my mentor but also a good friend who has supported me all throughout my journey, from a lowly bachelor student all the way to the end of my PhD, throughout the tough scientific path and countless personal problems. To Nicolas I must thank most of all his patience and ability to answer countless questions about all the incredible ways in which I managed to destroy the models. He has guided me throughout the steep learning curve which was numerical modelling, and I will forever be grateful for it.

I acknowledge and thank the Fundação para a Ciência e Tecnologia (FCT) for funding my PhD scholarship PD/BD/135067/2017 - Earthsystems-IDL for the past four years. I also thank IDL (Instituto Don Luiz), FCUL (Faculdade de Ciências da Universidade de Lisboa) for supporting my research.

I thank Prof. João Duarte for the tireless help with the research presented in this thesis. João is as much of a mentor and friend as Filipe or Nicolas are to me and is, undoubtedly, someone who has made me a better scientist.

I would like to thank Prof. Wouter Schellart for the insightful discussions on subduction zone dynamics which were fundamental for the development and improvement of this work. I would also like to thank Ricardo Tomé for all the help in using the cluster as well as for solving countless technical issues which arose during the past years.

I also thank Afonso Gomes, Xu Wang, and Zé Dias for their friendship and support throughout this process. With them, there is always a better outlook and a barrel of laughs whenever something goes (horribly) wrong, and I thank you for it.

I must also thank to Paula and Adolfo Cartaxo for their encouragement and support over the last years of this PhD.

I would also like to thank my parents Isilda Carneiro and Nuno Canto Moreira and my brothers and sisters for all their love, support, and encouragement over my entire scientific career.

Finally, I must thank my amazing wife Luísa, my rock and my support throughout this entire journey. Without her, I have no question that this work would have been far harder to complete.

Abstract

Subduction zones are one of the most widely studied geodynamic settings, representing the primary driver for mantle convection and plate tectonics. Despite this, one question still sparks controversy to the present day: how does a subduction zone initiate? Over the past half century, multiple theories have been suggested to explain subduction zone initiation (SZI). One widely cited conceptual model for SZI is polarity reversal, resulting from the shutdown of a pre-existent subduction zone due to the arrival of a buoyant block at the trench. However, the dynamic conditions by which this process occurs remain elusive.

To shed light on this complex topic and assess the geodynamic constraints behind polarity reversal SZI, two geodynamic numerical modelling studies were conducted. In both studies, it was shown that this SZI mechanism is dynamically viable, without external forcing, occurring simply as the result of the evolving force balance during an oceanic plateau collision. Additionally, the efficiency of a polarity reversal event is increased by the presence of old subducting plates, relatively young overriding plates, and/or narrow oceanic plateaus. The results were shown to be consistent with a widely studied natural polarity reversal case, the collision of the Ontong-Java Plateau and formation of the Vanuatu subduction zone.

Beyond the complexity of SZI, subduction zone modelling studies have predicted the existence of double-sided subduction (i.e., the simultaneous sinking of both plates) for years. As this type of subduction zone has not been found on Earth, its inexistence has been previously tied to strong subducting plates and the constant maintenance of a weak subduction interface. Additional exploratory numerical modelling was also carried out, expanding the scope of previously tested conditions by systematically exploring the effective strength contrast between the two intervening plates. The preliminary results suggest that, under top free slip conditions, two strong plates and a weak interface are needed to ensure single-sided subduction, as opposed to a strong subducting plate and a weak interface.

Keywords: geodynamic modelling, oceanic plateau, polarity reversal, subduction zone initiation, subduction zone stability

Resumo

As zonas de subducção são um dos ambientes geodinâmicos mais estudados, representando a principal fonte de força por detrás das correntes de convecção mantélica e da tectónica de placas em si. No entanto, não obstante a imensa quantidade de estudos sobre dinâmica de zonas de subducção ao longo dos últimos 50 anos, ainda não existe uma explicação completa e satisfatória para como e porquê uma zona de subducção se inicia ("*subduction zone initiation"*). Actualmente, graças a uma série de publicações sobre este tema, existem hoje diversas teorias e cenários conceptuais que, com base em casos naturais, procuram explicar este processo complexo. Estas incluem, por exemplo, o clássico início de subducção por colapso de margem passiva ou falha transformante, a reactivação de antigas suturas, ou início de subducção induzido por plumas mantélicas.

De entre os diversos cenários conceptuais propostos para o início de subducção, um dos mais recorrentemente citados é a formação de novas zonas de subducção através de uma inversão de polaridade. Neste cenário, um bloco litosférico de baixa densidade numa placa a ser subductada chega à fossa de subducção, sendo forçado a colidir com a placa superior (no texto, "*overriding plate*"). Esta colisão promove um rompimento local da placa inferior ("*subducting plate*"), bem como um dobramento simultâneo da placa superior. Devido à força exercida pela placa em subducção fora da frente de colisão, a placa superior dobrada é forçada a mergulhar para o interior do manto. Na eventualidade desta placa conseguir alcançar uma profundidade crítica de cerca de 200 km, devido à sua elevada densidade, esta começa a afundar sozinha, iniciando assim uma nova subducção auto-sustentável e completando a inversão da polaridade. No entanto, e apesar desta sequência de eventos se encontrar registada na natureza, as condições geodinâmicas específicas que a controlam não são conhecidas.

Como tal, e a fim de elucidar a complexidade dinâmica que subjaz a este processo, foram elaborados dois estudos de modelação geodinâmica de início de subducção no âmbito desta tese. No primeiro destes estudos foi explorada sistematicamente, através de modelação 2D, a influência da idade inicial das duas placas na formação de uma nova zona de subducção por inversão de polaridade. No segundo estudo foi explorado, através de modelação 3D, não só o efeito da idade inicial das duas placas, mas também o da largura do planalto oceânico e da presença de um arco vulcânico, no início de subducção por inversão de polaridade.

Nos dois trabalhos, uma das conclusões fundamentais é de que a inversão de polaridade representa um mecanismo dinâmicamente viável para o início de subducção, sendo capaz de funcionar sem qualquer tipo de imposição cinemática externa. Uma nova zona de subducção é gerada apenas como resultado evolução do equilíbrio dinâmico existente durante uma colisão com um planalto oceânico. Através da exploração sistemática das idades iniciais das duas placas, foi possível observar que o domínio de estabilidade para início de subducção por inversão de polaridade restringe-se a sistemas em que a placa superior tem idade inferior a 60 Myr e a placa inferior tem uma idade superior a 80 Myr. Foi também constatado que a eficiência de uma inversão de polaridade (ou seja, o intervalo de tempo entre a colisão do planalto oceânico e a geração de uma nova subducção autónoma) varia directamente com o aumento de idade inicial da placa em subducção, e inversamente com o aumento da idade inicial placa superior e da largura do planalto oceânico. Adicionalmente, um aumento extremo tanto da idade inicial da placa superior (e.g., acima de 100 Myr) e da largura do planalto oceânico (e.g., acima cerca de 2000 km) tem a possibilidade de inviabilizar o desenvolvimento de uma nova subducção, resultando geralmente na acreção do planalto oceânico à placa superior.

De forma a validar os modelos obtidos nos dois estudos, foi elaborada em ambos uma comparação com um caso natural de inversão de polaridade bem conhecido. O caso escolhido foi a colisão de idade miocénica (entre 10 a 5 Ma) do Planalto de Ontong-Java ("*Ontong-Java Plateau"*) com a placa Australiana, e o subsequente início da chamada zona de subducção de Vanuatu como consequência. Esta comparação permitiu verificar que a sequência de eventos que levou ao desenvolvimento da subducção de Vanuatu é consistentemente reflectida reflectida nos resultados obtidos na modelação 3D levada a cabo. Especificamente, estes resultados mostraram o início da nova subducção ao longo da frente de colisão, a migração lateral da nova zona de subducção e, por fim, o início do desenvolvimento de uma bacia extensional entre a antiga e a nova zona de subducção. Adicionalmente, as idades geralmente associadas ao planalto de Ontong-Java e placa Australiana encontram-se dentro da gama de idades obtida para uma inversão de polaridade anteriormente obtidos (placa superior com idade inferior a 60 Myr e a placa inferior com idade superior a 80 Myr).

Para além dos estudos elaborados sobre início de subducção, esta tese também inclui um estudo preliminar sobre estabilidade de zonas de subducção. Esta investigação em curso parte da observação de que, apesar de as zonas de subducção terrestres serem marcadamente assimétricas (com uma placa inferior a mergulhar no manto e uma placa superior continental ou oceânica à superfície), vários estudos anteriores previram a existência de zonas de subdução

convergentes duplas ("*double-sided subduction*"). Este cenário geodinâmico em que ambas placas mergulham simultaneamente, embora já procurado, não foi detectado até hoje.

Com base em estudos de modelação numérica, publicações anteriores propuseram que a sua inexistência fosse o resultado da presença de: (a) uma placa inferior forte (i.e., resistente à deformação); (b) um canal de subducção (i.e., interface entre as duas placas) permanentemente fraco, e/ou (c) a capacidade para formação de relevo (i.e., através de uma atmosfera/superficie livre, ou "*free surface*"). No entanto, apesar destas teorias, em muitas das experiências numéricas levadas a cabo no âmbito desta tese, foi detectado múltiplas vezes o desenvolvimento deste tipo de zona de subducção anómalo em condições consideradas improváveis, nomeadamente em modelos utilizando condições do tipo "*free surface*". Dado este resultado inesperado, foi iniciado um estudo que permitisse clarificar as condições exatas que mantêm uma zona de subducção assimétrica (i.e., com apenas uma placa a afundar no manto).

Até ao momento, foi testado o efeito exercido pela idade inicial da placa superior, utilizando apenas condições de fronteira do tipo "*free slip*", tendo sido obtido um campo de estabilidade para diferentes tipos de zonas de subducção. Estes resultados preliminares sugerem que o desenvolvimento de zonas de subducção instáveis decorre da presença de, pelo menos, uma placa fraca no sistema ($\eta_{eff} < 1.5x10^{22}$ Pa·s). Foi ainda constatado que o tipo específico de instabilidade formado é função da viscosidade efectiva (η_{eff}) das duas placas, occorrendo: (a) alternância entre inversões de polaridade e eventos de subducção dupla, em sistemas de subducção com duas placas igualmente fracas ($\eta_{eff} < 2\times10^{22}$ Pa·s); (b) formação rápida de zonas de subducção dupla, em sistemas com uma placa superior fraca ($\eta_{eff} < 1.5x10^{22}$ Pa·s) e uma placa inferior mais forte ($\eta_{eff} > 1.8x10^{22}$ Pa·s); e (c) formação tardia de zonas de subducção dupla em sistemas com uma placa superior com viscosidade superior a $1.8x10^{22}$ Pa·s.

De futuro, será efectuada uma comparação directa destes resultados com os obtidos através modelos de subducção com idades iniciais idênticas, que incluam condições de fronteira superior do tipo "*free surface*".

Palavras-chave: inversão de polaridade, início de subducção, modelação geodinâmica, planalto oceânico, estabilidade de zonas de subducção

Publications arising from this thesis

During the development of the present thesis, I have published 3 papers in international peer-reviewed journals (EPSL, Journal of Structural Geology and BMC Bioinformatics), have one accepted in principle (Communications Earth and Environment) and have another currently under review (Tectonophysics). A final paper, directly arising from the core research implied by the carried-out PhD, is still to be submitted (and is part of the present thesis).

Additionally, I've also reported and discuss the progression of my work in different conferences through poster and oral presentations (a total of 6).

Publications arising from the core of the research implied by the present thesis:

Published

- *Almeida, J.*, Riel, N., Rosas, F. M., Schellart, W. P., Duarte, J. C. (2022) Polarity-reversal subduction initiation triggered by buoyant plateau obstruction. Earth and Planetary Sciences Letters, 577, p. 117195. http://dx.doi.org/10.1016/j.epsl.2021.11719

Accepted

- *Almeida, J.*, Riel, N., Rosas, F. M., Duarte, J. C. (2022) Self-replicating subduction initiation by polarity reversal. Communications Earth and Environment. Accepted in principle

To be submitted

- *Almeida, J.*, Riel, N., Rosas, F. M., Schellart, W. P., Duarte, J. C. (*in prep*) Single-sided subduction stability under free slip modelling conditions.

Publications arising from collaborations (journal articles as co-author):

Published

- Gomes, A.S., Rosas, F.M., Duarte, J.C., Schellart, W.P., *Almeida, J.,* Tomás, R., Strak, V., 2019. Analogue modelling of brittle shear zone propagation across upper crustal morpho-rheological heterogeneities. J. Struct. Geol. 126, 175–197. https://doi.org/10.1016/j.jsg.2019.06.004

- Cartaxo, A.L., *Almeida, J.*, Gualda, E. J., Marsal, M., Loza-Alvarez, P., Brito, C., Isidro, I. A. (2020) A computational diffusion model to study antibody transport within reconstructed tumor microenvironments. BMC Bioinformatics 21, 529. https://doi.org/10.1186/s12859-020-03854-2

Under review

- Oliveira, M. E., Gomes, A. S., Rosas, F. M., Duarte, J. C., França, G. S., *Almeida, J.*, Fuck, R. A, 2021. Double-rift nucleation above inherited crustal weaknesses: insights from 2D numerical models, Tectonophysics, under review.
- Duarte, J., Riel, N., Civiero, C., Silva, S., Rosas, F., Schellart, W., Custodio S., *Almeida, J.*, Terrinha, P., Ribeiro, A., pre-print. Evidence of oceanic plate delamination in the Northern Atlantic. Nature. https://doi.org/10.21203/rs.3.rs-690433/v1

Participation in international conferences

Oral presentations

- Almeida, J., Riel, N., Rosas, F. M., Duarte, J. C. (2019) Numerical modelling of induced subduction initiation: thermal control exerted by plate ages in polarity reversal during plateau docking. EGU2019, April 7th-19th 2019, Vienna, Austria

Poster presentations

- Almeida, J., Riel, N., Rosas, F. M., Duarte, J. C. (2020) Subduction initiation by polarity reversal. Ciências Research Day 2020, October 28th, Lisbon, Portugal
- Almeida, J., Riel, N., Rosas, F. M., Duarte, J. C. (2019) Subduction initiation by polarity reversal. RELiCT, September 12th-13th, Lisbon, Portugal
- Almeida, J., Riel, N., Rosas, F. M., Duarte, J. C. (2018) Preliminary numerical modelling results of induced subduction initiation: the slab vs. overriding plate thermal control on subduction polarity flip. EGU2018, April 8th-13th 2018, Vienna, Austria.

- Almeida, J., Riel, N., Rosas, F. M., Duarte, J. C. (2018) Preliminary numerical modelling results of induced subduction initiation: the slab vs. overriding plate thermal control on subduction polarity flip. Ciência 2018, July 2nd-4th 2018, Lisbon, Portugal

List of figures

List of tables

List of acronyms and abbreviations

The following acronyms and abbreviations are used in this thesis:

BCs – Boundary Conditions

DP – Downgoing plate

ED – Early double-sided

FEM – Finite Element Method

F_B – Negative buoyancy of the slab

F_{SP} – Slab-pull Force

HPC – High-Performance Computing

IBM – Izu-Bonin-Mariana

INSZ – Inductively Nucleated Subduction Zones

LaMEM – Lithosphere and Mantle Evolution Model

LAB – Lithosphere/asthenosphere thermal boundary

LD – Late double-sided

LIPs – Large Igneous Provinces

L_{NSZ} – Length of the newly formed subduction zone

MOR – Mid-ocean ridge

OJP – Ontong-Java Plateau

OP – Overriding Plate

PIC – Particle-in-Cell

PIV – Particle Image Velocimetry

PV – Paraview

SNSZ – Spontaneously Nucleated Subduction Zones

SS – Single-sided

SP – Subducting plate

SU – Systematically unstable

SZ – Subduction zone

SZI – Subduction zone initiation

UW – Underworld

V_{OP} – Horizontal overriding plate velocity

V_{SP} – Horizontal subducting plate velocity

W_P – Along-trench width of the oceanic plateau

W_R – Width ratio

YOL – Young oceanic lithosphere

Table of contents

Chapter 1. Introduction

(this page has been left intentionally blank)

1.1. Introduction to subduction zones

When we think about subduction zones, we think of a type of plate boundary where oceanic lithosphere (the subducting plate) sinks into the upper mantle (Stern, 2002), leaving another plate at the surface (the overriding plate). In fact, they are far more than this. They represent the primary driving force behind mantle convection, of which Plate Tectonics is the surface expression (Stern, 2002) and, as the sinking oceanic lithosphere is significantly colder than the surrounding mantle, they are also the main cooling mechanism of our planet (Crameri et al., 2018).

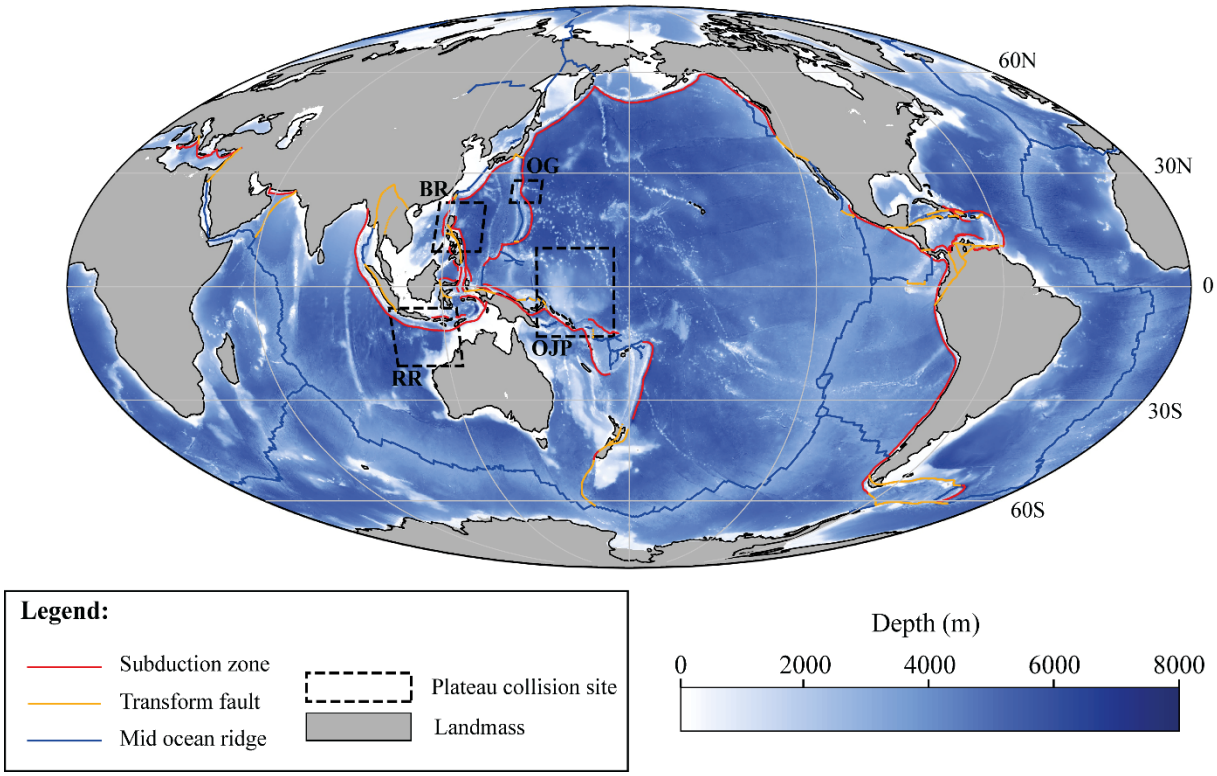

Figure 1.1 – Global plate boundary distribution. Plate boundaries data from Bird (2003). The dashed squares represent exotic terrane collision sites, which are further detailed in section 3, specifically in Figure 1.7. BR – Bentam Rise, RR – Roo Rise, OG – Osagawara Plateau, and OJP – Ontong-Java Plateau.

1.2. Long-term impact of subduction zones

The continuous motion of subduction zones has shaped the surface of our planet since the onset of Plate Tectonics. This motion has been shown to be the primary drive behind continental collision (e.g., Stern, 2002), by pulling continents together until they inevitably collide, closing the ocean between them. Collision not only forms long mountain chains but also stitches

continents together (e.g., collision of the Indian plate with Eurasia). Even without the collision of continents, a subduction zone can trigger orogeny as the consequence of the subduction-induced mantle flows (e.g., Schellart, 2017). Furthermore, previous studies have argued that the production of felsic materials by subduction zone volcanic arcs may have significantly contributed to the formation of continental crust (e.g., Hawkesworth, Cawood and Dhuime, 2020). Thus, subduction zones represent not only one of the main drives for continental growth and orogeny, but also one of the main reasons behind the existence of continents themselves.

This continuous reshaping of the surface of our planet, induced by subduction zones, has also been shown to have a significant impact on biodiversity. Subduction zones change the topography of the continents, as well as the morphology of the seafloors, leading to shifts in the atmospheric and oceanic currents, which have been shown to have fundamental implications for biodiversity (e.g., Leprieur et al., 2016). Additionally, the opening of oceans by subduction zones (i.e., back-arc basins, which include for instance the Sea of Japan) can lead to the isolation of different biological communities (e.g., by opening an ocean between them), while a closing ocean promotes competition by bringing them together.

1.2.1. Impact of subduction zones on humanity

Even without considering the long-term biological impacts of a subduction zone, they exert a tremendous effect on humanity itself. Consider the location of subduction zones. A vast majority of these plate boundaries are located around the Pacific Ocean (see the red lines in Figure 1.1), a narrow region also known as the Pacific Ring of Fire or the Circum-Pacific belt. This region, where ca. 90% of all recorded earthquakes and 75% of all known volcanoes can also be found, is inhabited at least 400 million people (Pesaresi et al., 2016) which are permanently impacted by subduction zones.

While the looming threat of megathrust earthquakes or explosive volcanic eruptions constitute a clear danger for populations living in the vicinity of a subduction zone, the volcanic products (i.e., lavas and ash) provide excellent growing soils and nurture a highly diverse sea life. Even more, the inherent beauty of volcanic peaks helps to boost local economies by driving tourism. Although a subduction zone can help nurture civilization, it will inevitably cause massive damage upon it. It is, therefore, vital to better understand its dynamics as to minimize the threat.

1.3. Anatomy of a subduction zone

1.3.1. General structure

A subduction zone is geometrically simple. If we were able to open our planet and look at one from its side (Figure 1.2), we would see the subducting plate (or slab) plunging into the mantle while the overriding plate remains at the surface. These features are clearly observable in seismic tomography studies (e.g., Zhao, 2004). Looking closely, we would see that the two plates are separated by a thin, highly mobile channel (Duarte et al., 2015; Gerya et al., 2008) – the subducting channel or interface – and that a portion of the sediments of the subducting plate were being scraped off and accumulating along the edge of the overriding plate – accretionary wedge (Figure 1.2). At the surface, the area which marks the transition between the two plates is represented by a deep oceanic chasm or trench (i.e., the subduction trench). While in a cross-section this is marked by a single point (Figure 1.2), its 2D geometry is normally curved, as seen in Figure 1.1. The type of curvature depends on factors such as the length of the subducting slab (e.g., Schellart et al., 2007; Schellart, 2017) or the type of weakening mechanisms present the overriding plate (e.g., Munch et al., 2020).

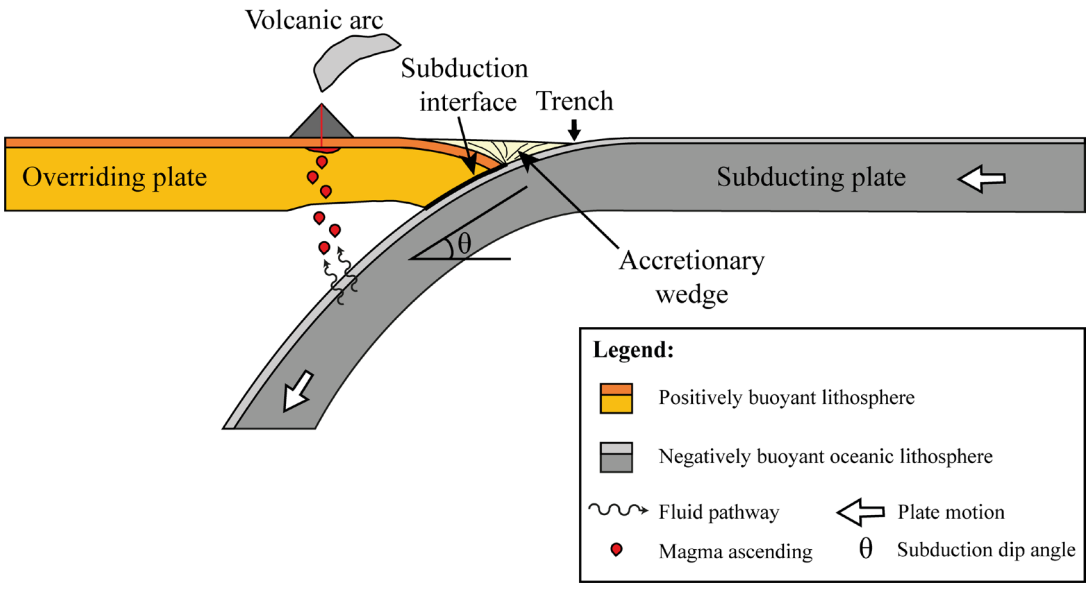

Figure 1.2 – Schematic cross-section of a subduction zone (not to scale). The thin, wavey arrows indicate the water/fluid ascent path from the dehydrating slab into the mantle wedge; the large white arrows indicate plate motion; the red blobs mark the magma ascent path; and the thick black line marks the subduction zone interface.

On average, subducting plates dip into the mantle with an angle of ca. 30 degrees (shallow subduction zone dip angle, θ in Figure 1.2), a value which increases at depth (Lallemand et al., 2005). This low dip helps inducing a strong compression on both the overriding plate and subduction interface. Occasionally, due to both this compression and asperities on the surface of the slab, the subduction interface (Figure 1.2) is locally locked (e.g., Wells et al., 2003). This leads to a strong accumulation of elastic strain along the interface (e.g., Scholz, 2019), which is inevitably released in massive megathrust earthquakes (e.g., Meier et al., 2017). Although the magnitude of the resulting earthquake may not be affected by the shallow slab dip (e.g., Schellart and Rawlinson, 2013), recent studies have suggested that a shallower dip may enhance the occurrence of tsunamis during these events (Oryan and Buck, 2020).

1.3.2. Lithology and fluids in subduction zones

In terms of lithology, the (oceanic) subducting plate is composed by two major layers, a thin crust and thicker lithospheric mantle. In theory, the oceanic crust is composed by a sedimentary layer of variable thickness, a sequence of different (mafic) basaltic formations (i.e., pillow lavas, dyke complexes and a gabbroic root), while the lithospheric mantle is mostly composed by different types of (ultramafic) peridotites. In practice, by the time a given portion of the oceanic plate reaches the subducting trench, it has been strongly altered by percolation of ocean water within it (e.g., Escartín et al., 2001; Prigent et al., 2020; Searle and Escartín, 2004). The role of this hydration process during subduction is essentially twofold:

1) It turns the dry and stronger basalts/peridotites into weaker and hydrated lithologies, such as serpentinites (Deschamps et al., 2013; Escartín et al., 2001). When entering the subduction interface, these materials act as a lubricant which maintain the subduction interface weak (e.g., Reynard, 2013 and references therein), and

2) As the subducting slab sinks into the mantle, it heats up and, at depths between 70 and 300 km progressively dehydrates releasing large quantity of fluids (i.e., primarily trapped in the mineral lattice structure of hydrated minerals such a micas and amphibole, Faccenda et al., 2012b).

This dehydration process also removes the lighter (more mobile) elements present in the mineral structure, increasing the overall density of the slab, facilitating its sinking into the

deeper regions of the mantle. This water released from the slab ascends into the mantle wedge (see Figure 1.2), chemically inducing its partial melting (Stern, 2002). The newly formed magmas ascend through the mantle and begin pooling beneath the crust (at the Moho level) due to their high density (White, 2013). Over time, the pooled magmas precipitate out the denser (i.e., high MgO-FeO) phases. Eventually, these differentiated (more silica-rich) magmas ascend through the lithosphere (Figure 1.2), allowing the magma to interact with the surrounding lithosphere, which results in a further enrichment in both silica and water contents (e.g., Farner and Lee, 2017). Finally, the silica-rich magmas reach the surface, feeding the volcanic arcs.

1.3.3. Force balance and mantle flows in a subduction zone

A subduction zone is driven by the negative buoyancy of the subducting slab (F_B, see Figure 1.3), or put in other words, it is driven by its relatively higher density of the subducting slab when compared with the surrounding mantle. The negative buoyancy of a subducting slab is directly proportional to its age, as oceanic plate ages becomes thicker and denser as they spread from the mid ocean ridge (Gurnis et al., 2004; Oxburgh and Parmentier, 1977).

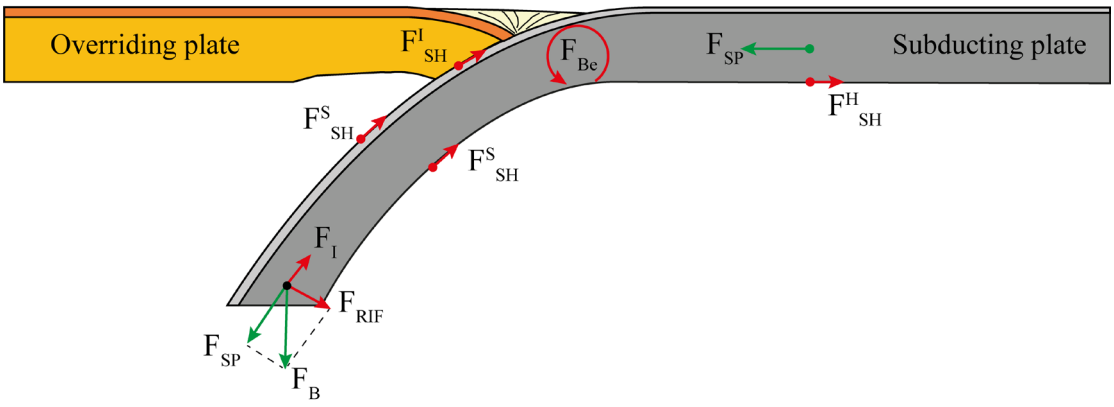

Figure 1.3 – Forces present in a subduction zone. The only driving force is the negative buoyancy of the subducting slab (F_B), which is resisted by the inertial force (F_I), the bending force (F_{Be}), the different viscous shear resisting forces (F^I_{SH}, F^S_{SH}, F^H_{SH}) and the rollback-induced flow force (F_{RIF}). The slab-pull force (F_{SP}) is the tangential expression of the buoyancy force (F_B). The vector lengths do not reflect the absolute magnitude of the different components. Red and green vectors represent resisting and driving forces, respectively.

Furthermore, is has been shown (e.g., Schellart, 2004a; Irvine and Schellart, 2012) that stable (steady-state) subduction zones show relatively constant subducting plate velocities (i.e., the velocity at which the subducting plate moves towards the trench). If a velocity is constant, according to the laws of motion, no acceleration can be present on the system and, thus, the resulting force balance must be null. As gravity is ever-present and drives the system forward (buoyancy force, F_B), there must exist a set of resisting forces (e.g., Turcotte and Schubert, 2002) which counter-act its effects:

$$F_B = F_I + F_{Be} + F_{RIF} + F_{SH}^{I} + F_{SH}^{H} + F_{SH}^{S} \quad (1.1)$$

These resisting forces (Figure 1.3) stem from the motion of the slab through a viscous body (viscous shear forces, F_{SH}), the geometry of the slab itself (bending force, F_{Be}), the retreat of the slab (rollback-induced flow, F_{RIF}) and inertia (F_I).

As the slab moves, the friction between the lithosphere and sub-lithospheric mantle (viscous shear forces, F_{SH}^{S} and F_{SH}^{H}) hinder this motion, dissipating part of the energy supplied by the negative buoyancy of the slab. A similar, but minor, viscous shear resistance is also imposed by the subduction interface (F_{SH}^{I}).

As the deeper portions of the slab are dehydrated and their density increases, their negative buoyancy increases. By increasing F_B, there is a simultaneous increase of the normal component of this force (F_{RIF}), which induces a horizontal retreat of the slab, displacing the mantle around and beneath it (e.g., Schellart, 2004a; Schellart et al., 2007; Strak and Schellart, 2016). This normal component of the buoyancy force imposed on the upper mantle (rollback-inducing force, F_{RIF}) generates a trench-parallel type of mantle flow (Figure 1.4) – toroidal flow. The sinking of the slab itself (specifically the drag it exerts on the upper mantle, F_{SH}^{S}) induces a trench-normal, mostly vertical mantle-flow (Figure 1.4) – poloidal flow. Both of which help dissipating part of the energy by the negative buoyancy of the slab tip.

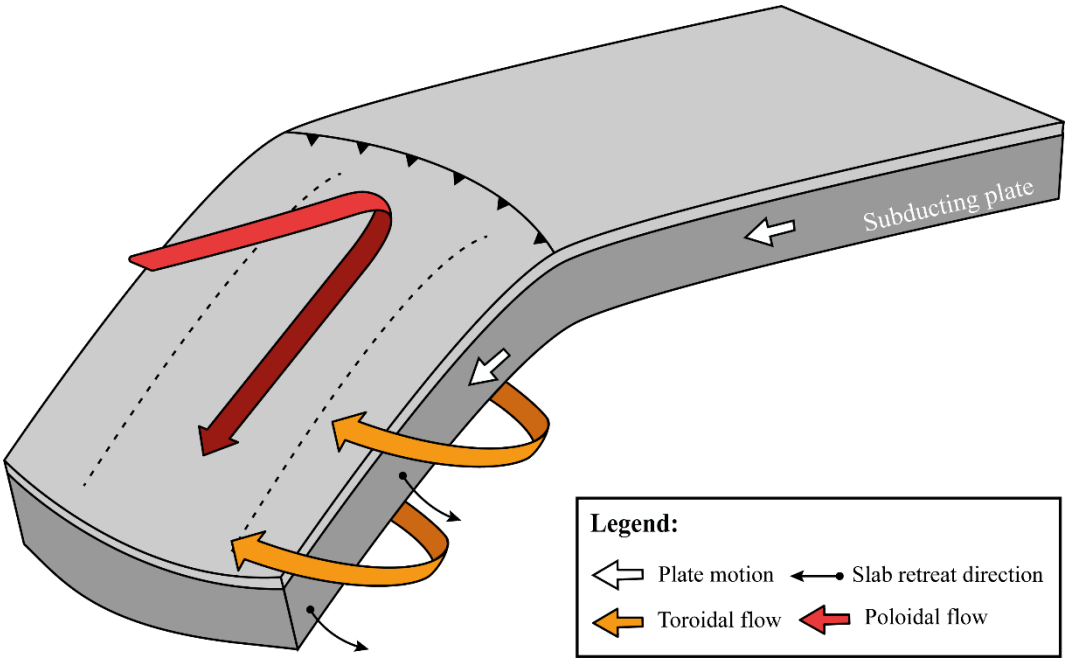

Figure 1.4 – Simplified sketch of the three-dimensional subduction induced mantle flows. The orange arrows represent flow from behind the slab into the front while red arrows indicate flow from the surface into the deeper mantle along the front of the slab.

The geometry of subduction zones can also contribute to resist the imposed negative buoyancy. The vertical curvature of the slab, an ubiquitous property of a subduction zone, helps dissipate part of the energy imposed by the sinking slab (Irvine and Schellart, 2012). This dissipation is expressed by the bending force (F_{Be}), the magnitude of which is a function of plate age (Irvine and Schellart, 2012). Specifically, in older (thicker and colder) oceanic plates, less energy is dissipated in their bending (Irvine and Schellart, 2012), which results in wider bending radius.

Last, and truly least, the inertial force (F_I) corresponds to the intrinsic resistance of any moving body to changes in acceleration. However, as the geological accelerations of ca. 10^{-22} m/s^2 (e.g., Gerya, 2010) are far lower than the gravitational acceleration ($g = 9.81$ m/s^s), this force is generally considered to be negligible. This is further expanded in Chapter 2.

As we've seen before, the dynamics of subduction zones have been extensively studied (e.g., Stern, 2002; Gerya, 2011, and references therein) and, by now, are relatively well understood. However, over the past few decades, one simple question has inspired debate and controversy: how and why does a subduction zone initiate?

1.4. The problem of subduction zone initiation

1.4.1. Why is forming a subduction zone difficult?

The initiation (or birth) of a subduction zone has always been a fundamental part of the Wilson cycle (Dewey and Burke, 1974; Wilson, 1966). According to this concept, after a period of oceanic spreading, an oceanic plate should begin subducting. This can be deduced from the rather simple observation that the oldest seafloors are far younger than the surrounding continents and generally younger than ca. 200 Ma (Müller et al., 2008), which suggests that, somehow, they must be consumed. However, despite numerous different explanations (cf. Stern, 2004; Gerya, 2011; Stern and Gerya, 2018; Crameri et al., 2020 and references therein), subduction zone initiation (SZI) is still a missing link in the geological knowledge.

The underlying problem behind any explanation for subduction zone initiation is deceivingly simple, and can be divided in two questions:

1. What is the driving force behind it?
2. Where and how is a new subduction interface formed?

While these may seem simple enough questions to answer, they have shown to be far from it, and have driven controversy over the past few decades.

It has been well established in the scientific community that the main driving force behind plate tectonics is the gravitational instability of oceanic plates (Vlaar and Wortel, 1976), also known as its negative buoyancy. So, it should be relatively straight-forward that old, dense, highly negatively buoyant oceanic plates simply yield to their weight, rupturing the lithosphere and sinking into the mantle. However, previous studies have shown that the bending force required to cause full lithospheric rupture and subsequent subduction zone initiation was ca. 7 x 10^{13} N/m (e.g., Cloetingh et al., 1989; Duarte et al., 2013; Gurnis et al., 2004; Hall et al., 2003; Mueller and Phillips, 1991). If we compare these values with the naturally available forces, such as the estimated ridge push force of ca. 2-3 x 10^{12} N/m (e.g., Parsons and Richter, 1980; Schellart, 2004a) or the estimated slab pull force of ca.1 x 10^{13} N/m (e.g., Conrad and Lithgow-Bertelloni, 2002; Hall et al., 2003), it would seem that only a subduction zone can exert the necessary force to trigger the lithospheric failure required to nucleate another subduction zone. In essence, and quite paradoxically, under present-day conditions, a new subduction zone cannot be formed without a pre-existent one.

The second problem lies in the formation of the subduction zone interface. This weak, highly localized shear zone (e.g., Duarte, Schellart and Cruden, 2015) must be formed either during or before the initiation of a subduction zone. Consequently, it needs to be either inherited from previous lithospheric heterogeneities such as continental margins (e.g., Lévy and Jaupart, 2012), pre-existing transform faults (e.g. Nikolaeva, Gerya and Marques, 2010) or previous subduction zone interfaces (e.g., Lallemand et al., 2001); or formed by one or more different strain localizing processes such as fluid weakening (e.g., Dymkova and Gerya, 2013), grain-size reduction (e.g., Platt and Behr, 2011) or shear heating (e.g., Thielmann and Kaus, 2012; Crameri and Tackley, 2016).

These two criteria – the source of driving force and type of lithospheric weakness which forms the subduction interface – have served as the fundamental classification tools for different subduction zone initiation (SZI) events (e.g., Stern, 2004a; Stern and Gerya, 2018; Crameri et al., 2020).

1.4.2. Classification of SZI events by Stern and Gerya

The first classification established for SZI events was presented by Stern in 2004, and later expanded (Stern and Gerya, 2018). In these studies, the authors proposed classifying these events based on the presence or absence of external forcing (see Figure 1.5), specifically if they were, or not, triggered by a pre-existent active subduction zone. Thus, SZI events were divided in two major groups: spontaneous nucleation of subduction zones (SNSZ, Figure 1.5A) and induced nucleation of subduction zones (INSZ, Figure 1.5B).

In this classification, SNSZ implies the gravitational collapse of oceanic lithosphere into the mantle without any external forcing, in three general geodynamic contexts:

1. Along passive continental margins under specific conditions of large sediment accumulation and critical lithostatic loading (Figure 1.5-A1).
2. Along a transform fault, laterally juxtaposing plates of strikingly contrasting age (Figure 1.5-A2).
3. Along the edge of an active mantle plume (Figure 1.5-A3).

The nucleation of subduction zones as the consequence of the foundering of old lithosphere at passive margins and transform faults has been the most widely studied and modelled

subduction initiation mechanism (e.g. McKenzie, 1977; Cloetingh, Wortel and Vlaar, 1982, 1989; Mitchell, 1984; Mueller and Phillips, 1991; Kemp and Stevenson, 1996; Faccenna et al., 1999, 2002; Nikolaeva, Gerya and Marques, 2010, 2011; Marques et al., 2013; Mariana et al., 2015; Zhong and Li, 2019), and has been the primary explanation for the formation of the Izu-Bonin-Mariana (IBM) subduction zone (e.g. Nikolaeva, Gerya and Connolly, 2008; Reagan et al., 2019) and the Tonga-Kermadec subduction zone (e.g., Niu, O'Hara and Pearce, 2003). Regardless, to this day, no examples of spontaneous subduction initiation nucleating at old passive margins are known to have occurred anywhere during the Cenozoic Era (Duarte et al., 2013; Gurnis et al., 2004; Stern and Gerya, 2018) and the possibility of the spontaneous formation of a subduction zone at a transform fault has been shown to require unrealistically high forces and/or weakening conditions (e.g., Arcay et al., 2019). By contrast, the formation of a new subduction zone by the interference of a mantle plume has been shown to be a possible explanation for the formation of the Lesser Antilles subduction zones (e.g., Whattam and Stern, 2015), the Cascadia Subduction zone (e.g., Stern and Dumitru, 2019), and even for the triggering of plate tectonics itself (e.g., Gerya et al., 2015),

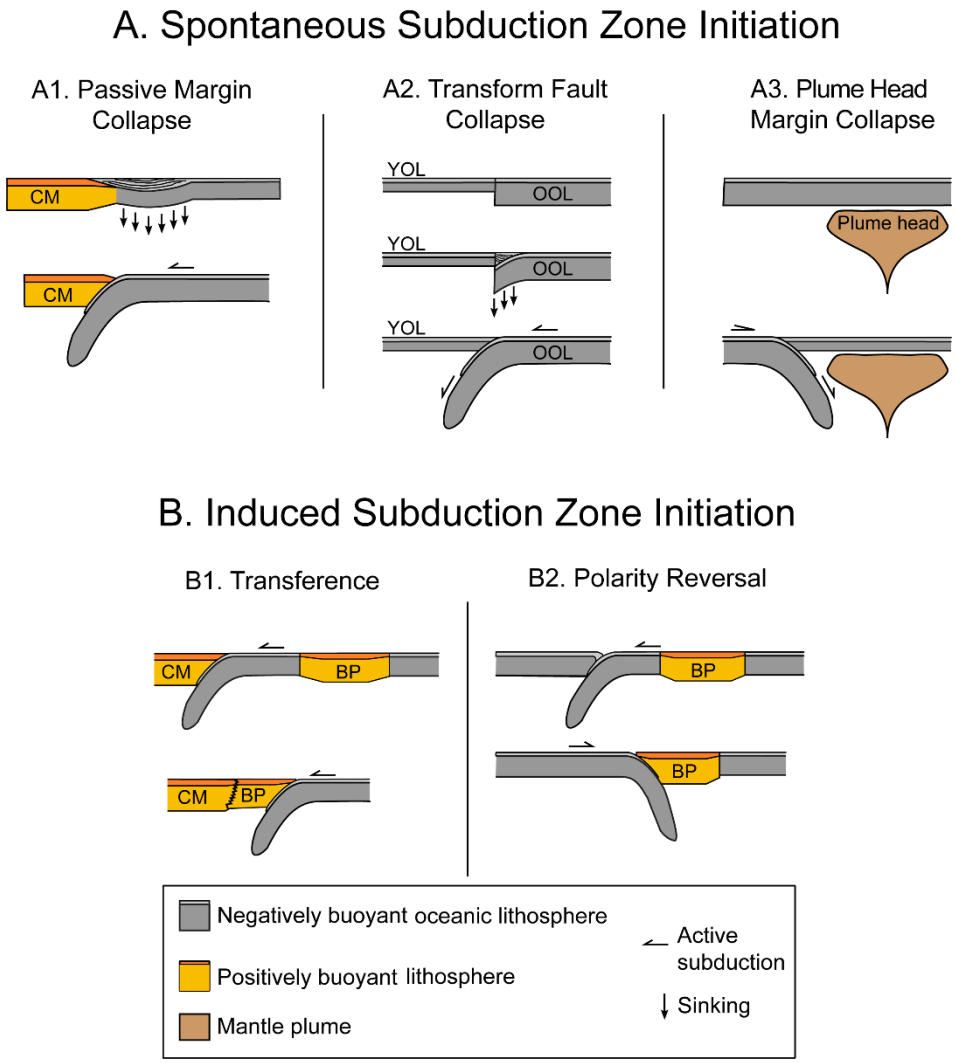

Figure 1.5 – Different fundamental modes of SZI according to Stern (2004) and Stern and Gerya (2018). **A.** SNSZ. **A1.** Passive margin gravity-driven collapse: the new subduction zone is assumed to form by rupture across the strong and thick lithosphere; **A2.** Collapse along a transform fault laterally juxtaposing two oceanic plates of markedly different ages: the new subduction zone is formed by gravitational foundering of the older oceanic plate. **A3.** Margin collapse by plume head: the oceanic plate collapses due to thermal induced mantle flow as the result of the ascending mantle plume. **B.** INSZ; **B1.** Transference subduction initiation: the arrival of a buoyant plateau at an active continental margin triggers the transference of the subduction zone to the back of the plateau, where a new subduction zone is nucleated; **B2.** Polarity-reversal subduction initiation: the arrival of a buoyant plateau (e.g., an oceanic ridge or a continental fragment) at an intra-oceanic subduction zone triggers the formation of a new subduction zone with an opposite polarity (i.e. dipping in the opposite direction). CM – Continental margin, YOL – Young oceanic lithosphere, OOL – Old oceanic lithosphere, BP – Buoyant plateau. Adapted from Stern and Gerya (2018).

The alternative INSZ assumes that new subduction zones are triggered when a positively buoyant block arrives at an active subduction zone (Figure 1.5B). Under specific conditions,

this cramming of the subduction trench can lead to the formation of a new subduction zone in one of two possible ways:

1. Subduction transference, or the formation of a new subduction behind the colliding block, with the same vergence as the original one (Figure 1.5-B1).
2. Polarity reversal, which implies the subduction of the overriding plate in the opposite direction relatively to the original subduction (Figure 1.5-B1).

Thus, under this classification, subduction zones are forced to initiate, and the type of initiation depends on the kinematic relationship with the original subduction zone.

1.4.3. Classification of SZI events by Crameri et al. *(2020)*

It is now accepted knowledge that a spontaneous foundering of lithosphere is unlikely, due to requiring unrealistic forces or weakening processes (e.g., Gurnis, Hall and Lavier, 2004; Arcay et al., 2019) and that, under present day Earth conditions, any subduction zone must be forced to initiate.

Under this assumption, a new classification has been recently suggested (Crameri et al., 2020), which focuses on the directionality of the force applied to initiate a subduction (Figure 1.6), rather than the specific geodynamic setting. In their study, the authors argue that all subduction zones are the product of both a combination of forcing mechanisms with different orientation/sources, and of the (re)activation of lithospheric scale weaknesses.

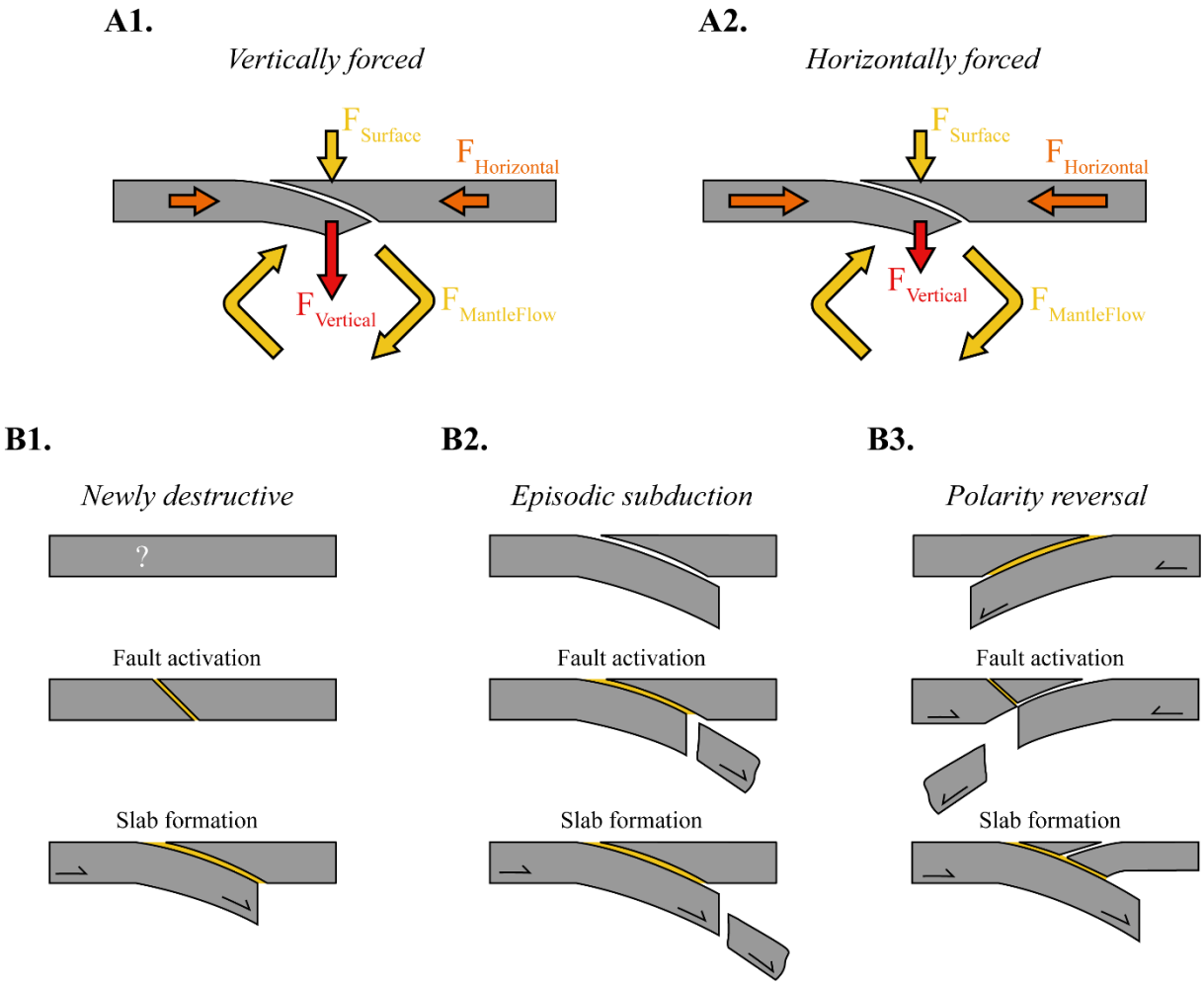

Figure 1.6 – Types of forcing and of SZI according to Crameri et al. (2020). **A.** Two non-exclusive end-members which indicate the dominant forcing in the triggering of a new subduction. Following this classification, the forcing can be either be **A1.** vertical, in which the forces are mainly derived from a combination of the negative buoyancy of the plate, the sedimentary load and/or mantle suction force, or **A2.** horizontal, in which the forces are derived from a combination of tectonic forcing and horizontal mantle flow. These two types of forcing are not mutually exclusive, and any natural case will be a combination of both types. The length of the arrows serves as a representation of the relative magnitude of their respective force. **B.** Classification of different types of SZI. The subduction zone can be formed because of: **B1.** a newly destructive event, in which a new interface is formed or migrates into an intact/pristine plate or at a non-subduction related weak zone (e.g., transform fault or continental margin); **B2.** the reactivation of an episodic subduction zone, maintaining the polarity; or **B3.** polarity reversal, where the previous overriding plate begins subducting in the opposite direction. The yellow shaded areas in B show the currently active subduction interfaces. Adapted from Crameri et al. (2020).

Under this classification, regardless of the mechanism that ultimately generates a new subduction zone (Figure 1.6B), the driving forces behind it are relatively well constrained (Figure 1.6A). While in nature, the formation of a new subduction zone will be the consequence of a plethora of differently oriented forces, Crameri et al. (2020) groups new subduction zones

in two non-exclusive end-members, which reflect the dominant force orientation for any specific initiation event:

1. *Vertically driven subduction zone initiation* (Figure 1.6-A1), in which the dominant forces behind SZI are mostly vertical, which include the gravitational potential of the sedimentary load (e.g., Erickson, 1993; Regenauer-Lieb, Yuen and Branlund, 2001) or an oceanic plateau (e.g., Niu, O'Hara and Pearce, 2003; Nair and Chacko, 2008), large scale mantle downwellings (e.g., mantle suction force, Baes, Govers and Wortel, 2011; Baes, Sobolev and Quinteros, 2018) or upwellings such as plumes (e.g., Ueda, Gerya and Sobolev, 2008; Whattam and Stern, 2015; Davaille, Smrekar and Tomlinson, 2017).
2. *Horizontally driven subduction zone initiation* (Figure 1.6-A2), in which the dominant forces behind SZI are mostly tectonic in origin. In these cases, new subduction zones are formed from plateau collision events (e.g., Pysklywec, 2001), due to tectonic convergence (e.g., Hall et al., 2003), or by horizontal mantle flows such toroidal flow (e.g., Baes, Govers and Wortel, 2011) or plume-induced flow (e.g., Gerya et al., 2015; Whattam and Stern, 2015).

The authors also group SZI events by assuming the existence of three types of the new subduction zone interface (Figure 1.6B), which can occur under both previously described force orientations:

1. *Newly destructive SZI* (Figure 1.6-B1). In this type of SZI, the subduction interface is either a new fracture zone along an otherwise intact plate; or the reactivation of a non-subduction related lithospheric-scale weak zone. This is, in essence, an expansion of the SNSZs proposed by Stern (2004) and is used to explain the same SZI events. As an example, under this new classification, the formation of the IBM subduction zone is indirectly triggered by the subduction of the Izanagi-Pacific ridge (Lallemand, 2016a) or the collision of the Olutorsky arc (Domeier et al., 2017).
2. *Episodic subduction SZI* (Figure 1.6-B2). Here, SZI corresponds to the reactivation of a pre-existing subduction zone interface, maintaining the polarity (or direction of subduction). After the original subduction is stopped during an unspecified tectonic event (e.g., plateau collisions, slab break-off, among others), the original interface is preserved as a lithospheric scale weak zone. This (fossilized) weak zone

can later be reactivated due to tectonic convergence, triggering a new subduction zone with identical polarity. The authors suggest this mechanism as an explanation for a few intermittent subduction zones such as Sunda-Java and Ryukyu.

3. Polarity reversal SZI (Figure 1.6-B2). This final SZI was the focus of this thesis and, accordingly, is more extensively explored below.

1.4.4. Exploring polarity reversal as a SZI mechanism

Both Stern (2004) and Crameri et al. (2020) defined polarity reversal as a subduction zone initiation mechanism (Figure 1.5-B2 and Figure 1.6-B3). This has been widely studied as the outcome of the attempted subduction of an exotic terrane (e.g., Tetreault and Buiter, 2014), such as:

1. oceanic plateaus (e.g., Cooper and Taylor, 1985; Mann and Taira, 2004; Kerr et al., 2005), which are regions of overthickened oceanic lithosphere by large igneous provinces (LIPs), such as the Ontong-Java Plateau (Mann and Taira, 2004) or the Caribbean Colombian Plateau (Wright and Wyld, 2011);
2. aborted submarine ridges such as the Bentham Rise (Lallemand, 2016b) or the Osagawara Plateau (Gong et al., 2019);
3. fragments of rifted continental lithosphere (e.g., Pysklywec, 2001b; Faccenda, Gerya and Chakraborty, 2008); or
4. oceanic arcs, such as the Olutorsky arc (e.g,. Konstantinovskaia, 2001; Baes, Govers and Wortel, 2011b).

The arrival of an exotic terrane to an active subduction zone is a relatively common feature (Tetreault and Buiter, 2012), and is currently occurring around the Pacific at several sites (Figure 1.7). Once it occurs, the active subduction zone is either partially or fully blocked, depending on the width of the colliding terrane. During such events, one possible outcome is the accretion of the exotic terrane onto the overriding plate (e.g., Tetreault and Buiter, 2012), the break-off of the prior subducting slab (Figure 1.8A, green shading) and consequent termination of the subduction system. The relative frequency of these break-off events is extensively discussed in Chapter 3.

However, despite the slab break-off and local subduction zone termination, it is possible that a lithospheric scale weak zone is formed on the overriding plate during a collision event

(Figure 1.8A, red shading), be it as the result of localized weakening (see Chapter 3) or the overthrusting of the volcanic arc above this plate (see Chapter 4). Once formed, this weak zone can be activated by the continuous convergence by the laterally active subduction (on both sides of the colliding block), underthrusting and driving the overriding plate into the mantle (Figure 1.8B). Once the underthrusted overriding plate reaches a critical depth (ca. 200 km), its negative buoyancy overcomes the mantle's viscous resistance. At this stage, the sinking of the overriding plate no longer requires the pull of the nearby active subduction zone (Figure 1.8C) and a complete reversal of polarity is achieved, with a new slab self-sufficiently subducting in an opposite direction to the previous one (Figure 1.8C).

In short, the collision of an exotic terrane with an active oceanic subduction zone can have two outcomes: local/total termination of the subduction zone (along with the break-off of the subducting slab), resulting in the accretion of the terrane to the overriding plate (e.g., Vargas and Mann, 2013) or the reversal of the subduction polarity.

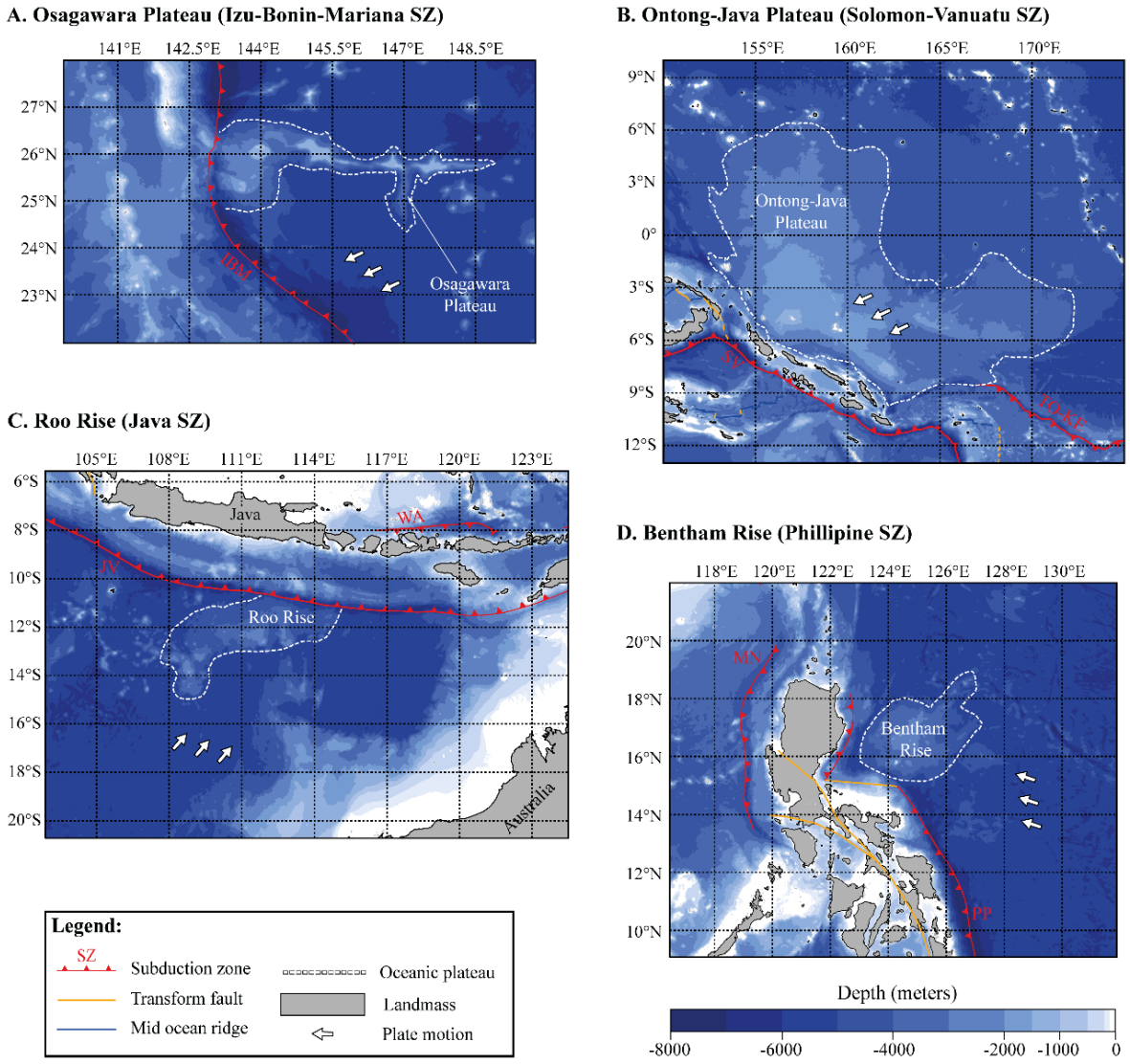

Figure 1.7 – Examples of ongoing exotic terrane collision events in and around the Pacific Ocean. The location of the insets can be found in Figure 1.1. **A.** Osagawara Plateau. This submarine ridge is presently being subducted at the Izu-Bonin-Mariana subduction zone, with no discernible development of a new subduction. A seismic study of the area (Gong et al., 2019) showed some normal fault development during the collision, which could hint at the formation of a new subduction zone interface. **B.** Ontong-Java Plateau. This large oceanic plateau initiated its collision with the Solomon arc during the Miocene, leading to local termination of the Pacific subduction zone and the triggering of the Solomon-Vanuatu subduction zone (Mann and Taira, 2004). A more detailed exploration of this case is found in Chapter 3 and Chapter 4. **C.** Roo Rise. This submarine ridge is presently subducting at the Java subduction zone and is the likely culprit of the formation of the Wetar subduction zone (Baes et al., 2011). **D.** Bentham Rise. This submarine ridge is presently subducting at the Phillipines subduction zone. This collision event has locally terminated the subduction zone, joining the two active segments with a transform fault (Lallemand, 2016). It is currently unclear if the formation of the Manila subduction zone was a consequence of

this collision (Crameri et al., 2020). Subduction zones in the figure: IBM – Izu-Bonin-Mariana, JV – Java, MN – Manila, PP – Phillipines, SV – Solomon-Vanuatu, TO-KE – Tonga-Kermadec, and WA – Wetar.

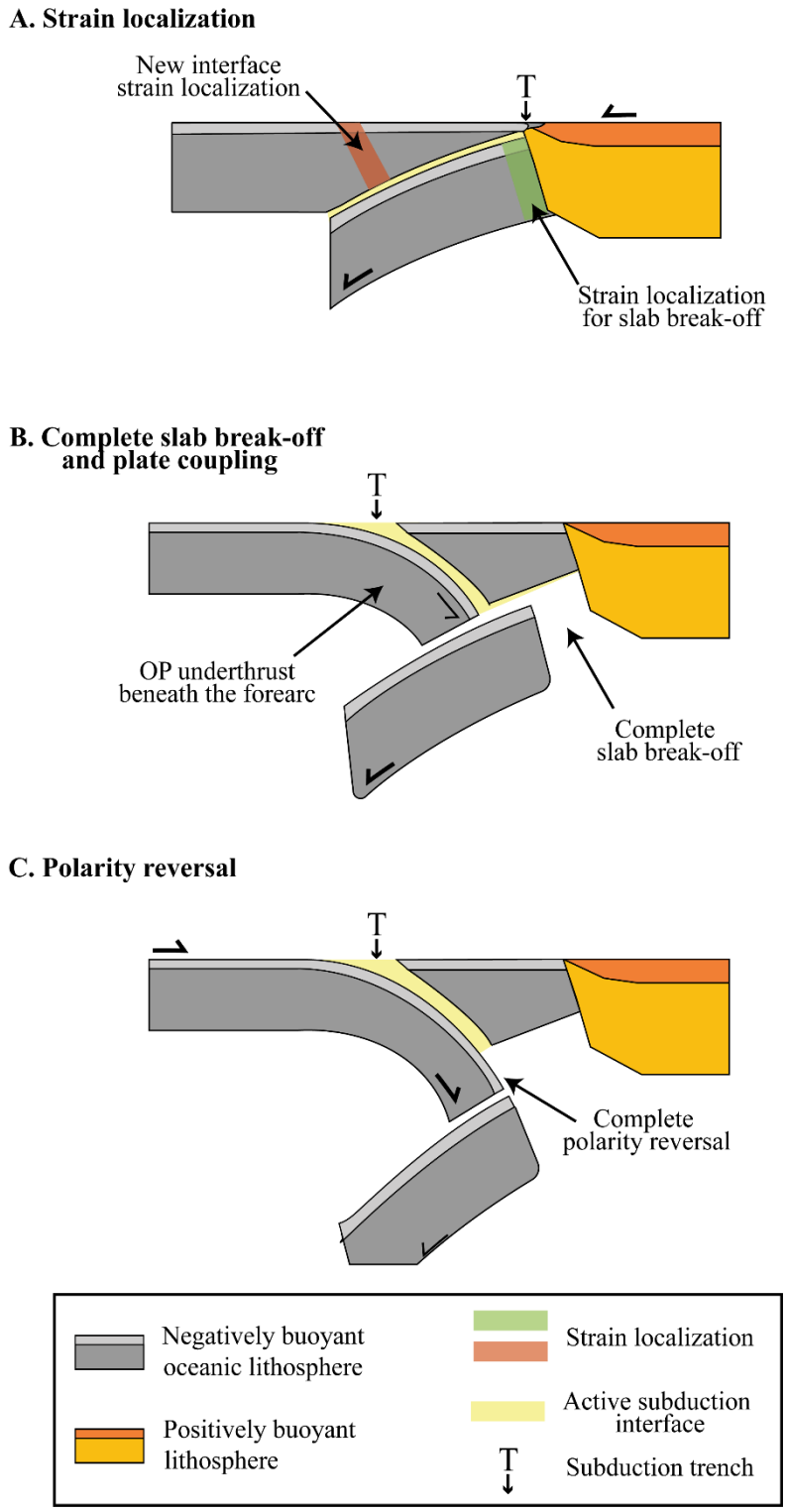

Figure 1.8 – Example of a polarity reversal SZI event sequence (figure not to scale). **A.** Arrival of a positively buoyant block to the active trench, causing strain localization on the overriding plate (red) and in the slab (green).

During collision, strain localization at the edge of the colliding plateau is inevitable, but relatively unlikely on the overriding plate. **B.** Slab breaks off and begins bending the overriding plate backwards, forming a new subduction interface along the previous strained areas. **C.** Polarity reversal. At this stage, the overriding plate has started subducting with opposite polarity. The previous slab continues sinking into the mantle and can still be attached to the new subducting plate. The half arrows represent the plate motion, with thicker arrows indicating which plate is currently actively subducting.

While both outcomes are well established in the geological record (e.g., Tetreault and Buiter, 2014), the specific dynamic conditions (i.e., force balance) that leads to the occurrence of polarity reversal SZI are remain elusive. Thus, it is the objective of the present thesis to shed some light into the geodynamic constraints which allow for the development of a new subduction zone by polarity reversal. Furthermore, it specifically focuses on polarity reversal events triggered by the arrival of oceanic plateaus to active subduction trenches, which has shown potential to explain some Cenozoic SZI processes, such as the Solomon-Vanuatu arc (e.g., Hall, 2002; Mann and Taira, 2004), the Lesser Antilles arc (e.g., Buchs et al., 2010; Wright and Wyld, 2011), or the Kamchatka/Aleutian arcs (e.g., Konstantinovskaia, 2001).

With this focus, two dynamical modelling studies were conducted (i.e., in the absence of any external forcing) to assess which different parameters can exert control over the dynamics of polarity reversal SZI. These included:

1. The thermal age contrast between the overriding and the subducting plates (i.e., as proxies for their effective strengths) under 2D conditions (see Chapter 3) and 3D conditions (see Chapter 4).
2. The along-trench width of the oceanic plateau (see Chapter 4).
3. The presence of a buoyant magmatic arc in the overriding plate above the subduction zone (see Chapter 4).

1.5. The problem of single-sided subduction zone stability

If we are to obtain a complete reversal of polarity, it is fundamental to have the overriding plate sink into the mantle while the previous slab is broken off. However, what prevents both plates from subducting simultaneously into the mantle? Previous subduction zone and whole-mantle modelling studies have shown a tendency for the development of this simultaneous sink of both overriding and subducting plates (e.g., Tao and O'Connell, 1992; Tackley, 2000; Gerya, Connolly and Yuen, 2008; Crameri et al., 2012; Crameri and Tackley, 2015) or, in other words,

for the formation of convergent double-sided subduction zones. This double-sided subduction can also be either symmetric or asymmetric (Figure 1.9), with asymmetry merely implying that one plate is significantly stronger than the other (Tackley, 2000; Gerya, Connolly and Yuen, 2008).

Crucially, these unnatural-looking subduction zones have, so far, never been recorded on Earth (Gerya et al., 2008) and, thus, are likely the result of some process that does not occur in our planet. To explain their prevailing occurrence in modelling studies, a few hypotheses have been put forward. Tackley (2000) argued that the subduction zones required the existence of a low friction channel between the overriding and subducting plates, which must be affected by strong strain localization/weakening. Gerya et al. (2008) explored the role exerted by the thickness of hydrated lithologies in the subducting plate (i.e., thickness of the weak crustal layers) and the strength of the subducting slab on the development of asymmetric single-sided subduction. In their study, using extreme plate age contrasts (1 Myr overriding and 100 Myr subducting plates), they demonstrate that a stable asymmetric subduction zone relies on a strong subducting plate ($\sin(\phi)>0.15$, with ϕ as the internal friction angle) separated from the overriding plate by a persistently weak subduction channel. Finally, Crameri et al. (2012) and Crameri and Tackley (2015) proposed that the occurrence of double-sided subduction zones hinges on the use of free-slip as opposed to free surface conditions, or that these could represent a temporary intermediate state between two episodes of single-sided subduction. In modelling, a free surface layer corresponds to a low viscosity layer with water- or air-like density (e.g., a more viscous atmosphere), allowing for the formation of topography. With the development of topography, the overriding plate can spread out above the subducting slab which, in turn, helps to enhance the bending of the subducting slab (Schmeling et al., 2008). By contrast, the use of top free slip conditions only allows the overriding plate to deform by bending downwards, which severely increases the possibility for the trigger of a double-sided subduction.

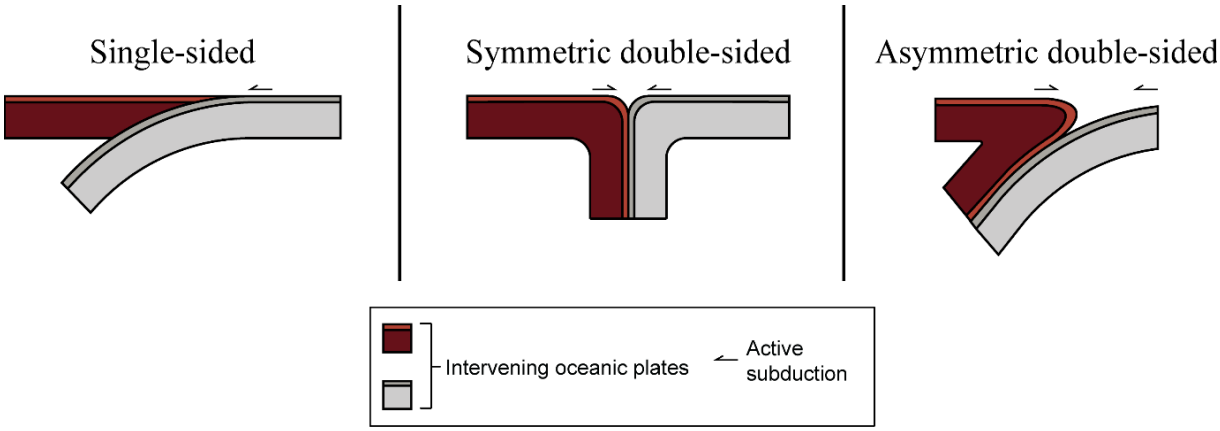

Figure 1.9 – Different modes of subduction, as described by previous geodynamic modelling studies. From left to right: "natural" asymmetric single-sided subduction; symmetric double-sided subduction, with two similarly strong plates (e.g., Tackley, 2000; Crameri et al., 2012); and convergent asymmetric double sided subduction, with a strong subducting slab paired with a weak overriding plate (e.g., Tao and O'Connell, 1992; Gerya, Connolly and Yuen, 2008).

In the two works regarding polarity reversal SZI conducted (Chapters 3 and 4), convergent double-sided subduction was observed under modelling conditions which were previously considered to hinder/counter this type of outcome, namely overriding plates older than the ones shown in Gerya et al. (see Chapter 3) and using free surface (see Chapter 4). This observation led to the development of a set of models which aim to explore the range of conditions in which modelling a single-sided subduction is possible, by both exploring:

1) The thermal age contrast between the initial overriding and subducting plates,
2) The use of both free-slip and free-surface conditions.

This work is still unfinished, but the current progress on it is discussed in Chapter 5.

1.6. Modelling subduction zone dynamics

1.6.1. What is modelling and why do we use it?

Up to this point, we have discussed the complex issue of forming a new subduction zone, why it remains single-sided, and the extent of our current understanding of the underlying dynamics. However, most subduction zone processes take place deep beneath the surface, at depths far beyond the reach of any drill. Not just this, but it can be remarkably difficult to

quantify variables in events that have taken place in the past. Our knowledge is, unsurprisingly, biased towards what we can observe and study today, close to the surface.

How can we then study these extremely long and prohibitively deep processes in an accessible manner? Simply, we use models to simulate a subduction zone in either a computer or a laboratory. Using modelling, it is possible to both shrink and simplify a subduction zone as to be simulated in a shorter and smaller scale (an exploration of this process can be found in Chapter 2).

Modelling has been successfully used to study subduction zones for decades, being used to explore a plethora of different topics such as the attempted replication of a specific natural subduction zone and its evolution (e.g., Capitanio et al., 2010; Betts et al., 2015; Meriaux et al., 2015; Schellart, 2017; Faccenna et al., 2018; Arcay et al., 2019; Schellart et al., 2019; Maunder et al., 2020), understanding how a subduction zone is formed (e.g., McKenzie, 1977; Cloetingh, Wortel and Vlaar, 1982; Regenauer-Lieb, Yuen and Branlund, 2001; Stern, 2004a; Nikolaeva, Gerya and Marques, 2010; Stern and Gerya, 2018; Crameri et al., 2020), how they are affected by different obstructing blocks (e.g., Faccenda, Gerya and Chakraborty, 2008; Capitanio et al., 2010; Tetreault and Buiter, 2012; Flórez-Rodríguez, Schellart and Strak, 2019) or the generic exploration of their dynamics and subduction induced mantle flows (e.g., Gurnis and Hager, 1988; Funiciello et al., 2003; Capitanio, Morra and Goes, 2007; Schellart and Moresi, 2013; Duarte, Schellart and Cruden, 2013; Chen, Schellart and Duarte, 2015; Strak and Schellart, 2016; Chen et al., 2016; Arcay, 2017; Riel, Capitanio and Velic, 2017; Ficini et al., 2017; Holt, Royden and Becker, 2017; Mériaux et al., 2018). Note that this is by no means an extensive list, and a complete account of the modelling studies in subduction zones would likely represent a thesis by itself.

The models used in previous studies can be broadly categorized in three types with increasing complexity: geometric, kinematic, and dynamic.

1.6.2. Geometric modelling of subduction zones

A great number of modelling studies use imposed different stress/velocity boundary conditions (e.g., imposed convergence velocity or background strain) as to match the regional conditions of the natural analogue or to mimic natural-like settings. This practice stems from

the early days of subduction zone modelling, in which authors tried to replicate the different observed subduction zone features such as the high heat flows in both marginal oceanic basins and supra-subduction volcanic island arcs (e.g., Andrews and Sleep, 1974, Figure 1.10) or the different geometries of subduction slabs (e.g., Gurnis and Hager, 1988), or even the formation of subduction zone trenches (e.g., McKenzie, 1977; Cloetingh, Wortel and Vlaar, 1989), by applying hard geometric and kinematic conditions on their models (also known as geometric modelling).

For instance, Andrews and Sleep, 1974 aimed to explain the occurrence of high heat flow below the volcanic arcs above subduction zones. The authors modelled a fast-sinking slab next to a fixed wedge of lithosphere (Figure 1.10) and quantified the associated material flow. The outcome of their study is a simplified thermal structure of a subduction zone, i.e., a cold anomaly which sinks into the upper mantle (Figure 1.11). Their modelling results also shows the sinking motion of slab into the mantle creating a return flow (poloidal flow), which drives hot mantle material into the mantle wedge (Figure 1.11). Noticing this, the authors argued that, based on their results, this induced return flow was a probable cause for the formation of both high heat flows and the formation of subduction zone volcanic arcs.

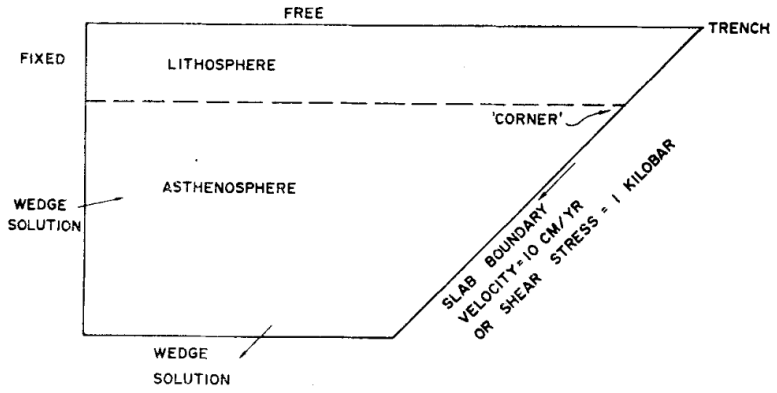

Figure 1.10 – Initial modelling setup from Andrews and Sleep (1974). This configuration allows the overriding plate (left) to not only stretch towards the trench but also to move upwards across the upper boundary.

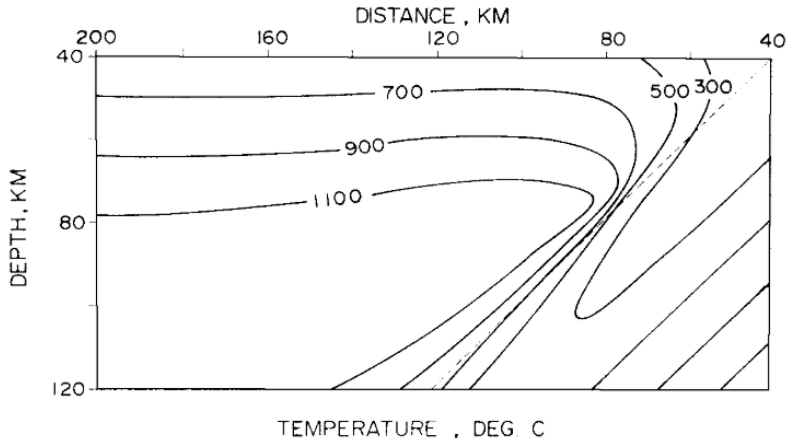

Figure 1.11 – Example of an early numerical subduction model, taken from Andrew and Sleep (1974). The dashed line marks the transition between the overriding (to the left) and subducting plate (to the right). The different solid lines represent isotherms.

As a second example, Gurnis and Hager (1988) ran a set of subduction zone models to constrain the range for the viscosity contrast between the upper and lower mantles. Although no forced convergence is imposed in the models, the authors set a no-velocity zone above the slab to artifically create an overriding plate. Consequently, they systematically tested different upper and lower mantle depth-dependent viscosities (η_U and η_L in Figure 1.12, respectively) using a relatively simple initial setup (Figure 1.12) which consisted of a fixed overriding plate, a mobile subducting plate and a mid-ocean ridge. The latter structure – mid ocean ridge – had two fundamental functions in the setup, namely that it acted as a natural stop point for the experiment (as its subduction triggered a slab break-off) and as a stabilizing structure to prevent the formation of cold drips along the edge of the model. Under their assumed model conditions, the authors showed that for a ratio between the upper and lower mantle viscosities (η_U/η_L) of 30, the obtained slab geometry closely mirrors the known seismographic patterns for Benioff areas around the world (Figure 1.13). Not just this, but their results closely mirrored the contorted nature of slabs which are present below the upper-lower mantle discontinuity and, thus, the authors argue that it stems from the sharp difference in viscosity between the layers.

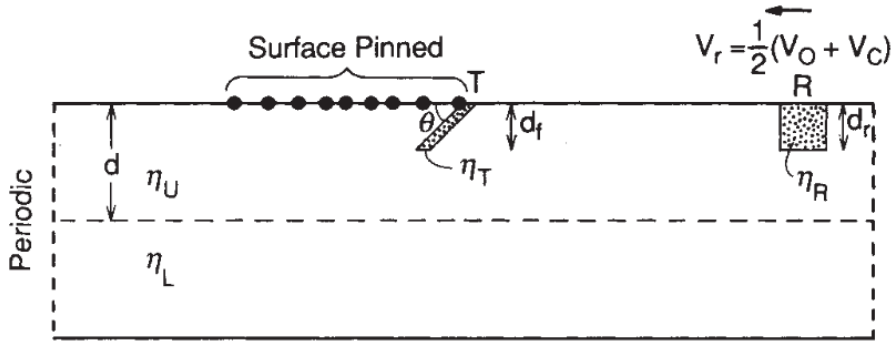

Figure 1.12 – Initial modelling setup from Gurnis and Hager (1988). The horizontal dashed line at a d depth marks the upper-lower mantle transition, d_f marks the depth of the initial slab and d_r marks the depth of the ridge. The spreading velocity (V_r) is imposed as a function of the velocity of plates on either side of the ridge. The surface of the overriding plate is fixed to prevent the plate from subducting.

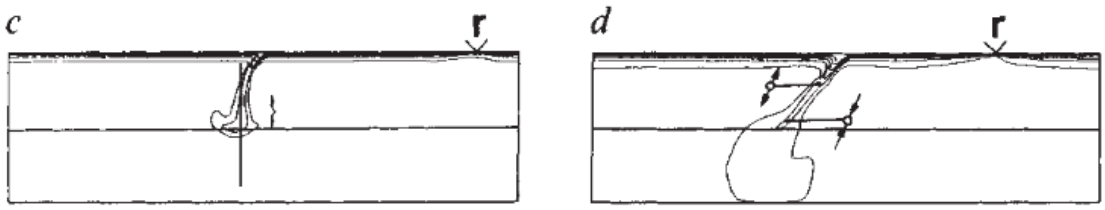

Figure 1.13 – Example of a subduction zone with $\eta_U/\eta_L = 30$ after 10 Myr (left) and 30 Myr (right). The younger slab, almost at the start of the simulation, subducts vertically into the upper mantle until reaching the upper-lower mantle transition. With increasing subducting plate age, the slab dip decreases, resulting in a shallower angle.

By *a priori* fixing the geometry of the model, this type of modelling approach can be a good way to obtain a first-order idea of the dynamics which control a subduction zone. For instance, by pinning the overriding plate, Gurnis and Hager (1988) were able to see how the slab bends and folds without struggling with double-sided subduction development. Both works represented an outstanding contribution to geodynamics, providing tremendous insight on the dynamics of subduction zones at the time.

However, due to the advancements in modelling, at present this type of modelling studies is highly restrictive as both kinematics and geometry are, for the most part, pre-determined.

1.6.3. Kinematic modelling of subduction zones

Over time, the usage of strong geometrically imposed conditions/boundaries has stopped being a common practice, but the imposition of convergence is still very common. By externally imposing convergence, modellers aim to reproduce the far-field forces which are exerted by the framework of plate tectonics. Thus, the expected outcome is a replica of the geometry and kinematics of natural subduction zones. Note that this is, by no means, an incorrect approach to modelling and, in some cases, imposing convergence is absolutely required. Take, for instance, a modelling study which explores the possibility of SZI along a passive margin. In such a case, without pre-imposed convergence, the model would simply stagnate, a result which is unlikely to produce relevant information. What must be avoided in these kinematic modelling studies is the imposition of forces which exceed those available in nature, a problematic well explored in Gurnis et al. (2004) and Arcay et al. (2019). When used correctly, this approach has led to highly relevant contributions which have explored in detail the evolution of the overriding-subduction plate interaction zone (e.g., Toussaint, Burov and Jolivet, 2004; Li, Gerya and Burg, 2010; Vogt et al., 2018); the formation of a new subduction zone along a passive margin (e.g., Marques et al., 2014, 2013; Nikolaeva et al., 2010; Regenauer-Lieb et al., 2001) and along a pre-existing fracture zone (Gurnis et al., 2004; Hall et al., 2003; Zhou et al., 2018); how the upper-most portion of a subduction zone evolves during a continental collision (e.g., Toussaint, Burov and Jolivet, 2004); or why a subduction zone is asymmetric (e.g., Gerya, Connolly and Yuen, 2008).

An example of a kinematic model which imposes stress boundaries is Regenauer-Lieb et al. (2001). In this work, the authors explored how the inclusion of water in an oceanic plate coupled with sediment loading can nucleate a new subduction zone. The objective was to obtain a lithospheric scale failure caused by just sediment accumulation along a passive (i.e., Atlantic-type margin), which resulted in the formation of a new subduction zone channel. To this extent, the authors ran models in which they use either wet basalt or dry basalt rheologies for their oceanic plate (Figure 1.14) and impose a far-field ridge-push force which is in line with the known natural forces (ca. 10^{12} N/m, according to Parsons and Richter, 1980; or Schellart, 2004). They argue that the by changing water content between the two, they can apply the effective weakening which is induced by the hydration.

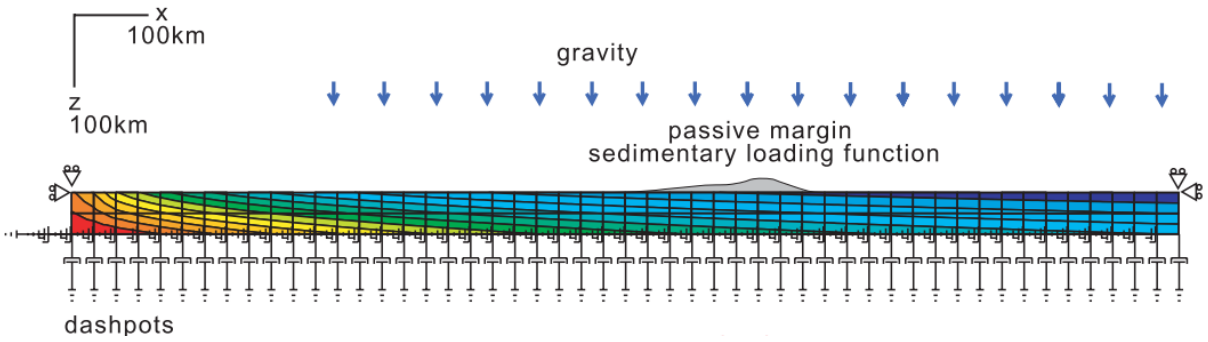

Figure 1.14 – Initial modelling setup from Regenauer-Lieb et al. (2001). The different colours represent the isotherms and describe the thermal profile of the plate. The dashpots below the plate describe the different pressure values. The edges of the model are fixed.

What they observed was that, for both dry and wet lithospheres, sediment loading was enough to produce lithospheric failure, albeit with different expressions. When the lithosphere was dry (i.e., dry basalt rheology, with a water content of 80 ppm), the uppermost portion of the lithosphere (the top 10 km) formed a set of faults while the lower-most portion produced a Rayleigh-Taylor instability (Figure 1.15, A-D). Conversely, a wet lithosphere showed strong lithospheric-scale strain localization which allows for the sinking of a portion of oceanic plate into the mantle. In this work, the authors show that, by merely introducing water in the system, a new lithospheric-scale weak channel can be formed (see Figure 1.15, E-H). As no subduction zone can be triggered without first forming a weak channel, understanding how strain is localized in the lithosphere due to weakening (under any mechanism) is fundamental.

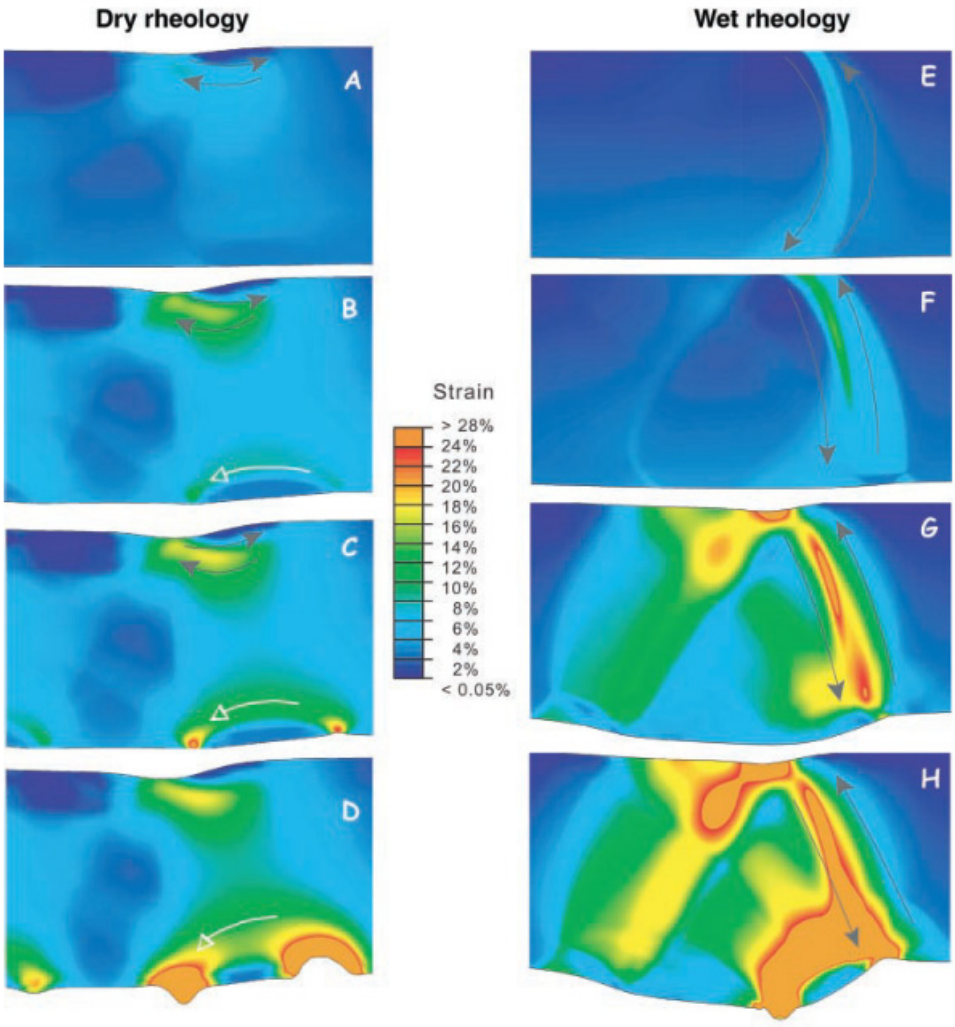

Figure 1.15 – Difference between the dry and wet rheologies for the oceanic lithosphere, as shown in Regenauer-Lieb et al. (2001). The dry lithosphere shows the formation of drip-like Rayleigh-Taylor instabilities along the base in D (centre), over a period of ca. 40 Myr. The wet lithosphere shows the quick development (ca. 10 Myr) of a subduction zone interface with high strain localization. The area shown represents 100 km thick and 100 km wide section of their model.

Although fundamental to be able to mimic specific types of subduction zone kinematics (e.g., simulating lateral pull in a 2D subduction zone model or convergence in 2D subduction zone initiation models), this modelling approach requires the modeller to be aware of the natural forces at stake. Under kinematic modelling, it is remarkably easy to either overlook or overestimate the forces behind a subduction system, which can result in a dynamically flawed model.

1.6.4. Dynamic or self-consistent subduction zone modelling

An alternative method of subduction zone modelling, which has gained popularity over the years, is the *dynamic* (also referred to as self-consistent or internally driven) approach of modelling. In these types of models, no externally imposed forces exist, and, in the case of subduction zones, the model is entirely driven by the negative buoyancy force of the slab. Therefore, the kinematics of the subduction system (e.g., convergence velocities, subducting plate velocities, trench migration) are emerging from the internal dynamic balance of the subduction system, as opposed to being imposed *a priori*. These models, although more difficult to numerically stabilize, provide essential insights on the physics which govern Plate Tectonics.

Using this approach, authors have explored different aspects of the dynamic behaviour of a subduction zone, which include but are not limited to, how the length of a subduction zone directly controls its evolving geometry (e.g., Stegman et al., 2006; Schellart et al., 2007) and kinematics (e.g., Guillaume et al., 2010, 2013) and how this is reflected in natural cases (e.g., Schellart, 2017); how the slab is internally deformed during trench retreat (e.g., Funiciello et al., 2003) and how the stress is dissipated during slab bending (e.g., Capitanio and Morra, 2012; Irvine and Schellart, 2012); how plumes and oceanic plateaus interact with subduction zones (e.g., Betts et al., 2015; Mériaux et al., 2020; Moresi et al., 2014); the influence of subduction induced stress on formation of topography (Riel et al., 2017); and a multitude of different subduction zone initiation mechanisms, such as plume heads (Burov and Cloetingh, 2010; Gerya et al., 2015), mantle flow (Lu et al., 2015) or fluid flow (Dymkova and Gerya, 2013).

Examples of the use of the dynamical modelling approach can be found in Schellart et al. (2007) and (Schellart, 2017a). In these works, the authors explored how the width of a subduction zone exerts fundamental control over the evolution of its geometry, trench kinematics, mantle flows and overriding plate deformation. In both works, the authors use 3D free subduction models – i.e., models in which an oceanic subducting slab is placed on top of the upper mantle without the accompanying overriding plate (Figure 1.16) – which are entirely driven by the negative buoyancy of the slab, without any externally imposed forces.

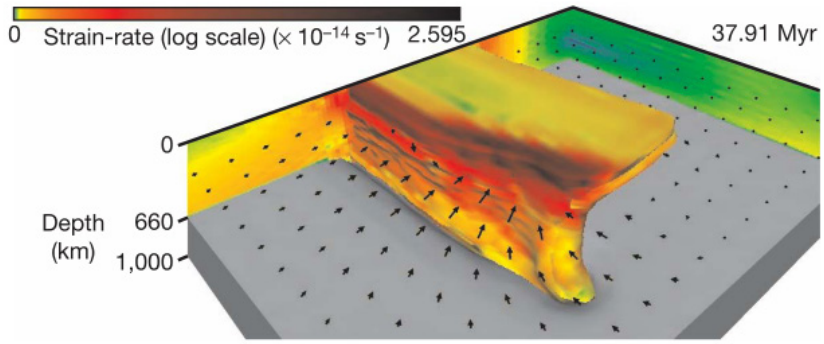

Figure 1.16 – Example of one of the 3D subduction models ran by Schellart et al. (2007) and Schellart (2017), in which slab width is 6000 km. No elasticity or overriding plate is present in these models which, according to the authors, overestimates the subduction dip angle.

In Schellart et al. (2007), the authors showed that the migration velocity of a subduction zone trench varies inversely with the width of a subduction zone, with longer subduction zones showing significantly slower values (Figure 1.17). Not just this, the width of the subduction zone controls its surface geometry, with narrower subductions showing strongly concave geometries and strong toroidal flows around the edges; while extremely long subduction zones are marked by stationary centres, the consequence of mantle stagnation zones, or to put in other words, areas of the mantle which are unable to flow due to the width of the slab.

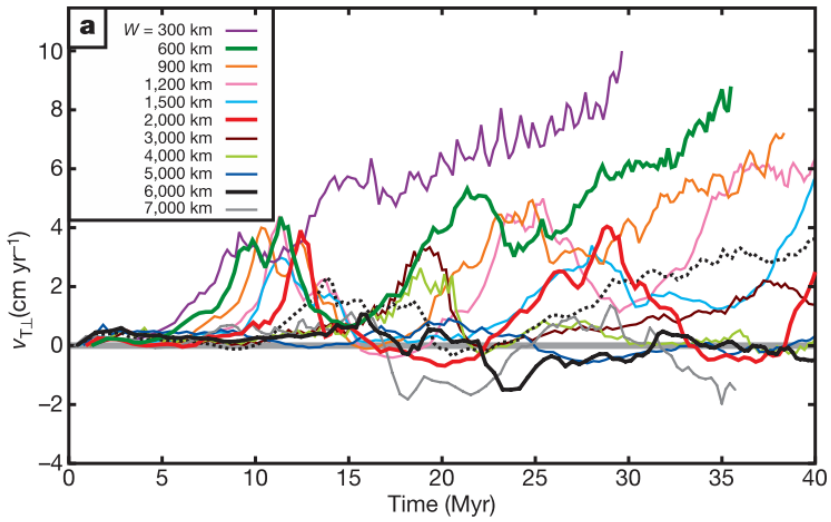

Figure 1.17 – Trench migration velocity over time, for different slab widths (Schellart et al., 2007).

These results were shown to agree with observations taken from both narrow (e.g., Scotia or Calabrian arc) and long (e.g., Andes) subduction zones, as well as with analogue modelling studies (e.g., Guillaume et al., 2010). The latter contribution – Schellart (2017) – builds upon these conclusions and demonstrates that the convex nature of long subduction slabs, as well as the buckling and folding of the subducting slab within the lower mantle, is responsible for inducing deformation (e.g., mountain building events) on the overriding plate.

By not imposing external conditions, the dynamical (or self-consistent) modelling approach ensures that the natural force balance (recall section 1.2.3) is present in the models. This internally driven approach forces kinematics to exist as an emergent process and not as a pre-imposed condition and, therefore, allows the simulated subduction zones to reflect naturally observed behaviour.

1.6.5. What type of modelling is used in this work?

In this thesis, all models are internally driven (dynamic, self-consistent), and therefore, no external forcing is applied on any subduction system. As such, and as described above, the kinematics of the model are an emerging process, being entirely derived from internal force balance between the negative buoyancy of the subducting slab and the accompanying viscous resistance forces, as opposed to being prescribed at the start of the model.

As to how the models are created and interpreted, this is discussed in Chapter 2. There, we will discuss the basics of numerical modelling, from the fundamental equations behind any approach, to building and apply post-processing to a self-consistent subduction zone model using two different modelling codes.

Chapter 2. Methodology and modelling cookbook

(this page has been left intentionally blank)

This chapter focuses on exploring the different modelling tools and processing codes used in the development of this thesis. This includes an explanation of the fundamental governing equations behind any numerical modelling, brief tutorials on the use of both Underworld/LaMEM and a presentation of different visualization toolboxes.

2.1. The fundamental equations

Regardless of the modelling code or numerical method applied, any numerical geodynamical modelling approach is based on simultaneously solving three conservation equations (also known as governing equations), which are:

1) the conservation of mass or continuity equation,
2) the conservation of momentum or Navier-Stokes equation and,
3) the conservation of energy or heat equation.

While multiple other equations may be included to account for more realistic behaviours and approximate the models to nature (e.g., creep laws, yield laws, thermally dependent densities, among many others), these vary in accordance with the specific geodynamic setting being modelled. For instance, a subduction model might benefit from complex dehydration and fluid alteration equations (e.g., Gerya et al., 2008; Munch et al., 2020) while a model focusing on a shorter time scale deformation (such as earthquake modelling) will need a stronger control over elastic (i.e. short term) deformation (Gerya, 2009). By contrast, the three conservation laws (mass, momentum, and energy) are common to most modelling approaches.

This small subchapter aims to briefly explore each of these conservation equations, allowing us to understand how they fundamentally govern the dynamics of any model. A complete detailed exploration of each of these equations has been published by Taras Gerya (Gerya, 2009) and is highly recommended for any aspiring numerical modeller.

To understand the conservation of mass and momentum under geodynamic conditions, we need to know that Earth can be regarded as a slow-moving fluid, assuming geological timescales. The consequence is that it is possible to describe the internal dynamics of the planet using fluid dynamics. One of its fundamental laws has been conceptually known since the time of Ancient Greece, and states that “nature abhors a vacuum”. In more scientific terms, it implies that any void left by a displaced fluid must be filled, or simply that any medium must be

continuous. Numerically, this is ensured by solving the continuity equation (or conservation of mass), eq. (2.1).

$$\frac{D\rho}{Dt} = \frac{\partial \rho}{\partial t} + \vec{v}\,\nabla\rho \tag{2.1}$$

Here, $\frac{D\rho}{Dt}$ is the Lagrangian time derivative of density (ρ), $\frac{\partial \rho}{\partial t}$ is the Eulerian time derivative of density, $\vec{v}$ is the velocity and $\nabla\rho$ is the density gradient. In most geodynamical modelling approaches however, we assume that the geological medium is incompressible, eq. (2.2). In these cases, a change in density over time ($\frac{\partial \rho}{\partial t}$) hinges on the existence of a non-zero velocity field and density gradient, eq. (2.3). If either the velocity or the lateral density variation in the medium is zero, no change will exist over time.

$$\frac{D\rho}{Dt} = 0 \tag{2.2}$$

$$\frac{\partial \rho}{\partial t} = -\vec{v}\,\nabla\rho \tag{2.3}$$

The second fundamental equation – the conservation of momentum – is also known as the Navier-Stokes equation of motion, eq. (2.4) and (2.5). This complex equation describes how a viscous fluid flows under the effect of both viscous and inertial forces.

$$\frac{\partial \sigma_{ij}^{'}}{\partial x_j} - \frac{\partial P}{\partial x_i} + \rho g_i = \rho \frac{Dv_i}{Dt} \tag{2.4}$$

$$\frac{Dv_i}{Dt} = \frac{\partial v_i}{\partial t} + \vec{v} \cdot \nabla v_i \tag{2.5}$$

Here, σ'_{ij} is the deviatoric stress tensor, P is the lithostatic pressure and g is the gravitational acceleration. The left-hand side of the equation describes the viscous forces which affect the fluid, while the right side describes the inertial forces. The ratio between the two is described by the Reynolds number, eq. (2.6). This non-dimensional number measures the relationship between the inertial and viscous forces applied on the fluid.

$$Re = \frac{\rho v L}{\mu} = \frac{\text{Inertial forces}}{\text{Viscous forces}} \tag{2.6}$$

Here, L represents the length of the material, an arbitrary geometric parameter. Geodynamic settings are marked by a very low Re, which implies that the viscous forces far outweigh the inertial forces (Gerya, 2009). This derives from the standard tectonic plate velocities (cm per year, or 10^{-9} m/s) and time required to observe any changes (millions of years, or 10^{13} seconds). Consequently, the inertial forces ($\frac{\mathrm{Dv_i}}{\mathrm{Dt}}$) become negligible in comparison with the gravitational forces (ρg_i), as seen in eq. (2.7) and (2.8).

$$\frac{\mathrm{Dv_i}}{Dt} \approx \frac{\Delta v}{\Delta t} = \frac{10^{-9}}{10^{13}} = 10^{-22} \approx 0 \tag{2.7}$$

$$\rho g_i = \rho \times 9.81 \tag{2.8}$$

In these conditions, the right-side term of eq. (2.4) is nullified, allowing us to obtain the Stokes law of motion, eq. (2.9), which describes the flow of highly viscous fluids over a long span of time, the precise description of geodynamics.

$$\frac{\partial \sigma'_{ij}}{\partial x_j} - \frac{\partial P}{\partial x_i} + \rho g_i = 0 \tag{2.9}$$

Finally, the third fundamental equation – the conservation of energy – describes how temperature in a system changes as a function of heat production (H), advection ($\vec{v} \cdot \nabla T$), and conduction ($\frac{\partial T}{\partial t}$), eq. (2.10) and (2.12).

$$\rho C_P \frac{DT}{Dt} = -\frac{\partial q_i}{\partial x_i} + H_r + H_s + H_a + H_L \tag{2.10}$$

$$q_i = -k \frac{\partial T}{\partial x_i} \tag{2.11}$$

$$\frac{DT}{Dt} = \frac{\partial T}{\partial t} + \vec{v} \cdot \nabla T \tag{2.12}$$

Here, C_P is the heat capacity of the material at a constant pressure, q is the heat flux, k is the thermal conductivity, and the H terms represent the different internal heat components. Heat production includes diverse components, such as shear heating (H_s, friction), adiabatic (H_a, pressure changes), radiogenic (H_r, radioactive isotopes) and latent (H_L, derived from phase changes) heating.

A few simplifications of this equation are frequently used while modelling, by removing/disabling some components (Gerya, 2009). The most common simplification assumes that both no advection and internal heat production exists in the system, resulting in a purely conductive heat transport. This is also known as the diffusive heat equation, shown in eq. (2.13).

$$\frac{\partial T}{\partial t} = \frac{k}{\rho C_P}\Delta t \tag{2.13}$$

In cases in which temperature is constant over time, the temperature equation is reduced to a steady state equation, which can be either Eulerian, Lagrangian or both (Gerya, 2009). When a Eulerian steady state is assumed, temperature is kept constant by the flow of material, under purely advective conditions, as described in eq. (2.14).

$$\frac{\partial T}{\partial t} = 0 \leftrightarrow \frac{DT}{Dt} = \vec{v}\cdot\nabla T \leftrightarrow \vec{v}\cdot\nabla T = -\frac{1}{\rho C_P}\left(\frac{\partial q_i}{\partial x_i} - H\right) \tag{2.14}$$

A Lagrangian steady state implies that the temperature is kept constant by the balance between the advected material and the internal heat production, as shown in eq. (2.15).

$$\frac{DT}{Dt} = 0 \leftrightarrow -\frac{\partial q_i}{\partial x_i} = H \tag{2.15}$$

Finally, a simultaneous Eulerian and Lagrangian steady state implies that no advection exists, and that temperature and pressure are constant over time. Consequently, it assumes a simple form, in which the temperature is entirely dictated by different amount of radiogenic heat production, as seen in eq. (2.16).

$$\frac{DT}{Dt} = 0, \frac{\partial T}{\partial t} = 0 \leftrightarrow -\frac{\partial q_i}{\partial x_i} = H_r \tag{2.16}$$

Out of the three governing equations, this is one which can be somewhat optional. It is entirely possible to run geodynamic models which do not include a temperature field and, therefore, do not require conservation of energy to be verified (e.g., Schellart and Moresi, 2013). Conversely, for any modelling approach that includes a temperature field and relies heavily on temperature contrasts, this would likely be the most crucial equation. An imbalance in the energy conservation equation (e.g., an abnormal reduction of heat flux or increase of heat

productions) can cause strong instabilities in the models. A subduction zone model with an extremely high value for shear heating can trigger plume events due to the friction between the slab and the base of the model.

As stated above, any geodynamical modelling approach hinges entirely on the solution of these three governing equations. Let us now explore two of these modelling codes (Underworld and LaMEM) and understand how we can use them to generate geodynamic models of subduction zones.

2.2. A trip to the Underworld (code)

2.2.1. What is the Underworld code?

The Underworld (UW) code (Moresi et al., 2007; Quenette et al., 2007) is a widely used modelling code in the field of geodynamics, which uses a staggered grid finite element method (FEM) and particle-in-cell (PIC) approach to solve the three fundamental governing equations. It employs a plethora of different viscoplastic rheologies, but no elasticity.

It was developed in Monash University (Melbourne, Australia) by Louis Moresi and his team with the purpose of creating a modelling code which could efficiently solve complex large-scale geodynamical problems. It has been used to model a wide range of geodynamical settings which include but are not limited to continental extension (e.g. Mondy et al., 2018; Salerno et al., 2016), dynamic topography (e.g. Arnould et al., 2018; Bodur and Rey, 2019), mantle plumes (e.g. Meriaux et al., 2015; Mériaux et al., 2020), strike-slip faults (e.g. Yang et al., 2020), and subduction zones (e.g., Capitanio, Morra and Goes, 2007; Capitanio et al., 2010; Schellart and Moresi, 2013; Farrington, Moresi and Capitanio, 2014; Sharples et al., 2016; Riel, Capitanio and Velic, 2017; Schellart, 2017a; Pall et al., 2018; Yang et al., 2018; Carluccio et al., 2019).

While the code is currently in its second version (https://www.underworldcode.org/), the work developed in this thesis was conducted with the first version and, therefore, all descriptions will pertain to it. The main difference between the two versions is the user interface, which has changed from the use of coupled XML (eXtensive Markup Language) files to Python. Running the models using UW1 requires some knowledge of Linux shell usage. Both

versions are also built upon the PETSc library (Balay et al., 1997), a highly efficient set of solvers for the discretized numerical systems.

FEM is a robust method for the solution of partial differential equations, which divides the modelling space into arbitrarily shaped small (finite) elements (Simpson, 2017). Once these small elements are created, shape functions (i.e., different weights) are attributed to the individual nodes, and a minimizing algorithm is applied to obtain the best values for the nodal properties. Once the nodal properties are solved, time is advanced by using a finite differences approach. This is a complex method which would far exceed the scope of this work to explain. An exceedingly detailed explanation of this method in application to geodynamics has been published previously (Simpson, 2017), and is highly recommended for anyone inclined to learn about it.

PIC is a well-established technique for preventing numerical diffusion (or error propagation) within models with advection (Gerya, 2009), which consists in using mobile particles within a static mesh. The fundamental properties are advected (or moved) by the particles and then their values are interpolated to the fixed mesh nodes, based on their relative distance to them. The algorithm is exemplified in Figure 2.1 and eqs. (2.17) and (2.18), both taken from Gerya (2010).

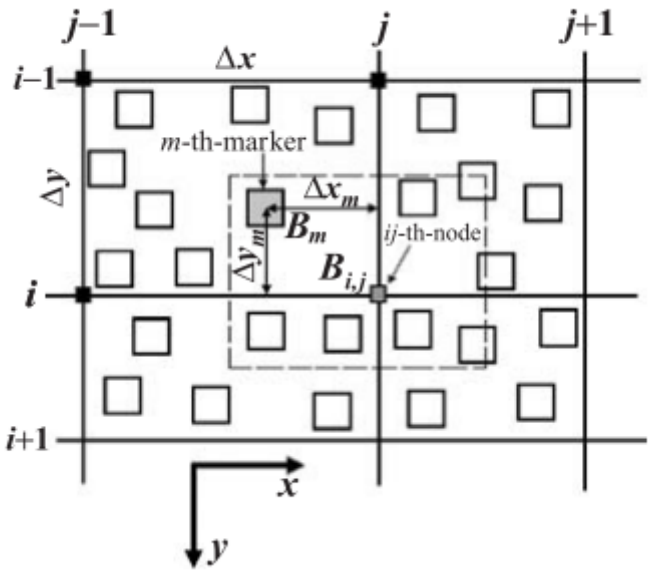

Figure 2.1 – Example of the algorithm for PIC, taken from Gerya (2010).

$$K_{i,j}^{t+\Delta t} = \frac{\sum K_m w_{m(i,j)}}{\sum w_{m(i,j)}} \tag{2.17}$$

$$w_{m(i,j)} = \left(1 - \frac{\Delta x_m}{\Delta x}\right)\left(1 - \frac{\Delta y_m}{\Delta y}\right) \tag{2.18}$$

Here, $K_{i,j}^{t+\Delta t}$ is the calculated material property at the (i,j)-th node for the next timestep, K_m is the same material property at the m-the marker of the same (i,j)-th node, and $w_{m(i,j)}$ is the weight of this same marker, calculated based on its Δx_m and Δy_m distances from the (i,j)-th node, as explained in eq. (2.18).

The full understanding of the underlying complex mathematics which compose a modelling code is not needed. However, having a grasp of the fundamental equations and how they can be discretized is useful to be able to understand how the methods have been implemented. Furthermore, knowing the advantages and drawbacks of each method is important as to correctly interpret the results and understanding when models inevitably fail. For instance, using FEM is more accurate and allows for the use of irregularly shaped grids, at the cost of computational efficiency. The inevitable drawback is that modelling codes which use this method take longer to run. Similarly, the use of PIC strongly reduces numerical instabilities but opens the possibility for more errors. As the particles move, some cells (space between nodes) may get depleted in markers, resulting in model failures. Knowing how PIC works allows us to use different particle configurations and mitigate these occurrences.

In more technical terms, it is beneficial but not crucial to know coding in C++ and XML to be able to read the source code and understand exactly how the input files are written, respectively. Conversely, knowing basic usage of Linux shell is all but mandatory to be able to run any model using UW1. In the following sections we will discuss how to create a model but will not discuss the different solver options that can be utilized.

2.2.2. How do we use it?

Before we can do anything, we need to install UW in our computers. The instructions on how to do so can be found at https://github.com/jaime-almeida/base-uw-install. Once that is done, to create and run an UW model, we need to observe a few crucial steps. It is fundamental to define:

a) the geometry of the model, which includes all the necessary shapes (i.e., plates, mantle, weak zones),
b) the rheology associated to each individual shape (i.e., how it will behave under stress),
c) the boundary conditions of the model (i.e., what happens to material along the edges/borders of the model).

Despite the versatility of the code, as this thesis verses on the topic of subduction zones, this chapter consists, therefore, of a brief tutorial on the different parts required to create a simple 2D subduction zone model using UW1. As the exact coding of any model is substantially different for each version of Underworld (XML vs Python), this chapter will not showcase the usage of UW2. A very detailed tutorial to the current code version can be found online at https://geodynamics-with-underworld.readthedocs.io/ which will help anyone to create models with the second version of the code. The complete scripts which were used to generate the model shown in this chapter **(**Figure 2.2**)** can be found as an appendix to this thesis (Appendix A). These scripts also contain the additional structures required to run the model, some of which are not described in this section (e.g., XML header, PIC information). While the order in which the structures are described section does not follow the input file, this allows us to follow a simpler conducting thread throughout.

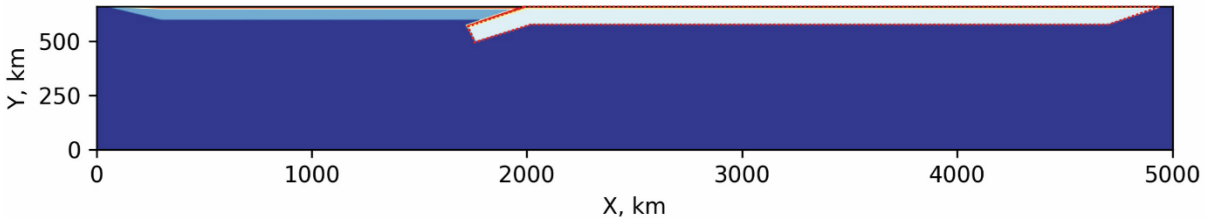

Figure 2.2 – Example of initial setup for a subduction zone model using UW1. The shape highlighted by the red dots represents the geometric shape of initial subducting plate.

An UW1 model is generally composed of at least three XML input files: a main file which contains the geometric and rheological information (see Appendix A – main file), a thermal file which contains the information for the temperature field (such as plate ages, see Appendix A – thermal file), and a velocity file, which contains the velocity boundary conditions (see Appendix A – velocity file). Occasionally, a file which contains configurations for irregular meshes (see Appendix A – node bunching) can be used. All files are appended to the main file using a simple *include* statement at the start of this file:

<include>main_V.xml</include>

```
<include>main_T.xml</include>
<include>optional_NB.xml</include>
```

The first part of the preparation of a model consists of defining the dimensions of the considered domain (i.e., minimum, and maximum values of x, y coordinates in 2D or x, y, z in 3D), the resolution (number of nodes along each axis[1]) and whether the model is two or three dimensional (2D and 3D, respectively). This is done in the first part of the main file, by simply stating the values, using the following code:

```
<param name="minX" units="km"> 0.0  </param>
<param name="minY" units="km"> 340.0 </param>
<param name="minZ" units="km"> 0.0  </param>
<param name="maxX" units="km"> 5000.0 </param>
<param name="maxY" units="km"> 1000.0 </param>
<param name="maxZ" units="km"> 0.0  </param>
<param name="elementResI"> 768 </param>
<param name="elementResJ"> 192 </param>
<param name="elementResK"> 1 </param>
<param name="dim"> 2 </param>
```

Note that the minimum and maximum "y" values are not zero and 660 km, as would be expected from what is seen in Figure 2.2. This derives from placement of the axis origin (i.e., x = y = 0) on the bottom left corner of any model. The surface is, therefore, marked by the highest value for the vertical coordinate "y" which is, in this case, equal to 1000 km. As for the base of the model (y = 340 km), this is simply a subtraction of 660 km (the natural depth of the upper-lower mantle transition) from the surface value. The 340 km which are missing from the model can be filled with a lower mantle shape which is present within the main file (see Appendix A – main file).

The number of nodes along each axis (i.e., the model resolution) must also reflect the dimensionality of the model. A model ran in two dimensions must always have one of the axes with a single element (in this case, the K resolution, or resolution along the z-axis). Furthermore, along the unused direction, both minimum and maximum are defined as zero.

[1] In this case, the notation (I, J, K) refers to the elements of the cartesian axes (x, y, z), respectively.

Note that UW is unable to generate non-rectangular (or non-parallelepiped) models and, therefore, always needs at least four values to be defined in 2D (max and min values for x and y) or 6 to be defined in 3D (which additionally includes another pair of equivalent values along z). It is also recommended, although not mandatory, that the values for the resolution are powers of two (e.g., 2^x) as it improves the performance and stability of the solvers. At minimum, the resolution should be divisible by two to prevent serious instabilities.

We also define the number of timesteps over which our model will be run, the output frequency and the output path for the model:

```
<param name="maxTimeSteps"> 3000 </param>
<param name="dumpEvery"> 50 </param>
<param name="checkpointEvery"> 50 </param>
<param name="outputPath">/example/output/path/for/uw1/model</param>
```

In the previous code snippet, the variables “dumpEvery” and “checkpointEvery” refer to the output frequency and number of timesteps between the restart checkpoints, respectively.

At this stage, our model is an empty rectangle, ready to be filled by different shapes. To this extent, the next step is to create these shapes which define the internal geometry of our model, such as the crust, the different lithospheric plates, and the sub-lithospheric mantle. These can be defined by using one of three distinct setups: boxes (in 2D, rectangles), spheres (in 2D, circles), and polygons. They can also be subjected to Boolean operations (intersect and union).

Let us see how to use the first two types by defining our upper mantle and our initial subducting plate (Figure 2.2). For simplicity’s sake (and for debugging reasons), the upper mantle is generally defined as a box shape that encompasses the whole model:

```
<struct name="upperMantleShape">
        <param name="Type">Box</param>
        <param name="startX" units="km"> 0.0 </param>
        <param name="endX" units="km"> 5000.0 </param>
        <param name="startY" units="km"> 340.0 </param>
        <param name="endY" units="km"> 1000.0 </param>
</struct>
```

While this might seem weird, the other defined shapes will overwrite some portions and we will obtain a proper upper mantle (seen in Figure 2.2).

By contrast, the initial subducting slab (red dotted shape in Figure 2.2) does not have a simple geometric shape. Thus. the only way to define it is by using a more complex polygon shape, where the coordinates for the vertices of the shape are sequentially listed (clockwise or counter-clockwise):

```
<struct name="slabLithosphereShape">
        <param name="Type">PolygonShape</param>
        <list name="vertices">
                <asciidata>
                        <columnDefinition name="x" type="double" units="km" />
                        <columnDefinition name="y" type="double" units="km" />
                                2020 920
                                1760 840
                                1724.1 902.3
                                2000 990
                                2700 990
                                3400 990
                                4700 990
                                4950 1000
                                4700 920
                                3400 920
                                2700 920
                </asciidata>
        </list>
</struct>
```

The last type of geometric setup – spheres – are not used in the present model but the code to generate one is simple. We define its 2D (or 3D) centre and its radius, the two geometric properties of a sphere:

```
 <struct name="exampleCircleShape" mergeType="replace">
            <param name="Type">Sphere</param>
            <param name="CentreX" units="km"> 1000 </param>
            <param name="CentreY" units="km"> 430 </param>
            <param name="radius" units="km"> 560 </param>
</struct>
```

Also not used in this model are more complex geometries created using Boolean operations. The two operations allowed by UW1 are Intersect and Union, for which an example code would be:

```
<struct name="IntersectedShape">
        <param name="Type">Intersection</param>
        <list name="shapes">
                <param>shape1</param>
                 <param>shape2 </param>
                 <param>!shape3 </param>
        </list>
 </struct>
<struct name="UnitedShape">
        <param name="Type">Union</param>
        <list name="shapes">
                <param>shape1</param>
                 <param>shape2 </param>
                 <param>!shape3 </param>
        </list>
 </struct>
```

The "!" symbol behind shape3 implies the negation of this shape, i.e., everything outside of it.

Once all the geometries have been set, the next step is to define the different rheological laws which affect our model, such as the viscous creep and yielding law or the thermal dependent parameters (e.g., density). These are widely variable and depend on both the geodynamic setting and the type of material/lithology being modelled. In fact, there are a multitude of different creep and yield laws within the source code, tailored for different settings. For this section, the laws shown and described are the ones employed in the described model. While the terminology varies between authors and has been thoroughly discussed in a recent publication (Wang, 2021), for the following sections, the use of the word "plastic" regarding deformation implies permanent deformation with a linear relationship with the stress and the strain, while "viscous" refers to a non-linear relationship between the stress and strain. The latter can be further divided into strain-hardening or strain-softening rheologies, in which the material increases or decreases in strength with increasing strain.

One of the most crucial rheological parameters is the viscous creep law. This is a mathematical formulation of the viscous (i.e., unrecoverable) deformation of a material. It

expresses the way through which the strength of the material (viscosity, η_{eff}) changes with increasing strain rate ($\dot{\epsilon}$). Knowing this value is crucial for the solution of the Stokes equation (2.4). The present model uses a simple empirical non-linear viscous creep law (Ranalli, 1997), eq. (2.19).

$$\eta_{eff} = \frac{1}{2} A^{-\frac{1}{n}} \times \dot{\epsilon}^{\frac{1}{n}-n} \times \exp\left(\frac{E_a + V_a P}{nRT}\right) \quad (2.19)$$

Here, A is the pre-exponential factor, n is the stress exponent, E_a is the activation energy, V_a is the activation volume, P is the pressure, R is the gas constant and T is the temperature. The first two terms, pre-exponential factor and stress exponent, are empirically derived and vary between different materials (Ranalli, 1997). The pre-exponential factor is an empirical relationship between the temperature and the reaction/defect propagation rate. The activation energy is a mineralogical parameter which depend on the bonding energy between the atoms in the crystal lattice, representing the minimum energy required to initiate a reaction. In our case, this is the minimum energy required to propagate a defect along the crystal lattice. Similarly, activation volume represents the pressure dependency of the creep law, a proxy of the compactness of the crystalline structure. Let us look at the specific example of the lithospheric and sub-lithospheric upper mantle, which are generally modelled by employing a dry olivine/peridotite creep law (Burov, 2011). The values assumed for our case are found in Table 2.1.

Table 2.1 – Rheological parameters which define the dry olivine creep law within the lithospheric and sub-lithospheric mantle.

Parameter	Value	Unit
Stress exponent - n	3.5	-
Pre-exponential factor - A	5.5×10^4	$MPa^{-n}s^{-1}$
Activation energy - Ea	5.3×10^5	J/mol
Activation volume - Va	1.0×10^{-6}	m^3/mol

The coding of viscous creep is simple, being resumed to merely listing the values with the correct unit and name:

```
<struct name="upperMantleViscosity">
        <param name="Type">PatriceArrhenius</param>
```

```
        <param name="StrainRateInvariantField">StrainRateInvariantField</param>
        <param name="TemperatureField">TemperatureField</param>
        <param name="PressureField">PressureField</param>
        <param name="StressExponent"> 3.5 </param>
        <param name="PreExponentialFactor" units="(MPa)^-3.5*s^-1">5.49e26</param>
        <param name="ActivationEnergy" units="J/mol">5.3e5</param>
        <param name="ActivationVolume" units="m^3/mol">10e-6</param>
        <param name="DefaultStrainRateInvariant" units="s^-1">1.0e5</param>
</struct>
```

Note the difference between the value of the pre-exponential factor (A) in Table 2.2 and the above transcribed code snippet. The 10^{22} difference hinges in the internal temporal scaling performed by Underworld. As geological time scales are fundamentally enormous, any modelling approach must solve this issue and the solution employed by UW is upwards time scaling. In short, a second in our model would correspond to 10^{22} seconds in nature (or c.a. 3.2 $\times$ 10^8 Myr), a value known as the scaling factor. Consequently, all parameters which rely on time – e.g., viscosity, strain rate, etc. – are also scaled in accordance with their temporal dependence. In the case of the pre-exponential factor, it varies inversely with time (see units in Table 2.1) and, therefore, must be divided by the scaling factor to be obtain the original/natural value. The same reasoning is applied to the default strain rate invariant, where the natural value of 10^{-17} s^{-1} has also been divided by the scaling factor and assigned to the variable.

It is also possible to define a constant viscosity (initially isoviscous rheology) which has no external dependency. In these cases, the code is merely a statement of the value, adjusted for the scaling factor:

```
<struct name="lowerMantleViscosity">
        <param name="Type">MaterialViscosity</param>
        <param name="eta0" units="Pa*s">3e-1</param>
</struct>
```

Again, like the previous variables, due to a linear dependence with time of the viscosity, the correct value is obtained by multiplying the input value by the scaling factor. Thus, for this example, the correct (unscaled) viscosity for the lower mantle layer would have been 3 $\times$ 10^{21} Pa·s.

Another fundamental part of the rheological profile is the plastic flow law (or yielding law) of the chosen materials. These laws define the critical stress at which the deformation on a

material becomes non-recoverable, or in a more geodynamic sense, at which point does the material transitions from a plastic to a viscous behaviour. Like the viscous creep laws, there are several yielding laws available in UW, each tailored for a specific type of behaviour.

The model here described employs a Drucker-Prager yield law, eq. (2.20), which represents an extension of the classic Coulomb-Mohr yield criterion. It defines the critical value for the second deviatoric stress invariant (σ'_{II}) as a function of the internal friction angle (ϕ) and cohesion (C).

$$\sqrt{\sigma'_{II}} = P\sin(\phi) + C\cos(\phi) \tag{2.20}$$

This critical value is then used to calculate the maximum strength (or viscosity) of the material, using eq. (2.21).

$$\eta_{eff} = \frac{\sigma'_{II}}{2\dot{\epsilon}} \tag{2.21}$$

Again, if we want to define the yield envelope for the lithospheric and sub-lithospheric upper mantles, only two parameters are required (Table 2.2).

Table 2.2 – Rheological parameters which define the Drucker-Prager yield criterion for the lithospheric and sub-lithospheric mantle.

Parameter	Value	Unit
Internal friction coefficient – tan(Φ)	0.25	-
Cohesion – c	30.0	MPa

Unlike the previous code snippets, the definition of the yield criterion is not straightforward. While the strain rate must be taken from the nodes, the pressure must be taken from the particles which requires additional swarm information to be provided. It is further defined which values both internal friction coefficient and cohesion attain once the stress threshold is surpassed, i.e., once the material has yielded.

```
<struct name="upperMantleYielding">
<param name="Type">DruckerPrager</param>
        <param name="StrainRateField">StrainRateField</param>
        <param name="PressureField">recoveredPressureField</param>
        <param name="MaterialPointsSwarm">materialSwarm</param>
        <param name="IntegrationSwarm">picIntegrationPoints</param>
        <param name="Context">context</param>
        <param name="cohesion" units="MPa">30.0</param>
        <param name="cohesionAfterSoftening" units="MPa">3.0</param>
        <param name="frictionCoefficient">0.25 </param>
        <param name="frictionCoefficientAfterSoftening">0.025</param>
        <param name="minimumViscosity" units="Pa*s">1e-3</param>
</struct>
```

Still regarding the deformation within the models, it is important to be able to limit the amount of stress which can emerge from the modelling setup (as stress is not unlimited in nature). This is done by imposing, in our case, a Peierls creep law (which acts as a stress cap).

```
<struct name="upperMantlePeierls">
        <param name="Type"> Byerlee </param>
        <param name="cohesion" units="MPa">900</param>
        <param name="depthCoefficient"> 0.0 </param>
        <param name="minimumViscosity" units="Pa*s">1e-3</param>
        <param name="StrainRateField"> StrainRateField </param>
        <param name="MaterialPointsSwarm">materialSwarm</param>
        <param name="FeMesh"> linearMesh </param>
        <param name="BlockGeometry"> geometry </param>
</struct>
```

This merely states that, at any depth, once the stress surpasses a defined threshold (in this case, 900 MPa), it is capped at the threshold. The consequence is that the strength of the material is also fixed at the value which corresponds to the stress threshold.

We can combine these fundamental rheological laws by comparing the plastic and viscous strength values at any given depth and saving only the lowest of the two (Figure 2.3). The strength value is obtained from the stress by solving eq. (2.21). This is a clear description of its

rheological behaviour, showing at which depth it changes from a plastic to a ductile flow, marked by a sharp drop in effective strength.

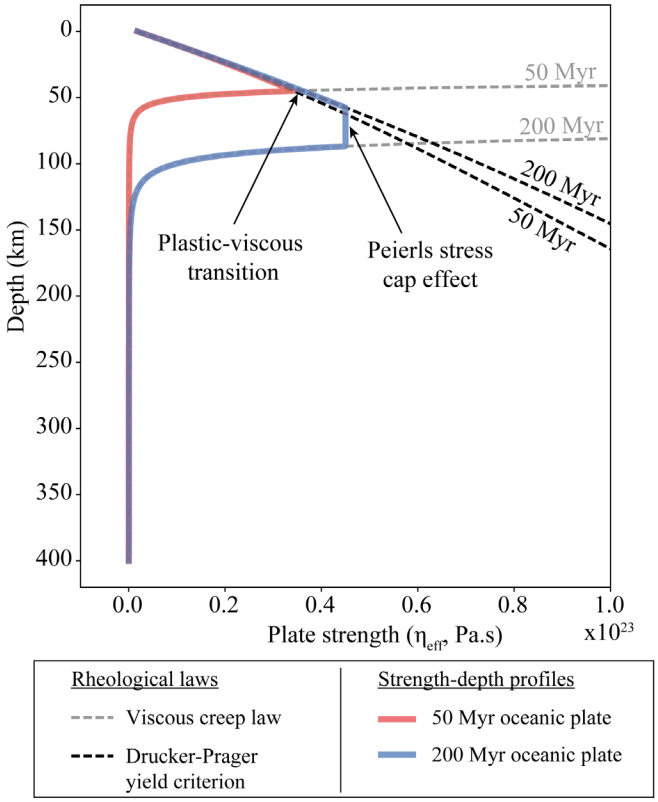

Figure 2.3 – Strength-depth profile for the lithospheric and sub-lithospheric mantle, as defined by in Table 2.1 and Table 2.2. The value for strength is obtained by solving eq. The black lines represent the strength profiles obtained with the Drucker-Prager yield criterion, eq. (2.20) and (2.20). The grey lines represent the strength profiles with the viscous creep law, eq. (2.19). The thick red and blues lines represent the effective strength profiles for plates with 50 and 200 Myr, respectively. Note the constant viscosity value that marks the transition between the plastic and viscous behaviours for the 200 Myr plate, which reflect the Peierls stress cap effect.

At this stage, our model has the shapes defined and has a list of rheological properties, without any association between them. These geometric features and rheological parameters must now be correctly paired together. This is done by using the most important UW1 structure, the RheologyMaterial:

```
<struct name="upperMantleRheology">
        <param name="Type">RheologyMaterial</param>
        <param name="Shape">upperMantleShape</param>
```

```
        <list name="Rheology">
                <param> upperMantleViscosity</param>
                <param> upperMantleYielding </param>
                <param> upperMantlePeierls </param>
                <param> viscosityFixLeft </param>
                <param> viscosityFixRight </param>
                <param> viscosityLimiter</param>
        </list>
        <param name="DensityLabel"> upperMantleDensity </param>
        <param name="DiffusivityLabel"> TheDiffusivity </param>
        <param name="CpLabel"> TheCp </param>
        <param name="ThermalExpansivityLabel"> TheAlpha </param>
        <param name="RadiogenicHeatProductionLabel" units="kg/(m*s*s*s)"> 0.022e16 </param>
        <param name="LatentHeatFusionLabel"> 0.0 </param>
</struct>
```

This code block associates to the *upper mantle* shape not only the previously defined rheological properties (viscosity and yielding) but also a few additional properties, namely a Peierls stress cap, two instability prevention fixes and a numerical limit for the viscosity (all italicized in the above snippet). The first property is the previously described Peierls stress cap. The effect of this can be seen in Figure 2.3, on the 200 Myr old plate strength-depth profile. The viscosity fixes were added to prevent numerical instabilities in the ridges placed on each plate tip (seen in Figure 2.2). More specifically, they prevent drips of cold material stemming from the ridge. Without them, the ridge would represent a material downwelling of material as opposed to a spreading centre. Finally, the viscosity limiter is simply a numerical control for the viscosity, keeping it within geodynamically reasonable values (in this case, between 10^{19} and 10^{24} Pa·s).

Once these three steps (defining geometry, defining rheology, assigning rheologies to shapes) have been performed for all the required shapes, the model is practically complete! The only thing left is the definition of boundary conditions (BCs). These include the initial and wall conditions for both temperature and velocity of our model.

The thermal conditions are defined in the aptly named thermal file (Appendix A - thermal file), which is separated in two major structures: the definition of initial thermal conditions for the individual shapes, and the definition of the model thermal boundaries. Let us explore how to define their initial thermal conditions for the subducting plate, as shown in Figure 2.4.

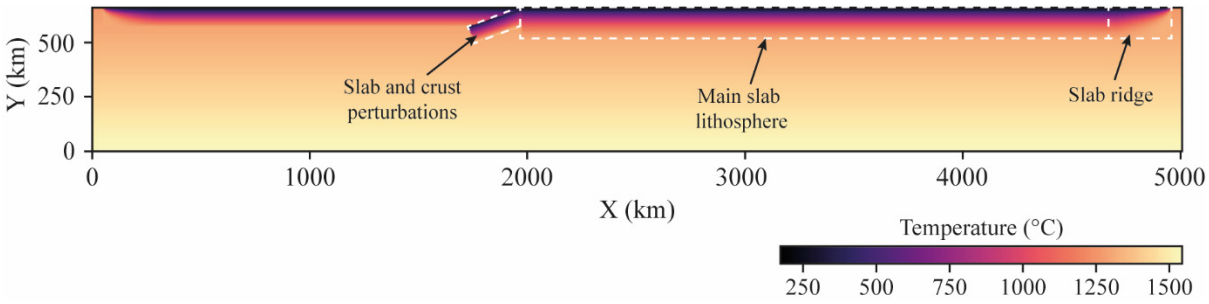

Figure 2.4 – Initial thermal conditions for the present model. The different highlighted shapes show the separation of the subducting plate into segments, which facilitate the thermal setup. Both horizontal crust and lithosphere segments are included in these larger shapes.

The thermal profile is not homogeneous along the slab, in the sense that there are different types of profiles from the ridge to the subducted slab. Consequently, it is not possible to simply associate a thermal profile to the geometric and rheologic profiles set for the slab. Therefore, the slab is decomposed into smaller sections, the ridge, the main slab, and the initial subducted segment (or perturbation) of the subducting plate. The ridge section (rightmost section in Figure 2.4) is marked by a tapered geometry, in which the thermal thickness of the plate increases with its distance to the spreading centre. While in nature, this tapered nature would continue until the slab reaches a critical age, our model assumes a simplification in which the "body" of the slab (from ridge tip to trench, Figure 2.4) has a constant thermal profile from the end of the ridge to the subducted segment (i.e., the same temperature at the same depth all across). Finally, the subducted slab has an inclined thermal profile, rotated in accordance with the slab dip. These different thermal profiles require the use of separate methods and shapes to define them:

```
<struct>
        <param name="setup"> 3 </param>
        <param name="Shape"> slabRidgeTShape </param>
        <param name="age_at_minX" units="yr">7.0e7</param>
        <param name="age_at_maxX" units="yr">0.0e7</param>
        <param name="SurfaceTemperature" units="K"> 273 </param>
        <param name="LithosphereBaseTemperature" units="K"> 1598 </param>
        <param name="ThermalDiffusivity" units="m^2/s"> 1e-6 </param>
</struct>
<struct>
        <param name="setup"> 3 </param>
        <param name="Shape"> slabLithosphereTShape </param>
        <param name="age_at_minX" units="yr">7.0e7</param>
```

```
        <param name="age_at_maxX" units="yr">7.0e7</param>
        <param name="SurfaceTemperature" units="K"> 273 </param>
        <param name="LithosphereBaseTemperature" units="K"> 1598 </param>
        <param name="ThermalDiffusivity" units="m^2/s"> 1e-6 </param>
</struct>
<struct>
<param name="setup"> 1 </param>
        <param name="Shape"> crustPerturbationUpTShape </param>
        <param name="originx" units="km"> 1970 </param>
        <param name="originy" units="km"> 990 </param>
        <param name="valueAtOrigin" units="K"> 423 </param>
        <param name="gradientx" units="K/km"> 0</param>
        <param name="gradienty" units="K/km">-25</param>
        <param name="rotation"> -18.4349 </param>
</struct>
<struct>
        <param name="setup"> 1 </param>
        <param name="Shape"> slabPerturbationUpTShape </param>
        <param name="originx" units="km"> 1820 </param>
        <param name="originy" units="km"> 920 </param>
        <param name="valueAtOrigin" units="K"> 823 </param>
        <param name="gradientx" units="K/km"> 0</param>
        <param name="gradienty" units="K/km">-15</param>
        <param name="rotation"> -18.4349 </param>
</struct>
```

The first method for defining initial thermal conditions (i.e., setup 3), uses the plate cooling model (Turcotte and Schubert, 2002) to set the thermal profile, in accordance with eq. (2.22).

$$T = T_{surface} + (T_{base} - T_{surface}) \times \left[\frac{y}{y_{L0}} + \frac{2}{\pi} \sum_{n=1}^{\infty} \frac{1}{n} exp\left(\frac{\kappa n^2 \pi^2 \Delta t}{y_{L0}^2} \right) sin\left(\frac{n\pi y}{y_{L0}} \right) \right] \quad (2.22)$$

Here, $T_{surface}$ is the temperature at the top of the plate (generally the surface), T_{base} is the temperature at the base of the lithosphere, κ is the thermal diffusivity, y is the depth, y_{L0} is the maximum thickness of the lithosphere, and Δt is the age of the plate.

This equation was used in the present model to define the thermal profiles for both the ridge and main body of the slab (Figure 2.4), by setting the age of these plates at the left and right boundaries of the shape (*age_at_minX* and *age_at_maxX*). The value set for the base of the lithosphere (1598 K or 1325 ºC) is the standard value (Burov, 2011) and marks the rheological

transition from plastic lithosphere to a viscous upper mantle. This type of setup is only applicable for box shapes and is not applicable for more complex geometries.

The subducted slab (Figure 2.4) was defined using a polygon shape (see main file in Appendix A) and as just stated, is unable to use the plate cooling model setup. The alternative is to use setup 1, which defines linear thermal profiles as a function of a thermal gradient, eq. (2.23).

$$T = T_{surface} + y\Delta T \tag{2.23}$$

Here, ΔT is the thermal gradient. A separation between the crust and mantle thermal shapes is employed to mimic the non-linear gradient change with depth, shown by the plate cooling model. A rotation angle can also be applied, which rotates the thermal gradient clockwise or counter clockwise a number of degrees, using positive or negative values respectively. A comparison between the two setups can be found in Figure 2.5, showing the approximation between the above defined linear profile and the application of the plate cooling model to a 25 Myr old oceanic plate.

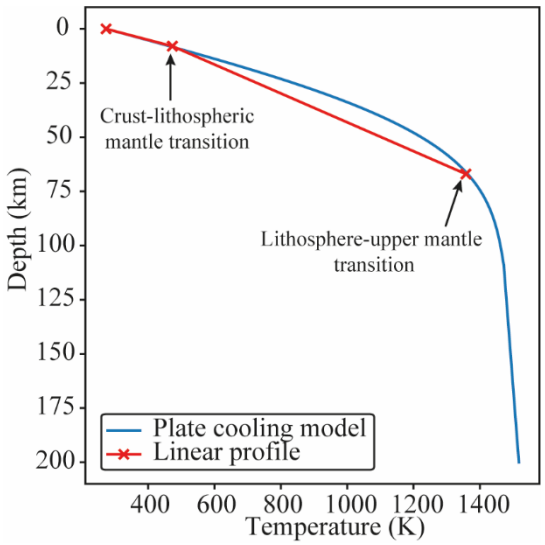

Figure 2.5 – Comparison between the linear thermal profile defined for the crust and mantle perturbations in Figure 2.4 and the plate cooling thermal profile for a 25 Myr old plate. The red x's represent, respectively, the surface, the base of the crust and the base of the lithospheric mantle for the linear thermal profile.

Once the initial conditions for the different thermal shapes were set, we can define the BCs for the model. This is done by assigning the correct values for the temperature at the surface (top wall of the model) and base of the upper mantle (bottom wall of the model). The former is

classically defined as 273 K or 0 ºC, while the latter depends on the adiabatic thermal gradient (Turcotte and Schubert, 2002) assumed for the upper mantle. In the present case, a gradient of 0.5 K/km was assumed, resulting in a basal temperature for the model of 1853 K or 1580 ºC.

```
<struct>
        <param name="type"> WallVC </param>
        <param name="wall"> bottom </param>
        <list name="variables">
                <struct>
                        <param name="name"> temperature </param>
                        <param name="type"> double </param>
                        <param name="value" units="K"> 1853 </param>
                </struct>
        </list>
</struct>
<struct>
        <param name="type"> WallVC </param>
        <param name="wall"> top </param>
        <list name="variables">
                <struct>
                        <param name="name"> temperature </param>
                        <param name="type"> double </param>
                        <param name="value" units="K"> 273 </param>
                </struct>
        </list>
</struct>
```

The final parameters which need to be defined are the kinematic BCs, or to put it in simpler terms, how the modelled materials should behave when reaching/crossing a model boundary. This fundamental as we do not implement any sort of stress or force initial conditions. Four types of kinematic BCs are used in geodynamic modelling along the model walls, in increasing level of restrictions:

1. open, in which material which crosses the boundary leaves the model (Figure 2.6a).
2. Periodic, in which material exiting through a wall, re-enters with the same value along the opposite one (Figure 2.6b). For example, along the left and right walls, the horizontal velocity is identical, eq. (2.24):

$$\vec{v}_{x-a} = \vec{v}_{x+a} \tag{2.24}$$

   where a is the width of the model.

3. Free slip, in which material cannot escape the model but is able to flow freely (without resistance) along the wall (Figure 2.6c). As an example, along the bottom wall, we would assume that no velocity exists along the vertical direction, eq. (2.25):

$$\vec{v}_y = \vec{0} \tag{2.25}$$

4. No slip, where any material which reaches the boundary is held at that position (Figure 2.6d), eq. (2.26):

$$\vec{v}_x = \vec{v}_y = \vec{0} \tag{2.26}$$

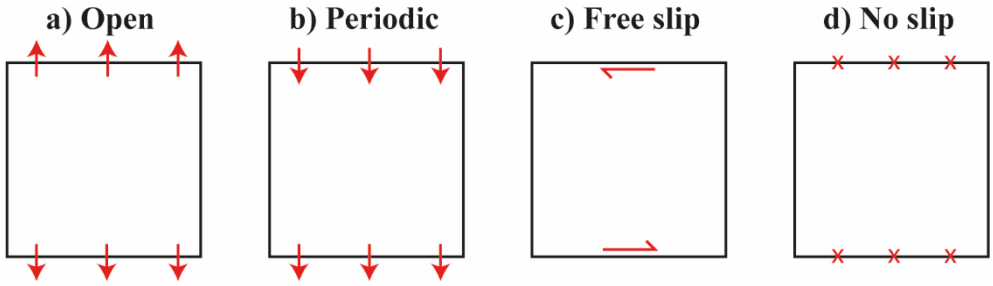

Figure 2.6 – Types of kinematic BCs applied along the top and bottom model boundaries. The half-arrows in c) represent the absence of a vertical velocity component along the wall. The "x" in d) represent a lack of motion, a "stitch" along the wall.

An additional type – free surface – represents a specific type of top wall, in which an open top boundary is combined with a viscous fluid layer above the model (Schmeling et al., 2008). It is a more complex type of boundary to stabilize in UW1 and, therefore, is not included in our simple 2D subduction model. A use of this type of boundary can be found in Chapter 3.2.

In UW1, kinematic BCs are mostly defined in as combinations of horizontal and vertical velocities in the velocity file (Appendix A – velocity file). The single exception lies with the use of periodic BCs, which are defined in the main file (Appendix A – main file).

In our simple 2D model, we employed free slip and no slip BCs along the horizontal walls (top and bottom, respectively). While this is a relatively standard approach, it has some drawbacks that are important to know. When the subducting slab reaches the bottom wall (which represents the upper-lower mantle transition), it will glide along it, never disappearing.

In nature, these slabs, while stagnant along this basal transition are also inevitably prone to collapse into the lower mantle, affecting the overall geodynamics of the subduction zone (e.g., Goes et al., 2017; Schellart, 2017a). As we are exploring relatively short-lived processes (subduction initiation) this limitation constitutes an acceptable simplification. If the work would include the lasting development and evolution of a subduction zone, slab sinking across the 660 km basal discontinuity into the lower mantle would have to be accounted for. Along the top wall, the absence of vertical material escape which would result in the creation of topography, favours instead the concentration of available stresses on the bending of the subducting slab and the overriding plate. This artificially increases the resulting dip of the subducting slab and leads to the occasional development of double sided subduction zones in the models (Crameri et al., 2012). The code structure for these walls is relatively simple, as we define the velocity across the wall as being zero (i.e., vertical velocity).

```
<struct name="velocityBCs">
        <param name="type">CompositeVC</param>
        <list name="vcList">

        <struct>
                <param name="type"> WallVC </param>
                <param name="wall"> bottom </param>
                <list name="variables">
                        <struct>
                                <param name="name">vy</param>
                                <param name="type">double</param>
                                <param name="value" units="m/s-^1"> 0 </param>
                        </struct>
                        <struct>
                                <param name="name">vx</param>
                                <param name="type">double</param>
                                <param name="value" units="m/s-^1"> 0 </param>
                        </struct>
                </list>
        </struct>
        <struct>
                <param name="type"> WallVC </param>
                <param name="wall"> top </param>
                <list name="variables">
                        <struct>
                                <param name="name">vy</param>
```

```
                                        <param name="type">double</param>
                                        <param name="value" units="m/s-^1"> 0 </param>
                                </struct>
                        </list>
                </struct>
        </list>
        </struct>
```

If a particular component is not defined in a velocity boundary condition structure – e.g., vx along the top wall – no constraints are applied, and we can assume free flow for that component. Furthermore, note that in the previous snippet, there is no definition for the side walls. In our model, these are periodic (Figure 2.6b), which as stated previously, are not defined in the velocity file. Instead, a structure is added to the end of the main file to inform UW1 that the side boundaries are periodic.

```
<struct mergeType="merge" name="components">
        <struct mergeType="merge" name="linearMeshGenerator">
                <param name="periodic_x">True</param>
        </struct>
        <struct mergeType="replace" name="sourceTerm" type="struct">
                <param name="Type">DummyComponent</param>
        </struct>
</struct>
```

There are, of course, additional blocks of code which are used to run an UW1 model but those are highly dependable on the type of model being run. These include structures such as: the types of modules to use (Appendix A – main file, lines 11 to 15), the PIC definition (Appendix A – main file, lines 85 to 98), which variables to have as an output (Appendix A – main file, lines 812 to 817), or heat equation parametrization (Appendix A – main file, lines 840 to 934). These structures are commented and explained in the codes attached to this thesis.

Once all these files are created, assuming the code has been installed, entering the following code in a Linux terminal would set the model to run:

```
mpirun -np number_of_processors $UW_EXE /path/to/main_file.xml -Uzawa_velSolver_ksp_type preonly -
Uzawa_velSolver_pc_type lu -Uzawa_velSolver_pc_factor_mat_solver_package mumps -mat_mumps_icntl_14
100
```

Now that we have learned a bit about what is and how to use Underworld, let us learn about the LaMEM code.

2.3. Another code, another method…

2.3.1. What is the LaMEM code?

The LaMEM (Lithosphere and Mantle Evolution Model) is a 3D numerical code which employs a staggered grid finite differences discretization coupled with a particle-in-cell approach (Kaus et al., 2016). Like UW, it has been used to model a wide variety of geodynamic settings which include, but are not limited to continental collision (Yang et al., 2020), mantle plume dynamics (Piccolo et al., 2020), fold-and-thrust belt development (Spitz et al., 2020, 2019), magmatic systems (Reuber et al., 2018) and, of course, subduction zone dynamics (Almeida et al., 2022; Pusok et al., 2018a). The source code for LaMEM can be found at https://bitbucket.org/bkaus/lamem/src/master/.

It differs from UW by employing a single set of non-linear visco-elasto-plastic rheology constitutive equations (Kaus et al., 2016; Piccolo et al., 2020), eq. 2.27-2.29. Both plastic and viscous creep follow the laws defined for UW1, eq. (2.19-2.20).

$$\dot{\epsilon}_{ij} = \dot{\epsilon}_{ij}^{viscous} + \dot{\epsilon}_{ij}^{elastic} + \dot{\epsilon}_{ij}^{plastic} = \frac{\tau_{ij}}{2\eta_{eff}} + \frac{J_{ij}}{2G} + \dot{\gamma}\frac{\partial Q}{\partial \tau_{ij}} \tag{2.27}$$

$$J_{ij} = \frac{\partial \tau_{ij}}{\partial t} + \tau_{ik}\omega_{ik} - \omega_{ik}\tau_{kj} \tag{2.28}$$

$$\omega_{ij} = \frac{1}{2}\left(\frac{\partial v_j}{\partial x_i} - \frac{\partial v_i}{\partial x_j}\right) \tag{2.29}$$

Here, J_{ij} is the Jaumann objective stress rate (i.e., reference independent stress derivative), ω is the spin tensor, G is the shear modulus and Q is the plastic flow potential.

This code is built upon the PETsc (Balay et al., 1997) libraries which, much like for UW1, allows for the efficient parallel solving of the discretized equations. Like UW1, running LaMEM requires some basic understanding of Linux shell usage.

2.3.2. How do we use it?

As this is an inherently 3D code, the following section aims to provide a brief tutorial on the development of a 3D subduction zone model (the full exploration of these model results can be seen in Chapter 4). But before we can do anything, we need to install the code. A tutorial can be found at https://bitbucket.org/bkaus/lamem/src/master/.

A LaMEM model consists of, at least, two file types: a *.dat (text) file* which contains crucial geometry-independent data such as resolution, time information, type of boundaries, which variables to output, rheologies and solver information (Appendix B – main.dat file); and a *partitioning file*, which contains the node/particle separation across different processing units (i.e., parallelized data). In simpler terms, this contains a pre-separation of the variable matrices, in a way that each portion is sent to a different CPU for solving during the solving stage. This last file must be generated per model and depends on the architecture of the operating system which will run the model. The instructions to generate it can be found in Appendix B. Like for the UW1 code, not all structures required to generate a model will be discussed in this section (all are commented in the scripts provided as appendixes).

The creation of a model using LaMEM follows the same steps as before, namely defining:

a) the geometry of the model (shown in Figure 2.7), which includes all the necessary shapes (i.e., plates, mantle, weak zones),
b) the rheology associated to each individual shape (i.e., how it will behave under stress),
c) the thermal and kinematic boundary conditions of the model (i.e., what happens to material along the edges of the model).

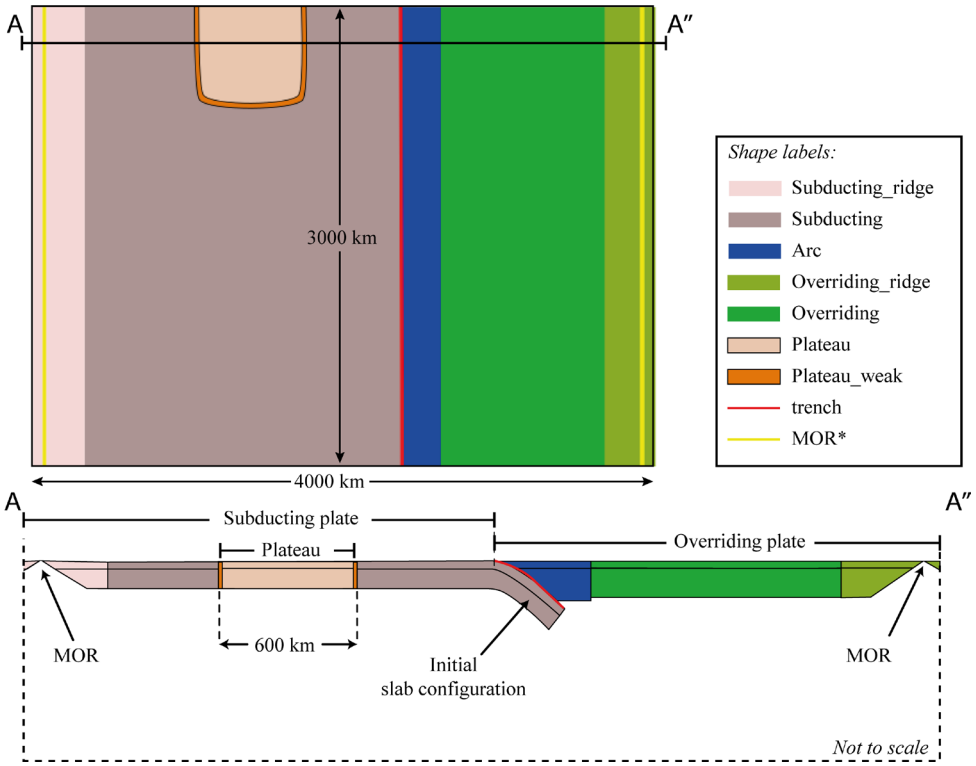

Figure 2.7 – Example of the surface geometry of a subduction zone initiation model. The * notation on the mid-ocean ridge (MOR) caption reflects the different internal labelling, with the left ridge being labelled as mor_subducting and the right ridge being labelled as mor_overriding. While the name might be similar, the linear ridge shapes mark the exact spreading center, while the rectangular ridge shapes mark the growth portion of the plate (see the ridge structures shown in the cross-section).

Setting the geometry of a LaMEM model is not complex, and a tutorial can be found on their website (https://bitbucket.org/bkaus/lamem/wiki/Home). The specific method used in this thesis is part of presently unpublished work and, therefore, cannot be presently elaborated upon. Nevertheless, the following section details on the allocation of rheological properties to the different model components (Figure 2.7). This geometry, shown in Figure 2.7, describes a half-model (e.g., Stegman et al., 2006; Stegman, Farrington and Capitanio, 2010), a modelling technique to reduce the computation power required. The boundary which crosses the oceanic plateau acts as a symmetry axis, effectively halving the size of our model.

The ridges defined in Figure 2.7 are used to set the initial thermal profile of the overriding and subducting plates. At each point, their age is defined by the distance to the spreading centre and the respective spreading velocity. Knowing the age, the vertical thermal profile is defined following the half-space cooling model, eq. (2.30).

$$T = T_{surface} + (T_{mantle} - T_{surface}) \times \mathrm{erf}\left(\frac{y}{\sqrt{\kappa \Delta t}}\right) \quad (2.30)$$

A comparison between this cooling model and the plate cooling model is shown in Figure 2.8. It is also possible to remove the dependence from the spreading centre and simply define the same age for the entire shape. While this is a simplification, it also allows for a better constraint on the non-linear influence of the plate age on the developing subduction zone.

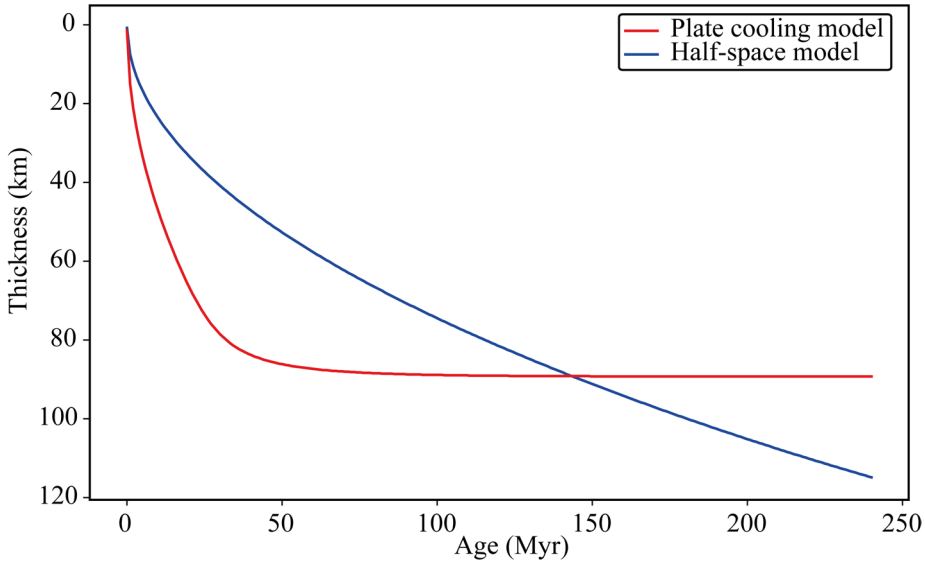

Figure 2.8 – Comparison of the thickness of an oceanic plate lithosphere, according to the plate and half-space cooling model, assuming a diffusivity of 10^{-6} m^2/s. The thickness is calculated assuming a lithosphere-asthenosphere boundary temperature of 1250 ºC or 1523 K. For older plates (older than c.a. 150 Myr), the half-space model produces unreasonably thick plates.

Once the geometry is set, we need to set up the running conditions (e.g., variables to output, amount of timesteps, etc.), boundary conditions for the model and allocate the different rheologies to the different shapes, all of which is done within the *dat* file (see Appendix B – main.dat file).

In this file, the first variables to be set are the basic model properties such as the resolution and running conditions, but before we investigate those, let us set up the rheological law for the different model components. The rheology list (located close to the end of the file) contains all the laws which govern our model and follows the ascending numerical order of phase ID (i.e., the different geometric components of the model). The first structure in this list is the upper

mantle rheology (typically associated with phase ID = 0), which has the properties of a peridotite, including a dry olivine viscous creep profile. A similar profile was applied for all the mantle portions of the model (such as the subducting plate lithospheric mantle). The crustal materials follow a different setup, as they are not peridotitic in nature. For this example, our crustal materials were set as being weak diabases (microgabbro), with lower density than the peridotitic upper mantle. The very weak rheology ensures that the crust can act as a subducting channel. A similar reasoning was applied to the other materials in the model, and all these structures can be found in Appendix B – main.dat file.

```
# ========== UPPER MANTLE ======
<MaterialStart>
        ID      =       0 # phase id  [-]
        rho     =       3300    # density [kg/m3]
        alpha   =       3e-5    # coeff. of thermal expansion [1/K]
        disl_prof       =       Dry_Olivine_disl_creep-Hirth_Kohlstedt_2003
        Vn      =       13.5e-6
        diff_prof       =       Dry_Olivine_diff_creep-Hirth_Kohlstedt_2003
        Vd      =       13.5e-6
        ch      =       30e6            # cohesion [MPa]
        fr      =       20              # friction angle
        G       =       5e10            # elastic shear module [MPa]
        # Thermal properties
        k       =       3               # conductivity
        Cp      =       1050            # heat capacity
        chSoftID =      0    # cohesion softening law ID
frSoftID        =       0    # friction softening law ID

<MaterialEnd>


# ======== CRUSTAL MATERIALS ==========
<MaterialStart>
        ID      =       3       # phase id  [-]
        rho     =       3300    # density [kg/m3]
        alpha    =      3e-5    # coeff. of thermal expansion [1/K]

        disl_prof       =       Maryland_strong_diabase-Mackwell_et_al_1998
        ch      =       5e6     # cohesion [MPa]
        fr      =       0       # friction angle
```

```
        G       =       5e10    # elastic shear module [MPa]

        # Thermal properties
                k       =   3               # conductivity
        Cp      =   1050    # heat capacity
<MaterialEnd>
```

Once this is done, our model setup is both geometric and rheological prepared. All that remains is to define the conditions in which our model will be ran, which can be found at the start of the file. The first things to be set are the coordinate grid, the model resolution, and time information:

```
# Grid & discretization parameters

# Refined grid in x-direction
        nel_x   = 256
        coord_x = -2000 2000
# constant grid in y
        nel_y = 192
        coord_y = -1500 1500
# Refined grid in z-direction
        nel_z = 96
        coord_z = -660 50

# Time stepping parameters
time_end  = 2000    # simulation end time
dt        = 0.01    # time step
dt_min    = 0.0001  # minimum time step (declare divergence if lower value is attempted)
dt_max    = 0.1     # maximum time step
CFL       = 0.5     # CFL (Courant-Friedrichs-Lewy) criterion
nstep_max = 10000   # maximum allowed number of steps (lower bound: time_end/dt_max)
nstep_out = 50      # save output every n steps
nstep_rdb = 50      # save restart database every n steps
```

Next, we define our kinematic and thermal BCs. By default, LaMEM employs free slip conditions on all boundaries but, for our case, we used an open top boundary (by adding *open_top_bound = 1*). This allows for material to escape through the top boundary and stabilizes the free surface. Thermally, the top was set at 20 ºC and the base at 1500 ºC (adiabatic upper-lower mantle transition temperature).

```
# NO Free surface top boundary flag
open_top_bound = 1

# No-slip boundary flag mask (left right front back bottom top)
noslip = 0 0 0 0 0 0

# Temperature on the top & bottom boundaries
temp_top = 20
temp_bot = 1500.0;
```

While there are several other parameters that are set in this file (solver parameters, different controls for viscosity and stress), the most interesting is the phase grouping for the output:

```
<PhaseAggStart>
        name     = _subducting_plate  # phase aggregate output vector name
        numPhase = 4                  # number of phases to aggregate
        phaseID  = 1 2 5 6                    # list of phase IDs to aggregate
<PhaseAggEnd>

<PhaseAggStart>
        name     = _overriding_plate  # phase aggregate output vector name
        numPhase = 4                          # number of phases to aggregate
        phaseID  = 3 4 7 8                     # list of phase IDs to aggregate
<PhaseAggEnd>

<PhaseAggStart>
        name     = _oceanic_plateau           # phase aggregate output vector name
        numPhase = 5                          # number of phases to aggregate
        phaseID  = 11 12 13 14 15 # list of phase IDs to aggregate
<PhaseAggEnd>
```

These structures consolidate the different phases into a single output, i.e., the subducting plate consists of phase 1, 2 (subducting plate crust and mantle) 5 and 6 (subducting plate ridge crust and mantle).

Like UW1, running LaMEM requires the installation of the code and using a simple command on a Linux shell:

```
mpirun number_of_processors /path/to/lamem/executable -ParamFile dat_file.dat
```

2.4. How do we visualize and process the model results?

We have now seen how the two modelling codes work, and how we can create models using them. Regardless of the modelling code, a model is just a set of accumulated information if we are not able to extract and visualize its data. It is therefore fundamental for any aspiring modeller to be well versed in at least one of the many data analysis and plotting tools available. While there is a virtually endless amount of these tools, for the development of this thesis the most relevant ones were Paraview and Python. While the former is a software created specifically to visualize 2D and 3D data, the latter is computational language (hence, an "infinite" tool), capable of doing (just about) anything if the user can code it into existence. Let us now explore each of these methods to study our models.

2.4.1. Paraview as a visualization tool

Paraview (PV) is an open-source, multi-platform analysis and visualization application. It was created as a method to analyse data efficiently and quickly at vastly different scales, from small resolution data on laptops to petascale data in high-performance computing (HPC) clusters. For our purposes, it serves as a relatively quick way to both observe and prepare high quality images of our models.

This section will serve as a brief tutorial on the use of PV to create a 3D image of subduction zone initiation model, which was run using LaMEM and described in the previous section. In this specific type of model, there are three main components that need to be highlighted: the subducting plate, the overriding plate and the oceanic plateau placed on the subducting plate. The objective is, therefore, to showcase these components and remove any unnecessary parts of the model, as to properly interpret the underlying geodynamics at play.

While some differences exist between UW1 and LaMEM models, these are fundamentally the type of variables which are generated by the codes. As an example, LaMEM automatically generates data to allow for an easy visualization of all different model components (recall from the previous section, the shapes defined within the *svg* file and coupled in the MATLAB and *dat* files), while UW1 does not. Regardless, the generic use of PV as a visualization tool does not hinge on the type of modelling code used. When relevant, the steps required to apply the same method to an UW1 model will be explained.

No editing has been performed on the figures; each represents a screenshot taken from the PV window. For publication, these are generally edited in a dedicated image editing software (e.g., Inkscape or Adobe Illustrator) to add labelling, highlights, or additional specialized information. Furthermore, this section is also based on PV 5.8.1, the most current version at the time of writing.

Before we can visualize anything, the model must be loaded onto PV. This is done by using the File/Open interface, selecting the correct file within the model output folder, and clicking on Apply. For LaMEM these can be either the *model_name.pvd* or the *model_name_surf.pvd* files (for the internal and topographic data, respectively), and for UW1 it can be either the *XMDF.temporalFields.xmf* or *XMDF.temporalSwarms.xmf* files (for nodal and particle data, respectively).

Once the model has been loaded, we select which variable to view by using the leftmost dropdown menu. For this section, the variable chosen was one which shows the different shapes/components generated in the model as a continuous variable (see Figure 2.9). Recall that in LaMEM this is represented by the "*phase [ ]*" variable, while in UW1 this is called "*MaterialIndexField*". Despite the name differences, these are identical variables.

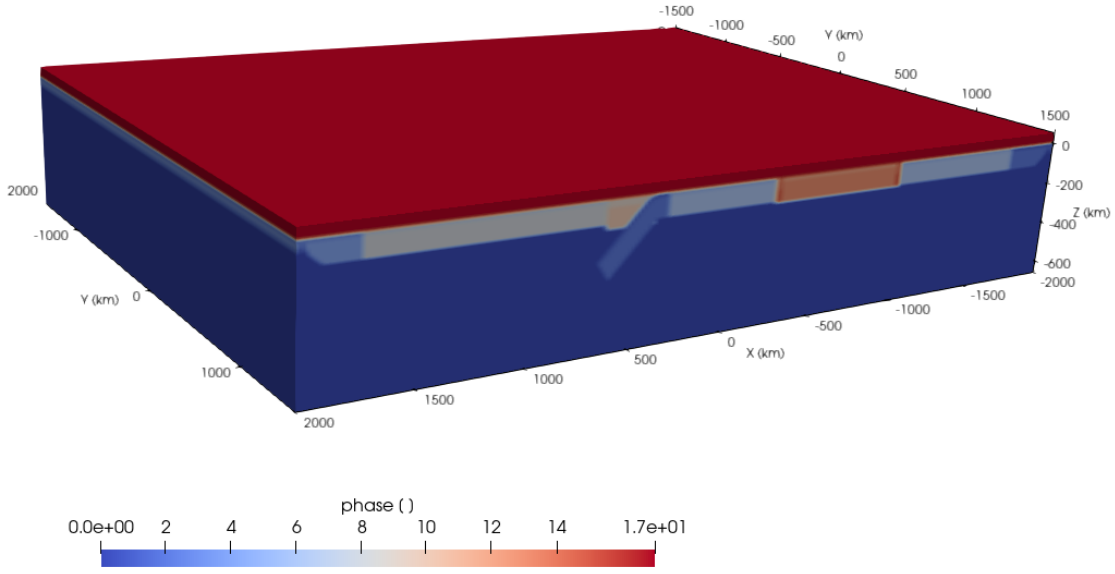

Figure 2.9 – Initial LaMEM model visualization using PV, at timestep zero. The different coloured components represent the shapes defined in the input file as a continuous variable (note the scale bar). For the present case, as an example, the top shape (in red) is the atmosphere, and the lower shape (in dark blue) is the sub-lithospheric

upper mantle. The axes labelling has been added using the Axes Grid option, in the Properties tab (by default on the lower left portion of the PV window).

While the current blocky aspect of the model might be fascinating (Figure 2.9), it does not show much of the dynamics of the subduction zone. Thus, it would be ideal to remove both the atmosphere and the upper mantle (uppermost and lowermost layers), leaving just the plates and oceanic plateau visible. This change is easily done by using the *Contour* menu. As any model component (i.e., plates) represents a range between a maximum and minimum value of the material/phase, we can simply contour the midpoint of the range to obtain a relatively accurate representation. If we take the case of the oceanic plateau, as its value ranges between 11.5 and 12.5, we simply contour the middle point, 12. In the specific case of LaMEM, the modelling code generates a variable which already contoured this data. Thus, we can contour the midpoint of the "*oceanic_plateau [ ]*" variable and obtain the same result. Once we repeat this process for remaining components of the model, the result is a much clearer picture of our subducting system (see Figure 2.10). It is also useful to know that it is possible to toggle each of these individual components, to observe the shape of the boundaries between them. This is done by clicking the eye symbol behind each layer on the pipeline browser (by default on the top left portion of the window).

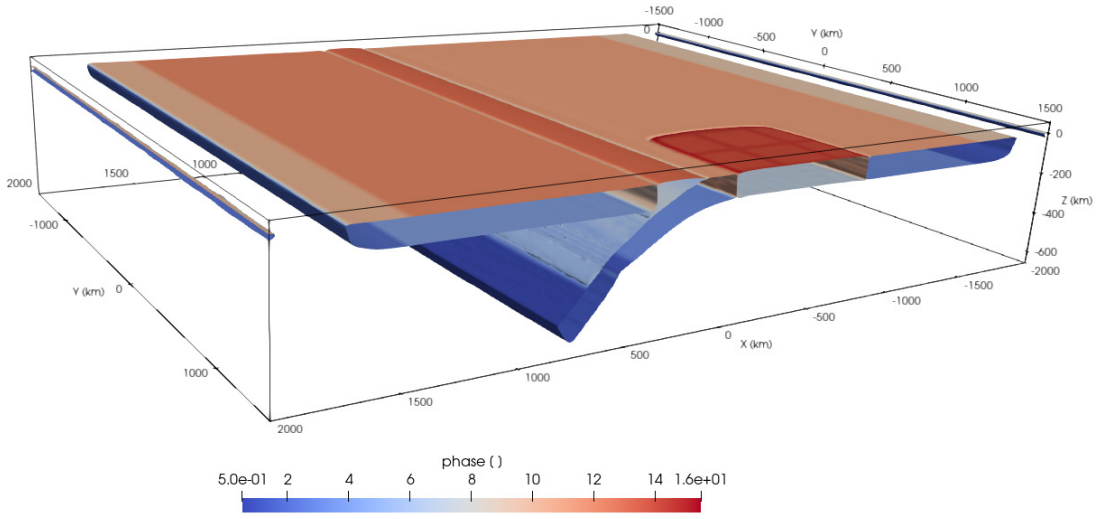

Figure 2.10 – Subduction zone initiation model with the atmosphere and upper mantle removed. At this stage, the model time is 6 Myr, which allows us to see the development of the subduction zone. The empty space along the edges of the X axis mark the position of a spreading centre.

When dealing with subduction zone dynamics, one of the most important factors is the sub-lithospheric mantle flow. This crucial flow of the upper mantle can also affect the surface volcanism and dynamics (Strak and Schellart, 2016). This can be easily observed in PV, by using the *Glyph* function, where individual arrows are placed to highlight the flow patterns. Within the *Glyph* menu, we select the velocity variable (LaMEM: "*velocity [cm/yr]*", UW: *"VelocityField"*) and both the *Scale* and *Orientation* dropdown menus, which allow the arrows to be oriented according to the different velocity components (Vx, Vy, Vz). This layer generally requires additional tweaking, as the default options generally result in either a cluttered or an empty view. The solution is to change the scale factor of the arrows, in the *Scale by Magnitude* option. For the case of this specific model, the value of 12 produces good sized arrows (see Figure 2.11).

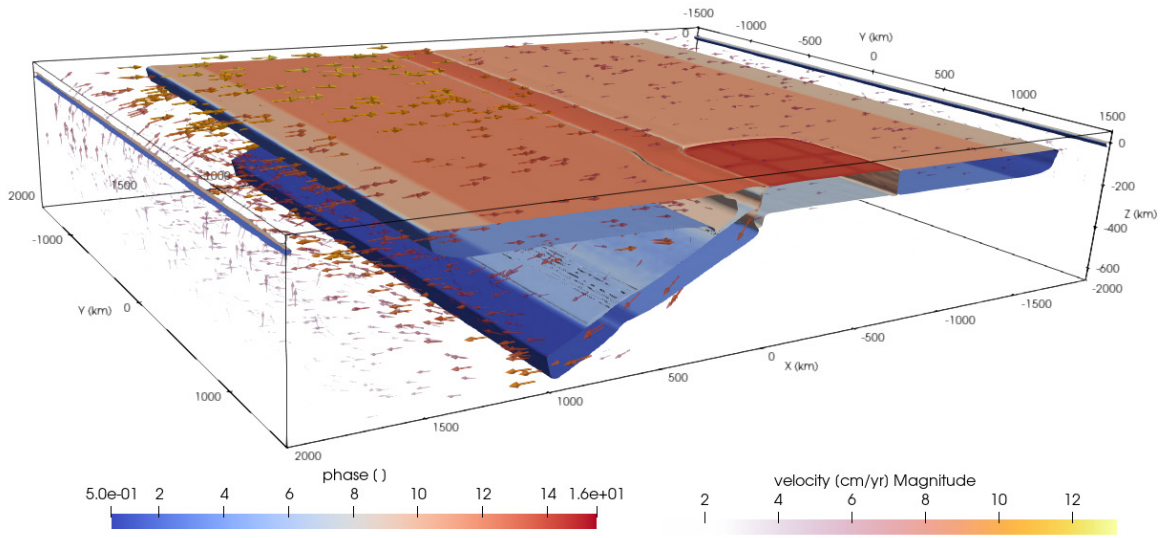

Figure 2.11 – Visualizing the flow pattern in a LaMEM model, using the Glyph function in PV.

While PV allows us to observe the model as whole, measuring and quantifying the evolution of certain key subduction zone parameters is not as simple. These include variables such as the position of the subducting trench, the migration velocity of each plate, among others. For that, we need to use more specialized processing scripts, created using Python.

2.4.2. geoProc, a Python library for geodynamical modelling

Python is one of the most popular programming languages being used in science. With it, it is possible to solve (almost) any problem, albeit less efficiently (i.e., slower) than with the use of low-level languages (i.e., C# or C++). Despite this, it has two major advantages for newcomers: its simple syntax and its immense module library. For most cases, if you can think about it, it is likely that someone, somewhere, has already written a Python module on the subject. Sadly, for more niche uses, such as subduction zone model processing, no such library existed. The consequence was that during the present PhD work, I had to develop my own library to read and process subduction zone models, which could have been run by either UW1 or LaMEM. While at first my solution consisted of simple, loose scripts, they slowly were consolidated into what became *geoProc*.

My objective with the development of this package was to be able to load data and detect specific features in any model, which could have been ran using either of the codes, with user-friendly functions. Even though it is still in development it can, at this stage, perform this exact task. The feature detection portion is still only applicable to subduction zone modelling, with automatic trench and trailing edge detection in simple 2D and 3D models. The source code can be found in Appendix C as well as at https://github.com/jaime-almeida/geoProc.

Installing it on a computer can be done using the files present in Appendix D and pip (the standard python package installer), using:

```
pip install geoProc-0.1-py3-none-any.whl
```

Note that this method requires that the user already has a working Python3.8+ installation.

In this package there are two major components: the loading modules (for each of the codes) and the post-processing modules. The loading modules gather the data generated by the modelling codes and convert it into a single, consistent format. This data conversion step prevents the need to code two different post-processing modules, allowing for data processing which is consistent between the two codes. In other words, we always use the same methods for processing and feature detection. It was developed using object-oriented programming. As so, some terminology classification must be done regarding the terms “class”, “object”, “instance”, “attribute” and “method”. The term *class* refers to the coding of a type of *object*,

while *instance* refers to different generations of this object. Within the class, we can assign different *attributes* to it, which can be either data or methods. The m*ethod* is simply a function which is contained by the object and is applied on it. As an example, we can define the class "animal" and then instantiate the objects "cat" and "dog", which are different versions of the class "animal". Each object could then have an attribute which contains the number of legs of the animal and a method to state which type of sound it makes.

The following sections aims to showcase its usage and to discuss some of the more complex points during the development (specifically, data loading and feature detection).

2.4.3. How to deal with data loading

If we akin geoProc package to a tree, the loading classes would, undoubtedly, be its roots. Without it, the entire library would fall apart. The core concept behind them is to have specialized classes which, when instantiated, "know" how to properly handle the model data. As each code uses a different format, with UW1 writing its data in HDF5 (Hierarchical Data Format) and LaMEM in PVD (PV Data), it was not possible to create a single function which could load the data from both types. Consequently, two specialized loaders were developed: UwLoader and LaMEMLoader. When instantiated, these loader objects can act as stand-alone objects or as input arguments for the post-processing classes. The latter type of usage will be explored/explained in a later subsection.

For both loaders, the parameters required to instantiate the object are the same: information regarding the model output folder and the timestep which needs to be read:

```
lamem_model_object = LaMEMLoader(model_dir='/model/directory/', ts=400)
uw1_model_object = UwLoader(model_dir='/model/directory/',  ts=400)
```

In the case of the UwLoader, it is also possible to specify the scaling factor being used in the model (which defaults to 10^{22}, as explained in a previous section). Both instances include an *output* attribute, the entire objective of the loader. It contains all the data created by the modelling code, which is stored by the loader as a Pandas dataframe. This choice of variable is not arbitrary and stems from the need to minimize the stress inflicted on both CPU and RAM. Most of us would consider our computers as "infinitely" powerful and able to perform as many operations as we want. In reality, that is not the case. When dealing with gigascale and terascale

data (as with our 2D and 3D models), the amount we can extract and process simultaneously is not only quite finite, but also directly proportional to the available RAM in the system. Given how most computers have a finite amount of RAM, it is quite frequent to cause a crash while trying to process a high-resolution model. Thus, Pandas dataframes were the solution, as a single complex object with highly efficient storage of multivariate data, where each individual variable is a column of a spreadsheet-like attribute (see Figure 2.12). When needed, individual variables can be extracted and converted to their numerical usable matrices using built-in methods.

	x	y	mat	vx	vy	e_xx	e_yy	e_xy	e_II	s_xx	s_yy	s_xy	eta	temp_K	temp_C
0	0.000000e+00	340000.0	2.0	0.000000	0.0	1.375279e+04	-1.575745e+04	-4.746531e+05	4.748834e+05	1.248856e+07	-1.248856e+07	-733481.638893	21.837294	1853.0	1579.85
1	6.510417e+03	340000.0	2.0	0.000000	0.0	-3.590948e+03	2.520232e+03	-5.978737e+05	5.978817e+05	1.250486e+07	-1.250486e+07	-777852.937889	21.780059	1853.0	1579.85
2	1.302083e+04	340000.0	2.0	0.000000	0.0	-1.332980e+03	1.886673e+03	-7.260403e+05	7.260421e+05	1.251550e+07	-1.251550e+07	-823012.255810	21.721997	1853.0	1579.85
3	1.953125e+04	340000.0	2.0	0.000000	0.0	4.453814e+03	-7.614521e+03	-8.485656e+05	8.485885e+05	1.250495e+07	-1.250495e+07	-861916.794161	21.675314	1853.0	1579.85
4	2.604167e+04	340000.0	2.0	0.000000	0.0	-7.495643e+03	9.089823e+03	-9.954946e+05	9.955295e+05	1.248388e+07	-1.248388e+07	-901850.387488	21.627563	1853.0	1579.85
...	...	...	...	...	...	...	...	...	...	...	...	...	...	...	...
148412	4.973958e+06	1000000.0	2.0	3.014801	0.0	4.600778e+08	-4.589769e+08	6.724587e+06	4.595769e+08	-1.207821e+07	1.207821e+07	13449.173955	19.000000	273.0	-0.15
148413	4.980469e+06	1000000.0	2.0	3.770462	0.0	3.921751e+08	-3.915651e+08	-2.940960e+06	3.918813e+08	-1.220119e+07	1.220119e+07	-5881.919201	19.000000	273.0	-0.15
148414	4.986979e+06	1000000.0	2.0	4.614154	0.0	3.423870e+08	-3.416302e+08	4.159168e+06	3.420341e+08	-1.230143e+07	1.230143e+07	8318.336452	19.000000	273.0	-0.15
148415	4.993490e+06	1000000.0	2.0	5.172795	0.0	3.091806e+08	-3.077846e+08	-4.692516e+06	3.085191e+08	-1.237747e+07	1.237747e+07	-9385.031906	19.000000	273.0	-0.15
148416	5.000000e+06	1000000.0	2.0	5.869244	0.0	2.664632e+08	-2.779980e+08	-2.775493e+06	2.723058e+08	-1.242330e+07	1.242330e+07	-5550.986240	19.000000	273.0	-0.15

Figure 2.12 – Example of the output attribute of a loader object, instantiated with a 2D model. Each column is a variable which was generated by the modelling code: x, y are the cartesian coordinate; mat is the material/phase variable; vx, vy are the horizontal and vertical velocities, respectively; e_xx, e_xy, e_yy are the non-redundant terms of the strain rate tensor; e_II is the second invariant of the strain rate tensor; s_xx, s_xy, s_yy are the non-redundant terms of the stress tensor; eta is the viscosity, stored in log form; and temp_K and temp_C are the temperature in Kelvin and Celsius degrees, respectively.

The collecting methods which gather the information for the *output* attribute are identical for most variables (for each type of modelling code), with just a change in the variable name. Let us see an example of the loading methods for the model velocity, for the different loaders.

When loading a UW1 model, the method to fetch the velocity would be:

```
def get_velocity(self):
    try:
                self.scf
    except NameError:
                raise ValueError('No Scaling Factor detected!')

    if type(self.output) == dict:
        self._get_mesh()
```

```
# Set the file path:
filename = self.model_dir + 'VelocityField.' + \
                                    self.current_step + '.h5'

# Read the h5 file:
data = h5.File(filename, 'r')

# Get the information from the file:
vel_info = data['data'][()]

# Write the info accordingly:
if self.dim == 2:
            velocity = pd.DataFrame(data=vel_info, columns=['vx', 'vy'])
else:
   # in 3D:
   velocity = pd.DataFrame(data=vel_info, columns=['vx', 'vy', 'vz'])

# Rescale
velocity = velocity_rescale(velocity, self.scf)

# Merge with the current output dataframe
self.output = self.output.merge(velocity, left_index=True, right_index=True)
```

This lengthy piece of code takes full advantage of the H5PY library, which allows us to read the output files created by UW1. We search for the velocity output files, with the general formulation */model/dir/variable_name.timestep.h5*, and extract the data from it. This data is then stored in a Pandas dataframe with two or three columns (for 2D and 3D models, respectively) which is then merged with the *output* attribute. As UW1 does not perform rescaling operations, these values need to be correctly converted into cm/yr, eq. (2.31), in this case using the *velocity_rescale* function.

$$v_{scaled} = \frac{v_{unscaled}}{scf} \times (365 \times 24 \times 60^2) \times 100 \qquad (2.31)$$

Here, v_{scaled} is the velocity in cm/yr, $v_{unscaled}$ is the default output from UW1 in m/s, and scf is the scaling factor (generally 10^{22}). The unnecessary brackets merely help to separate the different portions of the equation, the first term applies the scaling factor, the second converts to m/yr and the final to cm/yr.

When loading a LaMEM model, the method is much shorter:

```
def _get_velocity(self):
   # Get the velocity from the data files:
   velocity = v2n.vtk_to_numpy(self.__data.GetPointData().GetArray('velocity [cm/yr]'))

   # in 3D:
```

```
velocity = pd.DataFrame(data=velocity, columns=['vx', 'vy', 'vz'])

# Merge with the current output dataframe
self.output = self.output.merge(velocity, left_index=True, right_index=True)
```

The first line uses the VTK library (essentially a coding version of PV) to get the velocity matrix from the output files. As LaMEM automatically takes care of all scaling within the modelling code, the code is much simpler than the UW1 one. The next two lines are the same as before and, therefore, just generate and store a Pandas dataframe within the output variable.

A similar structure is applied for all the other variables during instantiation, resulting in a table such as the one seen in Figure 2.12. This said, these coding of these different methods may look somewhat daunting. The objective of this package was to make it user-friendly and, consequently, unless the user delves into the source code, they will never have to understand all of it. This section served merely to showcase the solution to the problem of having two different modelling codes.

The loader functions are called by the processing library, which should be the standard use of this package.

```
subduction_model_object = ModelProcessing(model_dir='/model/directory/',  ts=400)
```

The *ModelProcessing* detects which type of modelling code was employed and builds the appropriate output attribute. It contains different methods for data processing such as slicing, extraction by type of material and data interpolation, all of which contain documentation to explain their usage. A specialized version of this class called *SubductionModel*, also includes built-in 2D and 3D feature detection algorithms, such as automatic trench and polarity reversal detection.

2.4.4. Using geoProc to obtain features in a subduction zone model

In what concerns a subduction zone, we can look at an image like Figure 2.10 and locate the trench and the edges of our plates without any issue. This stems from the simple fact that for us, humans, it is relatively simple to look at a picture and recognize features. For a computer to do the same is no easy feat. It is required to either numerically define the features or to train

the computer using machine learning algorithms. In the present case, the former route was chosen as the features in question are easy to define.

To numerically identify a trench, we need to understand what defines it. A subduction trench, to reiterate what was said in Chapter I, is the location where the two plates meet and the slab sinks into the mantle. If the two plates meet, then it is also a place where the surface velocity changes direction. Mathematically speaking, we can use the *divergence* – the scalar function of a vectorial field, eq. (2.32) and Figure 2.13 – to find this point.

$$\mathrm{div}(\vec{v}) = \nabla \cdot \vec{v} = \frac{\partial v_x}{\partial x} + \frac{\partial v_y}{\partial y} + \frac{\partial v_z}{\partial z} \tag{2.32}$$

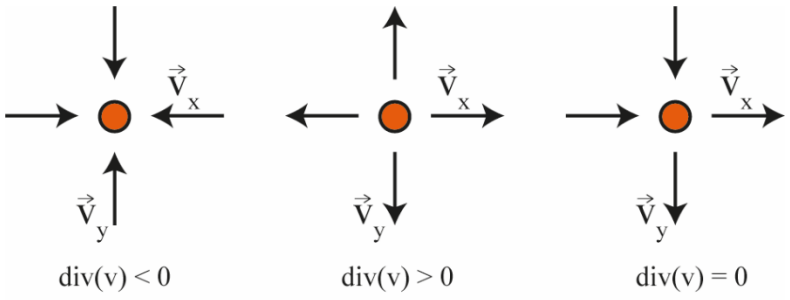

Figure 2.13 – Visual explanation of the divergence of a velocity field around a single point. A negative velocity divergence (left) describes a convergent velocity field (sink), a positive velocity divergence (middle) a divergent one (source), and a neutral divergence (right) implies flow along the point.

By detecting its minimum across the model surface (Figure 2.14), we can instantly find the location of the point of highest convergence which, normally, represents the location of the trench. This method is called by default by the SubductionModel class and can be called by the ModelProcessing class by:

```
model_object = ModelProcessing (model_dir='/model/directory/', ts=400)
trench_position = model_object.find_trench()
```

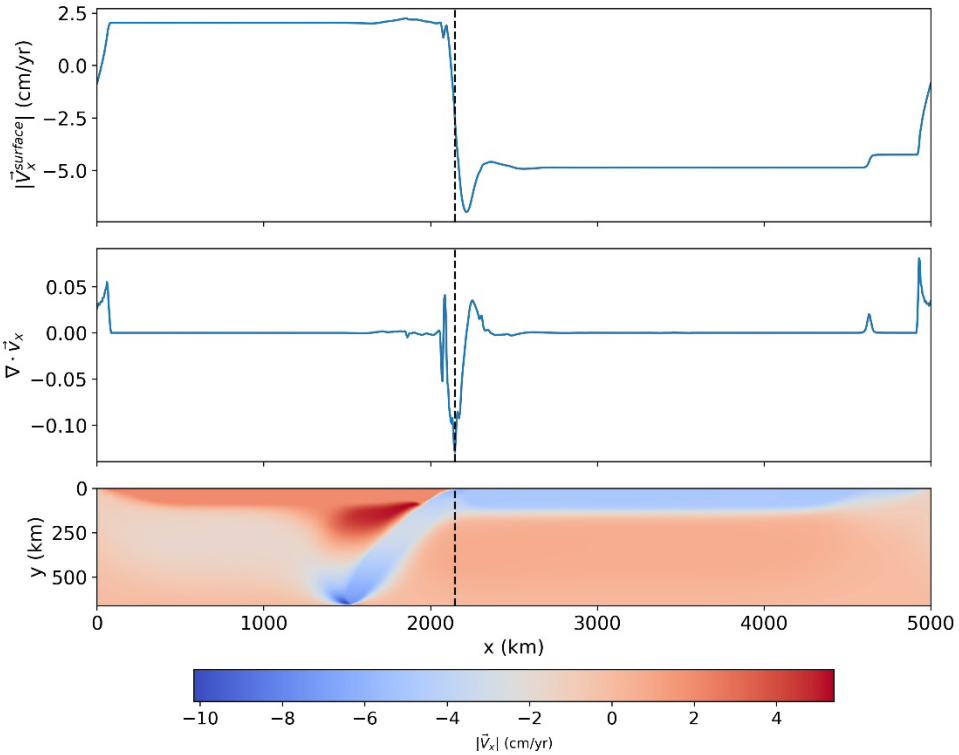

Figure 2.14 – Example of the trench detection algorithm in a 2D model. We use the horizontal velocity (v_x, top) and calculate its divergence (middle). The minimum point marks the position of maximum convergence, materialized by the trench. The position of the trench is shown by the vertical dashed line.

Another relevant feature to be detected are the edges of the plates, which can also be obtained by the calculating the two highest peaks of the velocity divergence (see Figure 2.14 and Figure 2.15). This method can be called by using:

```
subduction_model_object.find_plate_edges()
```

This returns two values (or vectors in 3D) with the coordinates for the two plate edges.

These divergence algorithms can, in theory, be expanded across trench normal slices of a 3D model to obtain the surface trace for both the trench and plate edges. For the case of the modelling runs in which the subduction zone is mostly parallel to one of the cartesian directions (such as the one shown in Figure 2.15), it is highly accurate. In other cases, such as circular or highly curved trenches, due to the numerical implementation, this method is strongly subject to both local minima and irregular subduction zone shapes. As an example, the circular subduction zone would require two minimum divergence detections per slice as opposed to one. A solution

for this problem – which is currently under development – is the use of image processing libraries to detect the trace of the subduction trench along the surface of the 3D model.

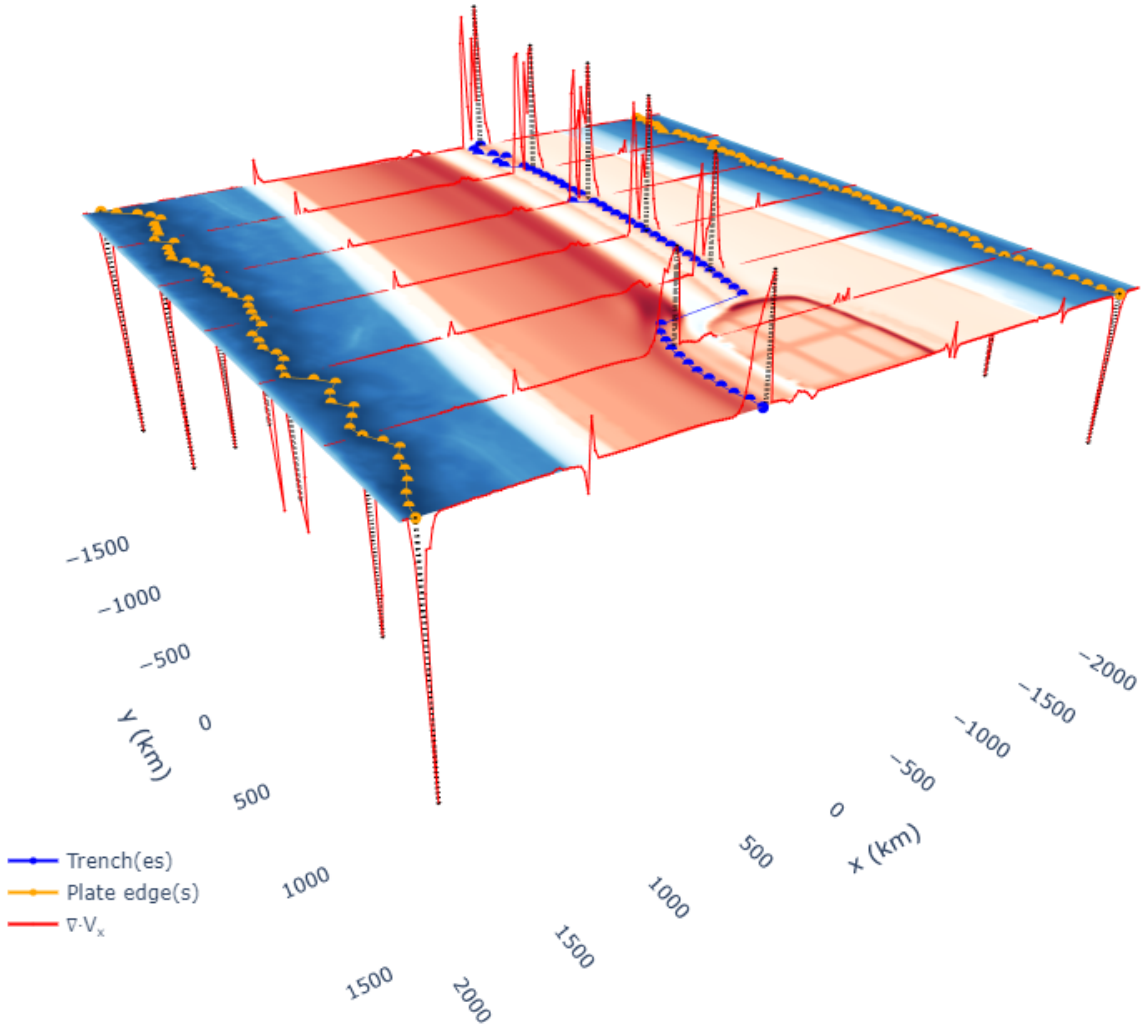

Figure 2.15 – Illustration of the 3D application of the trench detection algorithm. The subduction zone is dipping towards the right on the closest wall and towards the left on the farthest. The red lines represent the symmetric values for the velocity divergence along the x-axis. The use of the symmetric value is merely to simplify the visualization, as otherwise, the subduction trench peaks would not be visiable. A peak below the surface represents a divergent plate limit, while a peak above the surface implies a convergent plate limit. The blue dotted line shows the geometry of the trench along the surface of the model. The orange dotted lines show the geometric position of the plate edges. The black dotted lines which connect the vertices of the divergence lines represent the projection of the trench and plate edges to the surface.

Having both the position of the plate edges and subduction trench detected allows us to calculate other relevant variables such as the subducting and overriding plate velocities, the subduction velocity, the trench migration velocity (as in Schellart, 2008), among others.

Algorithms to automatically calculate these parameters have not been implemented as of now, as they are strongly geometry dependent.

The last algorithm implemented is the automatic detection of polarity reversal events. As most of the modelling studies conducted in this thesis included large sets (>50) of models, it was necessary to automatically identify when the polarity had reversed, to reduce the post-processing time. This method can be used by:

```
subduction_model_object.get_polarity(op_material=X)
```

This algorithm looks for the presence of crustal materials which belong to the overriding plate beneath the theoretical maximum lithosphere depth which is 110 km by default. The output from this method is a new column in the *output* attribute, which contains the polarity associated with each point: “0” for the original polarity and “1” for reversed polarity. In 2D, all points will have the same value (i.e., corresponding to either normal or reverse polarity), while in 3D this depends on the polarity along the considered trench-orthogonal slice. As an example, the trenches shown in Figure 2.15 have two different values, with the closest having a value of 1 (resulting from a reversal) and the more distant trench having a value of 0.

Chapter 3. Polarity-reversal subduction zone initiation triggered by buoyant plateau obstruction

---

Published as:

Almeida, J. et al. (2022) 'Polarity-reversal subduction zone initiation triggered by buoyant plateau obstruction', Earth and Planetary Science Letters, 577, p. 117195. doi: 10.1016/j.epsl.2021.117195.

(this page has been left intentionally blank)

Polarity-reversal subduction zone initiation triggered by buoyant plateau obstruction

J. Almeida [1,2]*, N. Riel [3], F.M. Rosas [1,2], J.C. Duarte [1,2,5], W.P. Schellart [4]

[1] Instituto Dom Luiz (IDL), Faculdade de Ciências, Universidade de Lisboa, Lisboa, Portugal.

[2] Departamento de Geologia, Faculdade de Ciências, Universidade de Lisboa, Lisboa, Portugal.

[3] Institut fur Geowissenschaften, Johannes Gutenberg-Universitat, Mainz, Germany

[4] Department of Earth Sciences, Vrije Universiteit Amsterdam, Amsterdam, Netherlands.

[5] School of Earth, Atmosphere and Environment, Monash University, Melbourne, VIC 3800, Australia.

*email: jealmeida@fc.ul.pt

3.1. Abstract

Oceanic lithosphere worldwide is younger than ca. 200 Myr, suggesting that it must have been globally recycled by the recurrent formation of new subduction zones since the existence of subduction on Earth. However, postulated subduction zone initiation processes remain difficult to explain in many cases, and the specific geodynamic conditions under which these might occur are still largely unknown. We here use numerical models driven by the internal force balance of a subduction system to better understand the (geo)dynamics governing (intra-oceanic) *polarity-reversal subduction zone initiation*. This initiation mode assumes that the birth of a new subduction zone could be triggered by buoyant plateau-obstruction of a pre-existent one dipping in the opposite direction. Our work provides a new insight on the key geodynamic conditions governing this type of subduction zone initiation and discusses their general compliance with known natural examples.

Keywords: subduction zones, subduction zone initiation, oceanic plateau, polarity-reversal, numerical modelling, internal force balance

3.2. Introduction

Subduction zone initiation (SZI) is one of the main unsolved problems in modern day plate tectonics theory (Cloetingh et al., 1982; Crameri et al., 2020; J. Duarte et al., 2013; Gurnis et al., 2004; Hall, 2019; Mueller and Phillips, 1991; Stern, 2004; Stern and Gerya, 2018; Zhong and Li, 2019). Most of the oceanic lithosphere worldwide is younger than ca. 200 Myr, which indicates that new subduction zones must be formed sometime after the opening of an ocean (cf. Wilson Cycle concept). SZI is thus mandatory to explain the recurrent recycling of ocean

floor lithosphere predicted by global plate tectonics as we know it (Davies, 1992). However, it is (geo)dynamically very difficult to envisage, since its spontaneous (buoyancy-driven) occurrence along old passive margins would require forces of very high magnitude, well above the ones generally acknowledged to exist in nature (Cloetingh et al., 1989; Mueller and Phillips, 1991). Furthermore, no clear examples of Cenozoic SZI along old passive margins are known anywhere on our planet, although some are interpreted to have been formed during Mesozoic times (Crameri et al., 2020; Gurnis et al., 2004). Spontaneous SZI is thus generally seen as unrealistic, since the contribution of tectonic forces is thought as inescapable for any considered tectonic setting on Earth (Arcay et al., 2019; Auzemery et al., 2020; Crameri et al., 2020). To try to solve this fundamental question, several alternative modes of subduction zone initiation have been previously proposed (Crameri et al., 2020; Stern, 2004; Stern and Gerya, 2018). Here, we present a geodynamic numerical modelling study of polarity-reversal subduction zone initiation, which seems to be one of the more common SZI mechanisms in the past 100 Ma (Crameri et al., 2020). Our main goal is to better understand the key combination of forces that, under the simulated modelling constraints, might drive the formation of a new opposite dipping subduction zone, and to evaluate its geodynamic feasibility as a SZI mechanism under similar general conditions in nature.

When a positively buoyant plateau (e.g., an oceanic ridge or a continental fragment) arrives at a subduction trench it resists being dragged downwards along the subduction channel, obstructing it, and ultimately blocking the pre-existent subduction zone. Depending on the thermo-mechanical state of both plates involved, and on the resulting changes in the stress distribution pattern caused by this blocking, a new subduction zone might nucleate either in the back of the obstructing plateau, dipping in the same direction as the original one – *subduction transference* (Stern, 2004; Stern and Gerya, 2018; Tetreault and Buiter, 2012); or at its front, dipping in the opposite direction – *subduction polarity reversal* (e.g., Hall, 2002; Konstantinovskaya, 2011; Mann and Taira, 2004; Zhang and Leng, 2021). The internal SZI driving forces at play in both these instances have an important horizontal component, rendering the corresponding SZI modes the designation of "horizontally forced" (Crameri et al., 2020).

Based on former (field, analogue and numerical modelling) studies three generic conditions were found indispensable for the formation of a new subduction zone, and acknowledged as common to all previously proposed SZI modes: i) initial bending of the future subducting plate, leading to subsequent underthrusting beneath the future overriding plate (Gurnis et al., 2004;

Nikolaeva et al., 2011, 2010); ii) efficient strain localization along a narrow weak zone between the two plates (Gurnis et al., 2004; Lu et al., 2015) facilitated by pre-existing mechanical weaknesses (e.g., transform faults, Uyeda and Ben-Avraham, 1972) and by positive feed-back strain-weakening mechanisms (e.g., chemical weakening or grain-size reduction, Hirauchi et al., 2016) and; iii) propagation of this narrow weak zone across the whole thickness of the lithosphere to form a subduction channel (Gurnis et al., 2004).

While polarity-reversal SZI has been one of the main mechanisms proposed to explain the possible origin of new subduction zones during the Meso-Cenozoic (Buchs et al., 2010; Crameri et al., 2020; Hall, 2002; Konstantinovskaya, 2011; Mann and Taira, 2004; Wright and Wyld, 2011), the fundamental dynamics governing this type of SZI remains poorly understood. Here, we present a series of numerical modelling experiments carried out to gain a new insight on the dynamics of this process. We specifically focus on understanding the way through which the internal balance of driving forces in a (pre-existent) subduction zone can be perturbed by the arrival of a buoyant plateau to the trench, as to render polarity-reversal SZI. Our models were conceived to exclusively account for the internal forces at play (i.e., buoyancy vs. viscous resistance) in the absence of any other (externally imposed) ones.

3.3. Methods

3.3.1. Numerical code and governing equations.

Numerical modelling experiments were carried using the code Underworld (Moresi et al., 2007). Underworld employs a finite element discretization coupled with a particle-in-cell approach to solve the equations of conservation of mass, momentum, and energy (eq. 3.1-3, respectively), assuming conditions of incompressibility:

$$\nabla \cdot \mathbf{v} = 0 \tag{3.1}$$

$$\nabla \cdot \boldsymbol{\sigma} = \rho \mathbf{g} \tag{3.2}$$

$$\rho C_p \left(\frac{\partial T}{\partial t} + \mathbf{v} \cdot \nabla T \right) = \kappa \nabla^2 T + H_s + H_A \tag{3.3}$$

in which $\mathbf{v}$ is the velocity vector, $\boldsymbol{\sigma}$ the stress tensor, ρ the density, $\mathbf{g}$ the gravity acceleration vector, κ the diffusivity, T is the temperature and C_p the specific heat. The shear heating (H_S) and the adiabatic heating (H_A) in equation 3.3 above are respectively defined as:

$$H_s = \sum [\boldsymbol{\sigma}' \cdot \dot{\boldsymbol{\varepsilon}}]_{ij} \tag{3.4}$$

$$H_A = \frac{-T\alpha \mathbf{v_y} g}{c_p} \tag{3.5}$$

in which, $\boldsymbol{\sigma}'$ represents the deviatoric stress tensor, $\dot{\boldsymbol{\varepsilon}}$ is the strain rate tensor, α the coefficient of thermal expansion and $\mathbf{v_y}$ the vertical velocity. The stress tensor is defined by:

$$\boldsymbol{\sigma} = \boldsymbol{\sigma}' - P\mathbf{I} \tag{3.6}$$

with P as the pressure and $\mathbf{I}$ the identity tensor. The deviatoric stress tensor ($\boldsymbol{\sigma}'$) is defined as a function of both strain rate ($\dot{\boldsymbol{\varepsilon}}$) and effective viscosity (η_{eff}):

$$\boldsymbol{\sigma}' = 2\eta_{eff}\dot{\boldsymbol{\varepsilon}} \tag{3.7}$$

The strain rate tensor ($\dot{\boldsymbol{\varepsilon}}$) is in turn defined as:

$$\dot{\boldsymbol{\varepsilon}} = \frac{1}{2}[\nabla \mathbf{v} + (\nabla \mathbf{v})^T] \tag{3.8}$$

and the effective viscosity is calculated by:

$$\eta_{eff} = A^{-\frac{1}{n}} \dot{\varepsilon}_{II}^{\frac{1}{n}-n} \exp\left(\frac{E_a + V_a P}{nRT}\right) \tag{3.9}$$

with A as the pre-exponential factor, $\dot{\varepsilon}_{II}$ the second invariant of the strain rate tensor, n the stress exponent, E_a the activation energy, V_a the activation volume and R the universal gas constant.

Plastic flow is implemented in all models assuming a Drucker-Prager yield criterion (Drucker and Prager, 1952), according to which a given material is set to yield plastically when stress surpasses a prescribed limit (yield value):

$$\sqrt{\boldsymbol{\sigma'_{II}}} = p\sin(\phi) + C\cos(\phi) \tag{3.10}$$

in which $\boldsymbol{\sigma'_{II}}$ is the second invariant of the deviatoric stress tensor, ϕ the internal friction angle and C the cohesion. When materials reach the yield stress, they are linearly softened until ϕ and cohesion reach 10% of the original value.

Plate age dependence of the thermal profiles follows the plate cooling model:

$$T = T_0 + (T_1 - T_0)\left[\frac{y}{y_{Lo}} + \frac{2}{\pi}\sum_{n=1}^{\infty}\frac{1}{n}\exp\left(\frac{\kappa n^2\pi^2 t}{y_{Lo}^2}\right)\sin\left(\frac{n\pi y}{y_{Lo}}\right)\right] \tag{3.11}$$

in which T_0 is the temperature at the surface of the model (set to 273 K), T_1 is the temperature at the lithosphere-asthenosphere boundary (y_{Lo}) set to 1473 K, y is the depth, and t is the age of the plate. All material densities are also temperature dependent according to:

$$\rho = \rho_0[1 - \alpha(T - T_0)] \tag{3.12}$$

in which ρ_0 is the density of the material at the reference temperature T_0.

3.3.2. Initial model setup and modelling approach.

A set of 2D numerical modelling experiments was conceived (Figure 3.1A), in which all model kinematics (i.e., the movement of the plates and the resulting flow in the sub-lithospheric mantle) are the result of the internal balance between the slab negative buoyancy driving force and the counteracting viscous resistance (e.g., Schellart, 2017; Stegman et al., 2010). No external forces (e.g., resulting from prescribed boundary conditions) were implemented in any of the models, which are thus fundamentally controlled by the way this internal force balance changes with time.

The considered (overriding vs. downgoing) plate age contrast was systematically varied, with initial overriding plate (OP) ages ranging between 10 and 70 Myr, for 10 Myr intervals. The assumed initial age variation for the downgoing plate (DP) was between 10 and 110 Myr, also for 10 Myr intervals (see Figure 3.2). A total of 77 numerical simulations was thus investigated, comprising all resulting combinations of initial OP vs. DP ages. This variety expresses different initial rheological and density contrasts between the two plates in each case, hence bearing a decisive influence on the final geodynamic outcome that follows from plateau accretion and collision (see Figure 3.2).

The considered 2D model domain is of 5000 x 660 km, with its maximum depth corresponding to the upper-lower mantle transition (see Figure 3.1A) and was discretized using a uniform 1536 x 384 grid. A 110 km thick positively buoyant plateau was set fixed to the subducting slab in the initial stage of all the experiments at 1100 km from the subduction trench (see inset of Figure 3.1A). In the plateau, both the crust and lithospheric mantle were initially set as positively buoyant (with ρ_0 reference densities of 2800 and 3200 kg/m^3, respectively) relative to the denser OP and DP, and to the asthenosphere (all with ρ_0 = 3300 kg/m^3 – see Table 3.1). A thin (ca. 15 km) weak zone was set between the overriding and downgoing plates, accounting for a pre-existent subduction channel. Subduction was triggered in all models by the negative buoyancy of the DP implied by the initial model configuration, in which the foundering of the tip of the subducting slab was set at a maximum depth of 160 km (see Figure 3.1A).

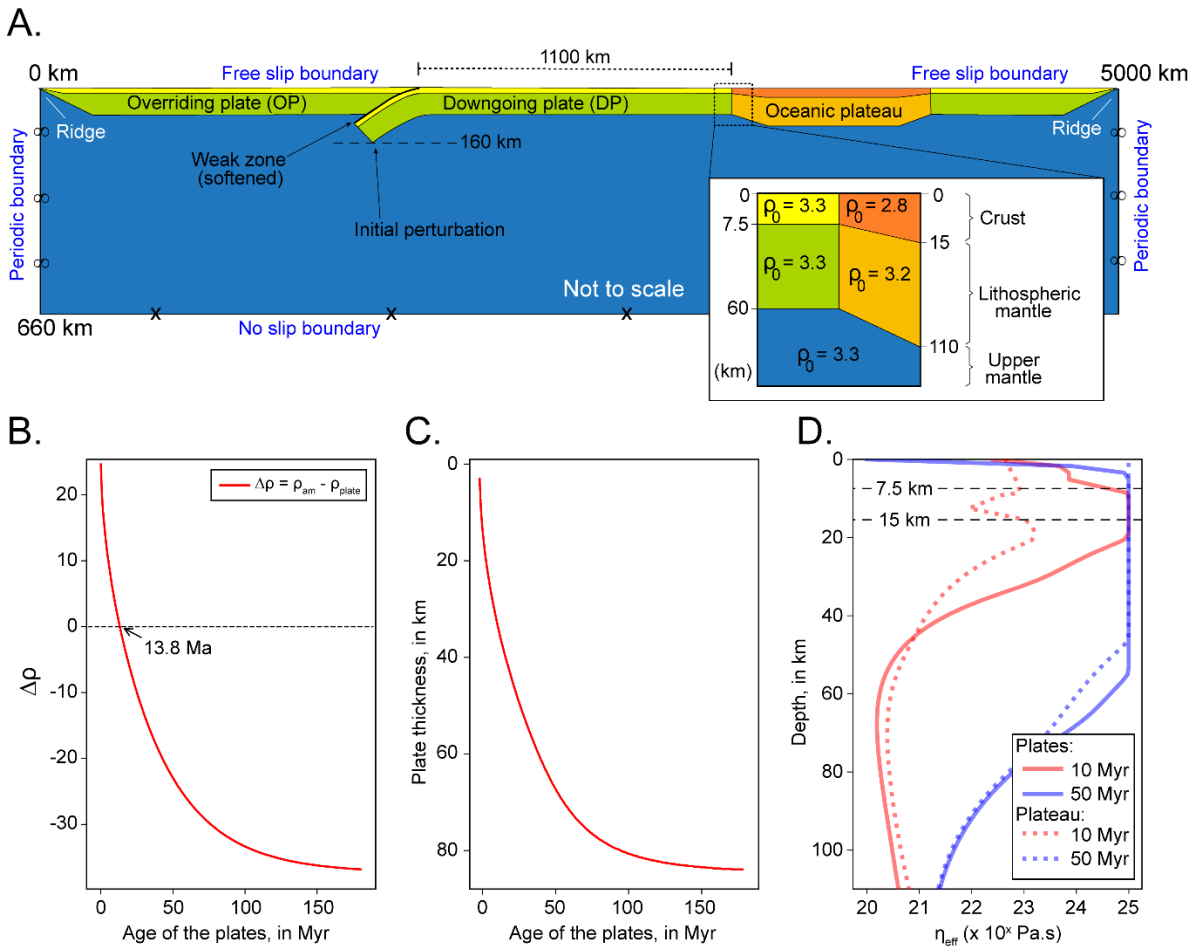

Figure 3.1 – A. Model setup for the experimental initial state (not to scale): schematic representation of the geometric configuration, model dimensions and prescribed boundary conditions (BCs). Inset shows comparative (normal plate vs. plateau) reference densities ($\boldsymbol{\rho_0}$ in g/cm^3) initially assumed for the crust, lithospheric mantle and asthenosphere. Note that unit shapes and corresponding $\boldsymbol{\rho_0}$ values in A do not reflect plate aging, nor associated cooling and implied effective lithospheric densities and thicknesses, which ultimately determine the changing buoyancy of the lithospheric plates relatively to its underlying mantle. **B.** Effective buoyancy, C. Effective maximum lithospheric thickness as a function of plate age. Effective buoyancy is expressed by the density contrast between the asthenosphere and the lithospheric mantle: $\Delta_\rho = \boldsymbol{\rho_{am}} - \boldsymbol{\rho_{plate}}$. Effective lithospheric thickness is given by the depth of the 1473 K (1200º C) isotherm. The depicted time-dependent evolution of both parameters is determined by the assumed plate cooling model (equations 3.11 and 3.12), and **D.** Strength-depth profiles for plates (solid lines) and corresponding plateaus (dashed lines) with differently assumed initial ages of 50 (in blue) and 10 Myr (in red). Strength of the plates is given by effective viscosity (η_{eff}).

The initial temperatures for both plates were defined in accordance with the plate cooling model (eq. 3.11), in which T is obtained as a function of both depth and time (plate age). Using this thermal model and the assumed density dependency on temperature (eq. 3.12), the effective

plate density contrast between the plate and the underlying asthenosphere can be calculated (eq. 3.13):

$$\Delta\rho^{plate}_{asthenosphere} = \rho_{am} - \rho_{plate} \quad (3.13)$$

with ρ_{am} as the density of the sub-lithospheric mantle and ρ_{plate} the average density of the plate. The resulting description of plate density contrast as a function of time (Figure 3.1B) shows that any plate becomes denser than the underlying mantle (i.e., negatively buoyant) after only ca. 14 Myr. The effective (rheological) thickness of the lithosphere (set by the 1473K isotherm), and the way it depends on time, are also deduced from the same plate cooling model (eq. 3.11) showing a consistent non-linear increase of plate thickness with its age (Figure 3.1C).

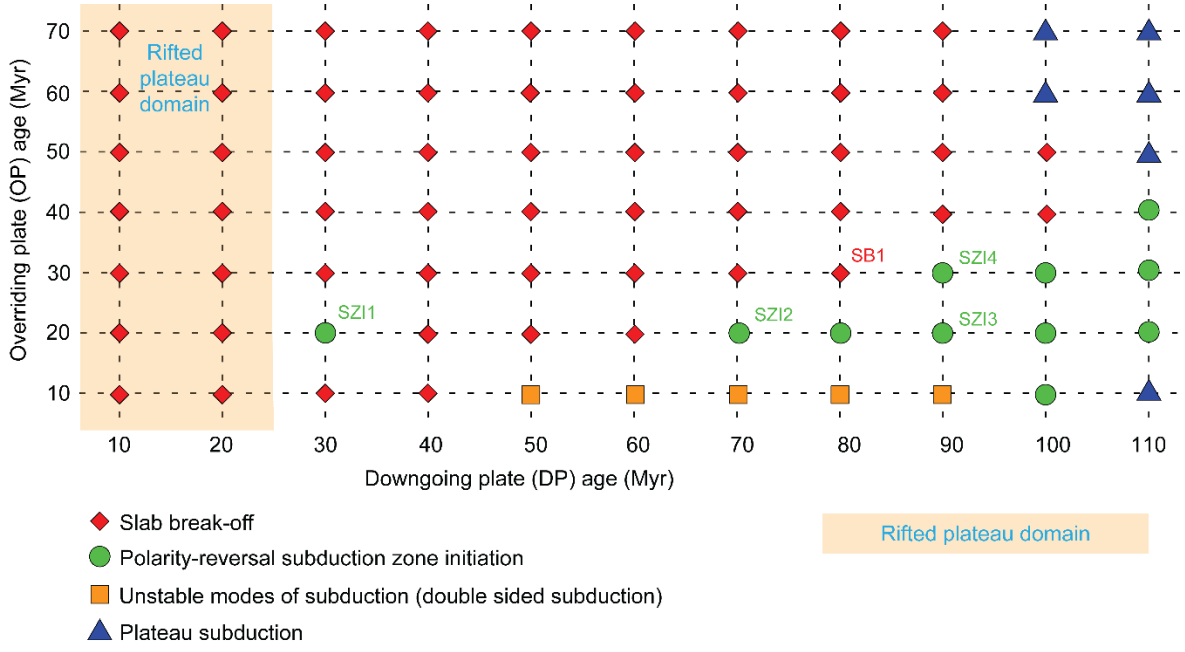

Figure 3.2 – Graphic grid depiction of all 77 plate age combinations considered in the carried out numerical modelling experiments. Vertical and horizontal axes represent the initial ages prescribed to the overriding and downgoing plates, (OP and DP) respectively. The symbols at the nodes of the grid represent the (general) results: **red diamonds** correspond to numerical model results that did not yield subduction polarity-reversal, and in which the initial subduction was always terminated by DP slab break-off after the arrival of the plateau at the subduction trench; **Green circles** correspond to numerical modelling results that yielded polarity-reversal subduction zone initiation; **Oranges squares** represent (transient, unstable) double-sided subduction, which was not investigated in detail in the present study; **Dark blue triangles** represent plateau subduction events (also not investigated in detail in the present study). The **shaded light-orange domain** corresponds to the results in which rifting was observed to occur in one of the plates (generally the DP).

The trailing edges of both plates are tapered, with the basal lithosphere isotherm bulging upwards near the left and right model boundaries, defining a pair or mantle upwelling ridge centres (see Figure 3.1A). This allows for free lateral migration of both plates, ensuring that slab negative buoyancy force and mantle viscous resistance act as the only main forces in our models (besides only minor ridge push at the lateral boundaries). It also prevents the otherwise strong downwelling of cooled material formed at the edges of the model, which would artificially perturb the mantle flow.

The model rheology of the oceanic plateau crust follows a plagioclase creep law (Ranalli, 1997), while the remaining model materials follow the dry peridotite law (Ranalli, 1997). Consequently, for younger plateaus (i.e., with higher thermal gradients), the crust of the plateau is weaker than the surrounding oceanic plate crust (see Figure 3.1D, dotted vs solid red lines). For older plates (i.e., with lower thermal gradients), the strength profile of the plateau and oceanic plates is almost identical (see Figure 3.1D, solid vs dotted blue lines).

The initial subduction interface (softened weak zone in Figure 3.1A) is defined by an isoviscous rheology (with a constant low viscosity of 10^{20} Pa·s) to achieve early on high strain localization in the subduction channel. This soft material channel is subducted in the early stages of the experiments and bears no relevant role in any of the model results.

All assumed parameters for the different considered model materials are presented in Table 3.1.

Table 3.1 – Parameters used in the definition of the non-linear (thermal dependent) model rheology/density configuration. The density (ρ_0) parameters represent the density at reference temperature (T_0, see equation 3.11).

Parameter	Value	Reference
Expansibility, α (K^{-1})	3.00 x 10^{-5}	-
Diffusivity, κ ($m^2\ s^{-1}$)	1.00 x 10^{-6}	-
Heat capacity, C_p ($J\ kg^{-1}\ K^{-1}$)	1.00 x 10^3	-
c_{crust} (MPa)	20	(Hui et al., 2014)
c_{mantle} (MPa)	30	(Hui et al., 2014)
Φ_0 (degrees)	~14	(Gerya et al., 2008)
$T_{surface}$ (K)	273	-

T_{base} (K)	1473	-
$\rho_{0\ oceanic\ crust}$ (kg m^{-3})	3300	-
$\rho_{0\ lithospheric\ mantle}$ (kg m^{-3})	3300	-
$\rho_{0\ asthenosphere}$ (kg m^{-3})	3300	-
$\rho_{0\ plateau\ crust}$ (kg m^{-3})	2800	-
$\rho_{0\ plateau\ mantle}$ (kg m^{-3})	3220	-
$A_{plateau\ crust}$ (MPa^{-n} s^{-1})	1.00 x 10^{-7}	(Ranalli, 1997)
$A_{upper\ mantle}$ (MPa^{-n} s^{-1})	5.49 x 10^{4}	(Ranalli, 1997)
$n_{plateau\ crust}$	2.00	(Ranalli, 1997)
$n_{plateau\ mantle}$	3.50	(Ranalli, 1997)
$E_{a\ plateau\ crust}$ (J mol^{-1})	1.50 x 10^{5}	(Ranalli, 1997)
$E_{a\ upper\ mantle}$ (J mol^{-1})	5.30 x 10^{5}	(Ranalli, 1997)
V_a (m^3 mol^{-1})	1.00 x 10^{-6}	(Ranalli, 1997)

3.3.3. Boundary conditions (BC).

The models have periodic boundary conditions along the horizontal axis (eq. 3.14, Figure 3.1A). Accordingly, material escaping through one of the lateral (vertical) boundaries is prescribed to re-enter the model across the other (opposite) one with the same velocity value:

$$\vec{v}_{x-a} = \vec{v}_{x+a} \tag{3.14}$$

where *a* is the width of the model. This allows for subduction slab roll-back/-forward and implied trench migration, as closed lateral boundaries hinder such motions in 2D models since no toroidal (return) mantle flow from beneath the slab is possible in these cases (Schellart, 2004a). Horizontal free-slip BC were ascribed to the model top boundary (eq. 3.15) deterring vertical escape/motion of material across this boundary (see discussion in section 3.8, paragraph g). No-slip BC, defined by equation 3.16, were instead implemented along the model bottom wall. Such basal BC account for the sharp viscosity contrast along the 660 km upper-lower mantle transition. This approximates slab anchoring at this discontinuity without accounting, however, for further subduction across this interface.

$$\vec{v}_y = \vec{0} \tag{3.15}$$

$$\vec{v}_x = \vec{v}_y = \vec{0} \tag{3.16}$$

Thermally, the model top wall was prescribed to correspond to the 273 K (0° C) isotherm, while the bottom boundary was set to correspond to 1873 K (1600° C).

3.4. Results

The initial subduction of the DP always drives the (thicker, buoyant) oceanic plateau to the trench, where it resists being further dragged downwards, obstructing the subduction channel, and ultimately bringing this initial subduction to an end (red diamonds in Figure 3.2). In most cases, this obstruction leads to slab break-off (Figure 3.3A-B, see Supplementary Video 1). This involves total tearing of the subducted DP from the adjacent buoyant plateau, with relatively little bending of the OP (Figure 3.3B).

In a smaller number of cases (green circles in Figure 3.2), the original OP is significantly bent and underthrust beneath the original DP, ultimately leading to the birth of a new subduction zone dipping in the opposite direction (Figure 3.3C, see Supplementary Video 5). This polarity-reversal SZI was observed only in 11 numerical experiments (~14% of the cases) for a variety of different initial age combinations between the OP and the DP (green circles in Figure 3.2 and Supplementary Videos 3-6). These initial ages influence the buoyancy, thickness, and strength of both plates at the time of the arrival of the plateau at the subduction trench (or plateau docking, Figure 3.4). Under our modelling setup, the dynamic conditions that eventually yield polarity-reversal SZI result mostly from the combination of younger overriding plates and older (stronger) downgoing plates. The results also show (Figure 3.4 and Supplementary Videos) that polarity-reversal SZI requires the DP to be negatively buoyant relatively to both the asthenosphere and the OP (see location of green circles in Figure 3.4 within the DP negative buoyancy domain). Accordingly, polarity-reversal SZI was never observed for OP with an age at docking greater than ca. 64 Myr or with an effective strength higher than ca. 10^{23} Pa·s (Figure 3.4A and 4B, respectively).

Unstable double-sided subduction was observed in ~6% of the results in models with initial OP ages = 10 Myr (orange squares in Figure 3.2, Supplementary Video 2). It always occurred at very early stages in our simulations, as a transient unstable result, when the buoyant plateau was still several hundreds of kilometres away from the trench. It may represent a transient mode

between different, oppositely facing single-sided subduction zones as shown in previous whole-mantle geodynamic studies (Crameri et al., 2014; Crameri and Tackley, 2015), or it could simply correspond to a model artefact arising from the adopted free-slip top boundary conditions (see section 3.8, paragraph g). In any case, this double-sided mode of subduction has never been recorded in the Earth's lithosphere (Gerya et al., 2008) and its specific study it is out of the scope of the present paper.

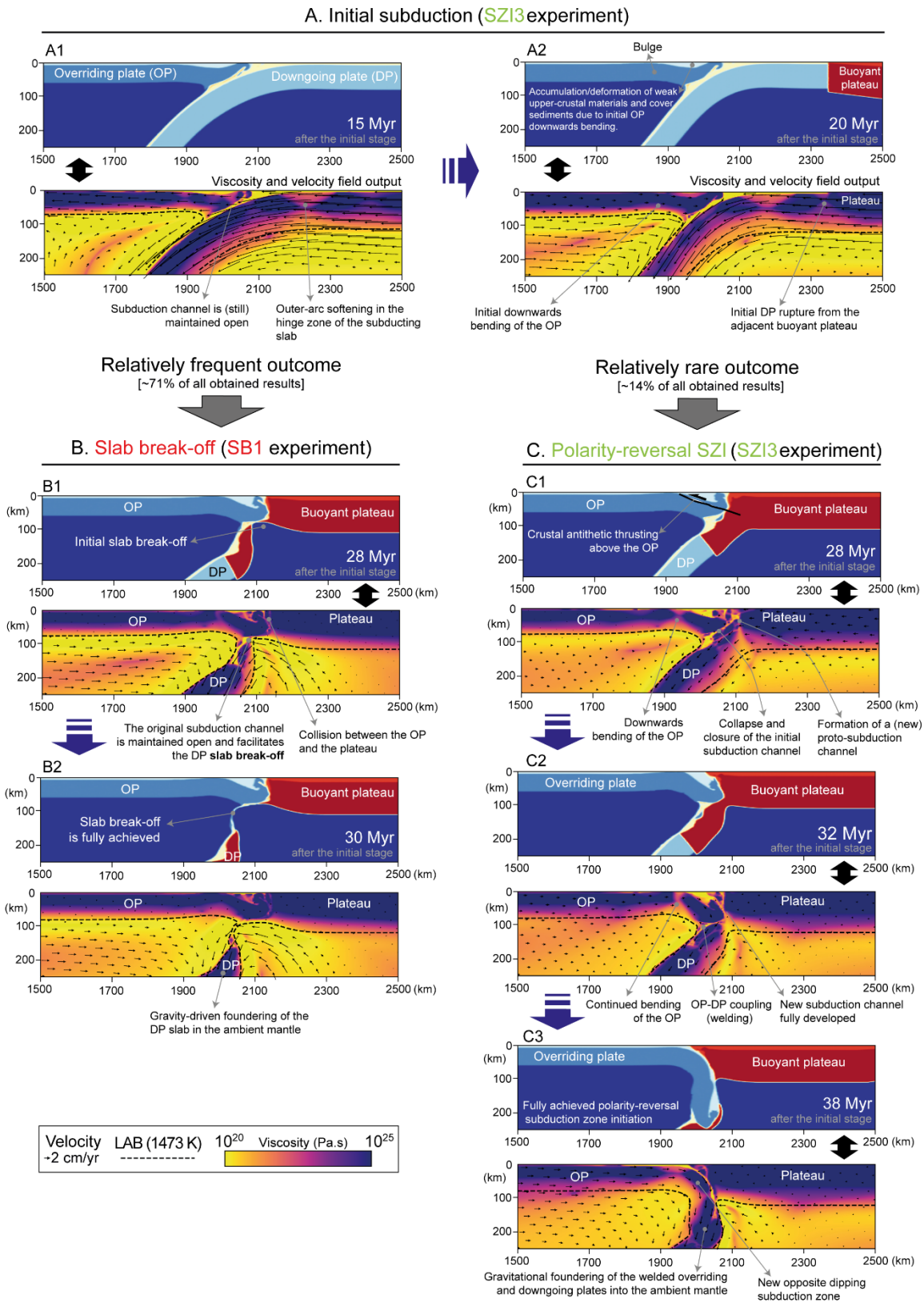

Figure 3.3 – Numerical model results: comparison between model evolution leading to slab break-off vs. polarity-reversal subduction zone initiation (geometry, viscosity, and velocity outputs are shown for each stage)**. A. Initial steady-state**

subduction between the arrival of the DP at the 660 km interface and the arrival of the buoyant plateau at the trench. A1-A2: The OP is slightly bent downwards, and DP starts to break apart from the adjacent buoyant plateau. Due to the initial OP downwards bending weak upper-crustal materials and cover sediments are accumulated and deformed (shortened and thickened) in a tectonically subsiding basin located in the arc-forearc region. **B. Slab break-off** outcome (observed in ~71% of the experimental results). B1-B2: OP is not bent any further and collides with the plateau closing a potential new subduction channel; the original subduction channel is maintained open and propagates the rupture of the DP; slab break-off is complete with total separation of the DP that sinks into the ambient mantle. **C. Polarity-reversal SZI** outcome (observed in ~14% of the experimental results). C1: Continued downwards bending of the OP and crustal antithetic thrusting above this plate; initial collapse of the original subduction channel and simultaneous opening of a new proto-subduction channel. C2: Further bending of the OP; full closure of the old subduction channel and OP-DP welding; continued development of the new subduction channel dipping in the opposite direction. C3: Completion of polarity-reversal SZI; subduction of the (original) OP is driven by negative-buoyancy foundering of both the OP and the DP in the ambient mantle. **OP** - Overriding pate; **DP** - Downgoing plate; **Thin black arrows** - velocity field; **Contour dashed black lines** - lithosphere/asthenosphere thermal boundary (LAB, marked by the 1473 K isotherm). Experiments SB1 and SZI3 are also fully depicted in Supplementary Videos 1 and 5, respectively.

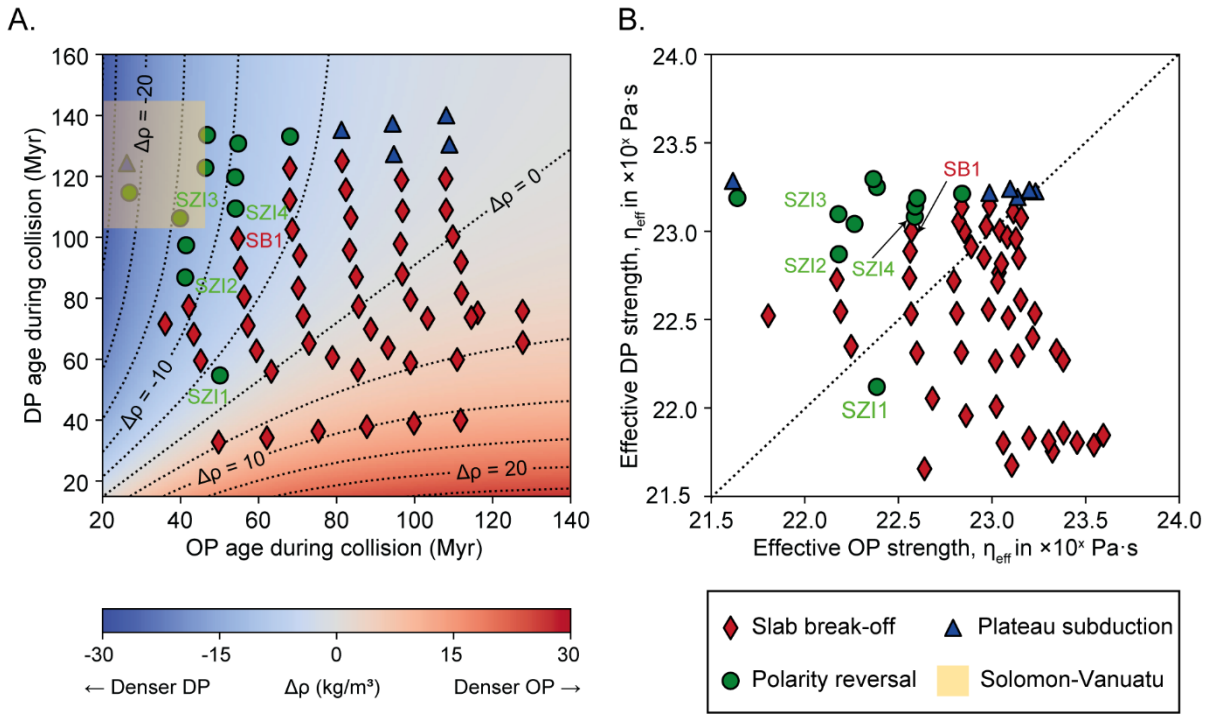

Figure 3.4 – A: Depiction of the general numerical modelling outcomes (polarity-reversal, slab break-off and plateau subduction) as a function of OP and DP ages at the time of the arrival of the plateau at the trench (plateau docking). The coloured background and associated dashed lines represent the buoyancy contrast field between the OP and the DP, which values are defined as $\Delta\rho_{DP}^{asthenosphere} - \Delta\rho_{OP}^{asthenosphere}$ (units in kg/m^3). Note that $\Delta\rho_{OP}^{asthenosphere} = \rho_{asthenosphere} - \rho_{OP}$ and $\Delta\rho_{DP}^{asthenosphere} = \rho_{asthenosphere} - \rho_{DP}$ are both negative, given that both the OP and the DP are negatively buoyant relatively to the asthenosphere since ~14 Myr of age (see Fig. 1B). The bluish negative part of the field thus represents conditions in which the DP is more negatively buoyant than the OP. Note also that most of the polarity-reversal SZI results fall into this negative subdomain. The yellow rectangle shows the plate age range for the occurrence of polarity-reversal SZI in the

Solomon-Vanuatu (SV) natural example. **B:** Depiction of the same general numerical modelling outcomes as a function of OP and DP effective strength (η_{eff}) at the time of plateau docking.

3.5. Discussion

3.5.1. General conditions favouring polarity-reversal SZI

The obtained model results show that triggering of polarity-reversal SZI at the time of plateau docking is favoured by older (thicker and more negatively buoyant) DPs relatively to the corresponding OPs (green circles in Figure 3.4A). The resulting rheological plate configuration must also comply with the following main (geodynamic) conditions (Figs. 3.3-3.5):

1. The crust of the OP must be weak enough to be bent upwards and locally underthrusted (beneath the DP), with intense strain localization along the resulting main antithetic shear zone enabling the formation of a new proto-subduction channel (Figure 3.3-C1, Figure 3.4B, and Figure 3.5A). This is generally attained even when slab break-off rather than polarity-reversal SZI occurs (see Figure 3.3B and Supplementary Videos). In most cases the DP detaches from the buoyant plateau, and the resulting gap is either to be closed again, as the OP collides against the plateau during the prevailing slab break-off outcome (Figure 3.3-B1), or to remain open resulting in the new opposite dipping subduction channel in the less common situation of polarity-reversal SZI (Figure 3.3-C1).

2. The OP must also be thin and weak enough to be able to bend downwards, promoting the collapse of the original subduction channel, its closure, and the definite coupling with the DP (Figure 3.3-C2, Figure 3.4B and Figure 3.5B). Results indicate that OPs with a docking age greater than ~64 Myr render plates too strong and thick to be able to accommodate the required plate bending, regardless of how negatively buoyant they might be (see Figure 3.4). In fact, plateau subduction (blue triangles in Fig. 3.2 and 3.4, see also Supplementary Video 7) occurs in models with older (stronger) OPs, which suggests that under these conditions even the sinking of the positively buoyant

plateau is more prone to occur than the bending and underthrusting of the (thick and strong) overriding plate.

3. The coupled (welded) OP and DP must yield a slab-pull strong enough to bend down the OP with a small enough bending radius so that the newly formed subduction channel is not closed, ultimately leading to the development of a new subduction zone with an opposite polarity (see Figure 3.3-C3 and Supplementary Videos). The welding between the two plates, controlled by the rheology of the DP crust (the interface between the plates), thus seems to be the critical factor for the occurrence of polarity-reversal SZI.

More detailed manifestations of these main geodynamic constraints are illustrated by the interpretation of the obtained polarity-reversal outcomes as follows.

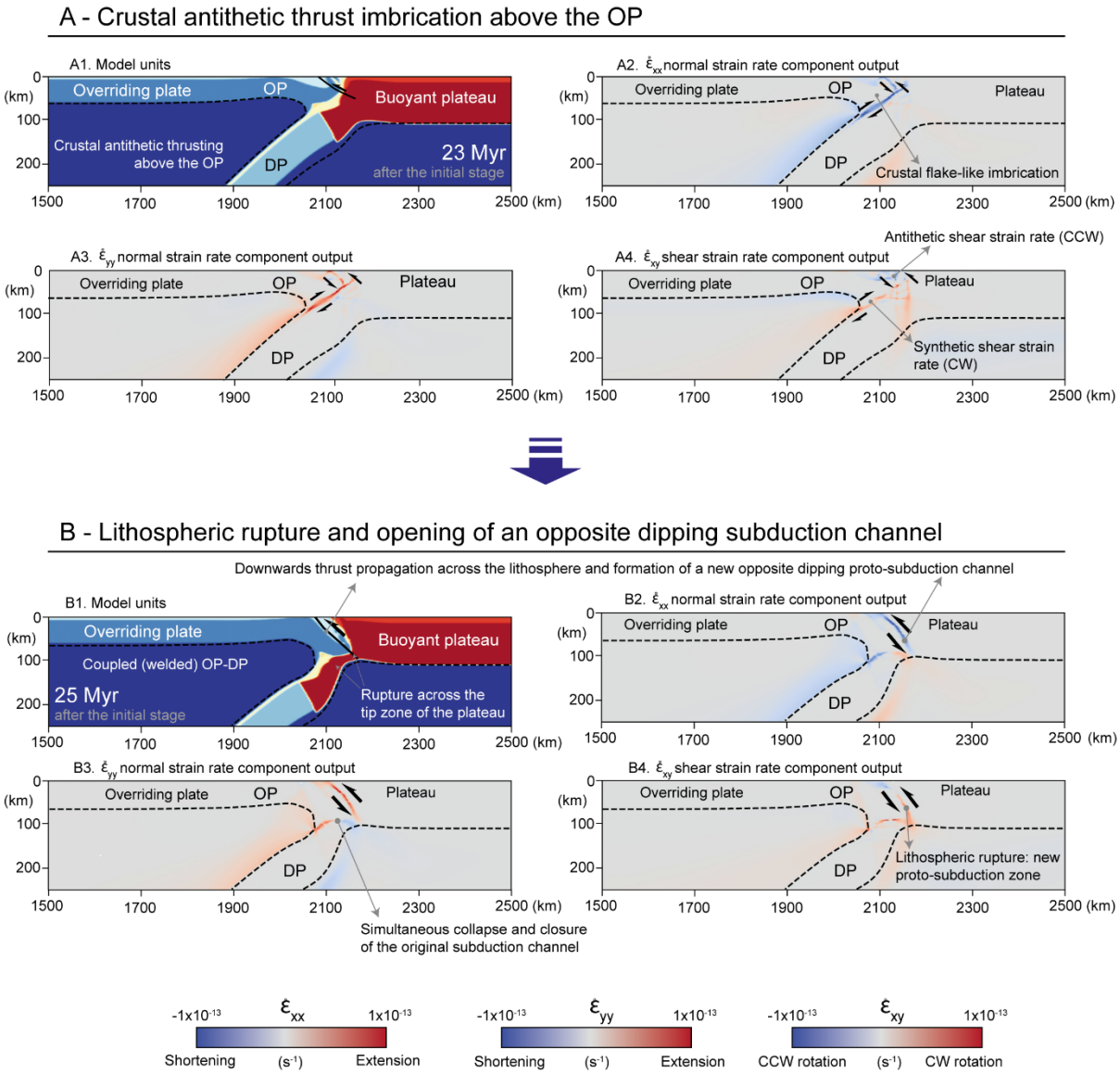

Figure 3.5 – Model results: polarity-reversal subduction zone initiation (experiment SZI2). Strain rate output illustrating the development of a new opposite dipping subduction channel. **A:** Initial antithetic thrust above the overriding plate yielding crustal flake imbrication (OP); **B:** Thrust propagation across the lithosphere (through the tip of the weaker buoyant plateau) to form a new proto-subduction channel. Simultaneous OP-DP coupling (welding) and closure of the old subduction channel. OP - Overriding plate: DP – Downgoing plate; CW - Clockwise; CCW – Counter-clockwise; Normal ($\dot{\boldsymbol{\varepsilon}}_{\mathbf{xx}}$, $\dot{\boldsymbol{\varepsilon}}_{\mathbf{yy}}$) and shear ($\dot{\boldsymbol{\varepsilon}}_{\mathbf{xy}} = \dot{\boldsymbol{\varepsilon}}_{\mathbf{yx}}$) strain rate components of the strain-rate tensor.

3.5.2. Initial subduction channel collapse and plate welding

Polarity-reversal subduction zone initiation was observed in experiments with different initial DP ages, but only for cases in which the DP was consistently older than the OP (see Figure 3.2). In these situations, different original subduction dip angles and bending radii were observed, depending on the strength and thickness of the DP implied by its assumed initial age (Irvine and Schellart, 2012). Accordingly, younger (weaker and thinner) DPs yielded steeper subductions zones with a tighter bending radius (Figure 3.6A), while older (stronger and thicker) DPs are more difficult to bend, forming gentler dipping subduction zones with a wider bending radius (Figure 3.6B). For all polarity-reversal outcomes, compression between the two plates (and implied increase in friction along the subduction channel) led to initial folding of the OP against the stronger DP (Figure 3.6-A1 and B1). The amplification of this folding at the time of plateau docking produced a downwards clockwise rotation of the tip of the OP, causing the initial subduction channel to collapse (Figure 3.6-A2 and B2 and respective insets). Simultaneously, the OP progressively cut through the weaker plateau, eventually rupturing the DP to nucleate a new subduction channel. With the definite shutdown of the initial subduction zone the OP and the DP became welded. This increased the (buoyancy-driven) sink of both plates in the ambient mantle (higher slab-pull), facilitating the tight bending of the OP and the continued propagation of the newly formed subduction channel (Figure 3.6-A2, B2 and B3). Polarity-reversal SZI was only observed for the cases in which this OP-DP welding was observed, showing its crucial importance for the triggering of this mode of subduction zone initiation.

Our results show that the initial folding of an OP against a stronger DP, the associated occurrence of antithetic thrust-shearing above the OP (nucleation of a proto-subduction channel) and the rupture of the DP from the adjacent plateau, are all quite common for different OP-DP age combinations (even during the frequent outcome of slab break-off). But it is only when OP-DP welding occurs that the shallower shear zone representing the proto-subduction channel can propagate downwards, rupturing across the whole lithosphere and maturing into a new opposite dipping subduction zone. Thus, our numerical results suggest that polarity-reversal SZI triggering is prone to occur under the ideal combination of thermo-mechanical conditions, expressed by older (stronger) DPs and relatively younger (weaker) OPs, that specifically favour this OP-DP coupling and welding.

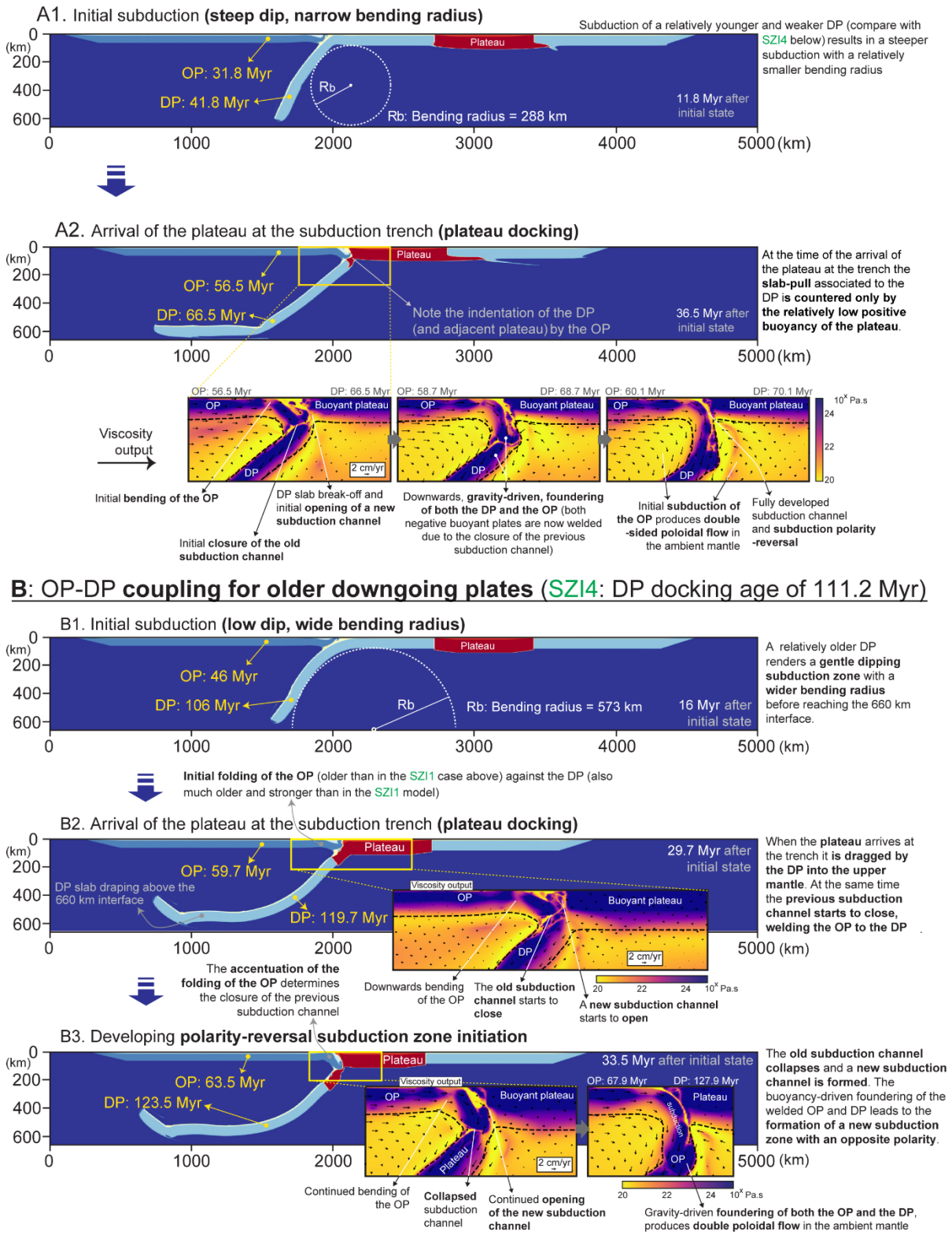

Figure 3.6 – Prevailing mechanisms of overriding - downgoing plate coupling during polarity-reversal subduction zone initiation. **A**: For relatively young (weak and deformable) downgoing plates (SZI1 model results); **B**: For relatively older (stronger and thicker) downgoing plates (SZI4 model results). OP - Overriding plate: DP – Downgoing plate.

3.5.3. Compliance with natural examples

The objective of the present generic numerical modelling was not to study any specific natural case, but rather to gain new insight on the main underlying dynamics governing the occurrence of polarity-reversal SZI for the assumed modelling conditions. This SZI mode has been previously proposed to explain the evolution of different natural tectonic settings (e.g., Kerr et al., 2005; Konstantinovskaya, 2011). In some of these cases, trench-obstruction is thought to have been caused by plateaus of different geological origin, e.g. oceanic ridges or seamounts, submarine volcanic structures and continental fragments (Tetreault and Buiter, 2012), or even by a continental margin attached to the downgoing plate during intra-oceanic subduction (Konstantinovskaya, 2011). In the emblematic example of the Solomon-Vanuatu subduction system polarity-reversal SZI is thought to have occurred during the late Miocene (Figure 3.7A), triggered by the arrival of the Ontong-Java Plateau at the North Solomon-Vitiaz subduction zone (Mann and Taira, 2004). In this tectonic setting, the age inferred for the (overriding) Australian oceanic plate lies between 49 and 25 Ma, based on plate tectonic reconstructions (Hall, 2002) and recent regional studies (Mortimer et al., 2014). The age of the polarity-reversal SZI in this subduction system has been proposed to fall between 15 and 5 Ma (Hall, 2002; Schellart et al., 2006). This renders a maximum age interval for the Australian OP at the time of the Ontong-Java plateau docking approximately between 44 and 34 Ma, and a minimum, between 20 and 10 Ma. On the other hand, based on the ~150 to 120 Ma age interval deduced for the downgoing Pacific plate (Nikolaeva and Gerya, 2009), its maximum age at docking is calculated between 145 and 135 Ma, whereas its corresponding minimum age would fall between 115 and 105 Ma. Despite some degree of uncertainty expressed by these age intervals, the available evidence conforms well with the general OP-DP plate age combinations that rendered polarity-reversal SZI in our models (i.e., older and stronger DPs paired with younger and weaker OPs). SZI7 experiment illustrates the polarity-reversal possibility for the Solomon-Vanuatu case under the contrasting thermo-mechanical conditions resulting from such plate age combinations (Figure 3.7B). In this experiment polarity-reversal SZI is achieved for a relatively younger OP (~41 Myr, Figure 3.7-B1) fitting the maximum age interval (44 to 34 Ma) for the Australian OP in the natural example. Likewise, a much older DP of ~111 Myr in this same experiment also agrees with the minimum age interval (115 to 105 Ma) estimated for the Pacific DP in the natural case (see yellow rectangle in Fig. 4A representing the range of the OP-DP age intervals for the Solomon-Vanuatu example).

3.5.4. Constraints of present modelling approach

Our models provide new insight on the process of polarity-reversal SZI resulting from the perturbation of the internal driving-force balance on a pre-existent subduction zone. Our restrict premise is thus to consider the internal dynamics of the system (and its thermo-mechanical configuration arising from the contrasting age of the plates involved) as the main governing cause for polarity-reversal triggering. Given this assumption, the adopted 2D modelling simplification of subduction zones could be problematic, since these natural objects are three-dimensional and governed by a dynamics that critically comprises an (inherently 3D) toroidal component of mantle flow (Schellart, 2004a; Schellart et al., 2007). Periodic boundary conditions were prescribed to the lateral vertical walls of our models to avoid mantle flow stagnation beneath the DP slab during roll-back subduction (see section 3.3.3 above). However, other dynamic effects of mantle toroidal flow on overall plate kinematics and deformation were not accounted for in the present models, which could result in a significant underestimation of the conditions favouring polarity-reversal SZI.

The absence of elasticity in our simulations, while widely adopted in many other modelling studies (Capitanio and Morra, 2012; Gerya and Meilick, 2011; Schellart, 2017b; Stegman et al., 2010), is also potentially relevant for our results since it is arguably expected to influence the dynamics of plate bending in subduction systems (e.g., Capitanio and Morra, 2012; Farrington et al., 2014; Thielmann and Kaus, 2012). Also important is the uncertainty pertaining to upper mantle rheology (e.g., Jain and Korenaga, 2020; King, 2016, and references therein) that allows for a somewhat aprioristic choice of parameters, relatively to which the obtained results are expected to be sensitive. This means that a slightly different choice of mantle rheology parameters (in equation 3.9 above) corresponding, for instance, to an increase in mantle stiffness, could potentially increase the viscous resistance to slab-pull, thus modifying the underlying governing dynamics of the system and implying considerably different results.

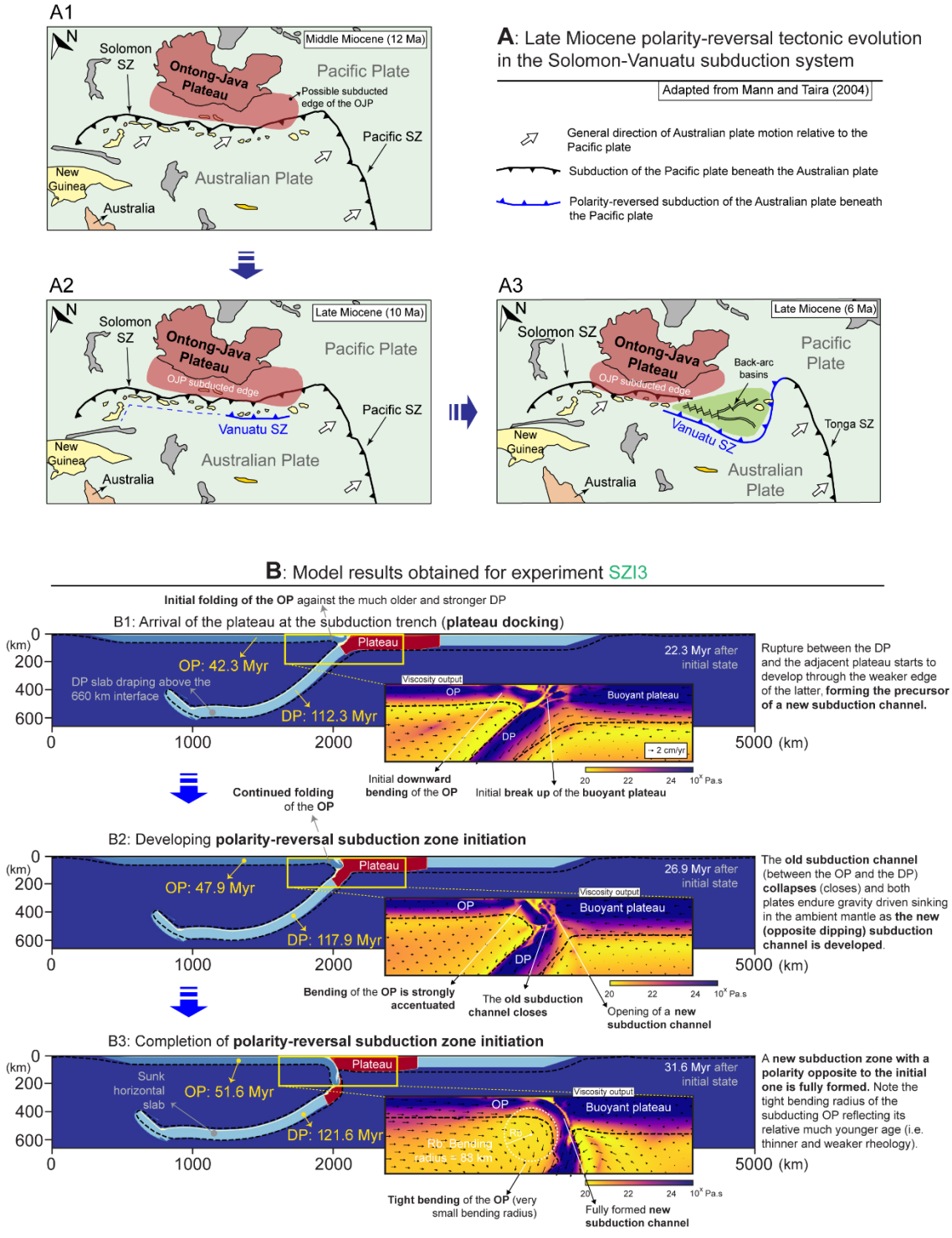

Figure 3.7 – Example of a natural case in which an oceanic plateau arrives at an active subduction zone and, due to the favourable interplay between resisting and driving forces, led to the development of a new subduction zone by polarity-reversal. **A**: Map depiction of **middle-late Miocene tectonic evolution of the Solomon-Vanuatu subduction systems**, in which the blocking of the North Solomon-Vitiaz subduction trench by the Ontong-Java plateau is interpreted to have triggered polarity-reversal subduction zone initiation, forming the opposite dipping Vanuatu subducting zone (adapted from Mann and Taira,

2004). The initial south dipping North Solomon-Vitiaz subduction zone comprised a much older (stronger and thicker) downgoing Pacific plate (~115 to 105 Ma) and a relatively much younger (weaker and thinner) overriding Australian plate (~44 to 34 Ma). **A1**: In middle Miocene (12 Ma) the Ontong-Java plateau was already blocking the southwards dipping North Solomon-Vitiaz subduction zone, triggering the polarity-reversal SZI; **A2-A3**: In late Miocene (from ~10 to 6 Ma) the new opposite dipping Vanuatu subduction zone is further developed. **B: Model step evolution obtained for SZI3 (polarity-reversal) experiment**, in which the OP, DP docking ages fit the ones of the natural example in A. The subduction polarity-reversal is dynamically driven by the older and much more negatively buoyant DP (age at docking is ~112 Ma), against which the much younger, thinner, and deformable OP (age at docking is ~42 Ma) is readily folded. OJP – Ontong-Java Plateau; OP - Overriding plate; DP - Downgoing plate; SZ – Subduction zone; dashed black line – Lithosphere-asthenosphere boundary.

Another model limitation with potential important dynamic consequences for subduction systems, and thus, capable of modifying the polarity-reversal stability field of Figure 3.2, is the assumed absence of a mature volcanic arc in the OP above the subducting slab. Whilst this is a widely assumed standard simplification in many subduction zone models (e.g., Gerya et al., 2008; Gurnis et al., 2004; Lu et al., 2015), natural volcanic arcs could exert a stabilizing effect on the OP, contributing to prevent the occurrence of double-sided subduction in nature (thus increasing the relative frequency of polarity-reversal outcomes).

The sensitiveness of polarity-reversal SZI to the resolution adopted for the numerical modelling experiments is also of critical importance. Robustness of results was only achieved for medium to ultra-highs resolution tests (see details in section 3.8 - Resolution dependency), but important differences arise from considering the carried out numerical experiments at either low or medium resolutions. Since polarity-reversal SZI is crucially dependent on OP-DP coupling, the resolution at which the subduction channel is considered influences the results in each case. Accordingly, low resolutions imply a less efficient localization of strain and a consequent increase in friction along the subduction channel, which favour both early double-sided subduction and polarity-reversal SZI. Conversely, from medium to ultra-high resolutions, the subduction channel becomes much better defined (resolved) rendering strain localization much more effective and decreasing the relative number of polarity-reversal outcomes.

A more exhaustive discussion of these and other (technical) modelling constraints is provided in section 3.8.

3.6. Conclusions

Our results show how polarity-reversal SZI might be possible to occur under geodynamic conditions similar to the ones considered in our models. These models illustrate how a new opposite dipping subduction zone can form, due to buoyant plateau obstruction of a pre-existent one, in the absence of any far field (external) forces. The experiments depict how certain overriding-downgoing plate age combinations, representing specific thermo-mechanical (rheological) plate configurations, can disturb the inner dynamic balance between (buoyancy driven) slab-pull forces and viscous resistance as to produce polarity-reversal SZI.

The results show that, for the assumed modelling constraints, the scenarios (i.e., plate rheological configurations) which favour polarity-reversal SZI always combine older (stronger and thicker) DPs and relatively younger (weaker and thinner) OPs. This general plate age combination allows for the development of a new subduction channel (while closing the pre-existent one), and for the efficient buoyancy-driven foundering (subduction) of the former OP in the ambient mantle.

Our experiments also show that rheological coupling, or plate welding, between the DP and the OP is key to achieve polarity-reversal SZI for the modelled conditions. This subduction zone initiation mode is thus greatly controlled by the evolving rheological conditions in the subduction channel. Accordingly, our results show that for polarity-reversal SZI to be triggered at the time of plateau docking, a simultaneous decrease in strain localization and increase in friction must occur along the subduction channel, as to eventually cause this channel to collapse and the plates to be welded.

By illustrating the feasibility of polarity-reversal SZI for the restricted conditions implied by our model assumptions, our results suggest that this SZI model might play a more important role than previously anticipated in the cyclic renewal of ocean floors, corresponding to an important process of subduction zone initiation in nature.

3.7. Acknowledgements

J. Almeida acknowledges funding by FCT PhD grant no. PD/BD/135067/2017 - Earthsystems-IDL. J. Almeida, F.M. Rosas and J.C. Duarte acknowledge financial support by FCT through project UIDB/50019/2020 - IDL. W.P. Schellart has been funded by a Vici

Fellowship (016.VICI.170.110) from the Dutch National Science Foundation (NWO). The authors thank Michael Gurnis, Wim Spakman, Fabio Crameri and an anonymous reviewer for their insightful and constructive feedback, which significantly contributed to improve the manuscript.

3.8. Model limitations (published as Appendix A)

Modelling techniques intrinsically assume some degree of simplification relatively to the natural process they target (see Zelst et al., 2021 for a discussion). These necessary simplifications imply the sacrifice of details which should not be relevant for the evaluation of the core problems under investigation, and that should be made clear for all. We thus provide the following list of the main model limitations assumed in the present numerical study.

a) 2D modelling approach

Subduction is an intrinsically 3D process in nature since the DP slab width is of key importance for the overall subduction dynamics (Dvorkin et al., 1993; Schellart, 2004b; Schellart et al., 2007). A relatively narrow slab allows for mantle material to escape from beneath the DP around its lateral edges, favouring (roll-back) slab retreat and significant toroidal flow in the ambient mantle, whereas wide slabs promote mantle flow stagnation under the same subducting DP. Mantle toroidal flow is also responsible for nucleating extension within the OP at a distance of ~250 to 400 km from the subduction trench (J. C. J. C. Duarte et al., 2013).

The 3D mantle toroidal flow was not accounted for in our 2D models. However, to allow for DP slab-retreat in 2D we adopted periodic boundary conditions for the limiting vertical walls in our models (see Figure 3.1A) making it possible for mantle material to escape from beneath the DP by exiting through these boundaries. This avoided the formation of an artificial upper mantle stagnation zone beneath the subducting slab (Schellart et al., 2007), which would adulterate the dynamics of the sinking DP. Additionally, the overall dimensions of the model were always prescribed to be larger than the generated mantle flow cells.

The toroidal flow-related extension within the OP is predicted to nucleate at a distance from the trench (~200 km) similar to the one at which the main hinge of the OP downwards bending

is located in our polarity-reversal SZI experiments. This suggests that the influence of the 3D mantle toroidal flow in the overlying OP would tend to facilitate polarity-reversal SZI, and thus, that our 2D results might correspond to an underestimation of its occurrence in nature.

b) Absence of a volcanic arc

As in many previous studies (Gerya et al., 2008; Gurnis et al., 2004; Lu et al., 2015), the absence of a volcanic arc has been adopted as a simplification in our numerical models. To our knowledge, no previous numerical modelling approach has systematically investigated the role of volcanic arcs in the overall dynamic control of subduction zones. However, the ubiquitous presence of arcs in all active intra-oceanic subduction zones suggests they might contribute, not only to thermo-mechanically stabilize the tip of the OP by adding to its positive buoyancy, but also to act as an effective mechanism for reducing the strength of this plate (Gerya and Meilick, 2011). As such, the presence of an arc in the OP could widen the domain of conditions under which polarity-reversal SZI could occur, contributing to a reduction in the number of unstable double-sided subduction results (see Figure 3.2). On the other hand, the presence of a positive buoyant arc could also impede polarity-reversal SZI by holding the leading edge of the overriding plate at the surface. However, in such a situation, it is also possible that the crustal flake-like imbrication observed in our models (Figure 3.5A) could be responsible for scraping off the buoyant volcanic arc atop one of the main antithetic thrusts propagating further into the OP (undercutting the buoyant arc crust). This would lead to accretion of the arc to the DP, separating it from the negatively buoyant OP, and thereby allowing polarity-reversal SZI to happen.

c) Absence of elastic behaviour

In our numerical study the elasticity of lithospheric plates was not accounted for. As in several other previous contributions (e.g., Capitanio and Morra, 2012; Gerya and Meilick, 2011; Schellart, 2017b; Stegman et al., 2010), the rheological behaviour of the lithosphere and upper mantle was here prescribed to follow strictly visco-plastic laws. The role of elastic behaviour in facilitating or hindering the bending of the DP slab in subduction systems has been discussed by Farrington et al. (2014), who considered that subduction slab geometry, subduction angle, and the amount of slab draping (above the 660 km basal discontinuity) were mostly unaffected

by elasticity. Instead, the subduction regime is thought as mostly dependent on the relative viscosity/density contrasts between the lithosphere and upper mantle (e.g., Capitanio and Morra, 2012). Additionally, the role of elasticity in the formation of lithospheric-scale weaknesses (i.e., new subduction channels) was explored in Thielmann and Kaus (2012). They showed that the inclusion of elastic behaviour, as opposed to pure visco-plastic laws, delayed the formation of lithospheric-scale weak zones, which however, once formed, would be more efficiently localized.

We acknowledge that the potential effects of direct or induced elasticity (i.e., plate stiffness) in the bending of the OP during polarity-reversal SZI remain largely unknown. We anticipate that these effects are probably complex and non-linear, as illustrated by the fact that a less pronounced plate bending may often translate into a lower energy dissipation involved in the subduction process (Irvine and Schellart, 2012). Also, initial OP bending, while potentially affected by the elastic properties of the oceanic crust, might lead to elastic stress weakening at the bending hinge (Farrington et al., 2014), causing a decrease in the plate bending radius. Finally, elastic behaviour is likely to help localizing the new subduction channel (Thielmann and Kaus, 2012) during plateau collision. As such, we acknowledge that further future modelling is required to precisely clarify the role of elasticity in polarity reversal SZI processes.

d) Simplified oceanic plateau

Our oceanic plateau was simplified as corresponding always to an overthickened segment of oceanic lithosphere, and never to a continental block. This implies that our oceanic plateau has a thermo-rheological profile identical to the one of an oceanic plate, i.e., with a simple (single) transition between a brittle lithosphere and a ductile upper (asthenospheric) mantle. By contrast, continental lithosphere typically shows a more complex rheological structure, comprising a brittle-ductile upper to lower crust transition, and a similar mantle lithosphere to asthenosphere transition (e.g., Kohlstedt et al., 1995a). In the latter case, the existence of a ductile intermediate layer (between the brittle upper crust and the upper lithospheric mantle) allows for the formation of a decollement between the continental crust and the mantle (e.g., Koptev et al., 2019). As such, during plateau docking, the crustal portion of a continental plateau could be antithetically thrusted and accreted on top of the overriding plate, while its corresponding mantle portion would continue to subduct. This would thus favour the formation

of a wedge-like structure (flake imbrication) like the one observed in our models (see Fig. 5A), which according to our results precludes polarity-reversal SZI if OP-DP plate welding is also achieved.

e) Upper mantle rheology uncertainty

At present, the rheology of the upper mantle is not entirely understood, and the corresponding constraints assumed in most numerical modelling approaches are essentially based on experimental mechanical studies of peridotites and olivines (e.g., Escartín et al., 2001; Hui et al., 2014). This uncertainty is relevant for our model results, since slight variations within the range of admissible parameters for the rheology of mantle could lead to markedly different outcomes. A stronger upper mantle rheology could contribute to a more efficient localization of the deformation making it more difficult for plate welding to occur. At the same time, it would also imply a higher viscous resistance to the slab-pull forces, significantly modifying the overall dynamics of the subduction system. Therefore, a slightly different upper mantle rheology could very well change the polarity-reversal stability field suggested by the present modelling results.

f) Resolution dependency

Model resolution can have an impact on the obtained numerical results, since the dynamics governing the target (tectonic system) under scrutiny is not necessarily scale independent. This means that for an overall similar geometry, e.g., a same subduction channel, the detailed rheological configuration and associated stress distribution across the channel might be sensitive to the resolved thickness of the corresponding shear zone in different cases. Different resolutions might thus imply different dynamic conditions, and therefore, different geometrical/kinematical model results (Arcay, 2017; Kaus, 2009; Sandiford and Moresi, 2019; Schellart and Moresi, 2013).

To gain some insight on the general resolution sensitivity of our models, we ran an initial set of 63 experiments (Supplementary Figure 1) using two main different resolutions: 768 x 192 (medium resolution - MR) and 1536 x 384 (high resolution - HR). The results showed that the unstable double-sided subduction is much less frequent at higher resolutions (changing from

37% at MR to 8% at HR, see Supplementary Figure 1). HR results also showed that polarity-reversal SZI does not occur for conditions characterized by younger DP ages, shifting the stability field for this outcome towards conditions preferably characterized by older DPs and relatively younger OPs. This suggests that the OP-DP coupling (i.e., plate welding) in polarity-reversal outcomes involving younger plates corresponds to an artificial effect, determined by the less efficient strain localization implied by the low resolution. Accordingly, a poorer definition of rheology (and a less detailed stress distribution configuration) in the subduction channel artificially favours the coupling between both plates and the consequent frequency of both polarity-reversal SZI and double-sided subduction. Conversely, in HR trials the subduction channel would be sufficiently resolved (sharpened and defined) to allow for an efficient strain localization, and to favour a more "realistic", dynamically driven, polarity-reversal outcome.

Further resolution tests of polarity-reversal SZI were carried out to evaluate the robustness of the polarity-reversal outcome under the thermo-mechanical conditions implied by a combination of older DPs and younger OPs. This was done by running models at four different resolutions comprising an OP of 20 Myr, paired with a DP of 90 Myr (black square in Supplementary Figure 1). Thus, besides the MR and HR trials, two other resolutions were additionally considered in this case: a lower most one of 384 x 96 (low resolution - LR), and a higher one of 2304x576 (ultra-high - UHR). The obtained test results show general coherent polarity-reversal SZI for almost all the tested resolutions, except in the LR case, in which efficient strain localization is not attained along the subduction channel, triggering early double-sided subduction instead (Supplementary Video 8). In the UHR case the accomplishment of polarity-reversal SZI takes more than double the time observed for the other models (MR and HR cases, Supplementary Video 8). This is probably due to a much widespread dissipation of the same initial energy, implied by the much higher resolution in this case, which ultimately also expresses a change in the overall dynamics of the model.

It is clear from these tests that changing the resolution significantly changes the dynamics of the modelled subduction zone. Although in the present case some degree of resolution robustness was achieved for relevant OP-DP initial age conditions, resolution dependence potentially constitutes an important limitation in the numerical modelling of subduction polarity reversal, introducing additional non-linearity to models and changing the underlying governing dynamics for different considered resolutions.

g) Lack of a free surface

The use of free-slip top boundary conditions in subduction models was previously reported as favouring double-sided subduction outcomes (e.g., Crameri et al., 2012; Schmeling et al., 2008).While most of our results obtained for free slip top BCs show the development of single-sided asymmetric subduction zones, a small percentage does lead to the formation of double-sided subduction zones (five out of 77 models, ca. 6%, Figure 3.2).

Since double-sided subduction zones have never been found in nature (Gerya et al., 2008), we have interpreted their occurrence in the present study as mostly corresponding to model artefacts. Our results show that these unnatural subduction outcomes are scarce, occurring only for the weakest/youngest overriding plates (10 Myr, see Figure 3.2), which are unable to resist the stresses imposed by the sinking and trench-retreat of the subducting slab from early stages of the experiments. As reported by the authors cited above, this propensity to bend downwards and subduct would be further facilitated by the here adopted top free-slip BCs (instead of free surface).

Moreover, the combination of young overriding plates and old downgoing ones also closely corresponds to the unravelled stability field for the occurrence of polarity-reversal SZI (Figure 3.2). As such, the implementation of top free surface BCs in our models (instead of the adopted free slip) could result in the reduction, or even the elimination, of the double-sided subduction outcome yielding, for the same conditions, polarity reversal SZI instead. Accordingly, free surface BCs would make it more difficult for the young overriding plates to be bent downwards and to subduct, lessening the frequency of the double-sided subduction outcome. This concurs with the possible underestimation of polarity reversal results in our models relatively to nature, which could also result from other causes (as discussed in paragraphs a and b above).

3.9. Supplementary material (published as Appendix B)

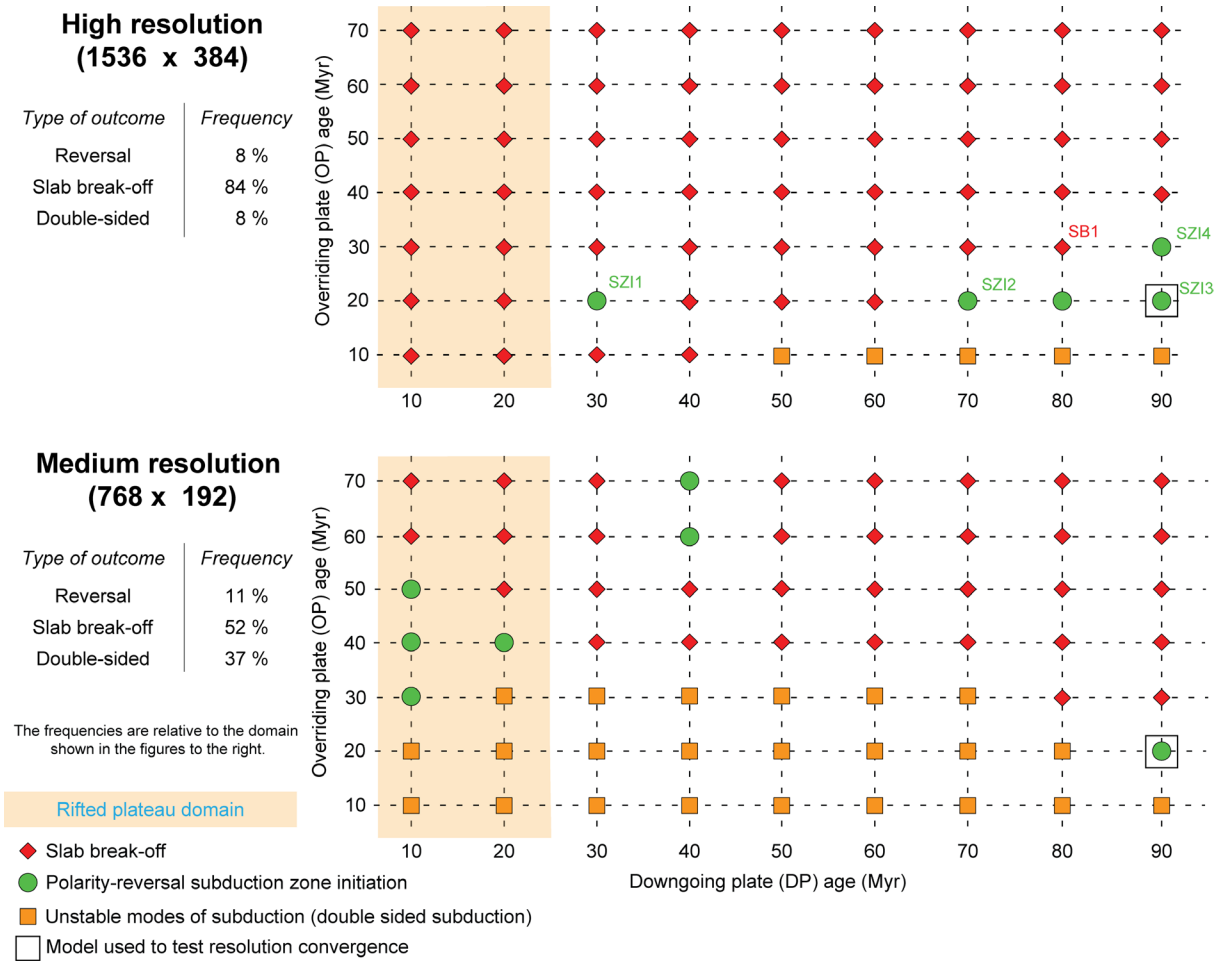

Supplementary Figure 3.1 – Resolution tests performed on the stability field of polarity-reversal SZI. A total number of 126 trials were conducted for the 63 illustrated cases of overriding-downgoing plate age combinations at two different resolutions: 768x192 (medium resolution – MR) and 1536x384 (high resolution - HR). At higher resolutions polarity-reversal SZI was found to be preferably stable for a combination of young overriding plates (OPs) and older downgoing plates (OPs), and practically disappears for conditions characterized by relatively younger DPs. Likewise, HR test results also show a much lower frequency of double-sided subduction. The black square marks the conditions at which polarity-reversal SZI sensitiveness to resolution was tested (considering four different resolutions - see Supplementary Video 3.8).

3.10. Supplementary Videos (published as Appendix B)

The supplementary videos for this chapter can be found in the online version of the published manuscript (https://doi.org/10.1016/j.epsl.2021.117195).

Supplementary Video 3.1 – Video depicting the evolution of a slab break-off subduction model. Initial overriding plate age is 30 Myr and initial downgoing plate age is 80 Myr. This experiment is referenced in Figure 2 and 4 as SB1.

Supplementary Video 3.2 – Video depicting the evolution of an unstable double sided subduction model. Initial overriding plate age is 10 Myr and initial downgoing plate age is 70 Myr.

Supplementary Video 3.3 – Video depicting the evolution of a polarity-reversal model. Initial overriding plate age is 20 Myr and initial downgoing plate age is 30 Myr. This experiment is referenced in Figure 2 and 4 as SZI1.

Supplementary Video 3.4 – Video depicting the evolution of a polarity-reversal model. Initial overriding plate age is 20 Myr and initial downgoing plate age is 70 Myr. This experiment is referenced in Figure 2 and 4 as SZI2.

Supplementary Video 3.5 – Video depicting the evolution of a polarity-reversal model. Initial overriding plate age is 20 Myr and initial downgoing plate age is 90 Myr. This experiment is referenced in Figure 2 and 4 as SZI3.

Supplementary Video 3.6 – Video depicting the evolution of a polarity-reversal model. Initial overriding plate age is 30 Myr and initial downgoing plate age is 90 Myr. This experiment is marked in Figure 2 and 4 as SZI4.

Supplementary Video 3.7 – Video depicting the evolution of a plateau subduction model. Initial overriding plate age is 50 Myr and initial downgoing plate age is 110 Myr.

Supplementary Video 8 - Resolution test results of polarity-reversal SZI for four different resolutions: from bottom to top: (LR) 384x74, (MR) 768x192, (HR) 1536x384 and (UHR) 2404x576 (horizontal and vertical number of cells, respectively). Initial overriding plate age is 20 Myr and initial downgoing plate age is 90 Myr (SZI3 experiment in Supplementary Figure 1). Result robustness is shown to hold except for the LR case, in which poor strain-localization, promotes early artificial double-sided subduction.

Chapter 4. Self-replicating subduction zone initiation by polarity reversal

---

Almeida, J., Riel, N., Rosas, F. M., Duarte, J. C., B. Kaus (2021) Self-replicating subduction initiation by polarity reversal. Communications Earth and Environment. Accepted in principle

(this page has been left intentionally blank)

Self-replicating subduction zone initiation by polarity reversal

J. Almeida (*, 1, 2); N. Riel (3); F. M. Rosas (1, 2); J. C. Duarte (1, 2), B. Kaus (3)

*Corresponding author: jealmeida@fc.ul.pt

1. Departamento de Geologia, Faculdade de Ciências da Universidade de Lisboa, 1749-016 Lisbon, Portugal

2. Instituto Dom Luiz (IDL), Universidade de Lisboa, 1749-016 Lisbon, Portugal

3. Institute of Geosciences, Johannes Gutenberg University, Mainz, J.-J.-Becher-Weg 21, D-55128 Mainz, Germany

4.1. Abstract

Subduction zones have recurrently formed on Earth. Previous studies have, however, suggested that they are unlikely to start in the interior of a pristine ocean. Instead, they seem to be more likely to form from another pre-existing subduction zone. One widely cited conceptual model to start new subduction zones is polarity reversal, resulting from the shutdown of a pre-existent subduction zone due to the arrival of a buoyant block at the trench. However, the dynamic conditions by which this process occurs remain elusive. Here, we present 3D numerical models of subduction zone initiation by polarity reversal resulting from the arrival of an oceanic plateau at the trench. Our results show that this process is more likely to occur for old subducting plates and narrow plateaus, and that new subduction zones can form from previous ones in a self-replicating manner, without requiring any other external tectonic forcing.

4.2. Introduction

Subduction zone initiation (SZI) constitutes one of the main unsolved problems in geodynamics. Multiple mechanisms have been previously proposed to explain SZI, differing on their assumed geometries, kinematics and driving forces (Crameri et al., 2020; Stern, 2004; Stern and Gerya, 2018). These include the formation of subduction zones by mantle plumes (Gerya et al., 2015; Whattam and Stern, 2015), or by the reactivation of lithospheric scale weaknesses, such as transform faults (Arcay et al., 2019; Zhou et al., 2018) or old subduction zone interfaces (Faccenna et al., 2018). One commonly proposed mechanism for subduction zone initiation is subduction polarity reversal (Crameri et al., 2020; Stern, 2004; Stern and Gerya, 2018). This

assumes that the arrival of a buoyant terrane (Harris et al., 2014; Mortimer et al., 2017; Tetreault and Buiter, 2014) at the trench of an active intraoceanic subduction zone is capable of causing the local termination of the subduction system, and to force the overriding plate to subduct in the opposite direction. This type of SZI has been proposed to have occurred in several different natural instances (Cooper and Taylor, 1985; Konstantinovskaya, 2011; Mann and Taira, 2004; Miura et al., 2004), although the dynamic factors that govern the switch in the subduction polarity are still poorly understood. A reversal of subduction polarity must arise from the balance between driving forces (Gurnis et al., 2004) (e.g., slab pull force), resisting forces (Gurnis et al., 2004) (e.g., positive buoyancy of plate segments, and viscous resistance of plates and mantle), and facilitating/weakening mechanisms (Dymkova and Gerya, 2013; Gerya et al., 2015; Korenaga, 2007; Thielmann and Kaus, 2012) (e.g., grain size reduction, presence of fluids or shear heating).

Here, we investigate the dynamics of subduction initiation by polarity reversal using 3D self-consistent visco-elasto-plastic geodynamic models that include a free surface (see Methods). In these models, an oceanic plateau is incorporated into the subducting plate (Supplementary Fig. 1), eventually colliding with an oceanic overriding plate. Model plate velocities are never externally imposed in any of the experiments, arising instead from the evolving dynamic balance between internal driving and resisting forces. The only significant driving force in our system is the slab pull (F_{SP}), which results from the negative buoyancy of the subducting plates. This driving force is opposed by the viscous resistance forces of the plates/mantle and the by the deformation of the overriding plate during plateau collision.

We show that polarity reversal subduction initiation by plateau collision is geodynamically viable in the absence of external driving forces, but that it is limited by the along-trench width of the oceanic plateau. Also, the duration of the polarity reversal event is strongly controlled by the along-trench plateau width and by the age of the subducting plate.

4.3. Modelling rationale

The objective of this work is to understand the dynamics of the processes governing subduction initiation by polarity reversal. Specifically, we aim to understand the time-evolving force balance between the slab pull and the resisting forces that are implied in the deformation of the overriding plate during the collision with an oceanic plateau. Hence, we varied the following parameters/conditions to better understand how these influence the force balance as to trigger polarity reversal SZI:

1. Along-trench width of the oceanic plateau. Wider plateaus imply not only a higher volume of material that resists subduction when arriving at the trench, but also a smaller active subducting trench after collision (increasing effective slab-pull F_{SP}/W_{SP}). Consequently, varying the width of the plateau along the subduction trench allows us to simultaneously assess the impact of a narrower active subduction zone on the triggering of a new one by polarity reversal.

2. Age of the overriding and subducting plates. While F_{SP} is the main driving force of a subduction zone, its effects are balanced by the relative strength of the intervening plates, which is directly correlated to the plate's thermal age. Thus, to understand how the relative plate strength influences the evolution of the subduction system, we used different combinations of initial overriding and subducting plate ages. In our simulations, the oceanic plateau has the same age as the subducting plate, which means that a change in plate age directly (and proportionally) affects the implied F_{SP}.

3. Presence or absence of a positively buoyant magmatic arc along the tip of the overriding plate. These alternative conditions were considered to assess the potential role of the volcanic arc in the development of a new subduction zone by polarity reversal.

A total of eleven model runs were conducted (see Supplementary Table 4.1). All models were run considering half of a symmetrical domain (see detailed explanation in Methods). In all but one model, a new subduction zone is initiated on the overriding plate by polarity reversal, after the arrival of an oceanic plateau at the trench (plateau collision).

We monitored several parameters in each of the different models: the evolution of the emerging trench-normal subducting plate velocity (V_{SP}), as a proxy for the subduction dynamics;

the migration of the original and the newly formed subduction zones, to track the plate organization of the model; and the ratio (W_R) between the length of the newly formed subduction zone (L_{NSZ}) and the width of the oceanic plateau (W_P; Supplementary Figure 4.1B), to measure the efficiency of the plateau in triggering a new subduction zone.

4.4. Results and Discussion

4.4.1. Geodynamics of subduction polarity reversal

The evolution of the reference model, comprising 70 Myr old overriding and subducting plates, a 600 km wide plateau (W_P = 600 km) and a buoyant magmatic arc, is shown in Figure 4.1 (and Supplementary Video 4.1). In this model, we distinguish four different phases recognized in most of the carried out numerical simulations: I) evolution of the original subduction zone (Figure 4.1A); II) arrival of the plateau at the trench (i.e., plateau collision - Figure 4.1B); III) polarity reversal and subduction initiation of the former overriding plate (Figure 4.1C); IV) development of an opposite verging subduction system (Figure 4.1D and Figure 4.2).

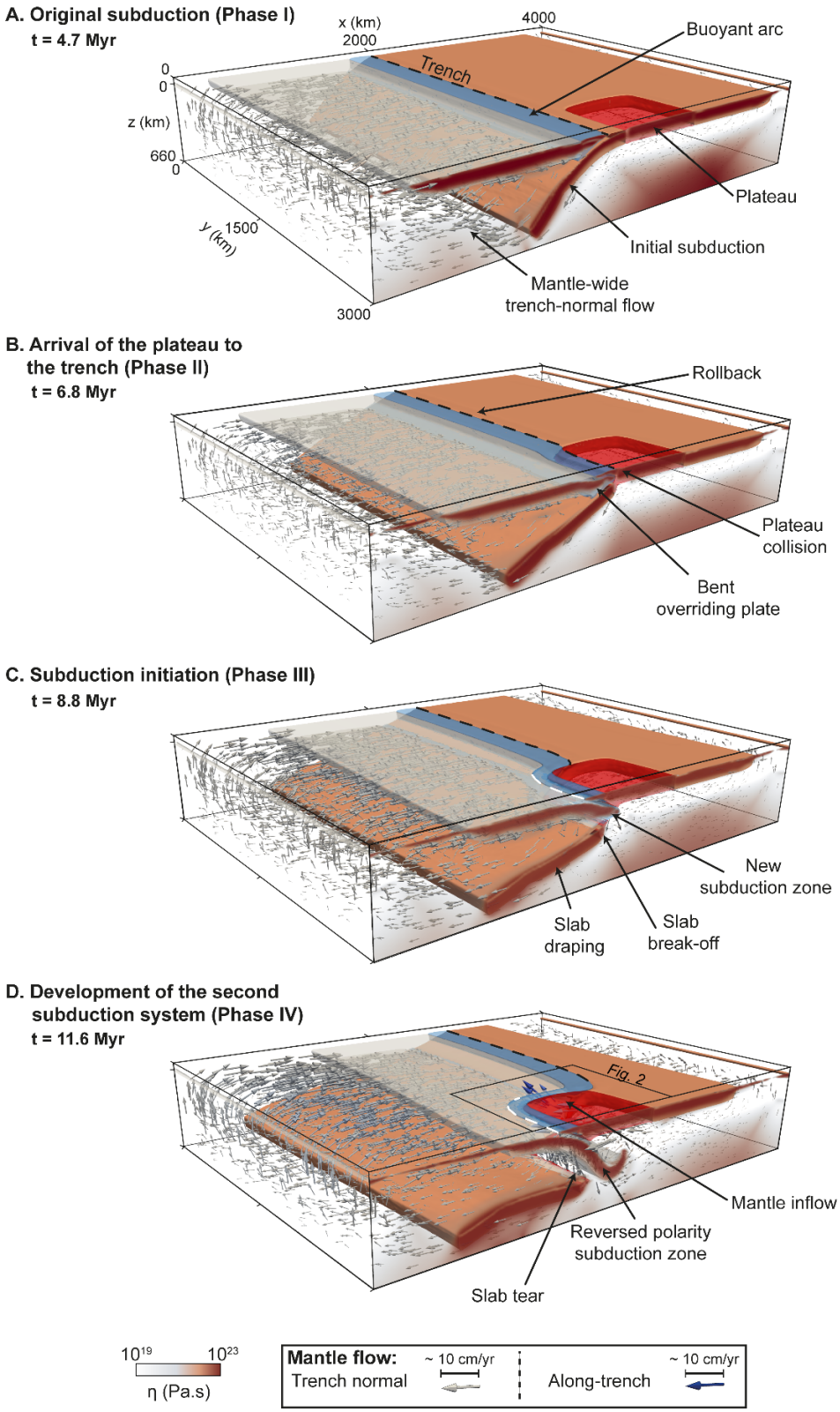

(figure caption in the next page)

Figure 4.1 – Reference model evolution of polarity reversal subduction initiation. The mantle flow is illustrated with arrows: trench-normal mantle flow is shown in white arrows; along-trench flow is marked by blue arrows. Subduction trenches are marked by dashed lines: initial subduction in black, newly formed opposite dipping subduction in white. **A. Phase I** – Early evolution of the original subduction. During this stage, the plateau is still moving towards the active subduction trench and a mantle-wide trench-normal flow is observed. **B. Phase II** - Initial plateau collision. During this stage, the plateau arrives at the subduction trench and, due to its positive buoyancy, blocks it. Laterally, the initial subduction is still active and continues to steadily rollback. **C. Phase III** - Subduction polarity reversal. Driven by the slab pull exerted by the laterally ongoing original subduction, the plateau is forced onto the overriding plate. Consequently, the overriding plate is underthrusted and, eventually forced to subduct in the opposite direction. The original slab is broken-off below the plateau. **D. Phase IV** – Opposite polarity double subduction system. At this stage, both subduction zones are dynamically maintained by the slab pull of each of their sinking slabs. As the newly formed subduction undergoes trench rollback and migrates laterally, a mantle upwelling forms below the plateau (see Figure 4.2).

During Phase I, the initial subduction zone develops as the original slab progressively sinks into the upper mantle resulting in an increase of the subduction velocity (see Figure 4.1A and Figure 4.3A). At around 4.7 Myr, the slab reaches the upper-lower mantle discontinuity, at 660 km depth (Figure 4.1A-B). This causes a deceleration in the subducting plate velocity (V_{SP}, Figure 4.3A), which is followed by a new period of slight acceleration as consequence of slab draping (backwards bending and accumulation along the upper-lower mantle transition (Schellart et al., 2007)). Shortly after, at around 6 Myr, the plateau arrives at the trench and resists subduction (Phase II in Figure 4.1; diamonds in Figure 4.3A-B). This happens not only because of the plateau's positive buoyancy, but also because of its relatively higher viscosity which makes it harder to bend (see Supplementary Figure 4.2). This obstruction eventually leads to the termination of the original subduction zone in this domain (Figure 4.1B-C) and to the tearing of the initial slab beneath the oceanic plateau (Figure 4.1C-D). Driven by the slab pull implied by the ongoing initial subduction, the oceanic plateau and buoyant arc are pushed against and above the overriding plate forcing it to bend downwards and to start subducting in the opposite direction (Phase III in Figure 4.1; triangles in Figure 4.3, and also Supplementary Figure 4.3). Plateau collision causes a shift in trench migration from pre-collision rollback to post-collision motion towards the overriding plate (Figure 4.3B). From ca. 8.8 Myr onwards, there are two fully developed opposite verging subduction zones (Phase IV; Figure 4.1D and Figure 4.2). The newly formed opposite dipping slab

initially accelerates quickly into the upper mantle (Figure 4.3A) before entering a steady roll-back stage (Figure 4.3B).

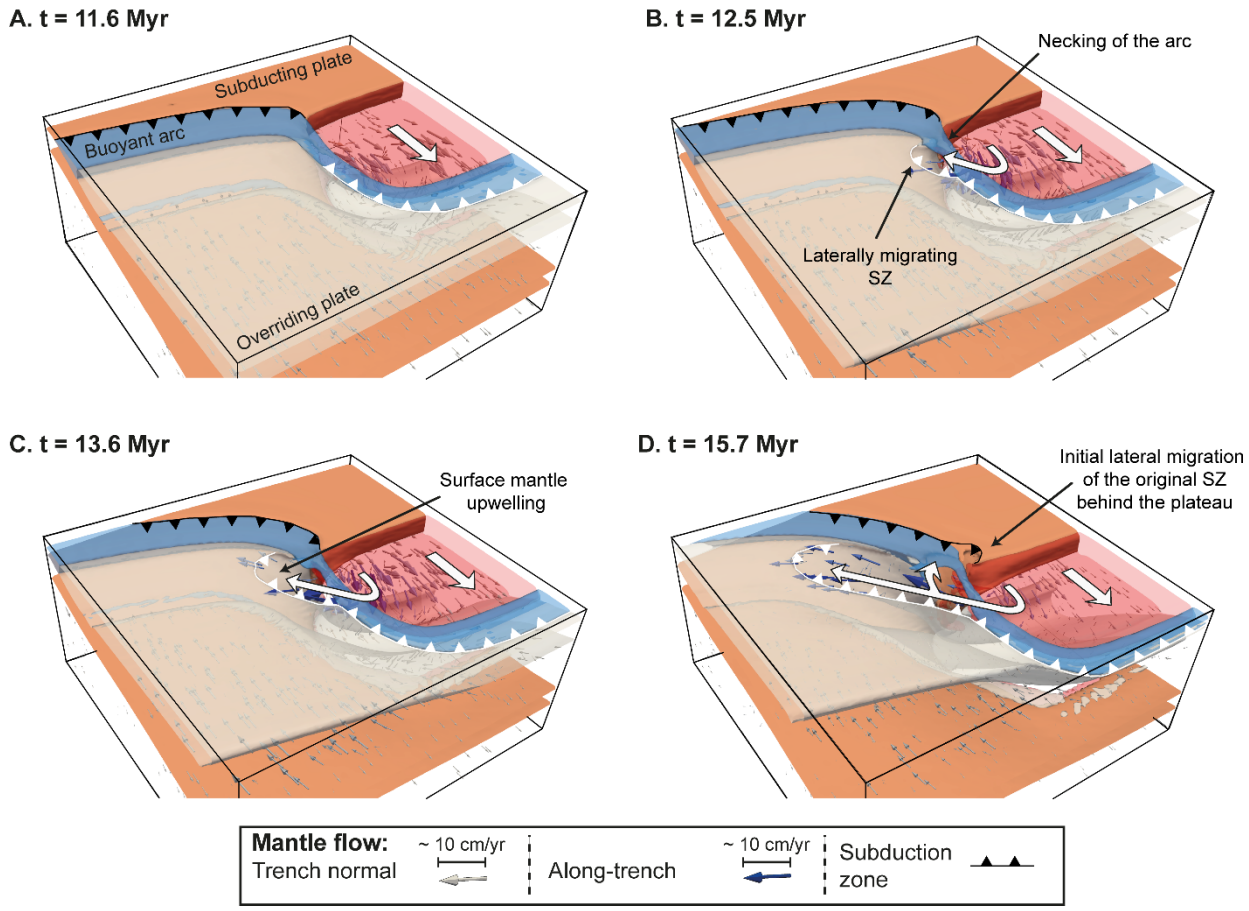

Figure 4.2 - Reference model post polarity reversal evolution: lateral migration of the newly formed subduction zone (see corresponding area marked by a square in Figure 4.1D). To better visualize the sub-lithospheric mantle flow, the plateau was made semi-transparent in the depicted evolutionary stages, which comprise: **A.** Initial opposite verging double subduction system (same stage as in Figure 4.1D). **B.** Early lateral migration of the newly formed SZ, aided by mantle flow funnelling beneath the arc. The arc itself is strongly strained, showing signs of necking. **C.** Evolving lateral migration with mantle upwelling. **D.** Bifurcation of mantle flow enhances incipient propagation of the original subduction zone behind the oceanic plateau. This is similar to what has been previously described for plateau-continent collisions (Betts et al., 2015; Moresi et al., 2014).

As the (initial) overriding plate sinks into the mantle, it is deformed and bent around the oceanic plateau (Figure 4.1D and Figure 4.2A-B). This causes the mantle flow to be laterally funnelled beneath the curved (and necked) magmatic arc (Figure 4.2B-D), assisting the trench retreat lateral propagation of the newly formed subduction zone (Figure 4.2B). Such a propagation occurs simultaneously with local mantle upwelling, which in nature could correspond to the formation of an oceanic basin (see example discussed below). The implied trench retreat and slab rollback (compare Figure 4.2B and D), further enhances the flow of mantle material in a positive feedback loop. Bifurcation of the laterally funnelled mantle flow also drives incipient propagation of the original subduction zone to the back of the oceanic plateau (Figure 4.2D). Given sufficient time, it is likely that this would aid to fully propagate the original subduction zone behind the plateau, leading to the development of two bordering side by side, opposite verging subduction zones.

This general model evolution shows that upon arrival of the plateau at the trench its viscous resistance to bending, and its positive buoyancy eventually determine the local shutdown of the original subduction zone. The initial main subduction zone, however, remains active laterally away from the collision zone, and its implied slab pull is enough to initiate thrusting of the plateau above the overriding plate, eventually causing this plate to subduct into the mantle. This is enabled by an initially strong dynamic coupling between the pre-existent and the emerging subduction systems, which allows the first to work as the source of the stress that drives the initial underthrusting and sinking of the overriding plate. However, such a dynamic coupling wanes as the original overriding plate progressively sinks into the mantle, and a new dynamically self-sustained subduction system is formed, driven by the slab pull force of the new subducting slab.

A similar evolution has previously been described in the context of a plateau-continent collision setting (Betts et al., 2015; Moresi et al., 2014). In these cases, the continental nature of the overriding plate prevents it from subducting. However, under the modelling conditions addressed by Moresi, plateau-continent collision can trigger the lateral formation of an extensional basin on the continental overriding plate, by favouring trench-rollback to the side of the collisional domain, in the lateral active segment of the subduction zone. Continued convergence subsequently forces the subduction zone to migrate to the back of the plateau, accreting it to the overriding continental plate. While our results show comparable lateral extensional basin formation, we infer that the new

opposite dipping subduction zone dissipates part of the energy that would otherwise assist a consistent rollback of the original subduction zone.

4.4.2. The role of the plateau's along-trench width

To understand the influence of the effective slab pull force of the original subduction zone (F_{SP}/W_{SP}) in the formation of a new opposite dipping one, four different initial along-trench widths of the plateau were tested (between 300 and 2400 km, see Supplementary Table 4.1 and Supplementary Figure 4.1). Note that a wider plateau implies a narrower active lateral subduction zone after plateau collision, which in turn leads to a stronger slab pull (higher effective slab pull F_{SP}/W_{SP}, see Supplementary Table 4.2). The evolution of these models can be seen in Supplementary Videos 4.1-4.4.

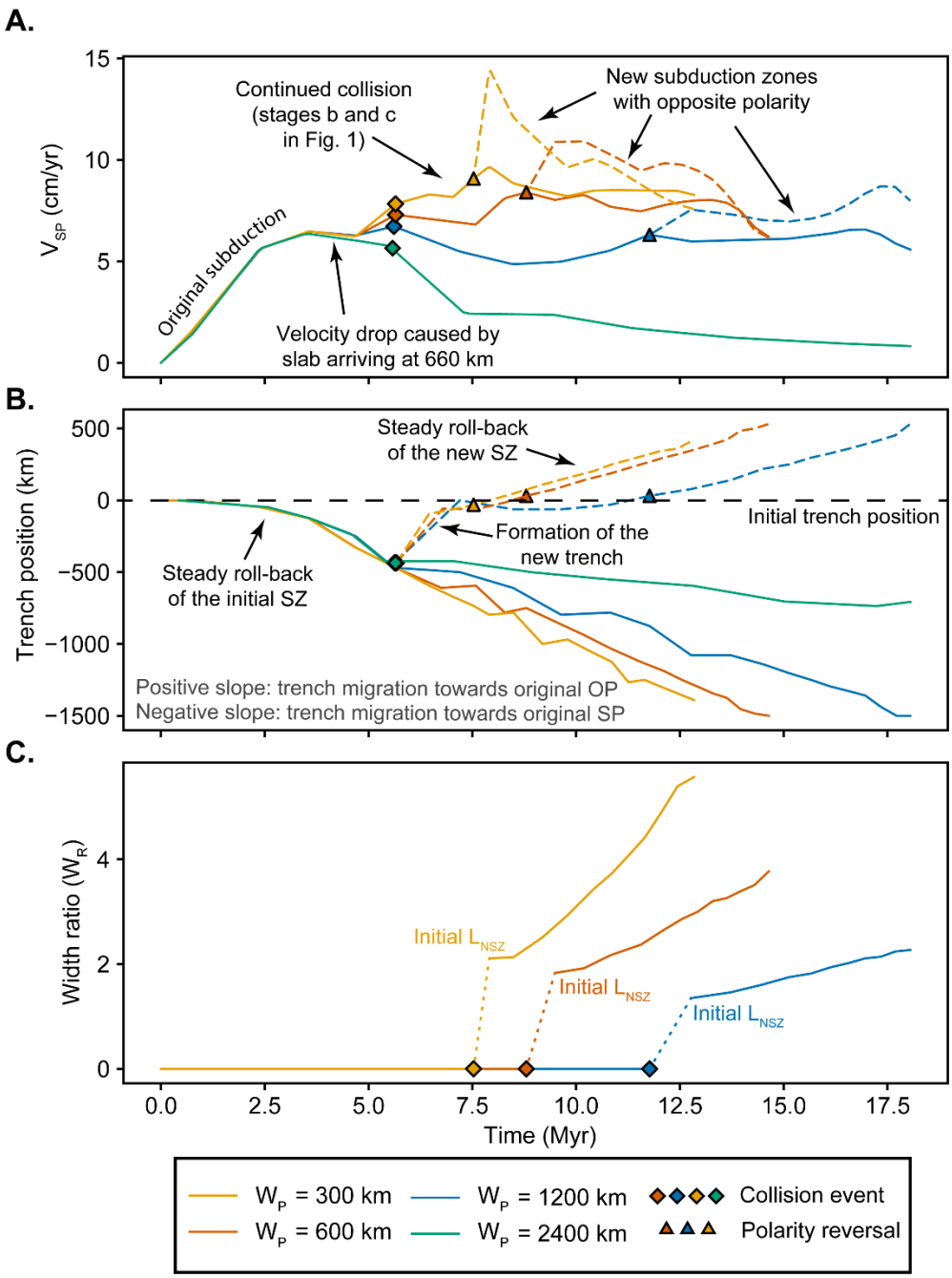

Figure 4.3 – Graphical depiction of the evolution of the model monitored parameters for the different considered plateau widths (W_P, see caption inset). The coloured diamonds indicate the moment at which collision with the plateau is initiated, while the coloured triangles indicate the time at which full polarity reversal is achieved. The subducting plate velocity (V_{SP}) is measured at the trailing edge of the subducting plate, along longitudinal sections both near the mirror symmetry boundary that cuts through the plateau (c.f. section A-A' in Supplementary Figure 4.1), and along the opposite model boundary that crosses only the initial intra-oceanic subduction zone. **A.** Evolution of subduction

plate velocity (V_{SP}) over time (subduction plate acceleration), for the original subduction zone (full lines), and for the newly formed opposite dipping one (dashed lines). Note that narrower plateaus imply a smaller indentation area and accompanying lower energy dissipation, resulting in both higher V_{SP} values and plate accelerations. Narrower plateaus also lead to an early trigger of polarity reversal events, expressed by the diminishing distance between diamonds and triangles in the graph. **B.** Subduction trench migration as a function of time (trench velocity), for the original subduction zone (full lines) and for the newly formed subduction trench (dashed lines). The plateau collision event causes an abrupt migration of the newly forming trench towards the overriding plate (OP), even before the new opposite dipping subduction zoned is fully formed. **C.** Plateau indentation efficiency, expressed by the time evolution of the W_R ratio (see Supplementary Figure 4.1B) between the growing length of the new subduction zone (L_{NSZ}) and the original along-trench width of the plateau (W_P). As no new subduction zones are formed before the collision of the plateau with the overriding plate, W_R values prior to this event are always zero. Narrower plateaus create notably longer subduction zone trenches relative to their initial widths. The W_P = 2400 km line was not included in C. due to the lack of a polarity reversal event. SZ – Subduction Zone; OP – Overriding plate; SP – Subducting plate; L_{NSZ} – Length of new subduction zone.

The evolution of the initial subduction zone is identical for all models until the arrival of the plateau at the trench (Figure 4.3A). However, from the plateau collision onwards, the subducting plate velocity (V_{SP}), and its variation along time, is consistently higher/steeper in models with narrower plateaus (i.e., with lower W_P widths and correspondingly higher, trench parallel, subduction zone lengths – Figure 4.3A). It has been previously shown (Guillaume et al., 2010; Schellart et al., 2007) that for the same volume of subducted slab, a narrowing of the subduction zone (i.e., the decrease of its trench-parallel length - W_{SP}) causes an increase in both V_{SP} and trench migration velocity, due to a resulting higher effective slab pull force at the surface. However, this is strikingly contrary to what we observe in Figure 4.3A. In the present case, the decrease of the subduction trench length in the models comprising wider plateaus is proportionally compensated by an increase in the width of the collision zone. This yields higher levels of horizontal resisting forces/stresses at the front of the plateau (see Supplementary Figure 4.4), which are capable of blocking the system, resulting in lower values of V_{SP} and trench velocity in these cases. In Supplementary Table 4.2 we list the buoyancy force and the effective slab pull force available to drive the polarity reversal. These show that higher effective slab pull forces are implied by wider plateaus as expected. However, the new subduction zone to be initiated is also much longer in these cases, since it will extend along the wider collisional front of the plateau, thus requiring even

higher forces to nucleate along the whole of its width (W_P). This is readily illustrated when considering the available buoyancy force divided by the length of the new subduction zone (Supplementary Table 4.2), which unambiguously shows that the resulting driving force available to initiate the new subduction zone is lower for cases comprising wider plateaus. For plateaus with the highest considered width (W_P = 2400 km) the collision area corresponds to ca. 80% of the whole model width, which renders only 25% of the slab pull force (per collision zone length) available to initiate the new subduction system. As a result, no new subduction zones are formed in this case, and instead, a complete termination of the whole subduction system occurs (as shown in Supplementary Video 4.4).

Furthermore, the duration of the polarity reversal event – i.e., the time interval between the initial stages of collision (diamonds in Figure 4.3) and the full achievement of polarity reversal (triangles) – is consistently longer for wider plateaus. Slower trench migrations (Figure 4.3B) and lower indentation ratios (expressed by the time variation of W_R in Figure 4.3C) are also observed for collisions with wider plateaus, in compliance with a more efficient dissipation of F_{SP} in these cases.

4.4.3. The role of plate age contrast

We have also investigated the effect of changing the age contrast between the overriding and subducting plates, by testing different initial age combinations for the same plateau width (W_P = 600 km, see Supplementary Table 4.1, and Supplementary Videos 4.1 and 4.9 to 4.11). Changing the thermal age of the subducting plate directly affects the negative buoyancy of the slab, thus allowing to modify F_{SP} without changing the width of the plateau or the implied indentation area.

Similar to the reference model, triggering a polarity reversal event requires the contribution of the driving slab pull force of a pre-existing subduction zone to bend the overriding plate. Therefore, a weaker and thinner overriding plate would, in principle, be easier to subduct (Gurnis et al., 2004; Irvine and Schellart, 2012; D. V. Kemp and Stevenson, 1996; Ulvrova et al., 2019) and hence favour polarity reversal subduction initiation. Our results confirm this assumption by showing that

in models with relatively weaker/thinner overriding plates, but identical subducting plate ages, polarity reversal occurs earlier (see Figure 4.4).

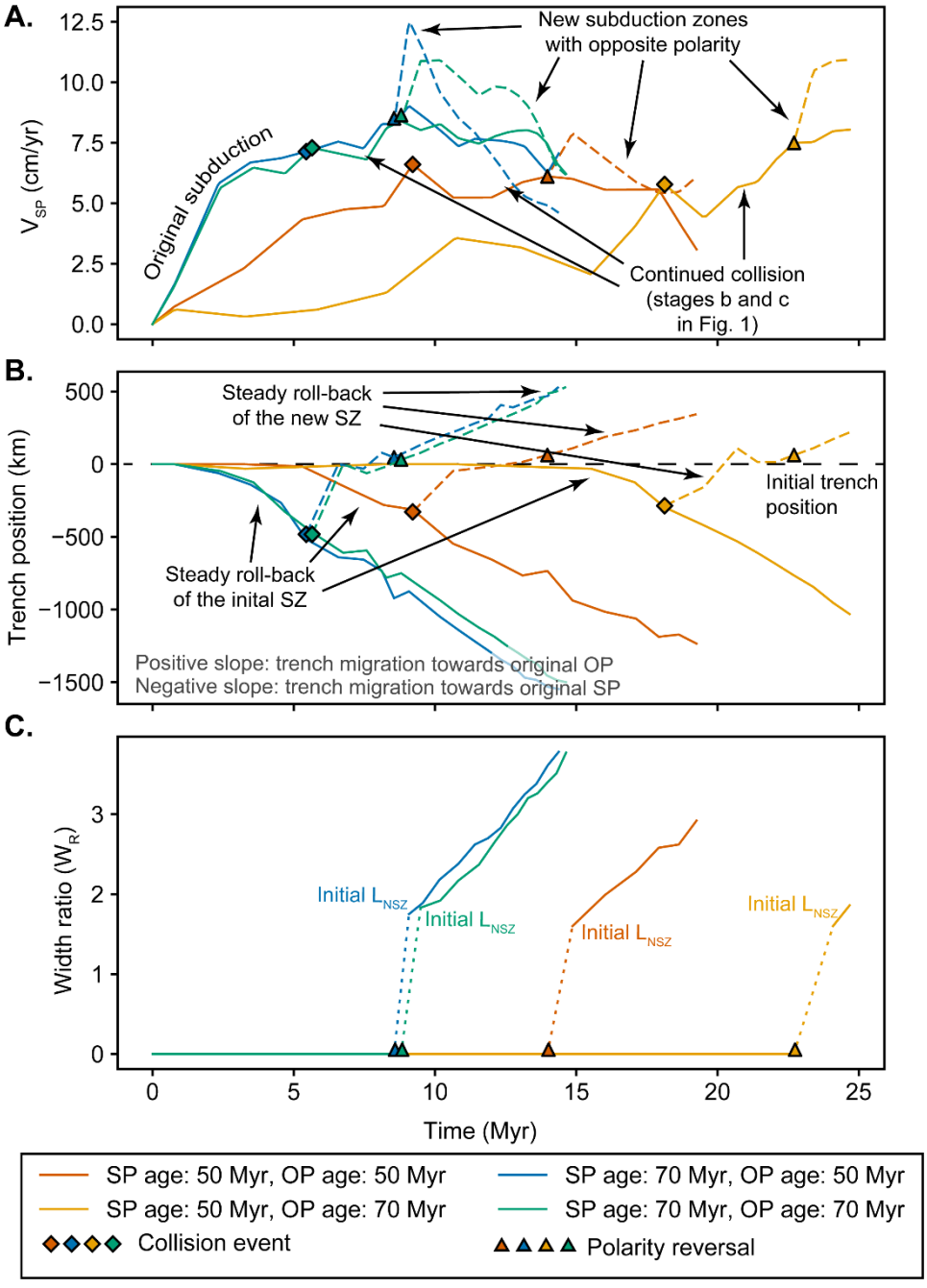

Figure 4.4 – Graphical depiction of the evolution of the model monitored parameters for the different considered (initial) plate age contrast between the overriding and the subducting plates (OP and SP age respectively, see caption

inset). Coloured diamonds and triangles, as well as V_{SP} measurements, with the same meaning, and obtained in the same way, as explained in the caption of Fig. 3. **A.** Evolution of subduction plate velocity (V_{SP}) over time (subduction plate acceleration), for the original subduction zone (full lines), and for the newly formed opposite dipping one (dashed lines). Note that older subducting plates show faster evolutions, expressed by the steeper variations over time, derived from their higher negative buoyancy and effective slab pull (see Supplementary Table 4.4). **B.** Subduction trench migration as a function of time (trench velocity), for the original subduction zone (full lines) and for the newly formed subduction trench (dashed lines). The plateau collision event causes an abrupt migration of the trench towards the overriding plate (OP). Younger subducting plates show longer time gaps between plateau collision and the polarity reversal event. **C.** Plateau indentation efficiency, expressed by the time evolution of the W_R ratio (see supplementary Fig. 1B and caption of Fig. 3c). As no new subduction zones are formed before the collision of the plateau with the overriding plate, W_R values prior to this event are always zero. Despite the fact that older subducting plates trigger polarity reversal at earlier stages, plate age appears to have no significant influence in the effectiveness of plateau indentation (expressed by a similar steepness of all the curves). SZ - Subduction Zone; OP - Overriding plate; SP – Subducting plate; L_{NSZ} – Length of new subduction zone.

For the same considered width of the plateau (W_P = 600km) and for equal initial ages of the subducting plate, the resulting driving forces should also be similar. However, in models with younger overriding plate thermal ages their corresponding lower strength and lower thickness facilitate, not only a more efficient indentation by the plateau, but also an earlier development of polarity reversal SZI (see Figure 4.4). In accordance, the models with younger overriding plates also show an overall higher V_{SP} (see Figure 4.4A). This higher velocity of the subduction plate cannot be ascribed to an increase in the available driving forces but can instead be easily explained by a relatively weaker and thinner overriding plate, and therefore an implied lower dissipation of F_{SP} during and after the collision.

By contrast, models with younger, and therefore weaker, less negatively buoyant subducting plates, but identical overriding plate ages, show an overall slower evolution (see Figure 4.4). At the start of the model, the younger subducting plates have a lower density contrast with the underlying mantle and, consequently, a lower F_{SP} (ca. 17% lower, see Supplementary Table 4.4). Therefore, there is a delay in the initial sinking phases of the original subduction (see Figure 4.4B, and Supplementary Video 4.11), resulting in an overall slower evolution of the system.

4.4.4. The role of a mature volcanic arc

Lastly, we ran a set of models with the same variation of plateau widths (W_P), but without the buoyant magmatic arc on the overriding plate. This allowed for a straightforward comparison between the two sets of experiments (with and without arc), in which any observed difference must derive from the missing arc. Regardless of the considered (W_P) width of the plateau, models without an arc developed convergent double sided subduction systems, in which both the overriding and the subducting plates sink into the ambient mantle (see Supplementary Figure 4.5 and Supplementary Videos 4.5-4.8). Different nuances of this same conspicuous double-sided subduction mode have been previously reported in several other numerical studies, although this type of subduction was never recorded in the Earth's lithosphere (Gerya et al., 2008).

In the present models, during the formation of the original subduction zone, the lithospheric mantle at the tip of the overriding plate is dragged downwards by the slab, forming a slab-dominated asymmetric double-sided subduction (i.e., the direction of subduction is controlled by the slab, see Supplementary Video 4.5-4.8). During collision, the original subduction zone is terminated in front of the oceanic plateau and, as in previous models, the overriding plate begins subducting. However, unlike in the previous models, no extensional basin is formed on the overriding plate in this case. Rather, the polarity reversal event is triggered along the entire width of the plate, resulting in a nearly model-wide symmetrical double-sided subduction zone (see Supplementary Figure 4.5 and Supplementary Video 4.5-4.8). Thus, under the assumed model conditions, we argue that the buoyant magmatic arc on the tip of the overriding plate plays a fundamental role, not only in stabilizing this plate by avoiding it being initially dragged into the mantle by the original subducting plate, but also in preventing the immediate plate-wide propagation of the newly formed subduction after the collision with the plateau, and the consequent formation of a double-sided subduction zone also at this later stage.

4.4.5. Natural systems and tectonic implications

The objective of the present generic numerical modelling study was not to explore the specific geodynamic constraints of a natural case, but rather to gain new insight on the main underlying

dynamics governing the occurrence of polarity reversal SZI. Nevertheless, we consider our results to be comparable to one of the most well studied cases of subduction initiation by polarity reversal, the Vanuatu subduction zone in the southwest Pacific (Mann and Taira, 2004; Miura et al., 2004; Schellart et al., 2006, 2002) (Figure 4.5).

Here, a new subduction system was initiated as a consequence of the Late Miocene arrival of the Ontong-Java plateau at the trench. This oceanic plateau, carried by the 150 to 120 Myr old Pacific plate, was driven to collide with the 49 to 25 Myr old overriding Australian plate (Mann and Taira, 2004; Schellart et al., 2006, 2002). While these ages are not in accordance with the modelled conditions, the event sequence in our models generically agree with this natural example. The collision of the oceanic plateau triggered the initiation of the Vanuatu subduction zone with an opposite (northwards) polarity in front of the Ontong-Java plateau (Mann and Taira, 2004; Schellart et al., 2006). As this system continues to propagate across the front of the plateau, we argue that the present-day Solomon arc setting (west side) is likely to closely mimic what was observed in the Late Miocene along the eastern side of the plateau. Under this assumption, during the collision, the Ontong-Java plateau would have been forced to overthrust the Australian plate. Consequently, this plate would have been wedged between the plateau and the Pacific plate (see cross-section in Figure 4.5A). This geometric configuration is coherently observed in equivalent frontal-plateau sections in our models (see model inset in Figure 4.5A).

The arrival of the Ontong-Java Plateau to the subduction trench eventually led to the cessation of the original subduction of the Pacific plate between c.a. 10 Ma (Mann and Taira, 2004) to 5 Ma (Schellart et al., 2006). Once subduction polarity is reversed, the rollback and lateral migration of the newly formed subduction zone creates extension in the region between the two trenches, to the side and front of the plateau (Figure 4.5B), with the associated mantle inflow (Heyworth et al., 2011). Both the formation of a lateral extension basin and mantle inflow patterns are coherent with our model observations (Figure 4.5B, model overview and section A-A').

A. Formation of the Vanuatu subduction zone

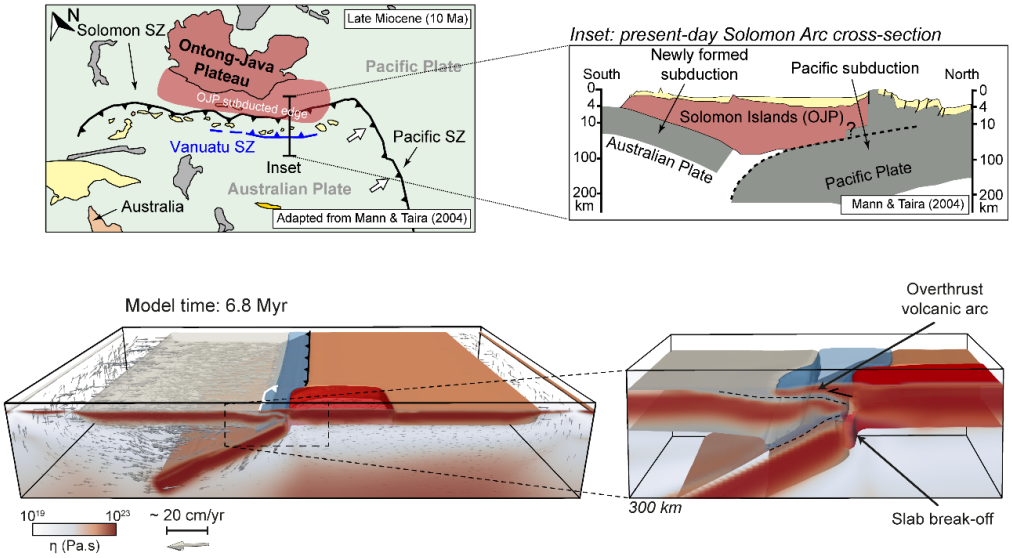

B. Formation of the extensional basin and termination of the original subduction

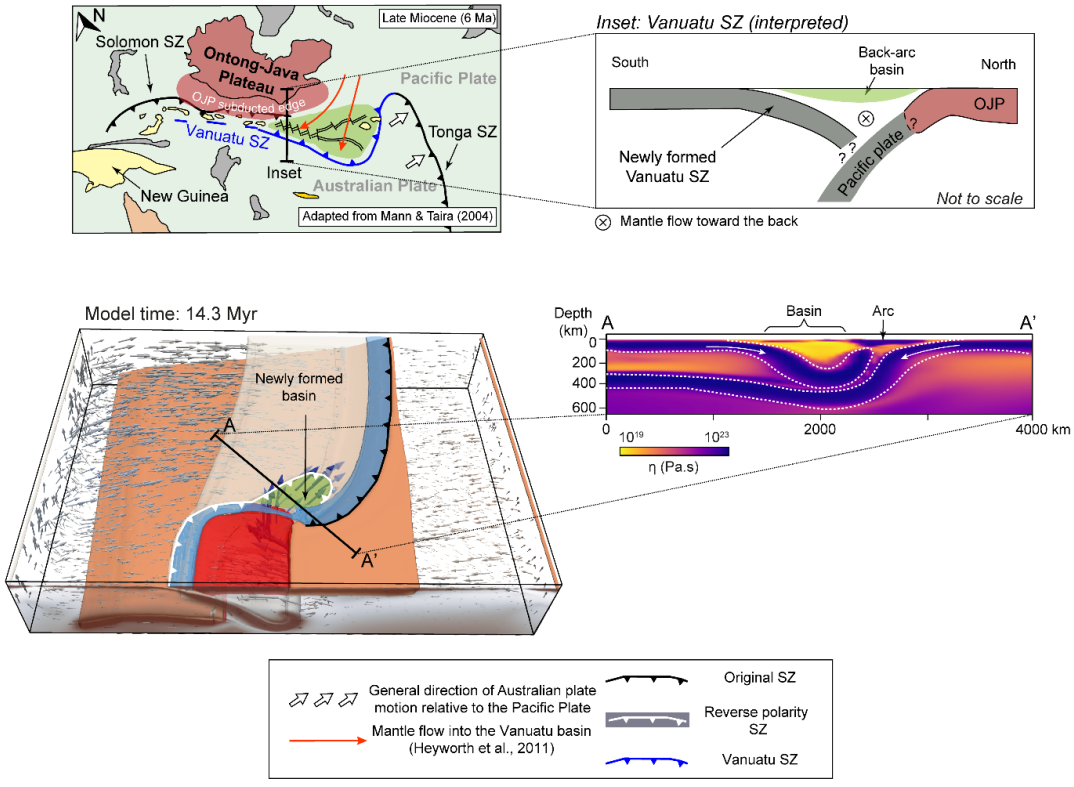

(figure caption in the next page)

Figure 4.5 – Comparison between the carried-out reference model and the formation and early evolution of the Vanuatu subduction zone. **A.** Incipient formation of the Vanuatu subduction zone. During the late Miocene, the Ontong-Java plateau (OJP) begins to dock along the Pacific trench triggering the initiation of the subduction of the Australian plate with an opposite polarity. The currently observed cross-section along the Solomon Islands arc (inset), still allows the recognition of the incipient new subduction zone corresponding to the initial development of the Vanuatu SZ. This configuration is also coherently observed in the shown model (Model 1, 70 Myr overriding and subducting plate and W_P = 600 km). **B.** Formation of an extensional basin in the Pacific plate after termination of the original subduction zone. The trench rollback/lateral migration of the newly formed Vanuatu subduction zone triggers extension in the new overriding plate area, forming an extensional basin ridges between this subduction zone and the Ontong-Java plateau (Schellart and Lister, 2005). This consistent with our models, along the A-A' cross-section, where a newly formed basin is found between two subduction zones of opposite polarity. The proposed mantle inflow at that time (Heyworth et al., 2011) as well as the end of the Pacific subduction zone in front of the Ontong-Java plateau are also mirrored by the model results.

The collision of the Ontong-Java plateau with the ancient Solomon subduction zone, and consequent reversal of the subduction polarity, is a good example of the transmission of a subduction zone from one plate to another, in this case, from the Pacific plate to the Australian plate. Our modelling results support the geodynamic viability of such a transmission and show that this is possible to occur in the absence of any external forcing mechanism, just due to the interplay between the driving and resisting forces that govern a subduction system. This bears fundamental implications for the understanding of the elusive process of subduction initiation throughout the history of our planet. It has been shown that subduction zones require unrealistic forces to initiate along Atlantic-type or passive oceanic margins (Gurnis et al., 2004), i.e. ocean-continent transitions without a subduction zone. Our work shows that once a subduction system has initiated, it has all the ingredients to dynamically self-replicate and to transfer subduction zones from ocean to ocean, without the need of external forces. A new subduction zone can be born from the interplay between slab pull of a subduction zone and resistive forces implied in an oceanic plateau collision. Oceanic plateaus are common features on the Earth's oceans and may arrive frequently at intra-oceanic trenches, leading to the formation of new subduction zones. If one assumes that subduction initiation was easier in the past because the Earth was hotter and plates were weaker (Gerya et al., 2015; Rey et al., 2014), subduction may have persisted on Earth by self-sustaining and self-replicating mechanisms such as subduction initiation by polarity reversal induced by

plateau collision. This also supports the idea that subduction zones are likely to propagate from plate to plate, and eventually from ocean to ocean, instead of starting new in Atlantic-type margins.

4.5. Acknowledgements

J. Almeida, F.M. Rosas and J.C. Duarte acknowledge financial support by FCT through project UIDB/50019/2020 – IDL. J. Almeida also acknowledges FCT PhD grant no. PD/BD/135067/2017 – Earthsystems - IDL. NR and BK were funded by the European Research Council through the MAGMA project, ERC Consolidator Grant # 771143. The authors would like to thank Wouter Schellart for the insightful discussion on the dynamics of subduction and subduction initiation. The authors would also like to thank José G. Almeida for the editing of the supplementary videos. The authors also would like to thank Taras Gerya and two anonymous reviewers for their insightful and constructive reviews which substantially improved the manuscript.

4.6. Author contributions

J.A. and N.R. designed and carried out the numerical models. J.A. conducted the post-processing analysis. B.K. contributed to the development of the numerical code. J.A., N.R, F.M.R. and J.C.D. discussed the implications for subduction initiation dynamics. All authors contributed equally to writing the paper.

4.7. Data availability

All the data and metadata will be made available in a repository.

4.8. Methods

4.8.1. Numerical approach

All numerical models were run using the LaMEM code (Kaus et al., 2016), with no artificially imposed forcing. The models are visco-elasto-plastic and self-consistent (i.e., internally driven), in which the only driving force is the slab pull exerted by the subducting slab.

LaMEM employs a finite difference staggered grid discretization coupled with a particle-in-cell approach (Kaus et al., 2016) to solve the equations of conservation of mass, momentum, and energy (eq. 4.1-4.3), assuming conditions of incompressibility.

$$\frac{\partial v_i}{\partial x_j} = 0 \tag{4.1}$$

$$-\frac{\partial P}{\partial x_i} + \frac{\partial \tau_{ij}}{\partial x_j} + \rho g_i = 0 \tag{4.2}$$

$$\rho C_p \left(\frac{\partial T}{\partial t} + v_i \frac{\partial T}{\partial x_i}\right) = \frac{\partial}{\partial x_i}\left(\kappa \frac{\partial T}{\partial x_i}\right) + H_R + H_S \tag{4.3}$$

Here, v_i is the velocity, x_{ij} the cartesian coordinates, P the pressure, τ_{ij} the shear stress, ρ the density, g the gravitational acceleration, C_p the specific heat, T the temperature, t the time, κ the thermal conductivity, and H_R and H_S represent the radiogenic and shear heating components, respectively. The shear heating component is defined as:

$$H_S = \tau_{ij}\left(\dot{\varepsilon}_{ij} - \dot{\varepsilon}_{ij}^{elastic}\right) \tag{4.4}$$

Here, $\dot{\varepsilon}_{ij}$ is the total strain rate tensor and $\dot{\varepsilon}_{ij}^{elastic}$ is the strain rate imposed by the elastic deformation.

Our models were run using non-linear visco-elasto-plastic rheology constitutive equations (Kaus et al., 2016; Piccolo et al., 2020).

$$\dot{\varepsilon}_{ij} = \dot{\varepsilon}_{ij}^{\,viscous} + \dot{\varepsilon}_{ij}^{\,elastic} + \dot{\varepsilon}_{ij}^{\,plastic} = \frac{\tau_{ij}}{2\eta_{eff}} + \frac{\mathring{\tau}_{ij}}{2G} + \dot{\gamma}\frac{\partial Q}{\partial \tau_{ij}} \quad (4.5)$$

$$\mathring{\tau}_{ij} = \frac{\partial \tau_{ij}}{\partial t} + \tau_{ik}\omega_{kj} - \omega_{ki}\tau_{kj} \quad (4.6)$$

$$\omega_{ij} = \frac{1}{2}\left(\frac{\partial v_j}{\partial x_i} - \frac{\partial v_i}{\partial x_j}\right) \quad (4.7)$$

Here, η_{eff} is the effective viscosity, $\mathring{\tau}_{ij}$ is the Jaumann objective stress rate, ω_{ij} is the spin tensor, G is the elastic modulus and Q is the plastic flow potential.

The effective viscosity, η_{eff}, is calculated according to the following model:

$$\eta_{eff} = \frac{1}{2}A^{-\frac{1}{n}} \times \dot{\varepsilon}_{II}^{\frac{1}{n}-n} \times \exp\left(\frac{E_a + V_a P}{nRT}\right) \quad (4.8)$$

Here, A is the diffusive or dislocation pre-exponential factor, n is the stress exponent, $\dot{\varepsilon}_{II}$ is the second invariant of the strain rate tensor (eq. 4.5), E_a is the activation energy, V_a is the activation volume and R is the gas constant. For phases where both dislocation and diffusive creep laws are defined (see Supplementary Table 4.5), the viscosity is calculated using the two sets of values at each timestep. The lowest value is defined as the effective viscosity after a simple comparison.

Plastic flow is ensured by employing a Drucker-Prager yield criterion (Drucker and Prager, 1952):

$$\sigma_{II} = C\cos(\phi) + P\sin(\phi) \quad (4.9)$$

Here, σ_{II} is the second invariant of the stress tensor, ϕ is the internal friction angle and C is the cohesion. Plastic weakening occurs when mantle materials accumulate at least 10% of total plastic strain and stops once at least 60% of total plastic strain has been accumulated. During softening, the materials' cohesion and internal friction angles are linearly reduced to 1% of their initial values. The weakening is not applied to crustal materials as they are defined as being frictionless, allowing them to act as subduction interface layers (see Supplementary Table 4.5).

The age dependence of the thermal profiles of the plates follows the half-space cooling model:

$$T = T_{surface} + (T_{mantle} - T_{surface}) \times \mathrm{erf}(\frac{y}{\sqrt{\kappa t}}) \quad (4.10)$$

Here, $T_{surface}$ is the temperature at the surface of the model (273 K), T_{mantle} is the temperature at the lithosphere-asthenosphere boundary (1523 K), y is the depth, κ the diffusivity, and t is the age of the plate. The effective (rheological) lithosphere thickness throughout the model is set by the 1523 K (1250 °C) isotherm. The upper mantle thermal profile follows the mantle adiabat, with a gradient of 0.5 K/km.

All material densities are temperature and pressure dependent:

$$\rho = \rho_0 + \alpha(T - T_0) + \beta(P - P_0) \quad (4.11)$$

Here, ρ_0 is the density of the material at the reference temperature T_0, α is the thermal expansibility and β is the compressibility.

4.8.2. Experimental setup

Models were run in 3D conditions, simulating the arrival of an oceanic plateau to an active subduction system. The prescribed model domain was 4000 km long, 3000 km wide and 710 km thick (see Supplementary Figure 4.1A and B) discretized along a 256x96x192 resolution grid. The model includes a 50 km thick sticky-air layer which acts as a free surface. The top boundary is open, ensuring a free movement of this layer. All other boundaries are free slip, allowing for motion along the direction of the boundary but not across it.

The initial subduction was prescribed from the start in all numerical runs by always considering that the slab was already present at a depth of 300 km (initial slab configuration in Supplementary Figure 4.1C), along the entire width of the model. Such an initial setting allowed for a gravity driven, fully dynamic, model as the weight of the slab is enough to create a self-sustained steady state subduction (Riel et al., 2017; Stegman et al., 2010, 2006), as required for any model of induced subduction initiation (Stern, 2004; Stern and Gerya, 2018). The original interface between the two plates was prescribed as a thin, weak layer with very low viscosity and denser than the surrounding oceanic plate crust (see Supplementary Table 4.5). This initial weak layer is subducted

during the onset of the run and does not interfere with the original subduction zone. The sticky-air free surface is an insulating layer with a low density (1000 kg/m^3) and constant low viscosity (10^{19} Pa·s).

Both overriding and subducting plates are oceanic and assumed to be composed of olivine. The crust and lithospheric mantle have maximum thicknesses of 15 and 90 km, respectively (see inset of Supplementary Figure 4.1C). The base density (ρ_0) of both layers is 3300 kg/m^3. Their initial thermal profiles (i.e., vertical temperature distribution) were defined following the half-space cooling model (eq. 4.10). The oceanic plate crustal materials follow a plagioclase viscous creep law but, due to their low cohesion and lack of friction coefficient (see Supplementary Table 4.5), they are controlled by plastic flow. This allows crustal materials to act as subduction interfaces once the initial weak layer is subducted.

All lithospheric and sub-lithospheric mantle materials follow a dry olivine creep law (Supplementary Table 4.5), standard for the depleted upper mantle. On the trailing edges of both plates, the isotherms are tapered, allowing for ascension of material, defining a pair of corresponding initial ridge centres (see Supplementary Figure 4.1c). This allows for free plate migration and prevents the otherwise strong downwelling of cold material formed at the edges of the model, that would perturb the mantellic flow (Capitanio et al., 2010; Riel et al., 2017). Note that these correspond to initial geometric conditions and that no continuous spreading rates were prescribed. Any spreading observed is entirely caused by the adjacent subduction zone and the respective slab pull force.

The modelled oceanic plateau was defined with a parallelepipedal geometry, with four different along-trench widths (W_P in Supplementary Figure 4.1A and Supplementary Table 4.1). The plateau is located along a free slip mirror symmetry plane boundary, which divides the model into two halves along its middle length, with the modelled domain corresponding only to one of them. As such, calculations are performed in just half of the whole conceptual domain (Stegman et al., 2010). As an example, a 600 km wide plateau in the model would correspond to a 1200 km wide plateau in nature. The plateau crust and the plateau lithospheric mantle have thicknesses of 20 and 90 km and base densities of 2800 kg/m^3 and 3220 kg/m^3, respectively (see inset in Supplementary Figure 4.1C). The crust follows a quartzite law viscous creep law (see Supplementary Table 4.5),

with a higher cohesion and friction angle than the surrounding oceanic plate crust. This setup allows for our oceanic plateau to be both less dense than the underlying asthenosphere (i.e., positively buoyant – see inset on Supplementary Figure 4.1C) and simultaneously stronger than the surrounding oceanic plate crust.

The arc was modelled using a trapezoidal geometry which spans the entire length of the model, has a trench-normal width of 200 km, with a maximum crustal thickness of 9 km and a maximum lithospheric mantle thickness of 90 km (see Supplementary Figure 4.1A and C). It represents a mature volcanic arc and is less dense than the underlying asthenosphere (see inset Supplementary Figure 4.1c and Supplementary Table 4.5).

The initial strength depth and thermal profiles for the different model phases can be seen in Supplementary Figure 4.2,

The slab pull force (Schellart, 2004a) is estimated using:

$$F_{SP} = (\rho_{slab} - \rho_{astenosphere})gV_S \quad (4.12)$$

where F_{SP} represents the slab pull force, g is the gravity acceleration, ρ_{slab} is the average density of the subducted slab, $\rho_{astenosphere}$ is the density of the underlying asthenosphere, and V_S represents the volume of subducted slab. The effective slab pull force is only c.a. 10% of the calculated value (Schellart, 2004a). The calculated values for the effective slab pull forces in all models can be found in Supplementary Table 4.2 and Supplementary Table 4.3.

4.9. Supplementary Material

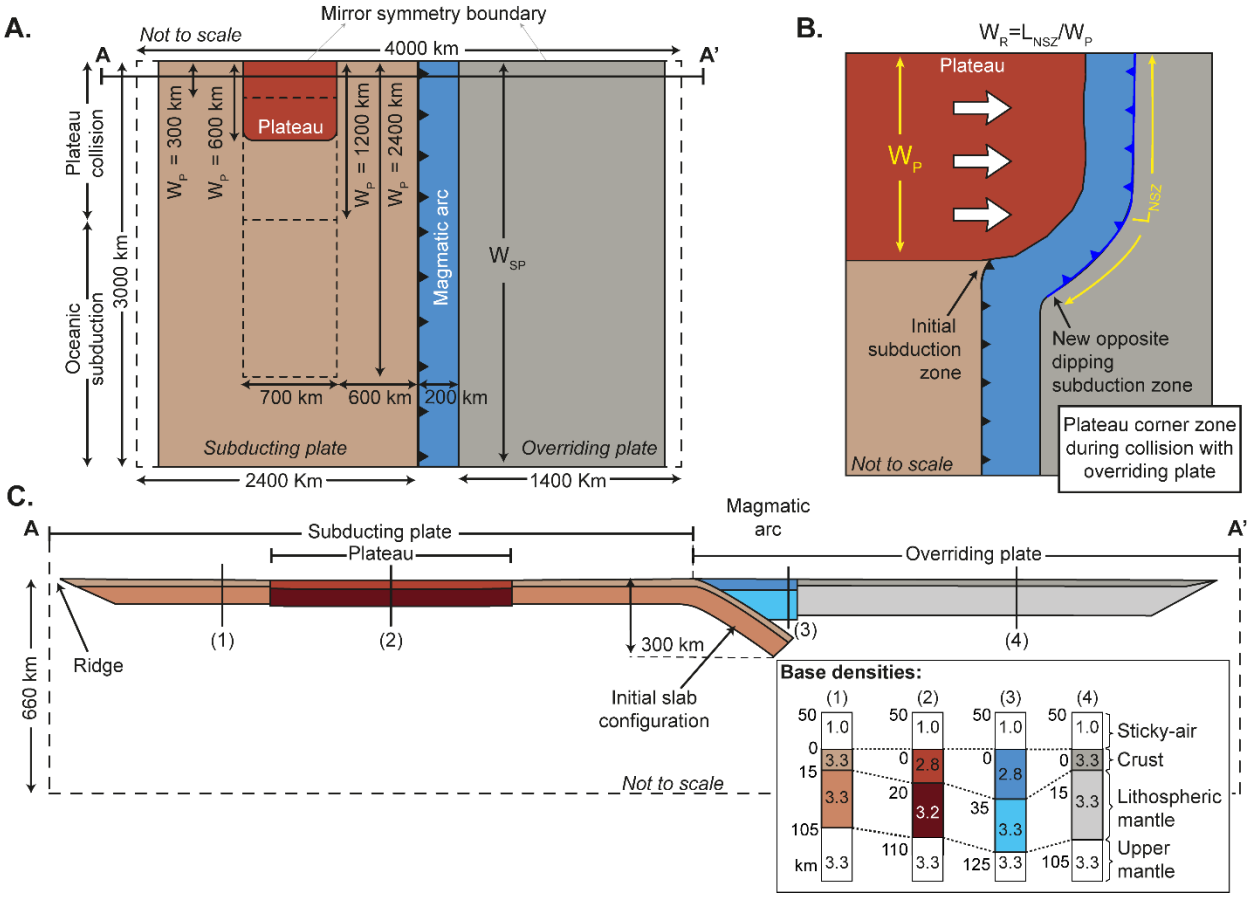

Supplementary Figure 4.1 – A. Top view of the general model initial state configuration, showing four different plateau widths (W_P). The plateaus (red square and dashed lines) are located within the subducting plate (light brown) and are cut in the middle by the model mirror symmetry boundary (the modelled domain corresponding to one symmetric half only, see detailed explanation in Experimental Setup of the Methods section). In each experiment, the plateaus are always placed at an equal distance of 600 km from the active trench. A-A' marks the position of the cross-section in Figure 4.1C. **B.** Illustration of the way through which the ratio (W_R) between the length of the newly formed subduction zone (L_{NSZ}) and the width of the oceanic plateau (W_P), was considered in the present work. **C.** Cross-section A-A' along the plateau and initial subduction zone (see location in Figure 1A). The inset shows the effective densities (in g/cm^3) of the different model layers (from bottom to top: sticky air, oceanic crust, lithospheric mantle, and upper mantle) for each of the different numbered domains: (1) - Subducting plate; (2) - Oceanic plateau; (3) - Magmatic arc; (4) – Overriding plate.

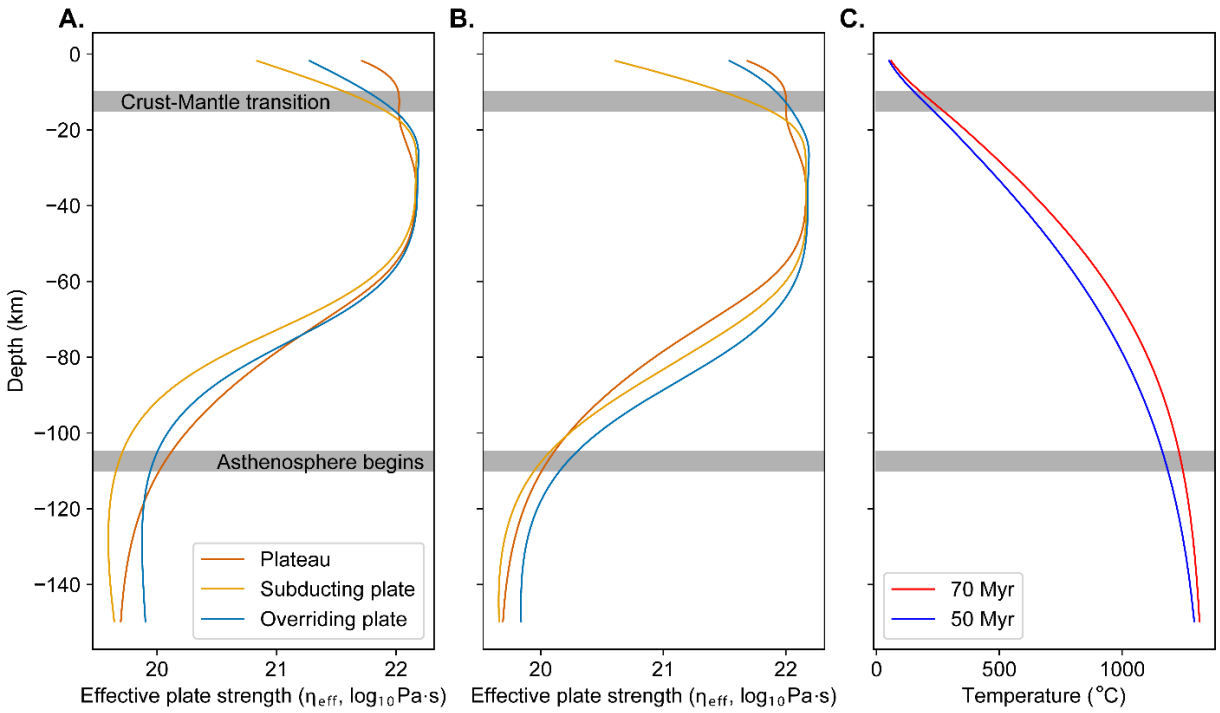

Supplementary Figure 4.2– Initial strength depth profile for the plateau and overriding/subducting plates for: **A.** a 70 Myr initial plate age and **B.** a 50 Myr initial plate age. **C.** Initial thermal profiles for the two different initial plate ages. The two shaded areas mark the crust-lithospheric mantle and lithosphere-asthenosphere transitions (from the top, respectively).

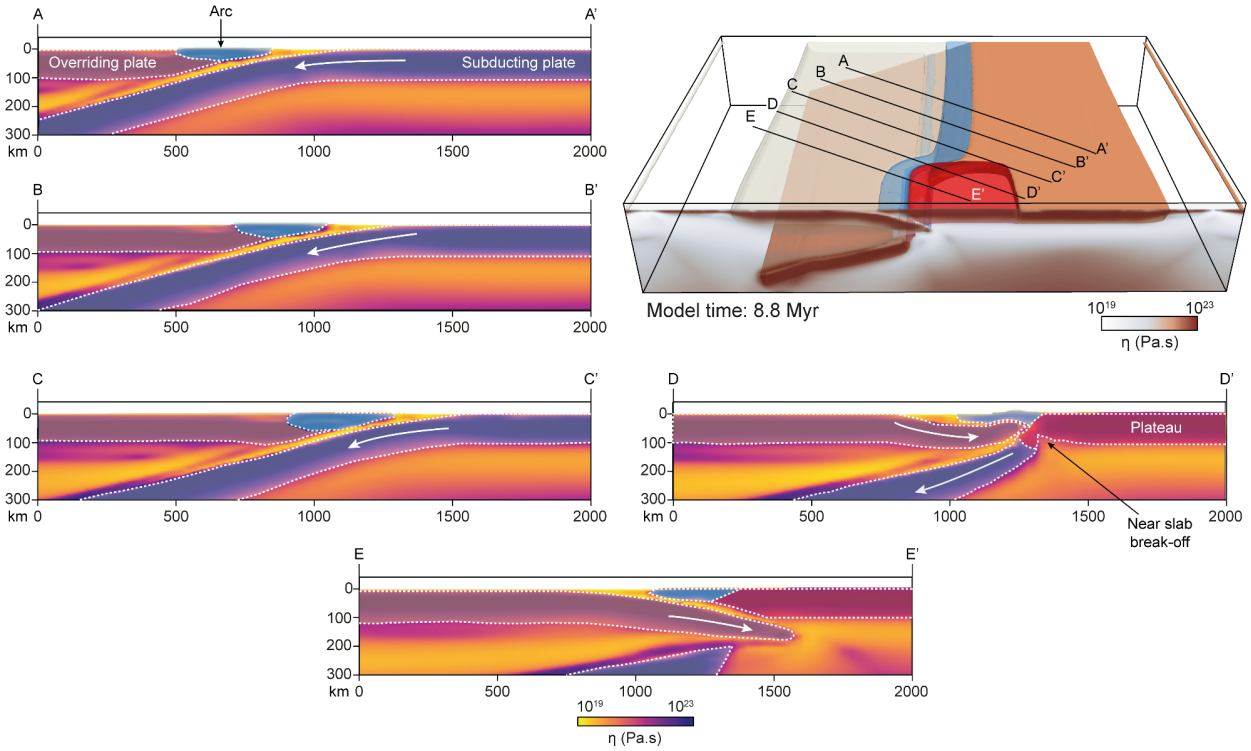

Supplementary Figure 4.3 – Effective viscosity slices across the newly formed subduction zone, in the reference model. The model stage shown here is described in detail in Figure 4.1C.

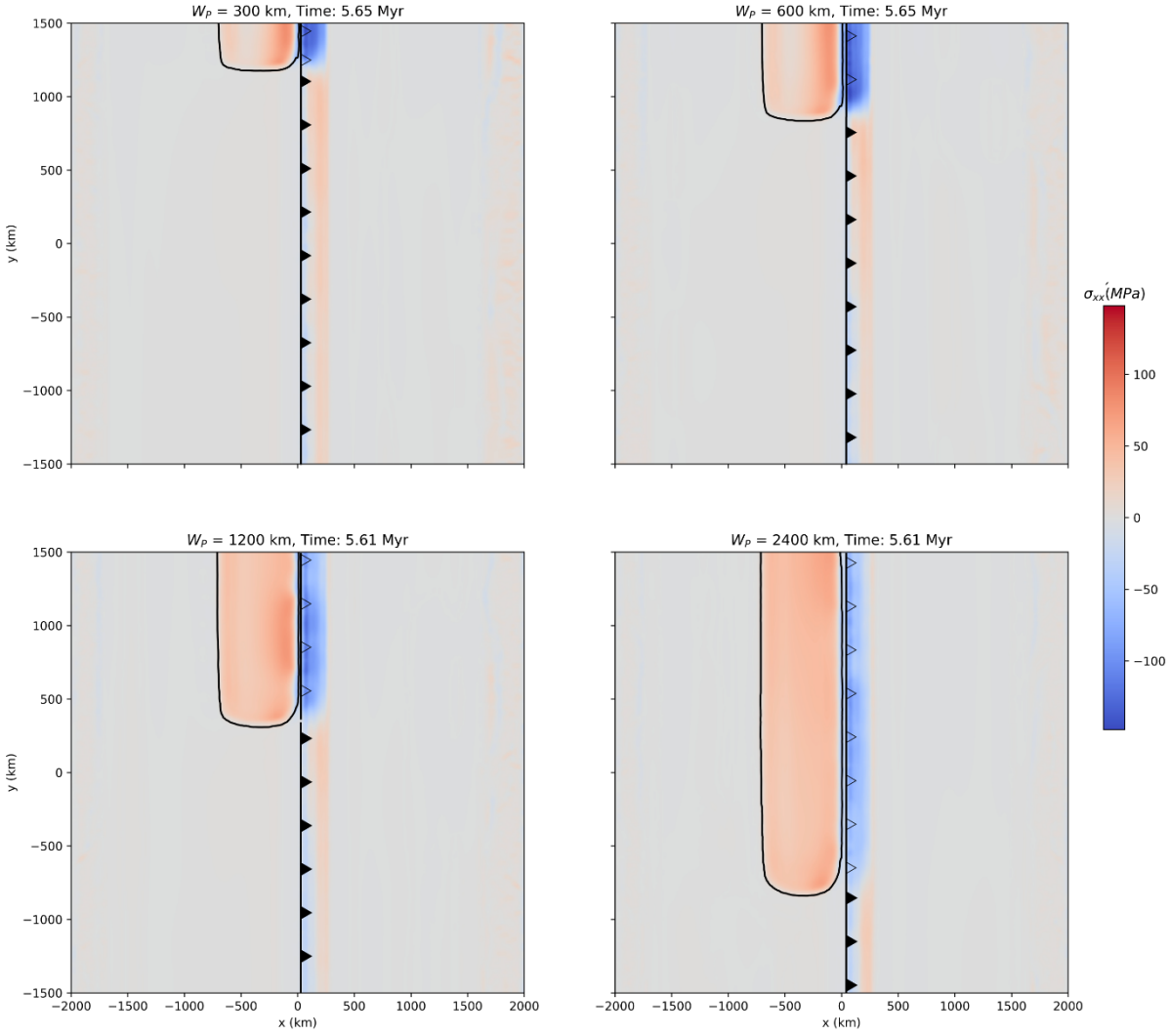

Supplementary Figure 4.4 – Top view of the surface deviatoric stress along the trench-normal axis (σ'_{xx}) during the collision of the oceanic plateau. A positive value indicates extension, while a negative value indicates compression. Note that a longer along-trench width of the oceanic plateau shows lower (absolute) values on the overriding plate, which is consistent with a more significant dissipation of the collision stresses. The open triangles represent a collision zone while the filled triangles mark the active subduction zone.

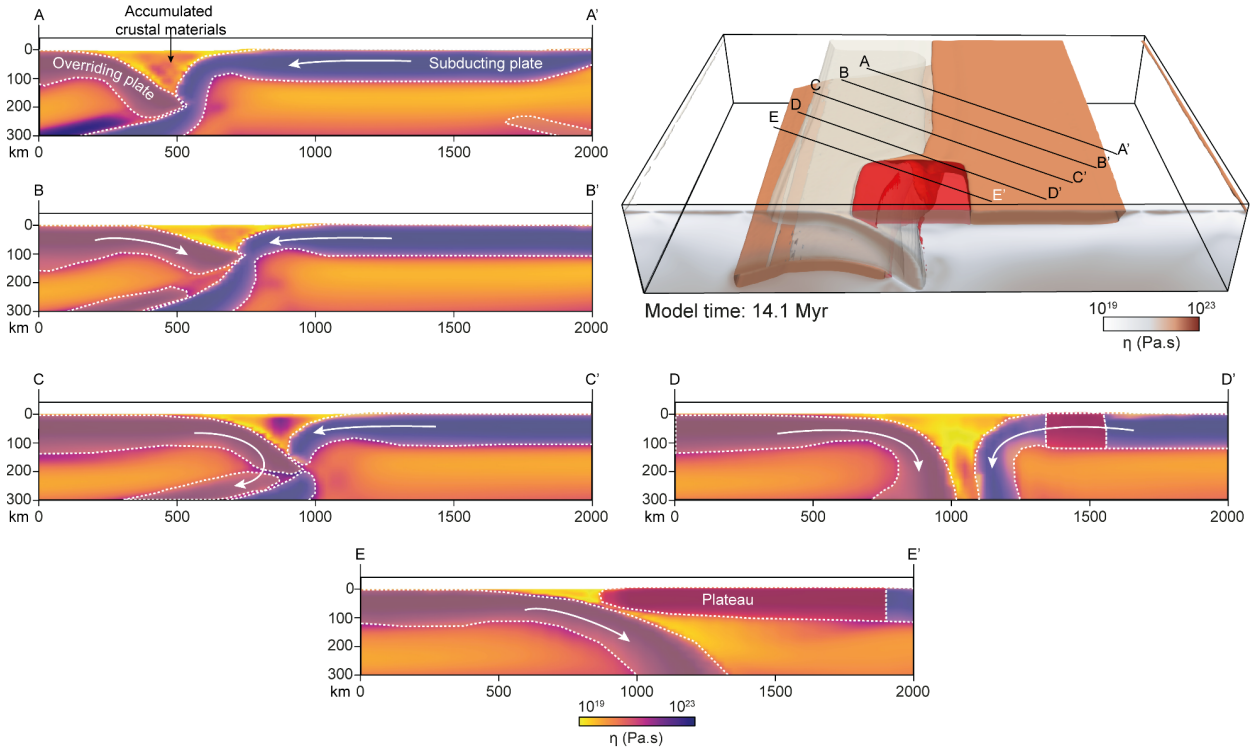

Supplementary Figure 4.5 – Effective viscosity slices across the newly formed subduction zone, in a model with plate ages identical to the reference model (70 Myr old overriding and subducting plates) but without a buoyant magmatic arc.

Supplementary Table 4.1 – List of the different models and respective tested variables. The underlined row corresponds to our reference model.

Model	Oceanic plateau width - W_P (km)	Plate age (Myr)		Buoyant arc
		Overriding	Subducting	
1	600	70	70	Present
2	300	70	70	Present
3	1200	70	70	Present
4	2400	70	70	Present
5	300	70	70	Absent
6	600	70	70	Absent
7	1200	70	70	Absent
8	2400	70	70	Absent
9	600	50	50	Present
10	600	50	70	Present
11	600	70	50	Present

Supplementary Table 4.2 – Estimation of the effective slab pull force for the different along-trench plateau widths and estimation of the available energy to initiate a new subduction zone, after slab break-off and before polarity reversal. Vs – Volume of the subducted portion of the main slab.

		W_P = 300 km	W_P = 600 km	W_P = 1200 km	W_P = 2400 km
	ρ_{slab} (kg/m^3)	3220	3220	3220	3220
	$\rho_{asthenosphere}$ (kg/m^3)	3162	3162	3162	3162
	$\Delta\rho$ (kg/m^3)	58	58	58	58
	Volume of subducted slab – V_S (m^3)	3x10^{17}	3x10^{17}	3x10^{17}	3x10^{17}
Driving	**Length of the active subduction zone (km)**	2700	2400	1800	600
	Buoyancy force or F_{SP} (N)	1.8x10^{20}	1.8x10^{20}	1.8x10^{20}	1.8x10^{20}
	Buoyancy force per meter (N/m)	6.5x10^{13}	7.3x10^{13}	9.8x10^{13}	2.9x10^{14}
Resisting	**F_{SP} / W_P (available buoyancy force for subduction zone initiation)**	5.9x10^{14}	2.9x10^{14}	1.5x10^{14}	7.3x10^{13}
	% of reference model	200%	-	50%	25%

Supplementary Table 4.3 – Estimation of the slab pull force during plateau collision for the models with different along-trench plateau width and constant initial overriding and subducting plate ages, following eq. 4.12. During collision, before any slab break-off, the volume of subducted slab is identical for all plateau sizes. The collision event takes place after ca. 5.6 Myr in all models. The subduction length is identical to the width of the model, 3000 km. Vs – Volume of the subducted portion of the main slab.

ρ_{slab} (kg/m^3)	3220
$\rho_{asthenosphere}$ (kg/m^3)	3162
$\Delta\rho$ (kg/m^3)	58
Volume of subducted slab – V_S (m^3)	2.32×10^{17}
Length of active subduction zone (km)	3000
Buoyancy force or F_{SP} (N)	1.32×10^{20}
Effective buoyancy force F_{SP}/W_{SP} (N/m)	4.40×10^{13}

Supplementary Table 4.4 – Estimation of the effective slab pull force at the start of the model for the different initial subducting plate ages, following eq. 4.12. The volume of subducted slab is identical for all plateau sizes. The subduction length is identical to the width of the model, 3000 km. Vs – Volume of the subducted portion of the main slab.

Initial SP age (Myr)	50	70
Model number	9	10
ρ_{slab} (kg/m^3)	3210	3220
$\rho_{asthenosphere}$ (kg/m^3)	3162	3162
$\Delta\rho$ (kg/m^3)	48	58
Volume of subducted slab – V_S (m^3)	6.91×10^{16}	6.91×10^{16}
Length of active subduction zone (km)	3000	3000
Buoyancy force or F_{SP} (N)	3.3×10^{19}	3.9×10^{19}
Effective buoyancy force F_{SP}/W_{SP} (N/m)	1.1×10^{13}	1.3×10^{13}
% of reference model	86%	-

Supplementary Table 4.5 – Physical parameters applied in the models, for each of the different phases. The softening parameters are found in Methods section.

			Subducting and overriding plate			Magmatic arc		Plateau	
		Upper mantle	*Crust*	*Lithospheric mantle*	Initial weak zone	*Crust*	*Lithospheric mantle*	*Crust*	*Lithospheric mantle*
	ρ_0 – kg/m^3	3300	3300	3300	3200	2800	3300	2800	3220
Dislocation creep	B_n – Pa^{-n}s^{-1}	2.50×10^{4}	8	2.50×10^{4}	-	6.70×10^{-6}	2.50×10^{4}	6.70×10^{-6}	2.50×10^{4}
	n	3.5	4.2	3.5	-	2.4	3.5	2.4	3.5
	E_n – J/MPa/mol	5.30×10^{4}	4.45×10^{5}	5.30×10^{4}	-	1.56×10^{5}	5.30×10^{4}	1.56×10^{5}	5.30×10^{4}
	V_n – m^3/mol	1.35×10^{-5}	-	1.35×10^{-5}	-	-	1.35×10^{-5}	-	1.35×10^{-5}
Diffusion creep	B_l – Pa^{-n}s^{-1}	1.50×10^{9}	-	1.50×10^{9}	-	-	1.50×10^{9}	-	1.50×10^{9}
	n	1	-	1	-	-	1	-	1
	E_l – J/MPa/mol	3.75×10^{5}	-	3.75×10^{5}	-	-	3.75×10^{5}	-	3.75×10^{5}
	V_l – m^3/mol	1.35×10^{-5}	-	1.35×10^{-5}	-	-	1.35×10^{-5}	-	1.35×10^{-5}
Plastic flow	Cohesion – MPa	30	5	30	5	30	30	30	30
	Softened cohesion – MPa	0.3	-	0.3	-	-	0.3	-	0.3
	Φ – degrees	20	0	20	0	20	20	20	20
	Softened Φ – degrees	0.2	-	0.2	-	-	0.2	-	0.2
Elasticity	G – Pa	5.00×10^{10}	5.00×10^{10}	5.00×10^{10}	5.00×10^{10}	5.00×10^{10}	5.00×10^{10}	5.00×10^{10}	5.00×10^{10}
Thermal properties	Expansivity (α) – 1/K	3.00×10^{-4}	3.50×10^{-4}	3.00×10^{-4}	3.00×10^{-5}	3.50×10^{-5}	3.00×10^{-4}	3.50×10^{-5}	3.00×10^{-4}
	Conductivity (κ) - W/m/k	3	3	3	3	3	3	3	3
	Heat capacity - J/kg/K	1050	1050	1050	1050	1050	1050	1050	1050

4.10. Supplementary videos

The supplementary videos for this paper can be found in Appendix D of this thesis.

Supplementary Video 1 – Video file that shows the evolution of the reference model (Model 1). The plateau along-trench width is 600 km. In this model, the overriding plate and subducting plate are 70 Myr old and the buoyant magmatic arc is present.

Supplementary Video 2 – Video file that shows the evolution of Model 2. The plateau along-trench width is 300 km. In this model, the overriding plate and subducting plate are 70 Myr old and the buoyant magmatic arc is present.

Supplementary Video 3 – Video file that shows the evolution of Model 3. The plateau along-trench width is 1200 km. In this model, the overriding plate and subducting plate are 70 Myr old and the buoyant magmatic arc is present.

Supplementary Video 4 – Video file that shows the evolution of Model 4. The plateau along-trench width is 2400 km. In this model, the overriding plate and subducting plate are 70 Myr old and the buoyant magmatic arc is present.

Supplementary Video 5 – Video file that shows the evolution of Model 5. The plateau along-trench width is 300 km. In this model, the overriding plate and subducting plate are 70 Myr old and the buoyant magmatic arc is absent.

Supplementary Video 6 – Video file that shows the evolution of Model 6. The plateau along-trench width is 600 km. In this model, the overriding plate and subducting plate are 70 Myr old and the buoyant magmatic arc is absent.

Supplementary Video 7 – Video file that shows the evolution of Model 7. The plateau along-trench width is 1200 km. In this model, the overriding plate and subducting plate are 70 Myr old and the buoyant magmatic arc is absent.

Supplementary Video 8 – Video file that shows the evolution of Model 8. The plateau along-trench width is 2400 km. In this model, the overriding plate and subducting plate are 70 Myr old and the buoyant magmatic arc is absent.

Supplementary Video 9 – Video file that shows the evolution of Model 9. The plateau along-trench width is 600 km. In this model, the overriding plate and subducting plate are 50 Myr old and the buoyant magmatic arc is present.

Supplementary Video 10 – Video file that shows the evolution of Model 10. The plateau along-trench width is 600 km. In this model, the overriding plate is 50 Myr old and the subducting plate is 70 Myr old and the buoyant magmatic arc is present.

Supplementary Video 11 – Video file that shows the evolution of Model 11. The plateau along-trench width is 600 km. In this model, the overriding plate is 70 Myr old and the subducting plate is 50 Myr old and the buoyant magmatic arc is present.

Chapter 5. Stability of single-sided subduction zones

(this page has been left intentionally blank)

5.1. Foreword

In Chapter 3, the conditions required for the development of polarity reversal subduction initiation were discussed. While exploring this topic, some models showed the formation of double-sided subduction zones which, at that point, we argued to likely represent model artefacts derived from the usage of top free-slip boundary conditions. Despite this, in Chapter 4, the same double-sided subduction zones were observed in 3D free-surface models. Thus, a set of modelling experiments was prepared to understand the conditions under which these conspicuous subduction zones might form.

We conducted a set of subduction zone models, in which the initial overriding and subducting plate ages were systematically varied, to assess the impact of plate strength on the development of subduction zone instabilities, potentially leading to the development of double-sided subduction zones. The objective was to map the stability domains for the different modes of subduction.

The following chapter discusses the influence that different plate strength combinations might exert on the formation of double-sided vs. single-sided subduction systems. Both the wide range of plate ages assumed in out models, and the fact that these are dynamically self-sufficient, constitute a novel contribution for the understanding of this problem, which will soon be submitted to an international peer-reviewed journal.

5.2. Abstract

Natural subduction zones are known to be both single-sided and asymmetric, with an overriding plate above a constantly subducting slab. Despite this, early geodynamic models have predicted the occurrence of convergent double-sided subduction, which later was shown to depend on the existence of a strong slab and a weak subduction interface. Here, we present 2D internally driven subduction zone models, in which we systematically test the strength of both subducting and overriding plates by varying their initially prescribed thermal ages, under free slip top boundary conditions. Our preliminary results suggest that both subducting and overriding plates must be strong to maintain a stable asymmetric single-sided subduction. When at least one weak plate is present in the subduction system, recurrent instabilities are observed, manifested as spontaneous polarity reversals and/or convergent double-sided subduction events. The timing of these events is shown to be determined by the initial age of the overriding plate, with stronger overriding plates delaying the triggering of double-sided subduction outcomes.

5.3. Introduction

Subduction zones are one of the most widely studied geodynamical settings on Earth, not only for their role on the recycling of the Earth's surface but also for providing the main driving force in Plate Tectonics (Carlson et al., 1983; Conrad and Lithgow-Bertelloni, 2002; Forsyth et al., 1975; Stern, 2002). Modern day subduction zones are markedly asymmetric (Zhao, 2004) with one plate moving beneath the other (see Figure 5.1). Nevertheless, both fluid dynamics (Tao and O'connell, 1992) and early global-scale tectonic models (e.g., Tackley, 2000) predicted the formation of simultaneous downwelling of both intervening plates, or convergent double-sided subduction (see Figure 5.1).

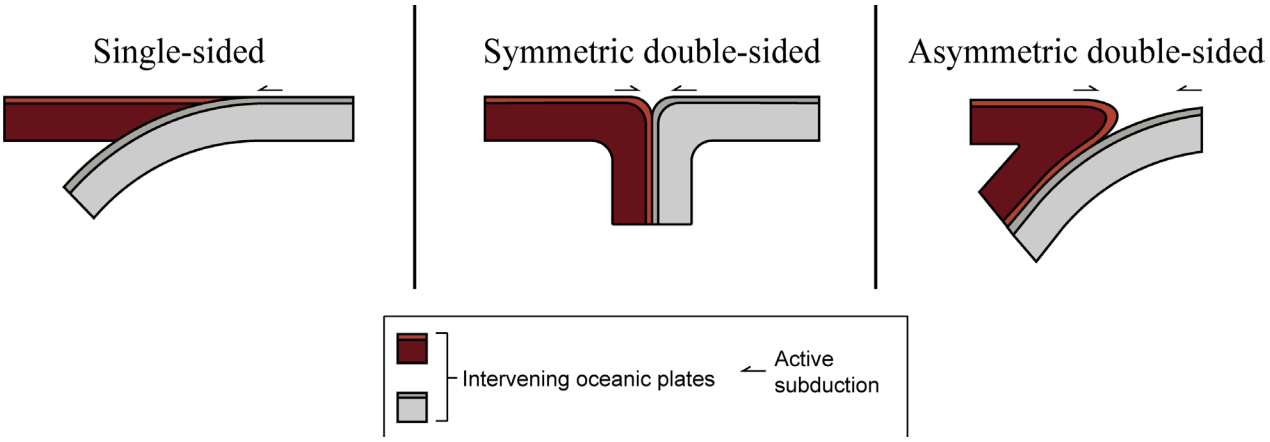

Figure 5.1 – Possible subduction types described by previous authors. From left to right: stable symmetric single-sided subduction, with one plate above the other; convergent symmetric double-sided subduction, with two similarly strong plates (e.g. Tackley, 2000); and convergent asymmetric double-sided subduction, with a strong subducting slab paired with a weak overriding plate (e.g. Tao and O'Connell, 1992; Gerya, Connolly and Yuen, 2008).

To our knowledge, the earliest reference to convergent double-sided subduction is by Tao and O'Connell (1992), being referred to in their work as "ablative subduction". By employing self-consistent numerical models, they suggest that this process is viscosity- and buoyancy-driven, being the result of the viscous drag of the overriding plate by a denser oceanic plate. They argued that the relative amount of overriding plate subduction was dependent on the efficiency of the coupling between the two plates. They further suggested that the occurrence of double-sided subduction could lead to observations of "apparent subduction reversal" in nature, in which the newly formed slab would comprise the simultaneous subduction of the two plates.

While exploring the conditions required to maintain plate-like behaviour on Earth, Tackley (2000) also discussed the formation of convergent double-sided subduction zones. The author argued that to maintain single-sided subduction behaviour, low friction and strong strain localization/weakening are both required along the subduction channel. Without these, all convergent centres developed symmetrical double-sided subduction zones.

Subsequent geodynamical modelling studies (Gerya et al., 2008) showed that, in order to maintain a single-sided asymmetric subduction zone, both a strong subducting plate exists

($\sin(\phi)>0.15$, with ϕ as the internal friction angle) and a permanent weak interface must simultaneously exist.

Here, we present internally driven (or dynamically self-consistent) 2D free-slip subduction zone models in which we systematically test different initial thermal ages (and by extent, the effective strength) of the subducting and overriding plates. In this work, we build on the contribution by Gerya et al. (2008) by expanding the range of overriding and subducting initial plate ages from 1 Myr overriding and 100 Myr subducting plates (used in Gerya et al., 2008). In the present work, the initial overriding plate age ranges from 10 Myr to 90 Myr, while the initial subducting plate age ranges from 30 Myr to 100 Myr (with 10 Myr intervals), respectively. We further assume that the subduction zone has already initiated, as opposed to studying subduction zone initiation.

The objective was to better understand the way through which the strength of the plates in a subduction system might govern the formation of single-sided or double-sided subduction zones. With this in mind, we used our experimental results to map the different stability fields for the different obtained subduction zone modes, arising from the different prescribed initial plate age combinations.

5.4. Materials and Methods

5.4.1. Governing equations

The numerical modelling experiments were carried out using the code Underworld (Moresi et al., 2007), which employs a finite element discretization coupled with a particle-in-cell approach to solve the equations of conservation of mass, momentum, and energy (eq. 5.1-5.3, respectively), assuming conditions of incompressibility:

$$\nabla \cdot \mathbf{v} = 0 \tag{5.1}$$

$$\nabla \cdot \boldsymbol{\sigma} = \rho \mathbf{g} \tag{5.2}$$

$$\rho C_p \left(\frac{\partial T}{\partial t} + \mathbf{v} \cdot \nabla T\right) = \kappa \nabla^2 T + H_s + H_A \tag{5.3}$$

in which $\mathbf{v}$ is the velocity vector, $\boldsymbol{\sigma}$ the stress tensor, ρ the density, $\mathbf{g}$ the gravity acceleration vector, κ the diffusivity, T is the temperature and C_p the specific heat. The shear heating (H_S) and the adiabatic heating (H_A) in equation 5.3 are defined as:

$$H_s = \sum [\boldsymbol{\sigma}' \cdot \dot{\boldsymbol{\varepsilon}}]_{ij} \tag{5.4}$$

$$H_A = \frac{-T\alpha \mathbf{v_y} g}{c_p} \tag{5.5}$$

in which $\boldsymbol{\sigma}'$ is the deviatoric stress tensor, $\dot{\boldsymbol{\varepsilon}}$ is the strain rate tensor, α the coefficient of thermal expansion and $\mathbf{v_y}$ the vertical velocity. The stress tensor is defined by:

$$\boldsymbol{\sigma} = \boldsymbol{\sigma}' - P\mathbf{I} \tag{5.6}$$

with P as the pressure and $\mathbf{I}$ the identity tensor. The deviatoric stress tensor ($\boldsymbol{\sigma}'$) is a function of both strain rate ($\dot{\boldsymbol{\varepsilon}}$) and effective viscosity (η_{eff}):

$$\boldsymbol{\sigma}' = 2\eta_{eff}\dot{\boldsymbol{\varepsilon}} \tag{5.7}$$

The strain rate tensor is defined as:

$$\dot{\boldsymbol{\varepsilon}} = \frac{1}{2}[\nabla \mathbf{v} + (\nabla \mathbf{v})^T] \tag{5.8}$$

and the effective viscosity is defined as:

$$\eta_{eff} = A^{-\frac{1}{n}} \dot{\varepsilon}_{II}^{\frac{1}{n}-n} \exp\left(\frac{E_a + V_a P}{nRT}\right) \tag{5.9}$$

with A as the pre-exponential factor, $\dot{\varepsilon}_{II}$ the second invariant of the strain rate tensor, n the stress exponent, E_a the activation energy, V_a the activation volume and R the universal gas constant.

Plastic flow is implemented by assuming a Drucker-Prager yield criterion (Drucker and Prager, 1952), according to which a given material yields when the stress imposed upon it surpasses a prescribed limit (yield value):

$$\sqrt{\boldsymbol{\sigma'_{II}}} = p\sin(\phi) + C\cos(\phi) \tag{5.10}$$

in which $\boldsymbol{\sigma'_{II}}$ is the second invariant of the deviatoric stress tensor, ϕ the internal friction angle and C the cohesion. When materials reach the yield stress, they are linearly softened until ϕ and cohesion reach 10% of the original value.

Plate age dependence of the thermal profiles follows the plate cooling model:

$$T = T_0 + (T_1 - T_0)\left[\frac{y}{y_{Lo}} + \frac{2}{\pi}\sum_{n=1}^{\infty}\frac{1}{n}\exp\left(\frac{\kappa n^2\pi^2 t}{y_{Lo}^2}\right)\sin\left(\frac{n\pi y}{y_{Lo}}\right)\right] \tag{5.11}$$

in which T_0 is the surface temperature of the model (set to 273 K), T_1 is the temperature at the lithosphere-asthenosphere boundary, which is located at an y_{Lo} depth, and set to 1473 K. Additionally, y is the depth and t is the age of the plate.

All material densities are temperature dependent according to:

$$\rho = \rho_0[1 - \alpha(T - T_0)] \tag{5.12}$$

in which ρ_0 is the density of the material at the reference temperature T_0.

5.4.2. Initial setup and modelling rationale

In the present modelling study, we assume internally driven (or self-sufficient) conditions. This implies that plate velocities are never imposed, and instead arise from the evolving dynamic balance between internal driving forces and resisting forces (e.g., Schellart, 2017; Stegman et al., 2010). The only significant driving force in our system is the slab pull (F_{SP}), which results from the negative buoyancy of the slab, which is opposed by the viscous resistance forces of the plates/mantle (e.g., Schellart, 2004b). Thus, to assess the dynamic impact any given parameter exerts on the evolution of the subduction system, we can monitor the changes in the subducting plate and overriding plate velocities (V_{SP} and V_{OP} respectively).

Our initial configuration (Figure 5.2A) corresponds to a recently formed oceanic subduction zone, in which the tip of the subducting slab is prescribed at a depth of 200 km from the onset of the experiment. This starting configuration was conceived to study the conditions required to maintain an asymmetric single-sided subduction zone vs. the ones which might trigger double-sided subduction, and not to address subduction zone initiation, which is out of the scope of the present paper. The considered 2D model domain is 5000 x 660 km, with its maximum depth corresponding to the upper-lower mantle transition (see Figure 5.2A) and discretized along a uniform 768 x 192 finite element grid. A thin (ca. 12 km) weak zone was set between the overriding and subducting plates, accounting for a pre-existent subduction channel. The initial subduction interface (weak zone in Figure 5.2A) is defined by an isoviscous rheology (with a constant low viscosity of 10^{20} Pa·s) as to achieve high strain localization at the onset of the model. This soft material channel is subducted in the early stages of the experiments and bears no relevant role in any of the model results.

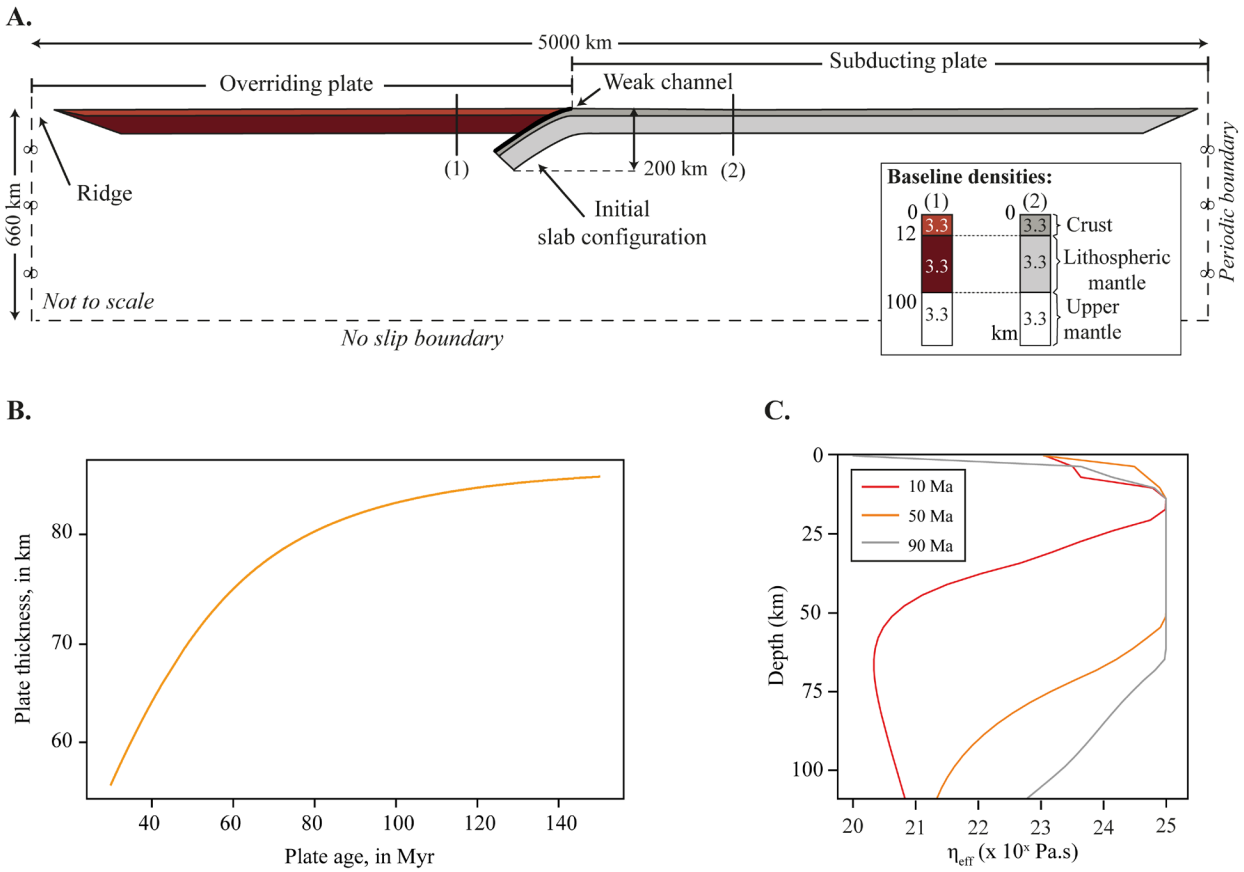

Figure 5.2 – A. Model setup for the experimental initial state (not to scale): schematic representation of the geometric configuration and prescribed boundary conditions. The inset describes the thickness and reference density (ρ_0) of each layer in the two intervening plates. The reference density does not account for plate aging, merely shows the initial value which is used in eq. 5.12. **B.** Effective maximum lithosphere thickness as a function of plate age, as defined by the depth of the 1473 K (1200 ºC) isotherm. **C.** Strength-depth profiles for different assumed initial thermal ages of 10 (in red), 50 (orange) and 90 Myr (grey). Strength of the plates is given by effective viscosity (η_{eff}).

Both overriding and subducting plates are oceanic and assumed to be composed entirely of peridotite, with a base density (ρ_0) of 3300 kg/m^3 and an olivine rheology. On both plates, the crust is set to be 12 km thick, and the lithospheric mantle is 88 km thick (see Figure 5.2). We are aware of the overestimation the thickness of the oceanic crust. This approach is used to resolve issues raised by the numerical resolution limitation and necessity for a continuously weak subduction interface, provided by the oceanic crust in self-consistent models.

Both initial thermal profiles (i.e., vertical temperature distribution, see Supplementary Figure 5.1) were defined following the plate cooling model (eq. 5.11), in which T is obtained as a function of both depth and time (plate age). The effective (rheological) thickness of the lithosphere (set by the 1473K isotherm), and the way it depends on time, are also deduced from the same plate cooling model (eq. 5.11) showing a consistent non-linear increase of plate thickness with its age (Figure 5.2B). Both rheologies are viscoplastic (eq. 5.9-10), following dry peridotite creep laws (Ranalli, 1997) and a plastic yielding criterion (Drucker and Prager, 1952). Modelled strength-depth profiles (Figure 5.2C) closely follow the behaviour associated with an oceanic lithosphere (e.g., Kohlstedt et al., 1995). The trailing edges of the plates are tapered, with the basal lithosphere isotherm bulging upwards near the left and right plate boundaries, defining a pair of upwelling centres (see Figure 5.2A). This allows for free lateral migration of the two plates and prevents the occurrence of cooled material downwelling at the edges of the model, which would influence the mantle flow. All assumed parameters for the different considered model materials can be found in Table 5.1.

Table 5.1 – Parameters used in the definition of the non-linear (thermal dependent) model rheology/density configuration. The density ($\boldsymbol{\rho_0}$) parameters represent the density at reference temperature ($\mathbf{T_0}$, see equation 3.11).

Parameter	Value	Reference
Expansibility, α (K^{-1})	3.00×10^{-5}	-
Diffusivity, κ ($m^2\ s^{-1}$)	1.00×10^{-6}	-
Heat capacity, C_p ($J\ kg^{-1}\ K^{-1}$)	1.00×10^{3}	-
Cohesion (MPa)	20	(Hui et al., 2014)
ϕ (Internal friction angle, in degrees)	~ 14	(Gerya et al., 2008)
$T_{surface}$ (K)	273	-
T_{base} (K)	1573	-
ρ_{crust} ($kg\ m^{-3}$)	3300	-

ρ_{mantle} (kg m^{-3})	3300	-
$\rho_{weak\ zone}$ (kg m^{-3})	3300	-
A_{mantle} ($MPa^{-3.5}$ s^{-1})	5.5 x 10^4	(Ranalli, 1997)
$A_{weak\ zone}$ ($MPa^{-3.5}$ s^{-1})	5.5 x 10^4	(Ranalli, 1997)
n_{mantle}	3.5	(Ranalli, 1997)
$n_{weak\ zone}$	3.5	(Ranalli, 1997)
Ea (J mol^{-1})	5.3 x 10^5	(Baes and Sobolev, 2017; Ranalli, 1997)
Va (m^3 mol^{-1})	1.0 x 10^{-6}	(Crameri and Tackley, 2016; Ranalli, 1997)

To better understand the main causes for the triggering of subduction zone instabilities (such as the drag of the overriding plate by the slab), we also calculate the rate of energy dissipation between slab bending and slab pull:

$$\frac{\phi_{Be}}{\phi_{Bu}} = \frac{A_C T_{SP}^2 \eta_{SP} V_S^2}{3\Delta\rho g R_B^3 L V_{sink}} \quad (5.13)$$

in which ϕ_{Be} is bending energy dissipation rate and ϕ_{Bu} the potential gravitational energy associated with the slab (e.g., Irvine and Schellart, 2012; Schellart, 2009). On numerator of this equation A_C is the ratio between the length of the bent portion of the slab (along its hinge zone) and its curvature radius (assumed to be a function of the slab dip angle α, such that $AC \approx 2\pi(\alpha/360)$, e.g., Schellart, 2009). T_{SP} and η_{SP} are the thickness and effective viscosity of the subducting plate, respectively; and V_S is the subduction velocity. On denominator, $\Delta\rho$ is the density contrast between the subducting slab and the surrounding upper mantle, R_B the bending radius of the slab, L the length of the slab which contributes to slab-pull (does not account for the slab already accumulated along

the base of the model) and V_{sink} the sinking velocity of the slab. As ϕ_{Be}/ϕ_{Bu} increases, more of the potential gravitational energy of the slab is dissipated by bending the slab, as opposed to other dissipation mechanisms (e.g., mantle displacement). The values for these individual parameters, measured for each model at the onset of subduction zone instability triggering, can be found in Supplementary Figure 5.2.

5.4.3. Boundary conditions

In the present modelling setup, lateral (vertical) boundary conditions are periodic (Figure 5.2A). Accordingly, any material escaping through one of the lateral boundaries re-enters the model across the opposite boundary with the same velocity value:

$$\vec{v}_{x-a} = \vec{v}_{x+a} \tag{5.14}$$

where a is the width of the model. These conditions allow for subduction slab roll-back/-forward and the associated trench migration. By contrast, closed lateral boundaries have been shown to hinder such motions in 2D models since no toroidal (return) mantle flow from beneath the slab is possible (Schellart, 2004a).

As stated earlier, the top boundary of the model is defined as free slip, which deters any vertical escape/motion of material across this boundary:

$$\vec{v}_y = \vec{0} \tag{5.15}$$

No-slip boundary conditions were set along the model bottom wall. These conditions reflect the sharp viscosity contrast observed at the upper-lower mantle boundary, and allow for an approximation of slab anchoring without further subduction across this interface:

$$\vec{v}_x = \vec{v}_y = \vec{0} \tag{5.16}$$

Thermally, the model surface is set at 273 K (0 ºC), and the bottom boundary corresponds to 1873 K (1600 ºC).

5.5. Results

In order to assess the dynamic impact which the effective strength of the overriding (OP) and subducting (SP) plates exerts on the evolution of a subduction zone, their initial thermal age was systematically varied, with initial overriding plate ages ranging between 10 and 90 Myr; and the subducting plate between 30 and 90 Myr, both with 10 Myr intervals (see Figure 5.3). A total of 63 initial plate age combinations was investigated, comprising all possible combinations of initial OP vs. SP ages. This variety expresses different initial age-depending rheological and density contrasts between the two plates in each case, which held a decisive influence on the final geodynamic outcome under free-slip conditions (see Figure 5.3).

The models show four fundamental modes of subduction zone evolution, arising from different specific plate age combinations (see Figure 5.3 and Supplementary Videos 1-4):

1. *Stable single-sided (SS) subduction zones*, which mostly occurs in models in which at least one of the plates is older than 50 Myr.
2. *Systematically unstable (SU) subduction zones,* in models with overriding and subducting plates younger than 50 Myr.
3. *Early developed double-sided (ED) subduction zones,* in models with a young overriding plate (≤ 20 Myr) paired with an old subducting plate (> 50 Myr).
4. *Late developed double-sided (LD) subduction zones*, in models with overriding plate and subducting plates with similar ages but still relatively young (< 60 Myr).

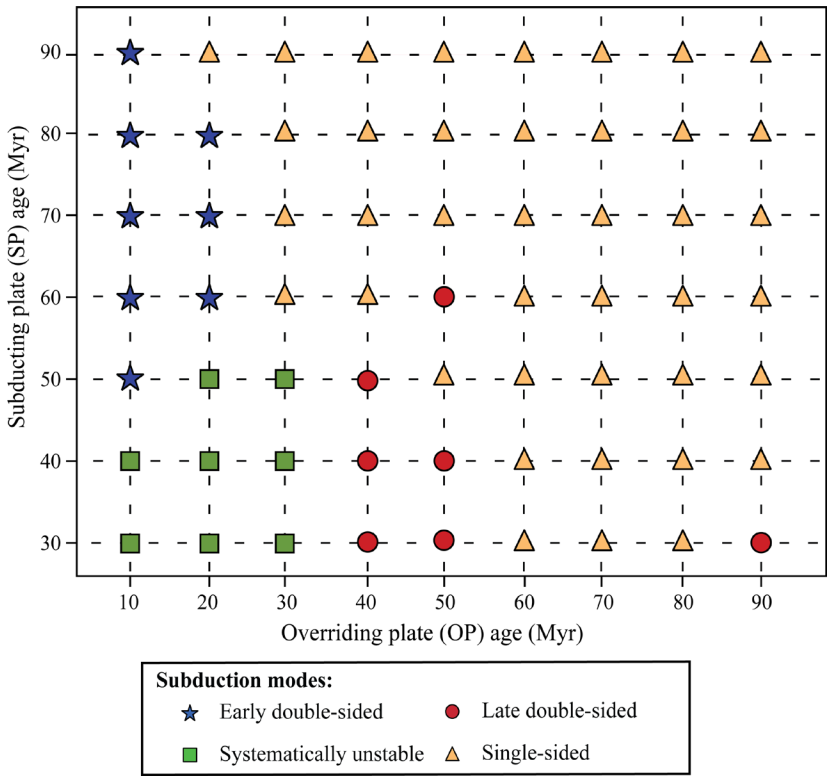

Figure 5.3 – Graphic description of the modelling space and the outcomes from the model runs. Blue stars represent early developed double-sided subduction zones, red circles late developed double-sided subduction zones, green squares the systematically unstable subduction zones, and yellow triangles the stable asymmetric single-sided subduction zones.

5.6. Evolution of the different subduction zone modes

5.6.1. Single-sided subduction (SS)

Stable single-sided asymmetric subduction (orange region in Figure 5.3 and detailed in Figure 5.4) – represents the most common outcome within the present modelling space, totalling 36 cases (ca. 57% of the total). Only minor differences in timing are observed in the results obtained for this subduction mode, which arise from different initial negative slab buoyancies as determined by their corresponding thermal ages.

Within this mode, the onset of subduction is marked by a period of trench retreat (or rollback) and an increase of the subducting plate velocity (V_{SP}), as the slab sinks into the mantle (Figure

5.4D and E). The final stages of this initial slab sinking, just before reaching the 660 km upper-lower mantle discontinuity, are marked by a brief period of trench forward motion (Figure 5.4A and D), with overriding plate being pushed towards the left side of the model (negative V_{OP}, Figure 5.4A and E). Once the slab hits the base of the upper mantle, it drapes above this discontinuity (Figure 5.4B), initiating trench rollback (Figure 5.4D) and producing a sharp decrease in subducting plate velocity (Figure 5.4E). After the initial draping (Figure 5.4C), V_{SP} continues to decrease at a slower pace, while V_{OP} remains relatively constant (Figure 5.4E). This deceleration of the subducting plate is the result of the limited width of the model and, thus, merely reflects the consumption of the subducting plate (see Supplementary Video 5.1).

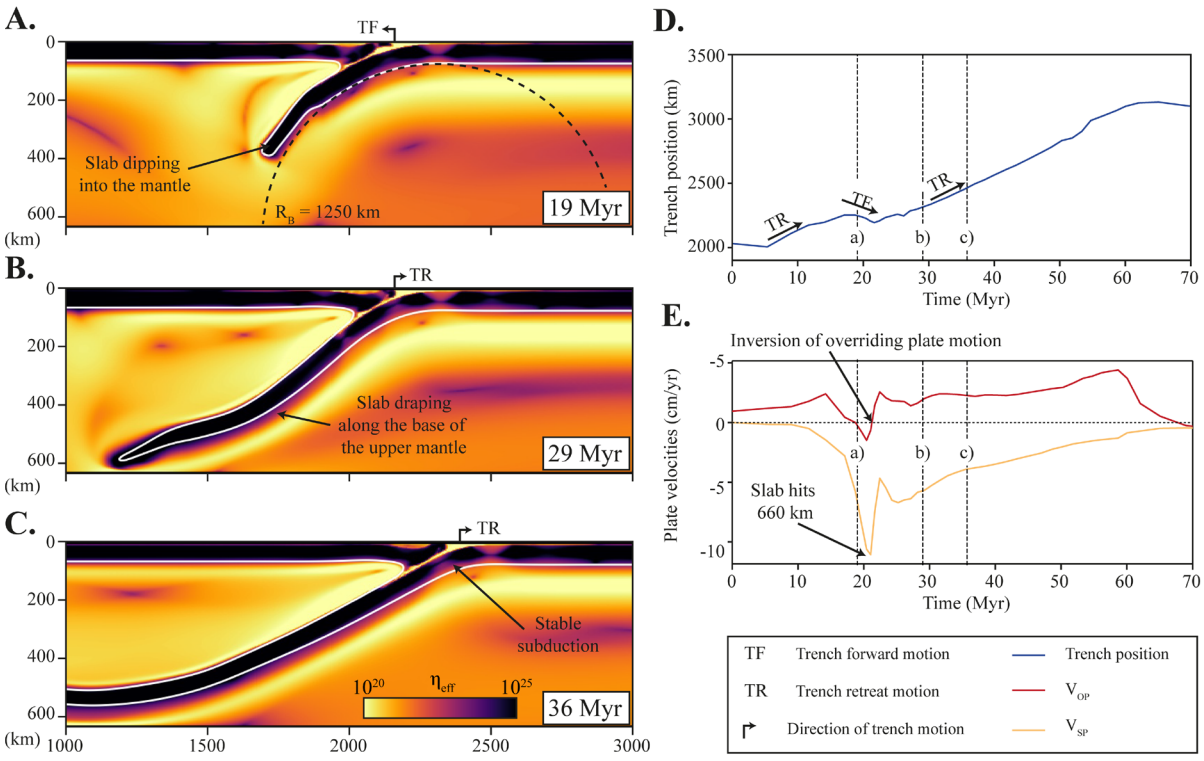

Figure 5.4 – Numerical model results: development of a stable asymmetric single-sided subduction zone (geometry, effective viscosity and trench motion shown for each stage). The cornered arrow in A-C shows the current direction of trench motion. **A.** Trench-forward motion induced by the sinking slab. The large bending radius of the slab minimizes the stress imposed on the overriding plate which helps to maintain it at the surface. **B.** Slab draping along the upper-lower mantle interface (at a 660 km depth). **C.** Continuous asymmetric single-sided subduction zone. **D.** Evolution of the position of the subduction trench over time. TF and TR stand for trench-forward and trench-rollback motions, respectively. **E.** Horizontal plate velocities as a function of time

for overriding plate (red curve) and subducting plate (yellow curve). The vertical dashed lines represent the position in time of the slices shown in A-C.

5.6.2. Systematically unstable subduction (SU)

The most unstable subduction zone mode occurs when the initial age of the overriding plate is lower than 40 Myr and the initial subducting plate age is lower than 50 Myr (green squares in Figure 5.3), which totals 8 cases (ca. 13% of the total). Under these initial thermal conditions, all models show a transient/intermittent occurrence of double-sided subduction, expressed by a systematic alternation between double- and single-sided subduction configurations (Figure 5.5 and Supplementary Video 5.1), separated by polarity reversal events.

In this mode, the subduction channel starts to closed from the initial stages of subduction, and the overriding plate is dragged downwards by the subducting plate (see Figure 5.5A), creating a temporary vertical double-sided subduction zone (see Figure 5.5B). This is marked by an inversion of V_{OP} (with the overriding plate being pushed towards the left), and by a subsequent increase of the V_{SP} (Figure 5.5E) The double-sided subduction zone is short lived, as the subducting plate is broken off from the remaining portion of the slab, reversing the original subduction polarity (Figure 5.5B-C, Supplementary Video 5.2). When the original overriding plate reaches the upper-lower mantle discontinuity and begins to drape (i.e., accumulate above the upper-lower mantle discontinuity, Schellart et al., 2007), this event sequence is repeated, with the original subducting plate being dragged downwards and triggering another double-sided subduction system (Figure 5.5D).

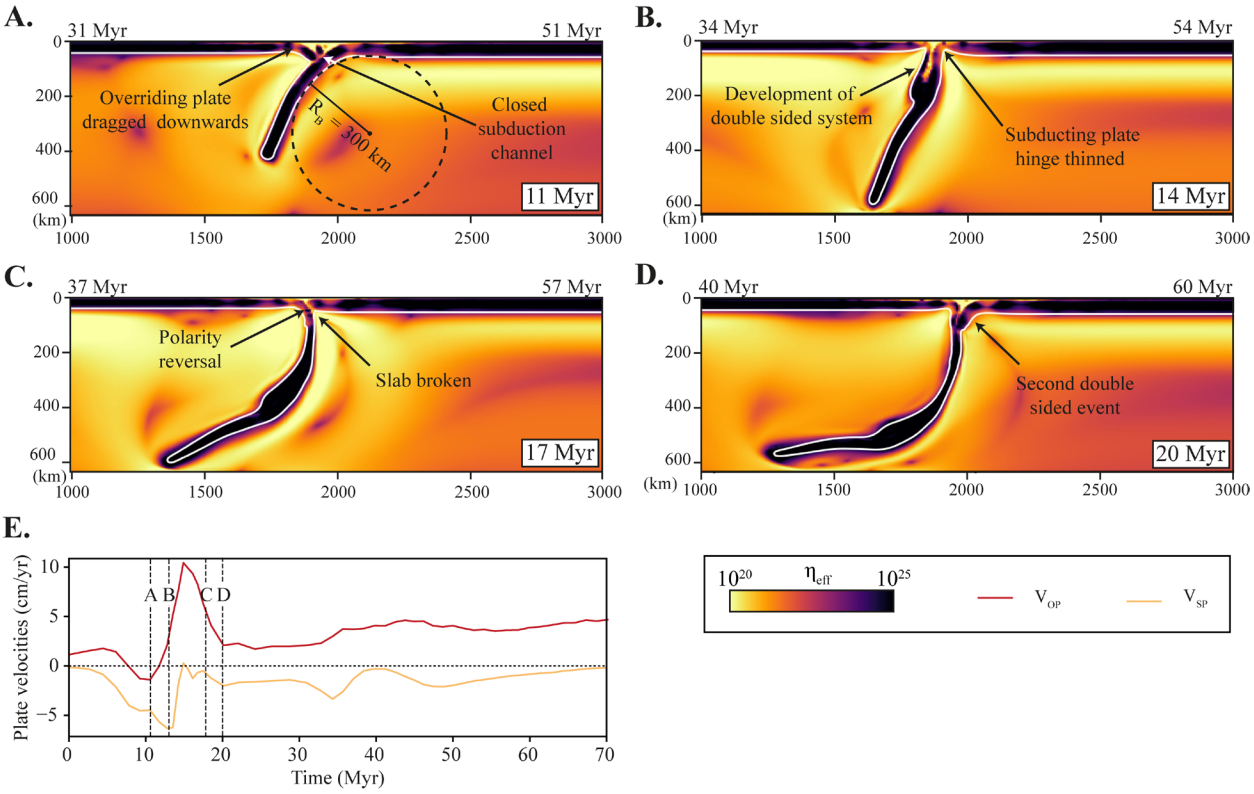

Figure 5.5 – Numerical model results: development of a systematically unstable subduction zone (geometry and effective viscosity shown for each stage). **A.** Closure of the subduction channel and drag of the overriding plate by the subducting plate. **B.** Development of a vertical double-sided subduction zone and thinning of the initial subducting plate hinge. **C.** Initial subducting slab break-off and spontaneous reversal of subduction polarity. **D.** Drag of the original subducting plate by the active subduction zone, triggering a second double-sided subduction event. **E.** Horizontal plate velocities as a function of time for overriding plate (red curve) and subducting plate (yellow curve). The vertical dashed lines represent the position in time of the slices shown in A-D.

5.6.3. Early developed double-sided subduction (ED)

If the initial thermal age of the subducting plate is significantly higher than the overriding plate (blue stars in Figure 5.3), the subduction zone quickly develops into an asymmetric double-sided subduction (Figure 5.6 and Supplementary Video 5.3). This unstable subduction mode was observed in 8 models, representing ca. 13% of the total.

During either the initial development of subduction or the draping of the slab, the subduction channel is closed, and the overriding plate is dragged downwards by the slab (Figure 5.6A-B), forming a stable asymmetric double-sided subduction. Similar to the previous cases, this is marked by an inversion of V_{OP} and an increase of V_{SP} (Figure 5.6D). This configuration is maintained until the end of the model, consuming both plates with similar velocities (Figure 5.6E).

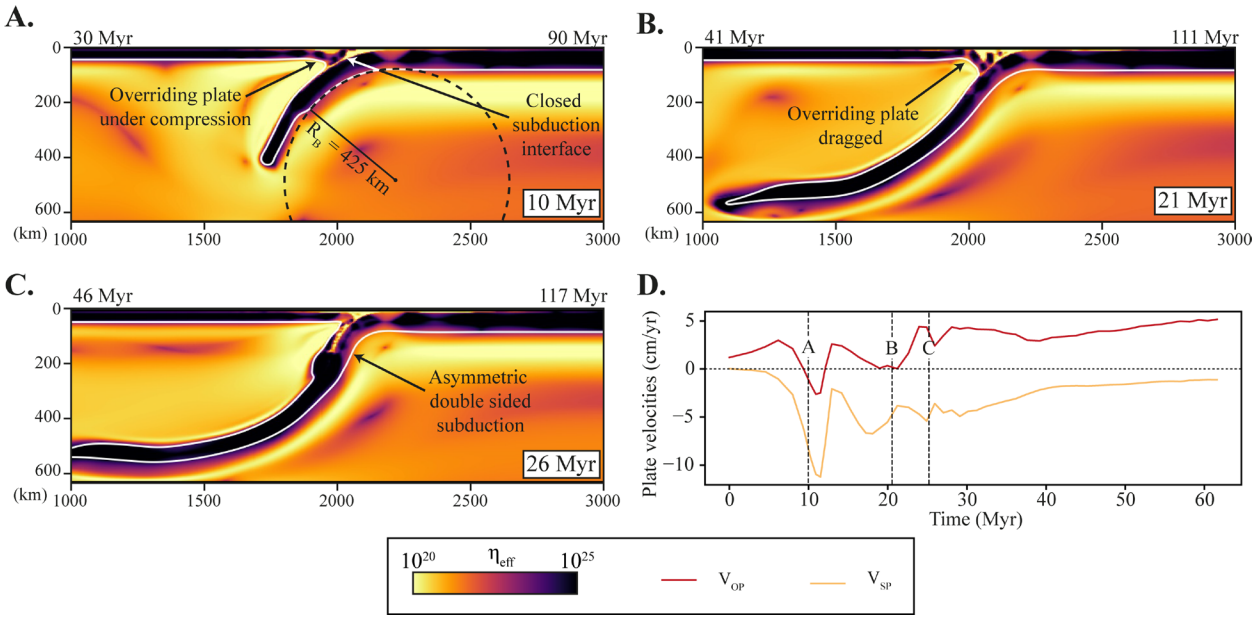

Figure 5.6 – Numerical model results: development of an early developed double-sided subduction zone (geometry and effective viscosity shown for each stage). **A.** Closure of the subduction channel and strong compression of the overriding plate. **B.** Drag of the overriding plate by the subducting slab. **C.** Development of a double-sided subduction zone, in which the asymmetry expresses the relatively higher strength of the subducting slab. **D.** Horizontal plate velocities as a function of time for overriding plate (red curve) and subducting plate (yellow curve). The vertical dashed lines represent the position in time of the slices shown in A-C.

5.6.4. Late developed double-sided subduction (LD)

If the initial thermal age of the overriding plate is similar to the subducting plate (red circles in Figure 5.3), and both plates are relatively young (initial ages below 60 Myr), the subduction zone develops into a long-lived, single-sided subduction zone, which later evolves into a vertical double-sided subduction system (Figure 5.7 and Supplementary Video 5.4). This unstable subduction mode was observed in 7 cases, representing ca. 11% of the total.

At the onset of slab draping, the subducting channel is closed, and the overriding plate is coupled with the slab (Figure 5.7A). However, unlike in previous case, the overriding plate is not immediately subducted, and instead is folded and thickened at the surface together with the subducting plate (Figure 5.7B). This plate accumulation event is accompanied by a severe decrease in the horizontal velocity of both plates (Figure 5.7E) and, once it reaches a critical point (e.g., a weight threshold), both plates collapse into the mantle (Figure 5.7C). The collapse evolves into a vertical double-sided subduction (Figure 5.7D), strongly accelerating the subduction system (Figure 5.7E). This configuration is maintained until the end of the model (see Supplementary Video 5.4).

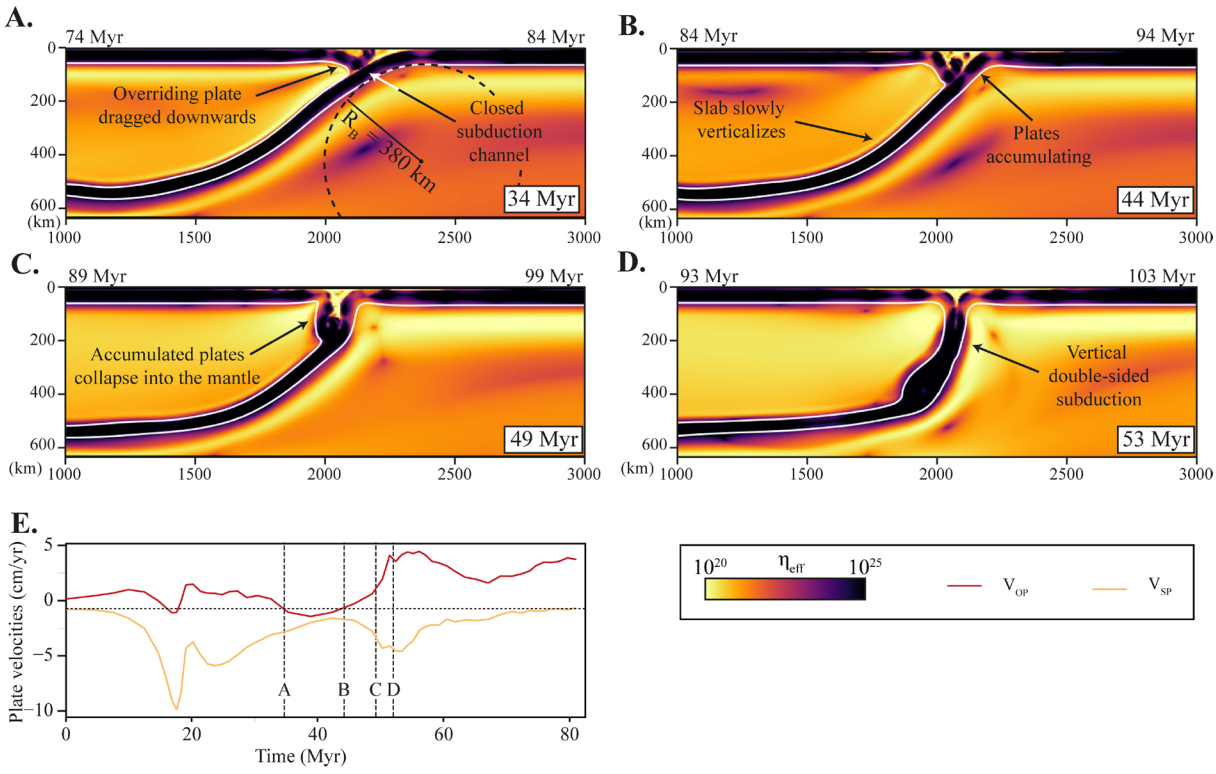

Figure 5.7 – Numerical model results: development of a late developed double-sided subduction zone (geometry and effective viscosity shown for each stage). **A.** Closure of the subduction channel at the onset of slab draping and slow drag of the overriding plate by the slab. **B.** Slow, yet continuous, convergence leads the overriding and subducting plates to bend an accumulate near the surface. **C.** The accumulation of plates near the surface becomes unstable and collapses into the mantle**. D.** Collapsed plates develop into a stable vertical double-sided subduction zone. **E.** Horizontal plate velocities as a function of time for overriding plate (red curve) and subducting plate (yellow curve). The vertical dashed lines represent the position in time of the slices shown in A-D.

5.6.5. Bending energy dissipation and timing of first instability

When the first manifestations of instability are observed (e.g., closure of the subduction channel and/or drag of the overriding plate by the slab), the age of the two plates reveals different stability fields of unstable subduction modes (see Figure 5.8):

1. SU is observed for models in which both plates are relatively young.
2. ED in models with a very young overriding plate (<30 Myr).
3. LD for cases in which the overriding plate is significantly older (>80 Myr).

Higher values of ϕ_{Be}/ϕ_{Bu} are observed in models with younger overriding plates, associated to the ED- and SU-type unstable modes.

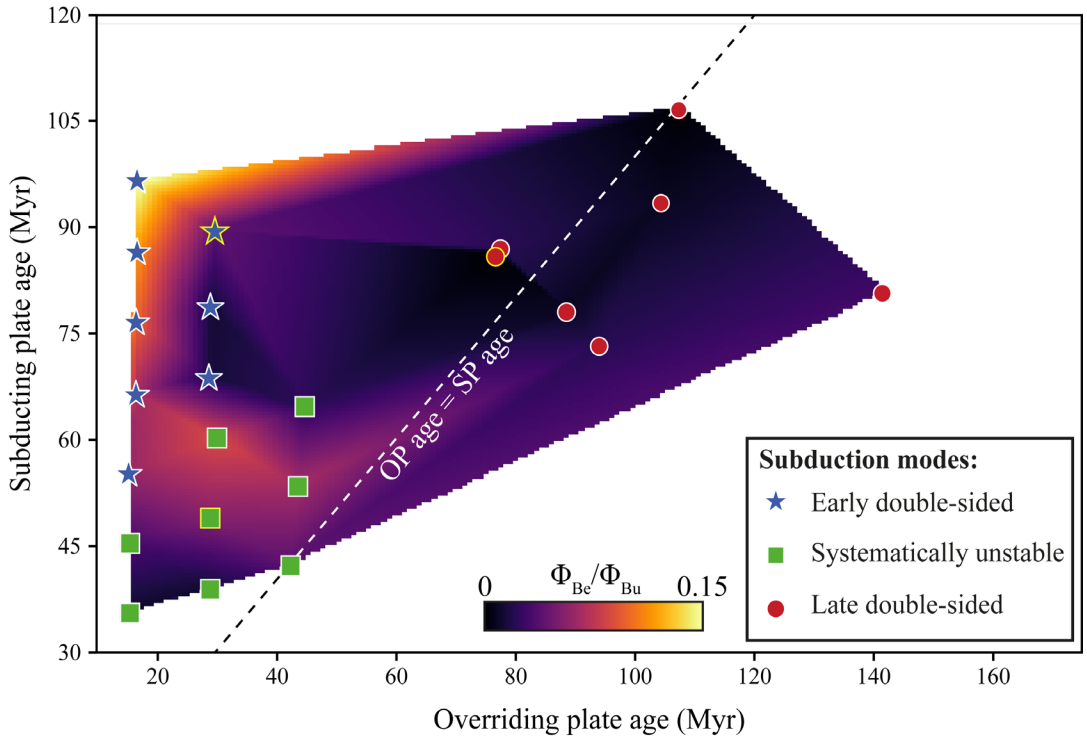

Figure 5.8 – Graphical overview of the different types of subduction zone instabilities formed as a function of ϕ_{Be}/ϕ_{Bu}. Blue stars represent early developed double-sided subduction zones, red circles late developed double-sided subduction zones, green squares the systematically unstable subduction zones, and yellow triangles the stable asymmetric single-sided subduction zones. The markers with yellow boundaries represent the models depicted in Figures 5.4-5.6.

5.7. Discussion

It has been established that the overall strength of an oceanic plate is directly proportional to its age (e.g., Gurnis, Hall and Lavier, 2004). Specifically, as plate age increases, so do its thickness and effective strength. Thus, older oceanic plates are increasingly harder to deform and/or to force into subduction initiation (Gurnis et al., 2004). This effect of plate age has not been fully explored in previous contributions to the study of the development of single- vs. double-sided subduction systems. Gerya et al. (2008) showed that the stability of a single-sided subduction system hinged on the presence of a weak zone above a strong subducting slab, in a set of models in which the older (thicker) plate was 100 Myr old and the younger (thinner) plate was 1 Myr old. The present modelling work expands on the plate age range adopted in Gerya et al. (2008), by systematically testing a wider set of overriding and subducting plate ages.

Furthermore, we assessed how the bending of the subducting slab can induce strong deformation of the overriding plate, and, by extent, trigger the formation of a double-sided subduction zone. It has been previously shown that plate strength has a direct impact on the bending radius of the slab (Irvine and Schellart, 2012), with stronger (older) plates showing larger bending radius. This larger bending radius has been previously correlated with a more efficient energy dissipation at the hinge of the subducting slab and a lower ϕ_{Be}/ϕ_{Bu}, Irvine and Schellart, 2012). A higher ϕ_{Be}/ϕ_{Bu}, implies a higher proportion of the potential gravitational energy associated with the slab being spent on bending the subducting plate, resulting in narrower bending radii which, in turn, implies a higher subduction dip and more pronounced overriding plate deformation (Schellart, 2008). In previous contributions (Irvine and Schellart, 2012), high ϕ_{Be}/ϕ_{Bu} was associated with young (weak) subducting plates, which is in disagreement with the results shown in Figure 5.8. While we suspect that this may derive from the presence of an overriding plate (not present in Irvine and Schellart, 2012), further modelling is required for a full explanation of these differences.

5.7.1. What renders a subduction zone unstable?

5.7.1.1. Systematically unstable subduction

The occurrence of SU-type subduction zones takes place when both intervening plates are very young, with the first signs of instability being observed shortly after the start of the model (see Figure 5.5). At this time, although the young subducting plates are already negatively buoyant, they are still relatively weak ($\eta_{SP}<10^{23}$ Pa.s, see Supplementary Figure 5.2).

Thus, as these young slabs sinks into the mantle, they develop small bending radii (see Figure 5.5) and steeper subduction angles (see Supplementary Figure 5.2), reflecting a higher proportion of the gravitational potential energy of the slab (i.e., its negative buoyancy) being dissipated by bending (see Figure 5.8; e.g., Irvine and Schellart, 2012; Schellart, 2009). As the trench is moved towards the overriding plate, the subduction channel is closed and, due to the strong overriding plate compression induced by the narrowly bent subducting slab, both plates are coupled together (see Figure 5.5A, e.g., Duarte et al., 2015).

While older overriding plates would be able to resist this temporary coupling process (perhaps undergoing subduction erosion to reopen the channel, e.g., Stern, 2011), the young overriding plates are too weak to resist being dragged by the coupled slab. Consequently, the two weak plates subduct together, developing into a nearly vertical double-sided subduction zone (see Figure 5.5B). The vertical subduction implies a narrow bend of both plates, which exerts strong stresses on their hinges. Eventually, one of the plates yields, triggering a slab-break off and reversal of original subduction polarity (see Figure 5.5C). However, in this specific case both plates are still weak after the polarity reversal. Thus, the subduction of the original overriding plate can induce the repetition of the same events leading to recurrent double sided and polarity reversal instabilities.

5.7.1.2. Early developed double-sided subduction

ED-type subduction zones occur when an older (>55 Myr) subducting plate interacts with a very young (<30 Myr) overriding plate. In this subduction mode, instabilities are developed under a small bending radius (see Figure 5.6) and high values for ϕ_{Be}/ϕ_{Bu} (see Figure 5.8).

The first signs of instability are generally seen either during or just before the onset of slab draping above the upper-lower mantle discontinuity (see Figure 5.6A). During the former, the overriding plate is affected by strong horizontal compression (see Figure 5.6), induced by the advancement of the subduction trench (e.g., Schellart, 2008). During the latter, the trench is retreating towards the slab, which induces overriding plate extension (e.g., Schellart, 2008). In either case, due to the narrow bending radius of the subducting slab (see Figure 5.6A) and continued convergence (see Figure 5.6D), the friction along the subduction channel increases and it closes (see Figure 5.6B), coupling the two plates together (e.g., Duarte et al., 2015).

Once the subduction channel is closed, and in similarity with the previous section, the still young (and weak) overriding plates are unable to resist being dragged by the slab (see Figure 5.6B) and, consequently, the two plates subduct together. However, as the subducting slab is significantly stronger, no further instabilities occur, resulting in the development of a stable asymmetric double-sided subduction zone (see Figure 5.6C).

5.7.1.3. Late developed double-sided subduction

The development of LD-type subduction zones (see Figure 5.7) occurs (mostly) in models in which the initial age for both overriding and subducting plates is between 40 Myr and 60 Myr. Although the subduction initially develops into a seemingly stable asymmetric single-sided subduction, a double-sided subduction is triggered much later in the model (see Figure 5.7C). This result is relatively counter-intuitive, as old oceanic lithosphere (e.g., >80 Myr) has been

demonstrated to be both hard to bend and unlikely to initiate subduction (e.g., Almeida et al., 2022; Gurnis et al., 2004).

As in all previous unstable subduction modes, the first signs of instability are marked by the closure of the subduction channel (see Figure 5.7A) and drag of the overriding plate by the slab (see Figure 5.7B). However, in LD-type subduction zones the bending energy dissipation rate is lower than in the previous cases (see Figure 5.8), indicating that it is not a significant energy dissipation mechanism. What was instead observed in these models, was a progressive deceleration of the subducting plate (see Figure 5.7E) during slab retreat and that, eventually, due to the lack of movement (see Supplementary Video 5.3) the subduction channel is sealed (see Figure 5.7A). The reason behind slab deceleration is unclear, but one possible reason might be the aging and progressive stiffening of the portion of the slab which remains at the surface. As the slab ages, its more trench-distal portions become harder to bend and, upon arriving at the trench, could induce a sudden lock of the subduction system and leading to the sealing of the subducting channel. Alternatively, it could derive from higher friction along the subduction channel, induced by an increase of the contact area between the overriding and subducting plate, resulting from the shallower subduction dips (see Supplementary Figure 5.2).

Despite the sealed subduction channel, the slab beneath continues to sink into the mantle, imposing a slow convergence on the subduction system, and forcing the accumulation of both plates at the surface (see Figure 5.7B). Contrarily to the previous subduction modes, as both overriding plate and subducting plate are old (see Figure 5.8) and have similar effective strengths, neither yields to allow for the immediate formation of an asymmetric double-sided subduction. Instead, over time, this accumulated plate mass catastrophically collapses into the mantle, quickly accelerating the system (see Figure 5.7E) and developing into a symmetric double-sided subduction. The symmetric double-sided event is similar to the one described in SU-type subduction zones and is has been previously been associated to unstable subduction systems with two similarly strong plates (e.g., Gerya et al., 2008).

There is a further possibility that this subduction mode may correspond to a model artefact, derived from the lack of a stabilizing buoyant arc and/or free surface conditions (this is discussed in section 5.8).

5.7.2. Why do subduction zones remain single-sided?

Under the present modelling conditions, SS-type subduction is the more common outcome (see Figure 5.3), representing over half of all model results. So why do these subduction zones never develop any form of instability?

As was discussed in the previous sections, the development of an unstable subduction begins with the drag of the overriding plate by the subducting slab, as the result of closure of the subduction channel (see Figure 5.5 and Figure 5.6), which results from the steep subduction dip (and increased friction) or by a deceleration of the convergence. Thus, to prevent double-sided subduction we need to ensure that both the subduction channel is maintained and that the overriding plate remains at the surface.

Regarding the first condition – maintaining a weak subduction channel – it has been previously shown that the dissipation of energy associated with the negative buoyancy of the slab by bending is more efficient in older subducting plates (e.g., Irvine and Schellart, 2012; Schellart, 2009). As the subducting slab bending radius increases, the compression imposed on the overriding plate decreases which, in turn, helps lower the friction along the subduction channel, preventing its closure and subsequent formation of double-sided subduction zones. We argue that stabilization induced by larger subducting slab bending radii explains the formation of stable asymmetric single-sided subduction zones in models with very young overriding plates. This mechanism mirrors the conclusions of Gerya et al. (2008), in which the stability of single-sided subduction zones is attributed to a strong subducting plate, which according to our results, would maintain a permanent weak subduction channel.

Regarding the second condition – preventing the subduction of the overriding plate – an additional stabilization mechanism is required. Our results show that any subduction zone instability is formed during either the onset of subduction (Figure 5.6) or during the initial stages of slab draping (Figure 5.7), due to the drag of the overriding plate. Thus, to prevent double-sided subduction, the overriding plate needs to be strong enough not to be deformed. This is crucial in models with a young subducting plate (<50 Myr), in which the narrow slab bending radius would impose strong deformation on the overriding plate. In these cases, only with a strong overriding plate (>60 Myr) can we obtain stable single-sided subduction.

This stabilization mechanism adds to the one discussed in Gerya et al. (2008), highlighting the need for both a strong overriding and strong subducting plate, separated by a constantly weak subduction channel.

5.8. Model limitations

Our models aim to expand the knowledge on the stability of single-sided subduction zones on Earth, arising from the internal force balance of a pre-existent subduction zone. However, any geodynamic model must assume some degree of simplification (see van Zelst et al., 2021 for an extensive discussion on the topic). These simplifications constitute limitations of the modelling approach, which we address here to outline the potential constraints of our conclusions:

1. Our models were run under 2D conditions. Natural subduction zones are inherently three-dimensional, and are governed by dynamics that include trench-parallel toroidal components of mantle flow (Schellart, 2004a; Schellart et al., 2007). Thus, our approach underestimates the available mantle flow, which could result in a significant deviation from the conditions which govern the stability of a subduction zone on Earth.
2. Our modelling setup does not account for elasticity. The absence of elasticity is a widely adopted approach in many other modelling studies (Capitanio and Morra, 2012; Gerya and Meilick, 2011; Schellart, 2017b; Stegman et al., 2010). However, it is expected that including elasticity would influence the dynamics of plate bending and unbending at the

hinge by improving the bending energy dissipation (e.g., Farrington et al., 2014). Thus, our results may represent an overestimation of the stability fields for the development of double-sided subduction zones.

3. Our models are run under free-slip conditions. In previous contributions, Crameri et al. (2012) and Crameri and Tackley (2015) suggested that double-sided subduction zones could mostly represent model artifacts, resulted from the use of free slip conditions. They argued that the simulation of a long-lived asymmetric single-sided subduction zone would require the use of free surface models, i.e., with a low viscosity top layer with water- or air-like density which allows for topography to develop in the model. Thus, under these boundary conditions, the folding of the overriding plate can be partly accommodated by surface relief. Conversely, the here used top free slip conditions would only allow the overriding plate to bend downwards, which would tend to favour the development of a double-sided subduction zones (Schmeling et al., 2008). However, it has been previously shown that the formation of a double-sided subduction zone is possible under top free surface conditions (see Chapter 4, Almeida et al., under review). Further modelling work is required as to ascertain the influence exerted by a free surface on the formation of double-sided subduction zones.
4. Different upper mantle rheological parameters could have been used. There is a degree of uncertainty regarding upper mantle rheology (e.g., Jain and Korenaga, 2020; King, 2016, and references therein) that allows for our choice of parameters, relatively to which the obtained results are expected to be sensitive. This means that a slightly different choice of mantle rheology parameters corresponding, for instance, to an increase in mantle stiffness, could potentially increase the viscous resistance to slab-pull and/or to subduction, modifying the underlying governing dynamics of the system and potentially leading to considerably different results.
5. There is no buoyant magmatic volcanic arc on the overriding plate. This simplification has been assumed in many previous studies (Gerya et al., 2008; Gurnis et al., 2004; Lu et al., 2015). To our knowledge, the role of volcanic arcs in the stability of a subduction zones has not yet been systematically investigated. However, all present-day overriding

plates on Earth show both a forearc and a magmatic arc, which represent stronger, more positively buoyant portions of oceanic lithosphere, which can act as stabilizers (as discussed in Chapter 4, Almeida et al., under review). Both structures are unlikely to be subducted and, therefore, could help prevent the development of any double-sided subduction zone. Nevertheless, further modelling is required to assess the impact of a buoyant magmatic arc on the development of double-sided subduction zones.

5.9. Conclusions

The present study aimed to explore the stability of single- and double-sided subduction zones derived from the effective strength of the overriding and subducting plates which, in this case, was a function of their initial thermal age. Under the present modelling conditions, our results show that:

1. Double-sided subduction occurs mostly for situations in which the overriding plate is young and, therefore, both weak and thin enough to be subducted. The specific type of double-sided subduction mode obtained is a function of the relative age contrast between the overriding and subducting plates.
2. With an increase of the overriding plate age, the overriding plate becomes strong enough not to bent, rendering single-sided subduction possible.
3. Unstable subduction zones can develop for any tested subducting slab age but are less prevalent in models with older subducting plates.

5.10. Supplementary Material

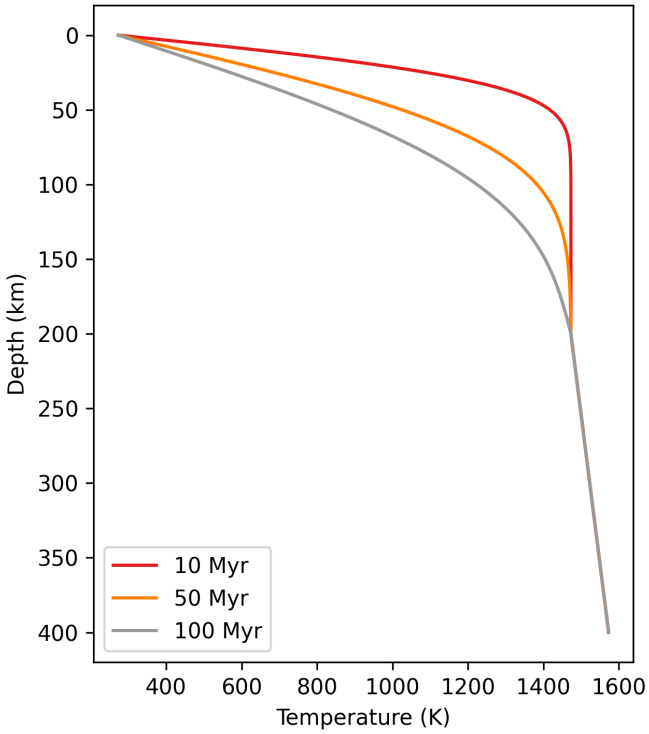

Supplementary Figure 5.1 – Initial temperature-depth profiles for different initial plate ages.

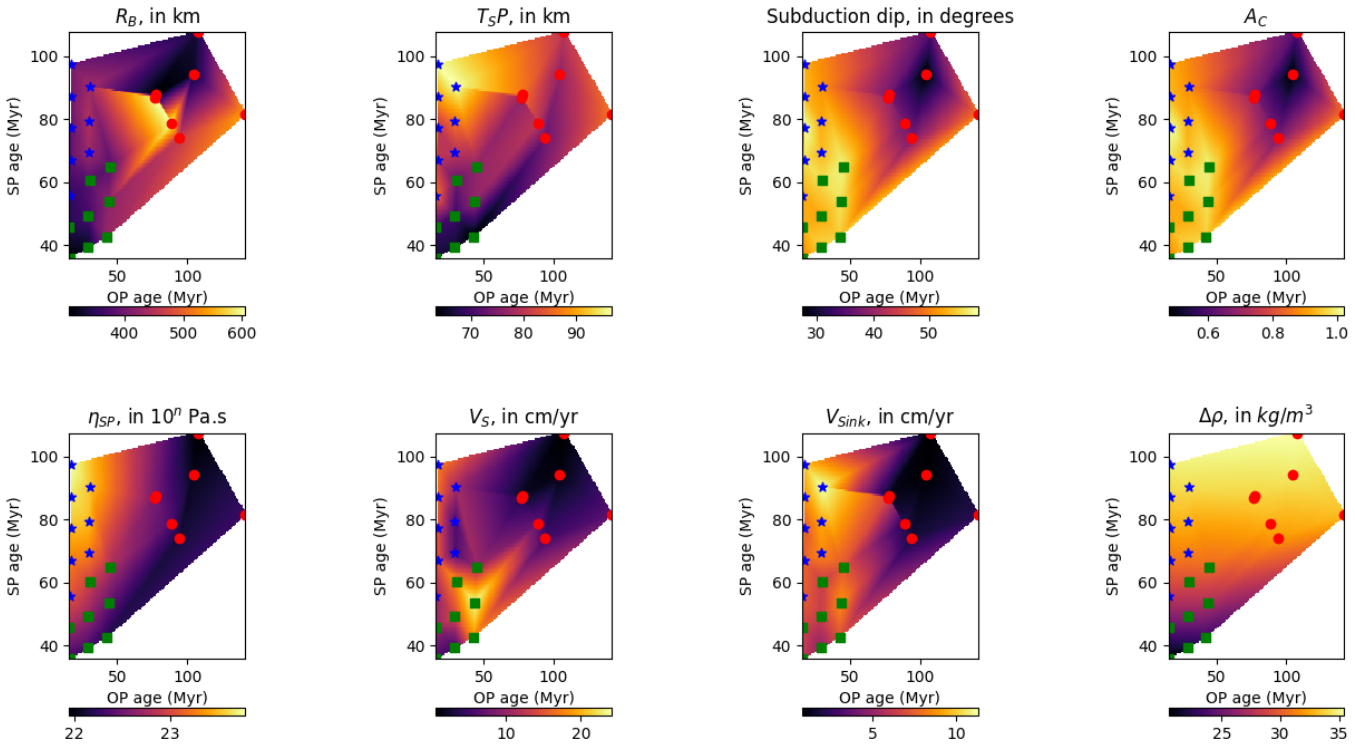

Supplementary Figure 5.2 – Parameters measured when the first signals of subduction zone instability were detected. *First row, from left to right*: R_B - bending radius of the subducting slab; T_{SP} – maximum thickness of the subducting plate; α – shallow subduction angle; and A_C – ratio between the length of the subducting plate hinge and the bending radius. *Second row, from left to right*: η_{SP} – effective strength of the subducting plate; V_S – subduction velocity; V_{Sink} – sinking velocity of the subducting slab; and Δρ – density contrast between the subducting slab and the surrounding upper mantle.

5.11. Supplementary Videos

The supplementary videos for this paper can be found in Appendix E of this thesis.

Supplementary Video 5.1 – Video file that shows the evolution of the single-sided subduction zone model. In this model, the overriding plate and subducting plate are 70 Myr old.

Supplementary Video 5.2 – Video file that shows the evolution of formation of the systematically unstable subduction zones. In this model, the overriding plate is 20 Myr old and subducting plate is 40 Myr old.

Supplementary Video 5.3 – Video file that shows the evolution of formation of the late developed double-sided subduction zones. In this model, the overriding plate is 70 Myr old and subducting plate is 30 Myr old.

Supplementary Video 5.4 – Video file that shows the evolution of formation of the early developed double-sided subduction zones. In this model, the overriding plate is 20 Myr old and subducting plate is 80 Myr old.

Chapter 6. Concluding works and future research

(this page has been left intentionally blank)

6.1. Key findings

The research carried out in this thesis aimed at gaining new insight on the process of subduction initiation by polarity reversal, a mechanism previously explored mostly as the result of field and plate reconstruction studies (e.g., Konstantinovskaia, 2001; Pysklywec, 2001; Mann and Taira, 2004; Phinney et al., 2004). To my knowledge, the present thesis represents the first systematic exploration of polarity reversal SZI by plateau collision, conducted using state-of-the-art 2D and 3D self-consistent numerical modelling techniques. Crucial variables such as the initial plate age, dimension of the colliding oceanic plateau, and the presence/absence of a volcanic arc on the overriding plate were systematically tested, as to assess their impact on the formation of a new subduction zone. The results of this work suggest that polarity reversal SZI is not only geodynamically viable but that it can also be triggered without an external forcing (such as pre-imposed convergence). This suggests that it may be more important to the formation of subduction zones in nature than previously anticipated.

During the development of this thesis, research was initiated which aims to clarify the underlying dynamic constraints behind the development of single- or double-sided subduction zones in nature. By employing 2D self-consistent numerical modelling techniques and systematically testing the initial overriding/subducting plate age configurations, we have so far explored the effects of effective plate strength on the development of subduction zone instabilities. Although this represents presently ongoing research, the preliminary results suggest that, under free slip conditions, single-sided subduction requires not only a strong subducting slab and weak interface (e.g., Gerya, Connolly and Yuen, 2008) but also a strong overriding plate, which is able to resist the stress imposed by the onset of subduction and/or slab draping.

Although the major conclusions of this work have been discussed and highlighted in chapters 3 to 5, the following sub-sections consist of a concise, integrated overview of these findings.

6.1.1. Polarity reversal SZI

In Chapter 3, by systematically changing the initial overriding/subducting plate age configuration, it was shown that the occurrence of a polarity reversal event was favoured by the

acting of old subducting plates onto relatively young overriding plates. However, as the overriding plates become older, the force required to bend them inevitably becomes greater than the one generated by the collision with the plateau. In this situation, the collision shuts down the subduction system, and the plateau is accreted to the overriding plate. Furthermore, under 2D conditions, polarity reversal hinged on an efficient overriding-subducting plate coupling during the collision of the plateau, in such a way that the original slab dragged the overriding plate and triggered its subduction.

The work conducted in Chapter 3 allowed for the demonstration that polarity reversal was a dynamically viable SZI mechanism which, under 2D conditions and top free slip, could occur in the absence of any external forcing or kinematically imposed conditions. In other words, these events could transpire merely as the result of the evolving force balance implied by an ongoing subduction system as the result of a plateau collision event. Despite this demonstration, these results presented some fundamental limitations which could preclude their strict applicability to natural cases, such as:

1. As no topography could be formed due to top free slip conditions, all stress imposed on the overriding plate could only be accommodated by bending the plated downwards.
2. The 2D nature of the models implied the complete disregard for the inherent 3D nature of mantle flows (specifically the trench-parallel toroidal flow).
3. The natural elastic behaviour of the crust was not included in the model, the effects of which had been demonstrated to affect the bending/unbending dynamics of a subducting slab.

All issues were solved in Chapter 4, in which the geodynamic constraints behind polarity reversal SZI were explored using self-consistent 3D free surface viscoelastoplastic numerical models. Using these techniques, it was not only possible to accommodate the 3D nature of subduction-induced mantle flows but also to prevent the enhanced slab deformation which derived from the use of top free-slip conditions. The models employed further included a buoyant magmatic arc, which had been not included in the previous runs and would likely limit the occurrence of double-sided subduction. Under these conditions, it was shown that the age

contrast between the overriding and the subducting plates controlled the efficiency of polarity reversal SZI such that:

1. Older (denser) subducting plates accelerate the formation of the new subduction zone, and
2. Younger (weaker) overriding plates tend to delay the formation of the new subduction zone.

Although this conclusion might seem conflicting with the results discussed in Chapter 3 (in which young overriding plates were associated with double-sided subduction), it was demonstrated in this chapter that presence of a buoyant magmatic arc on the overriding plate was fundamental to its stability. All models ran without this stabilizing arc led to the immediate formation of the double-sided subduction zones during plateau collision, complying with results from the previous chapter.

Furthermore, under 3D conditions, it was observed that the energy available to generate a new subduction zone was inversely proportional to the along-trench width of the colliding oceanic plateau. In fact, narrower oceanic plateaus were shown to be more efficient at triggering a new subduction zone during a collision. During a collision with a narrow plateau, all the energy available from the original subducting plate is focused along a much narrower area, leading to a more efficient bend and subduction of the overriding plate. Conversely, as the width of the plateau increases, this efficiency is reduced. Whilst the effective slab-pull in the progressively narrower active subduction zone increases, the area which must undergo subduction initiation is now also much wider. Eventually, the effective slab-pull of the narrow active subduction zone will not be enough to trigger the subduction of the overriding plate along the wider plateau-collision front, leading to the break-off of the slab attached to the plateau, and to its accretion to the overriding plate.

Under these 3D self-consistent modelling conditions, a polarity reversal always follows the same event sequence. As the plateau collides with the overriding plate, the slab is broken-off, producing a local termination of the subduction zone. Simultaneously, the buoyant magmatic arc is thrusted above the overriding plate due to the collision. As the subduction zone continues laterally, the continued convergence continues to force the magmatic arc further and further into the overriding plate, forcing it to bend and sink into the mantle. Upon reaching a critical

depth (ca. 200 km), its negative buoyancy takes over, initiating a self-sufficient subduction and completing the reversal of polarity. As both subduction systems evolve and their trenches retreat, the area between them undergoes extension, forming a basin, which can later evolve into a ridge. One natural example in which this sequence might have occurred was the late Miocenic collision of the Ontong-Java Plateau with the Australian plate and the subsequent formation of the Solomon-Vanuatu subduction zone.

Finally, and equally as relevant, this work has also shown that modelling of polarity reversal subduction zone initiation is highly resolution dependent. As most modelling codes do not yet account for phase changes and two-phase flow (e.g., simultaneous fluid and solid flow), it was important to develop a strategy which accounts for the weak subduction zone interface in self-consistent models. In both Chapter 3 and 4, our solution was the implementation of two-cell thick weak oceanic crusts which act as the subduction interface. However, this approach has a direct impact on the effective strength of the plates. As the resolution is increased, we directly reduce the thickness of the weak crustal layer (always two-cell thick), and proportionally increase the thickness of the stronger lithospheric mantle layer. Thus, as resolution increases, so does the ratio between the thickness of the strong lithospheric mantle and the weak oceanic crust proportionally increase, effectively increasing the strength of the plate. Due to this strong interplay between resolution and effective plate strength, it is fundamental to conduct extensive resolution testing to ensure that results are convergent.

6.1.2. Subduction zone stability: single-sided vs. double-sided

The work discussed in Chapter 5 represent ongoing research, in which we aimed to expand the previously tested range of overriding/subducting plate ages (1 Myr overriding and 100 Myr subducting plates, Gerya et al., 2008) regarding the formation of single- and double-sided subduction zones. To this extent, we systematically changed the initial overriding and subducting plate ages, ranging from 10 Myr to 90 Myr and 30 to 90 Myr, with increments of 10 Myr respectively. All models were conducted using 2D self-consistent free slip subduction zone models.

The results discussed in Chapter 5 suggest that the development of a double-sided subduction zone is determined by the existence of, at least, one young (<60 Myr) plate in a subduction system. Furthermore, they show that the occurrence of single-sided subduction requires not only a strong subducting plate and a consistently weak subduction channel (as demonstrated in Gerya et al., 2008) but also a strong overriding plate which can withstand the stresses imposed by onset of subduction and/or slab draping.

Finally, the specific type of unstable subduction mode developed (i.e., early/late double-sided subduction or systematically unstable subduction) relies on the efficiency of the energy dissipation at the hinge of the slab. Younger subducting slabs, with narrower bending radius, impose strong overriding plate deformation which, depending on the strength of the latter plate, could lead to the swift development of symmetric or asymmetric double-sided subduction zones. Furthermore, young overriding plates might be unable to resist even the slight deformation imposed by an older subducting plate (with a wider bending radius), which also results in the swift formation of an asymmetric double-sided subduction zone.

6.2. Future research

6.2.1. Future research in polarity reversal subduction zone initiation

In this work, we aimed to explore the first-order geodynamic constraints governing polarity reversal subduction zone initiation. Despite the extensive exploration of the thermal age contrast and the different along-trench width of the colliding oceanic plateaus, a full understanding of this fundamental SZI mechanism problem still requires further extensive research.

6.2.1.1. Subduction zones can be oblique

In this work, we assumed that the modelled subduction zones had no obliquity, i.e., that the convergence was strictly orthogonal to the trench. While this is a relatively standard simplification in subduction zone modelling (e.g., Stegman, Farrington and Capitanio, 2010; Moresi et al., 2014; Pusok, Kaus and Popov, 2018; among others), obliquity has been shown to

fundamentally alter subduction zone dynamics (e.g., Malatesta et al., 2013, 2016). For the present case, this implied that the collision of the oceanic plateau was orthogonal to the trench, unlike what is known to occur in many natural examples. According to the available plate reconstructions (e.g., Mann and Taira, 2004; Schellart, Lister and Toy, 2006), even the discussed example of the Ontong-Java Plateau is thought to have approached the Australian plate at an angle of ca. 30 degrees. As most subduction zones might be characterized by some degree of obliquity (Figure 1.7), more extensive research is necessary to assess its effect on polarity reversal SZI.

6.2.1.2. There is a diverse range of possible colliding blocks

In previous chapters, all simulated colliding blocks were assumed to be LIP-derived oceanic plateaus, corresponding to volcanically overthickened portions of oceanic lithosphere, with a felsic to intermediate (i.e., positively buoyant) crust. In nature, exotic terranes have a wide variety of origins (e.g., Tetreault and Buiter, 2014), which include island arcs, submarine ridges, seamounts, or even fragments of continental lithosphere, all with different dimensions, geometries and rheological configurations. As an example, an extinct mid-ocean ridge may represent a neutrally buoyant, overthickened portion of lithosphere, which in an intra-oceanic subduction setting is as strong as the subducting and overriding plates. The effect on polarity reversal SZI of considering colliding blocks of different natures (i.e., with different rheologies) is still considerably unknown. Further research is thus required to assess its potential impact, which would further allow us to expand on the dynamics of other on-going exotic terrane collisions in the Pacific (Figure 1.7).

6.2.1.3. Natural colliding blocks have complex geometries

The geometry of the colliding block is also not fully explored in the present work. Natural exotic terranes show complex geometries with irregular contours, variable thicknesses, and topographies (e.g., Tetreault and Buiter, 2014), none of which are explored in the present thesis. The geometry of the simulated oceanic plateaus discussed in previous chapters was always prismatic and, under this simplification, it was shown that the along-trench width of the

colliding block exerts a strong control on the efficiency of polarity reversal SZI. However, our simplified geometry implies the along-trench width of the block is constant along the trench-normal direction (i.e., a prismatic shape).

Assume now a more complex geometry, such as the one observed in the Bentham Rise (see Figure 1.7), in which the colliding block becomes wider away from the trench. Under such a scenario, it would be expected that once the subduction of the overriding plate has been triggered, the progressive widening of the colliding block would cause a gradual reduction of the available slab pull (by forcing the termination of a wider portion of the slab). This would, in turn, limit the force available to continue nucleating the new subduction zone. While there is a possibility that the newly formed subduction zone would simply continue to propagate laterally, this loss of slab pull could also imply its early termination and the accreation of the colliding block. This shift in collision dynamics caused by a progressive widening of the colliding block has not been modelled and could represent a fundamental resistance to polarity reversal SZI in natural settings.

6.2.1.4. Natural oceanic overriding plates are weakened by regional metamorphism and faulting

A variable which is entirely unexplored in this manuscript is the state of deformation of the overriding plate, and its impact on polarity reversal SZI. In all shown models, the overriding plate was considered pristine, i.e., undeformed, without any inherited structure and unaffected by regional metamorphism. However, as discussed in Chapter 1, natural oceanic plates of any age are affected by various degrees of regional metamorphism (such as serpentinization, e.g., Searle and Escartín, 2004), which reduces their effective strength. As shown in Chapters 3 and 4, weaker overriding plates are more prone to undergo subduction initiation and, consequently, chemical/physical weakening of the overriding plate represents an unexplored facilitating mechanism for polarity reversal SZI. Furthermore, as oceanic plates are affected by pervasive lithospheric scale fracturing such as active, or inactive transform faults (Hensen et al., 2019), it is likely that these would be present in the overriding plate. During a collision event, one possibility is that these weaknesses could act as stress guides, contributing to the propagation or nucleation of the new subduction zone. Alternatively, the stress induced by the collision

event could be dissipated by lateral displacement, hindering any attempt to initiate subduction. Thus, further modelling is required to assess whether the presence of a transform fault, and its angular relationship with the collision direction, could act as a facilitating or resisting mechanism for polarity reversal SZI.

6.2.1.5. The rheology of the upper mantle is poorly constrained

As discussed in Chapter 3, the rheology of the upper mantle is not fully constrained. At present, the values for the rheological parameters used in most numerical modelling approaches are based on experimental mechanical studies of peridotites and olivines (e.g., Escartín et al., 2001; Hui et al., 2014). Within the experimentally obtained range of values, modellers often adjust the parameters as to obtain realistic plate velocities. However, a slight variation within the range of admissible parameters for the rheology of mantle could lead to markedly different outcomes. A stronger upper mantle rheology would likely result in a more efficient localization of the deformation which could strongly favour the development of polarity reversal SZI. Simultaneously, a stronger upper mantle would also directly imply a higher viscous resistance to the slab-pull forces, which increases the resistance to bending and would likely hinder the development of a new subduction zone. These complex, non-linear, effects of upper mantle rheology require further modelling to assess their exact impact on subduction zone dynamics and, specifically, on polarity reversal SZI.

Additionally, as shown in Chapter 3, there is a likelihood that, during a collision event, a portion of the oceanic plateau is thrusted above the overriding plate. As the new subduction is formed, this remnant of colliding block remains at the surface, emplaced above the arc, representing an overthrusted sequenced of oceanic lithosphere. While this is unrelated to subduction zone initiation, to my knowledge, this overthrusting of oceanic lithosphere has not yet been explored in the context of intra-oceanic subduction zones.

6.2.2. Future research on subduction zone stability

During this thesis, a systematic investigation of the geodynamic constraints which govern the stability of single-sided subduction zones under top free slip was initiated. However, as

previously stated, it represents ongoing research and, thus still requires further modelling and analysis.

6.2.2.1. The models were run under free slip conditions

The models shown and discussed in Chapter 5 were run entirely under free slip conditions. Although this is a standard approach in geodynamical modelling, previous contributions to the topic (e.g., Crameri et al., 2012; Crameri and Tackley, 2015) have suggested that double-sided subduction zones could represent artifacts deriving from the use of these conditions. Although free surface is expected to hinder the spontaneous subduction of the overriding plate, the discussion surrounding the presence/absence of a volcanic arc in Chapter 4 showed a consistent occurrence of double-sided subduction. This suggests that the fundamental reasons behind double-sided subduction remain elusive and further research is required. Nevertheless, by replicating the overriding/subducting plate age configuration which resulted in the formation of late-developing double-sided subduction under free surface conditions we aim to assess its influence.

6.2.2.2. The rheology of the upper mantle is poorly constrained

Similar to what was discussed in the previous section concerning polarity reversal SZI, the uncertainty regarding the exact rheology of the upper mantle could also affect the development of double-sided subduction zones. Following the same example, a stronger upper mantle would result in a more efficient stress localization which could preclude the closure of the subduction zone interface and, consequently, prevent the formation of double-sided subduction. Thus, an extensive exploration of the rheological parameters of the upper mantle is paramount to the understanding of the underlying conditions which can maintain a single-sided subduction zone.

6.2.2.3. No elasticity has been implemented

The models shown in Chapter 5 were run under viscoplastic conditions. While the absence of elasticity is a widely adopted approach in many other modelling studies (Capitanio and

Morra, 2012; Gerya and Meilick, 2011; Schellart, 2017b; Stegman et al., 2010), the results obtained in Chapter 5 show that the bending of the slab and the corresponding dissipation of energy at the hinge of the slab are fundamental for the development of subduction zone instabilities. Elasticity has been shown to severely improve the bending energy dissipation efficiency (e.g., Farrington et al., 2014) and influence the dynamics of plate bending and unbending. Nevertheless, in Chapter 4, the formation of double-sided subduction zones was observed under viscoelastoplastic conditions.

Thus, given the uncertainty, if we are to understand the effects exerted by elasticity the development of double-sided subduction zones, it is fundamental that further modelling studies are conducted under viscoelastoplastic conditions.

6.2.2.4. No magmatic arc exists on the overriding plate

As in many subduction zone modelling studies (e.g., Gerya and Meilick, 2011; Crameri et al., 2012; Ficini et al., 2017), no buoyant magmatic volcanic arc exists on our simulated overriding plates. Nevertheless, and as shown in Chapter 4, the presence of a buoyant magmatic arc on the overriding plate precludes the development of double-sided subduction zones. Furthermore, this stabilizing magmatic arc exists in all present-day overriding plates on Earth. Given these results, further modelling is required to assess the exact impact of a buoyant magmatic arc on the prevention of double-sided subduction zones.

6.2.2.5. Double-sided subduction has been observed under 3D conditions

Although Chapter 5 aims to explores how plate strength might influence the occurrence of double- and single-sided subduction, all models were conducted under 2D conditions. However, and as in Chapter 4, we observed a systematic occurrence of double-sided subduction zones under 3D modelling conditions, additional 3D modelling is required to assess the specific geodynamic constraints which govern double-sided subduction under these conditions.

References

Almeida, J, Riel, N., Rosas, F.M., Duarte, J.C., Kaus, B.J.P., 2022. Self-replicating subduction zone initiation by polarity reversal. Commun. Earth Environ. Accepted i.

Almeida, J., Riel, N., Rosas, F.M., Duarte, J.C., Schellart, W.P., 2022. Polarity-reversal subduction zone initiation triggered by buoyant plateau obstruction. Earth Planet. Sci. Lett. 577, 117195. https://doi.org/10.1016/j.epsl.2021.117195

Andrews, D.J., Sleep, N.H., 1974. Numerical Modelling of Tectonic Flow behind Island Arcs. Geophys. J. R. Astron. Soc. 38, 237–251. https://doi.org/10.1111/j.1365-246X.1974.tb04118.x

Arcay, D., 2017. Modelling the interplate domain in thermo-mechanical simulations of subduction: Critical effects of resolution and rheology, and consequences on wet mantle melting. Phys. Earth Planet. Inter. 269, 112–132. https://doi.org/10.1016/j.pepi.2017.05.008

Arcay, D., Lallemand, S., Abecassis, S., Garel, F., 2019. Can subduction initiation at a transform fault be spontaneous? Solid Earth Discuss. 1–34. https://doi.org/10.5194/se-2019-63

Arnould, M., Coltice, N., Flament, N., Seigneur, V., Müller, R.D., 2018. On the Scales of Dynamic Topography in Whole-Mantle Convection Models. Geochemistry, Geophys. Geosystems 19. https://doi.org/10.1029/2018GC007516

Auzemery, A., Willingshofer, E., Yamato, P., Duretz, T., Sokoutis, D., 2020. Strain localization mechanisms for subduction initiation at passive margins. Glob. Planet. Change 195, 103323. https://doi.org/10.1016/j.gloplacha.2020.103323

Baes, M., Govers, R., Wortel, R., 2011a. Subduction initiation along the inherited weakness zone at the edge of a slab: Insights from numerical models. Geophys. J. Int. 184, 991–1008. https://doi.org/10.1111/j.1365-246X.2010.04896.x

Baes, M., Govers, R., Wortel, R., 2011b. Switching between alternative responses of the lithosphere to continental collision. Geophys. J. Int. 187, 1151–1174. https://doi.org/10.1111/j.1365-246X.2011.05236.x

Baes, M., Sobolev, S.V., 2017. Mantle Flow as a Trigger for Subduction Initiation: A Missing Element of the Wilson Cycle Concept. Geochemistry, Geophys. Geosystems 18, 4469–4486. https://doi.org/10.1002/2017GC006962

Baes, M., Sobolev, S. V, Quinteros, J., 2018. Subduction initiation in mid-ocean induced by mantle suction flow. Geophys. J. Int. 215, 1515–1522. https://doi.org/10.1093/gji/ggy335

Balay, S., Gropp, W.D., McInnes, L.C., Smith, B.F., 1997. Efficient Management of Parallelism in Object-Oriented Numerical Software Libraries, in: Arge, E., Bruaset, A.M., Langtangen, H.P. (Eds.), Modern Software Tools for Scientific Computing. Birkhäuser Boston, Boston, MA, pp. 163–202. https://doi.org/10.1007/978-1-4612-1986-6_8

Betts, P.G., Moresi, L., Miller, M.S., Willis, D., 2015. Geodynamics of oceanic plateau and plume head accretion and their role in Phanerozoic orogenic systems of China. Geosci. Front. 6, 49–59. https://doi.org/10.1016/j.gsf.2014.07.002

Bodur, Ö.F., Rey, P.F., 2019. The impact of rheological uncertainty on dynamic topography predictions. Solid Earth 10, 2167–2178. https://doi.org/10.5194/se-10-2167-2019

Buchs, D.M., Arculus, R.J., Baumgartner, P.O., Baumgartner-Mora, C., Ulianov, A., 2010. Late Cretaceous arc development on the SW margin of the Caribbean Plate: Insights from the Golfito, Costa Rica, and Azuero, Panama, complexes. Geochemistry, Geophys. Geosystems 11, n/a-n/a. https://doi.org/10.1029/2009GC002901

Burov, E., Cloetingh, S., 2010. Plume-like upper mantle instabilities drive subduction initiation. Geophys. Res. Lett. 37, n/a-n/a. https://doi.org/10.1029/2009GL041535

Burov, E.B., 2011. Rheology and strength of the lithosphere. Mar. Pet. Geol. 28, 1402–1443. https://doi.org/10.1016/j.marpetgeo.2011.05.008

Capitanio, F.A., Morra, G., 2012. The bending mechanics in a dynamic subduction system: Constraints from numerical modelling and global compilation analysis. Tectonophysics 522–523, 224–234. https://doi.org/10.1016/j.tecto.2011.12.003

Capitanio, F.A., Morra, G., Goes, S., 2007. Dynamic models of downgoing plate-buoyancy driven subduction: Subduction motions and energy dissipation. Earth Planet. Sci. Lett. 262, 284–297. https://doi.org/10.1016/j.epsl.2007.07.039

Capitanio, F.A., Morra, G., Goes, S., Weinberg, R.F., Moresi, L., 2010. India-Asia convergence driven by the subduction of the Greater Indian continent. Nat. Geosci. 3, 136–139. https://doi.org/10.1038/ngeo725

Carlson, R.L., Hilde, T.W.C., Uyeda, S., 1983. The driving mechanism of plate tectonics: Relation to age of the lithosphere at trenches. Geophys. Res. Lett. 10, 297–300. https://doi.org/10.1029/GL010i004p00297

Carluccio, R., Kaus, B., Capitanio, F.A., Moresi, L.N., 2019. The Impact of a Very Weak and Thin Upper Asthenosphere on Subduction Motions. Geophys. Res. Lett. 46, 11893–11905. https://doi.org/10.1029/2019GL085212

Chen, Z., Schellart, W.P., Duarte, J.C., 2015. Quantifying the energy dissipation of overriding plate deformation in three-dimensional subduction models. J. Geophys. Res. Solid Earth 120, 519–536. https://doi.org/10.1002/2014JB011419

Chen, Z., Schellart, W.P., Strak, V., Duarte, J.C., 2016. Does subduction-induced mantle flow drive backarc extension? Earth Planet. Sci. Lett. 441, 200–210. https://doi.org/10.1016/j.epsl.2016.02.027

Cloetingh, S., Wortel, R., Vlaar, N.J., 1989. On the initiation of subduction zones. Pure Appl. Geophys. PAGEOPH 129, 7–25. https://doi.org/10.1007/BF00874622

Cloetingh, S.A.P.L., Wortel, M.J.R., Vlaar, N.J., 1982. Evolution of passive continental margins and initiation of subduction zones. Nature 297, 139–142. https://doi.org/10.1038/297139a0

Conrad, C.P., Lithgow-Bertelloni, C., 2002. How mantle slabs drive plate tectonics. Science (80-.). 298, 207–209. https://doi.org/10.1126/science.1074161

Cooper, P.A., Taylor, B., 1985. Polarity reversal in the Solomon Islands arc. Nature 314, 428–430. https://doi.org/10.1038/314428a0

Crameri, F., Conrad, C.P., Montési, L., Lithgow-Bertelloni, C.R., 2018. The dynamic life of an oceanic plate. Tectonophysics. https://doi.org/10.1016/j.tecto.2018.03.016

Crameri, F., Magni, V., Domeier, M., Shephard, G.E., Chotalia, K., Cooper, G., Eakin, C.M.,

Grima, A.G., Gürer, D., Király, Á., Mulyukova, E., Peters, K., Robert, B., Thielmann, M., 2020. A transdisciplinary and community-driven database to unravel subduction zone initiation. Nat. Commun. 11, 1–14. https://doi.org/10.1038/s41467-020-17522-9

Crameri, F., Tackley, P.J., 2016. Subduction initiation from a stagnant lid and global overturn: new insights from numerical models with a free surface. Prog. Earth Planet. Sci. 3, 30. https://doi.org/10.1186/s40645-016-0103-8

Crameri, F., Tackley, P.J., 2015. Parameters controlling dynamically self-consistent plate tectonics and single-sided subduction in global models of mantle convection. J. Geophys. Res. Solid Earth 120, 3680–3706. https://doi.org/10.1002/2014JB011664

Crameri, F., Tackley, P.J., Foley, B.J., Becker, T.W., 2014. Spontaneous development of arcuate single-sided subduction in global 3-D mantle convection models with a free surface. J. Geophys. Res. Solid Earth 119, 5921–5942. https://doi.org/10.1002/2014JB010939

Crameri, F., Tackley, P.J., Meilick, I., Gerya, T. V., Kaus, B.J.P., 2012. A free plate surface and weak oceanic crust produce single-sided subduction on Earth. Geophys. Res. Lett. 39, 1–7. https://doi.org/10.1029/2011GL050046

Davaille, A., Smrekar, S.E., Tomlinson, S., 2017. Experimental and observational evidence for plume-induced subduction on Venus. Nat. Geosci. 10, 349–355. https://doi.org/10.1038/ngeo2928

Davies, G.F., 1992. On the emergence of plate tectonics. Geology 20, 963. https://doi.org/10.1130/0091-7613(1992)020<0963:OTEOPT>2.3.CO;2

Deschamps, F., Godard, M., Guillot, S., Hattori, K., 2013. Geochemistry of subduction zone serpentinites: A review. Lithos 178, 96–127. https://doi.org/10.1016/j.lithos.2013.05.019

Dewey, J.F., Burke, K., 1974. Hot Spots and Continental Break-up: Implications for Collisional Orogeny. Geology 2, 57. https://doi.org/10.1130/0091-7613(1974)2<57:HSACBI>2.0.CO;2

Domeier, M., Shephard, G.E., Jakob, J., Gaina, C., Doubrovine, P. V, Torsvik, T.H., 2017. Intraoceanic subduction spanned the Pacific in the Late Cretaceous–Paleocene. Sci. Adv.

3. https://doi.org/10.1126/sciadv.aao2303

Drucker, D.C., Prager, W., 1952. Soil Mechanics and Plastic Analysis or Limit Design. Q. Appl. Math. 10, 157–165. https://doi.org/10.1090/qam/48291

Duarte, J., Rosas, F.M.F.M., Terrinha, P., Schellart, W.P.W.P., Boutelier, D., Gutscher, M.A.M.-A., Ribeiro, A., 2013. Are subduction zones invading the atlantic? Evidence from the southwest iberia margin. Geology 41, 839–842. https://doi.org/10.1130/G34100.1

Duarte, J.C., Schellart, W.P., Cruden, A.R., 2015. How weak is the subduction zone interface? Geophys. Res. Lett. 42, 2664–2673. https://doi.org/10.1002/2014GL062876

Duarte, J.C.J.C., Schellart, W.P., Cruden, A.R., 2013. Three-dimensional dynamic laboratory models of subduction with an overriding plate and variable interplate rheology. Geophys. J. Int. 195, 47–66. https://doi.org/10.1093/gji/ggt257

Duarte, Rosas, F.M., Terrinha, P., Schellart, W.P., Boutelier, D., Gutscher, M.-A., Ribeiro, A., 2013. Are subduction zones invading the atlantic? Evidence from the southwest iberia margin. Geology 41. https://doi.org/10.1130/G34100.1

Dvorkin, J., Nur, A., Mavko, G., Ben-Avraham, Z., 1993. Narrow subducting slabs and the origin of backarc basins. Tectonophysics 227, 63–79. https://doi.org/10.1016/0040-1951(93)90087-Z

Dymkova, D., Gerya, T., 2013. Porous fluid flow enables oceanic subduction initiation on Earth. Geophys. Res. Lett. 40, 5671–5676. https://doi.org/10.1002/2013GL057798

Erickson, S.G., 1993. Sedimentary loading, lithospheric flexure, and subduction initiation at passive margins. Geology 21, 125. https://doi.org/10.1130/0091-7613(1993)021<0125:SLLFAS>2.3.CO;2

Escartín, J., Hirth, G., Evans, B., 2001. Strength of slightly serpentinized peridotites: Implications for the tectonics of oceanic lithosphere. Geology 29, 1023–1026. https://doi.org/10.1130/0091-7613(2001)029<1023:SOSSPI>2.0.CO;2

Faccenda, M., Gerya, T. V., Chakraborty, S., 2008. Styles of post-subduction collisional orogeny: Influence of convergence velocity, crustal rheology and radiogenic heat

production. Lithos 103, 257–287. https://doi.org/10.1016/j.lithos.2007.09.009

Faccenda, M., Gerya, T. V., Mancktelow, N.S., Moresi, L., 2012. Fluid flow during slab unbending and dehydration: Implications for intermediate-depth seismicity, slab weakening and deep water recycling. Geochemistry, Geophys. Geosystems 13. https://doi.org/10.1029/2011GC003860

Faccenna, C., Giardini, D., Davy, P., Argentieri, A., 2002. Initiation of subduction at Atlantic-type margins: Insights from laboratory experiments. J. Geophys. Res. Solid Earth 104, 2749–2766. https://doi.org/10.1029/1998jb900072

Faccenna, C., Giardini, D., Davy, P., Argentieri, A., 1999. Initiation of subduction at Atlantic-type margins: Insights from laboratory experiments. J. Geophys. Res. Solid Earth 104, 2749–2766. https://doi.org/10.1029/1998JB900072

Faccenna, C., Holt, A.F., Becker, T.W., Lallemand, S., Royden, L.H., 2018. Dynamics of the Ryukyu/Izu-Bonin-Marianas double subduction system. Tectonophysics 746, 229–238. https://doi.org/10.1016/J.TECTO.2017.08.011

Farner, M.J., Lee, C.T.A., 2017. Effects of crustal thickness on magmatic differentiation in subduction zone volcanism: A global study. Earth Planet. Sci. Lett. 470, 96–107. https://doi.org/10.1016/J.EPSL.2017.04.025

Farrington, R.J., Moresi, L.-N., Capitanio, F.A., 2014. The role of viscoelasticity in subducting plates. Geochemistry, Geophys. Geosystems 15, 4291–4304. https://doi.org/10.1002/2014GC005507

Ficini, E., Dal Zilio, L., Doglioni, C., Gerya, T. V., 2017. Horizontal mantle flow controls subduction dynamics. Sci. Rep. 7, 1–7. https://doi.org/10.1038/s41598-017-06551-y

Flórez-Rodríguez, A.G., Schellart, W.P., Strak, V., 2019. Impact of Aseismic Ridges on Subduction Systems: Insights From Analog Modeling. J. Geophys. Res. Solid Earth 124, 5951–5969. https://doi.org/10.1029/2019JB017488

Forsyth, D., Uyeda, S., Uyedaf, S., 1975. On the the relative relative importance importance of of the the driving driving forces forces of of On plate motion motion plate. Geophys. J. R. astr. Soc. 43, 163–200. https://doi.org/10.1111/j.1365-246X.1975.tb00631.x

Funiciello, F., Morra, G., Regenauer-Lieb, K., Giardini, D., 2003. Dynamics of retreating slabs: 1. Insights from two-dimensional numerical experiments. J. Geophys. Res. Solid Earth 108, 1–17. https://doi.org/10.1029/2001jb000898

Gerya, T., 2011. Future directions in subduction modeling. J. Geodyn. 52, 344–378. https://doi.org/10.1016/j.jog.2011.06.005

Gerya, T., 2009. Introduction to Numerical Geodynamic Modelling. Cambridge University Press, Cambridge. https://doi.org/10.1017/CBO9780511809101

Gerya, T. V., Connolly, J.A.D., Yuen, D.A., 2008. Why is terrestrial subduction one-sided? Geology 36, 43. https://doi.org/10.1130/G24060A.1

Gerya, T. V., Meilick, F.I., 2011. Geodynamic regimes of subduction under an active margin: Effects of rheological weakening by fluids and melts. J. Metamorph. Geol. 29, 7–31. https://doi.org/10.1111/j.1525-1314.2010.00904.x

Gerya, T. V., Stern, R.J., Baes, M., Sobolev, S. V., Whattam, S.A., 2015. Plate tectonics on the Earth triggered by plume-induced subduction initiation. Nature 527, 221–225. https://doi.org/10.1038/nature15752

Goes, S., Agrusta, R., van Hunen, J., Garel, F., 2017. Subduction-transition zone interaction: A review. Geosphere 13, 644–664. https://doi.org/10.1130/GES01476.1

Gong, W., Jiang, X., Xing, J., Xu, C., Xu, X., 2019. Heterogeneous strain regime at the west of the Ogasawara Plateau in the Western Pacific Ocean from inversion of earthquake focal mechanisms. J. Asian Earth Sci. 180, 103868. https://doi.org/10.1016/J.JSEAES.2019.103868

Guillaume, B., Funiciello, F., Faccenna, C., Martinod, J., Olivetti, V., 2010. Spreading pulses of the Tyrrhenian Sea during the narrowing of the Calabrian slab. Geology 38, 819–822. https://doi.org/10.1130/G31038.1

Guillaume, B., Husson, L., Funiciello, F., Faccenna, C., 2013. The dynamics of laterally variable subductions: Laboratory models applied to the Hellenides. Solid Earth 4, 179–200. https://doi.org/10.5194/se-4-179-2013

Gurnis, M., Hager, B.H., 1988. Controls of the structure of subducted slabs. Nature 335, 317–321. https://doi.org/10.1038/335317a0

Gurnis, M., Hall, C., Lavier, L., 2004. Evolving force balance during incipient subduction. Geochemistry, Geophys. Geosystems 5. https://doi.org/10.1029/2003GC000681

Hall, C.E., Gurnis, M., Sdrolias, M., Lavier, L.L., Müller, R.D., 2003. Catastrophic initiation of subduction following forced convergence across fracture zones. Earth Planet. Sci. Lett. 212, 15–30. https://doi.org/10.1016/S0012-821X(03)00242-5

Hall, R., 2019. The subduction initiation stage of the Wilson cycle. Geol. Soc. London, Spec. Publ. 470, 415–437. https://doi.org/10.1144/SP470.3

Hall, R., 2002. Cenozoic geological and plate tectonic evolution of SE Asia and the SW Pacific: computer-based reconstructions, model and animations. J. Asian Earth Sci. 20, 353–431. https://doi.org/10.1016/S1367-9120(01)00069-4

Harris, P.T., Macmillan-Lawler, M., Rupp, J., Baker, E.K., 2014. Geomorphology of the oceans. Mar. Geol. 352, 4–24. https://doi.org/10.1016/J.MARGEO.2014.01.011

Hawkesworth, C.J., Cawood, P.A., Dhuime, B., 2020. The Evolution of the Continental Crust and the Onset of Plate Tectonics. Front. Earth Sci. 8, 1–23. https://doi.org/10.3389/feart.2020.00326

Hensen, C., Duarte, J.C., Vannucchi, P., Mazzini, A., Lever, M.A., Terrinha, P., Géli, L., Henry, P., Villinger, H., Morgan, J., Schmidt, M., Gutscher, M.A., Bartolome, R., Tomonaga, Y., Polonia, A., Gràcia, E., Tinivella, U., Lupi, M., Çağatay, M.N., Elvert, M., Sakellariou, D., Matias, L., Kipfer, R., Karageorgis, A.P., Ruffine, L., Liebetrau, V., Pierre, C., Schmidt, C., Batista, L., Gasperini, L., Burwicz, E., Neres, M., Nuzzo, M., 2019. Marine transform faults and fracture zones: A joint perspective integrating seismicity, fluid flow and life. Front. Earth Sci. 7, 1–29. https://doi.org/10.3389/feart.2019.00039

Heyworth, Z., Knesel, K.M., Turner, S.P., Arculus, R.J., 2011. Pb-isotopic evidence for rapid trench-parallel mantle flow beneath Vanuatu. J. Geol. Soc. London. 168, 265–271. https://doi.org/10.1144/0016-76492010-054

Hirauchi, K., Fukushima, K., Kido, M., Muto, J., Okamoto, A., 2016. Reaction-induced

rheological weakening enables oceanic plate subduction. Nat. Commun. 7, 12550. https://doi.org/10.1038/ncomms12550

Holt, A.F., Royden, L.H., Becker, T.W., 2017. The dynamics of double slab subduction. Geophys. J. Int. 209. https://doi.org/10.1093/gji/ggw496

Hui, Y., Xueliang, J., Na, L., 2014. Experimental Study on Mechanical Property of Peridotite under Water-Rock Interaction Test procedure. Electron. J. Geotech. Eng. 19E, 1179–1188.

Irvine, D.N., Schellart, W.P., 2012. Effect of plate thickness on bending radius and energy dissipation at the subduction zone hinge. J. Geophys. Res. Solid Earth 117, 1–14. https://doi.org/10.1029/2011JB009113

Jain, C., Korenaga, J., 2020. Synergy of Experimental Rock Mechanics, Seismology, and Geodynamics Reveals Still Elusive Upper Mantle Rheology. J. Geophys. Res. Solid Earth 125, e2020JB019896. https://doi.org/10.1029/2020JB019896

Kaus, B.J.P., 2009. Factors that control the angle of shear bands in geodynamic numerical models of brittle deformation. https://doi.org/10.1016/j.tecto.2009.08.042

Kaus, B.J.P., Popov, A.A., Baumann, T.S., Pusok, A.E., Bauville, A., Fernandez, N., Collignon, M., 2016. Forward and Inverse Modelling of Lithospheric Deformation on Geological Timescales. NIC Ser. 48, 978–3.

Kemp, David V., Stevenson, D.J., 1996. A tensile, flexural model for the initiation of subduction. Geophys. J. Int. 125, 73–93. https://doi.org/10.1111/j.1365-246X.1996.tb06535.x

Kemp, D. V., Stevenson, D.J., 1996. A tensile, flexural model for the initiation of subduction. Geophys. J. Int. 125, 73–94. https://doi.org/10.1111/j.1365-246X.1996.tb06535.x

Kerr, A.C., White, R. V., Thompson, P.M.E., Tarney, J., Saunders, A.D., 2003. No Oceanic Plateau— No Caribbean Plate? The Seminal Role of an Oceanic Plateau in Caribbean Plate Evolution, in: The Circum-Gulf of Mexico and the Caribbean/Hydrocarbon Habitats, Basin Formation and Plate Tectonics. American Association of Petroleum Geologists, pp. 23–26. https://doi.org/10.1306/M79877C6

King, S.D., 2016. Reconciling laboratory and observational models of mantle rheology in geodynamic modelling. J. Geodyn. 100, 33–50. https://doi.org/10.1016/j.jog.2016.03.005

Kohlstedt, D.L., Evans, B., Mackwell, S.J., 1995a. Strength of the lithosphere: Constraints imposed by laboratory experiments. J. Geophys. Res. 100, 17587–17602. https://doi.org/10.1029/95JB01460

Kohlstedt, D.L., Evans, B., Mackwell, S.J., 1995b. Strength of the lithosphere: Constraints imposed by laboratory experiments. J. Geophys. Res. Solid Earth 100, 17587–17602. https://doi.org/10.1029/95JB01460

Konstantinovskaia, E.., 2001. Arc–continent collision and subduction reversal in the Cenozoic evolution of the Northwest Pacific: an example from Kamchatka (NE Russia). Tectonophysics 333, 75–94. https://doi.org/10.1016/S0040-1951(00)00268-7

Konstantinovskaya, E., 2011. Early Eocene Arc–Continent Collision in Kamchatka, Russia: Structural Evolution and Geodynamic Model, in: Frontiers in Earth Sciences. pp. 247–277. https://doi.org/10.1007/978-3-540-88558-0_9

Koptev, A., Ehlers, T.A., Nettesheim, M., Whipp, D.M., 2019. Response of a Rheologically Stratified Lithosphere to Subduction of an Indenter-Shaped Plate: Insights Into Localized Exhumation at Orogen Syntaxes. Tectonics 38, 1908–1930. https://doi.org/10.1029/2018TC005455

Korenaga, J., 2007. Thermal cracking and the deep hydration of oceanic lithosphere: A key to the generation of plate tectonics? J. Geophys. Res. Solid Earth 112, 1–20. https://doi.org/10.1029/2006JB004502

Lallemand, S., 2016a. Philippine Sea Plate inception, evolution, and consumption with special emphasis on the early stages of Izu-Bonin-Mariana subduction. Prog. Earth Planet. Sci. 3, 15. https://doi.org/10.1186/s40645-016-0085-6

Lallemand, S., 2016b. Philippine Sea Plate inception, evolution, and consumption with special emphasis on the early stages of Izu-Bonin-Mariana subduction. Prog. Earth Planet. Sci. https://doi.org/10.1186/s40645-016-0085-6

Lallemand, S., Font, Y., Bijwaard, H., Kao, H., 2001. New insights on 3-D plates interaction

near Taiwan from tomography and tectonic implications. Tectonophysics 335, 229–253. https://doi.org/10.1016/S0040-1951(01)00071-3

Lallemand, S., Heuret, A., Boutelier, D., 2005. On the relationships between slab dip, back-arc stress, upper plate absolute motion, and crustal nature in subduction zones. Geochemistry, Geophys. Geosystems 6. https://doi.org/10.1029/2005GC000917

Leprieur, F., Descombes, P., Gaboriau, T., Cowman, P.F., Parravicini, V., Kulbicki, M., Melian, C.J., De Santana, C.N., Heine, C., Mouillot, D., Bellwood, D.R., Pellissier, L., 2016. Plate tectonics drive tropical reef biodiversity dynamics. Nat. Commun. 7, 1–8. https://doi.org/10.1038/ncomms11461

Lévy, F., Jaupart, C., 2012. The initiation of subduction by crustal extension at a continental margin. Geophys. J. Int. 188, 779–797. https://doi.org/10.1111/j.1365-246X.2011.05303.x

Li, Z.H., Gerya, T. V., Burg, J.P., 2010. Influence of tectonic overpressure on P-T paths of HP-UHP rocks in continental collision zones: Thermomechanical modelling. J. Metamorph. Geol. 28, 227–247. https://doi.org/10.1111/j.1525-1314.2009.00864.x

Lu, G., Kaus, B.J.P., Zhao, L., Zheng, T., 2015. Self-consistent subduction initiation induced by mantle flow. Terra Nov. 27, 130–138. https://doi.org/10.1111/ter.12140

Malatesta, C., Gerya, T., Crispini, L., Federico, L., Capponi, G., 2016. Interplate deformation at early-stage oblique subduction: 3-D thermomechanical numerical modeling. Tectonics 35, 1610–1625. https://doi.org/10.1002/2016TC004139

Malatesta, C., Gerya, T., Crispini, L., Federico, L., Capponi, G., 2013. Oblique subduction modelling indicates along-trench tectonic transport of sediments. Nat. Commun. 4. https://doi.org/10.1038/ncomms3456

Mann, P., Taira, A., 2004. Global tectonic significance of the Solomon Islands and Ontong Java Plateau convergent zone. Tectonophysics 389, 137–190. https://doi.org/10.1016/j.tecto.2003.10.024

Mariana, B., Arculus, R.J., Ishizuka, O., Bogus, K.A., Gurnis, M., Hickey-vargas, R., Aljahdali, M.H., Bandini-maeder, A.N., Barth, A.P., Brandl, P.A., 2015. A record of spontaneous subduction initiation in. Nat. Geosci. 8, 728–733. https://doi.org/10.1038/NGEO2515

Marques, F.O., Catalão, J.C., DeMets, C., Costa, a. C.G., Hildenbrand, a., 2014. Corrigendum to “GPS and tectonic evidence for a diffuse plate boundary at the Azores Triple Junction” [Earth Planet. Sci. Lett. 381 (2013) 177–187]. Earth Planet. Sci. Lett. 387, 1–3. https://doi.org/10.1016/j.epsl.2013.11.029

Marques, F.O., Nikolaeva, K., Assumpção, M., Gerya, T. V., Bezerra, F.H.R., do Nascimento, A.F., Ferreira, J.M., 2013. Testing the influence of far-field topographic forcing on subduction initiation at a passive margin. Tectonophysics 608, 517–524. https://doi.org/10.1016/j.tecto.2013.08.035

Maunder, B., Prytulak, J., Goes, S., Reagan, M., 2020. Rapid subduction initiation and magmatism in the Western Pacific driven by internal vertical forces. Nat. Commun. 11, 1–8. https://doi.org/10.1038/s41467-020-15737-4

McKenzie, D.P., 1977. The initiation of trenches: A finite amplitude instability. pp. 57–61. https://doi.org/10.1029/ME001p0057

Meier, M.A., Ampuero, J.P., Heaton, T.H., 2017. The hidden simplicity of subduction megathrust earthquakes. Science (80-.). 357, 1277–1281. https://doi.org/10.1126/SCIENCE.AAN5643

Meriaux, C. a., Duarte, J.C., Duarte, S.S., Schellart, W.P., Chen, Z., Rosas, F., Mata, J., Terrinha, P., 2015. Capture of the Canary mantle plume material by the Gibraltar arc mantle wedge during slab rollback. Geophys. J. Int. 201, 1717–1721. https://doi.org/10.1093/gji/ggv120

Mériaux, C.A., May, D.A., Mansour, J., Chen, Z., Kaluza, O., 2018. Benchmark of three-dimensional numerical models of subduction against a laboratory experiment. Phys. Earth Planet. Inter. 283, 110–121. https://doi.org/10.1016/J.PEPI.2018.07.009

Mériaux, C.A., May, D.A., Mansour, J., Kaluza, O., 2020. Mantle plume dynamics at the rear of a retreating slab. Geophys. J. Int. 222, 1146–1163. https://doi.org/10.1093/gji/ggaa222

Mitchell, A.H.G., 1984. Initiation of subduction by post-collision foreland thrusting and back-thrusting. J. Geodyn. 1, 103–120. https://doi.org/10.1016/0264-3707(84)90023-1

Miura, S., Suyehiro, K., Shinohara, M., Takahashi, N., Araki, E., Taira, A., 2004. Seismological

structure and implications of collision between the Ontong Java Plateau and Solomon Island Arc from ocean bottom seismometer–airgun data. Tectonophysics 389, 191–220. https://doi.org/10.1016/J.TECTO.2003.09.029

Mondy, L.S., Rey, P.F., Duclaux, G., Moresi, L., 2018. The role of asthenospheric flow during rift propagation and breakup. Geology 46, 103–106. https://doi.org/10.1130/G39674.1

Moresi, L., Betts, P.G., Miller, M.S., Cayley, R.A., 2014. Dynamics of continental accretion. Nat. 2014 5087495 508, 245–248. https://doi.org/10.1038/nature13033

Moresi, L., Quenette, S., Lemiale, V., Mériaux, C., Appelbe, B., Mühlhaus, H.B., 2007. Computational approaches to studying non-linear dynamics of the crust and mantle. Phys. Earth Planet. Inter. 163, 69–82. https://doi.org/10.1016/j.pepi.2007.06.009

Mortimer, N., Campbell, H.J., Tulloch, A.J., King, P.R., Stagpoole, V.M., Wood, R.A., Rattenbury, M.S., Sutherland, R., Adams, C.J., Collot, J., Seton, M., 2017. Zealandia: Earth's hidden Continent. GSA Today 27, 27–35. https://doi.org/10.1130/GSATG321A.1

Mortimer, N., Gans, P.B., Palin, J.M., Herzer, R.H., Pelletier, B., Monzier, M., 2014. Eocene and Oligocene basins and ridges of the Coral Sea-New Caledonia region: Tectonic link between Melanesia, Fiji, and Zealandia. Tectonics 33, 1386–1407. https://doi.org/10.1002/2014TC003598

Mueller, S., Phillips, R.J., 1991. On The initiation of subduction. J. Geophys. Res. 96, 651. https://doi.org/10.1029/90JB02237

Müller, R.D., Sdrolias, M., Gaina, C., Roest, W.R., 2008. Age, spreading rates, and spreading asymmetry of the world's ocean crust. Geochemistry, Geophys. Geosystems 9, 1–19. https://doi.org/10.1029/2007GC001743

Munch, J., Gerya, T., Ueda, K., 2020. Oceanic crust recycling controlled by weakening at slab edges. Nat. Commun. 11. https://doi.org/10.1038/s41467-020-15750-7

Nair, R., Chacko, T., 2008. Role of oceanic plateaus in the initiation of subduction and origin of continental crust. Geology 36, 583–586. https://doi.org/10.1130/G24773A.1

Nikolaeva, K., Gerya, T. V., Connolly, J.A.D., 2008. Numerical modelling of crustal growth in

intraoceanic volcanic arcs. Phys. Earth Planet. Inter. 171, 336–356. https://doi.org/10.1016/J.PEPI.2008.06.026

Nikolaeva, K., Gerya, T. V., Marques, F.O., 2011. Numerical analysis of subduction initiation risk along the Atlantic American passive margins. Geology 39, 463–466. https://doi.org/10.1130/G31972.1

Nikolaeva, K., Gerya, T. V., Marques, F.O., 2010. Subduction initiation at passive margins: Numerical modeling. J. Geophys. Res. Solid Earth 115, 1–19. https://doi.org/10.1029/2009JB006549

Nikolaeva, K.M., Gerya, T. V., 2009. Numerical modeling of intraoceanic arc growth. Moscow Univ. Geol. Bull. 64, 230–243. https://doi.org/10.3103/S0145875209040048

Niu, Y., O'Hara, M.J., Pearce, J.A., 2003. Initiation of subduction zones as a consequence of lateral compositional bouyancy contrast within the lithosphere: A petrological perspective. J. Petrol. 44, 851–866. https://doi.org/10.1093/petrology/44.5.851

Oryan, B., Buck, W.R., 2020. Larger tsunamis from megathrust earthquakes where slab dip is reduced. Nat. Geosci. 2020 134 13, 319–324. https://doi.org/10.1038/s41561-020-0553-x

Oxburgh, E.R., Parmentier, E.M., 1977. Compositional and density stratification in oceanic lithosphere-causes and consequences. J. Geol. Soc. London. 133, 343–354. https://doi.org/10.1144/gsjgs.133.4.0343

Pall, J., Zahirovic, S., Doss, S., Hassan, R., Matthews, K.J., Cannon, J., Gurnis, M., Moresi, L., Lenardic, A., Müller, R.D., 2018. The influence of carbonate platform interactions with subduction zone volcanism on palaeo-atmospheric CO₂ since the Devonian. Clim. Past 14, 857–870. https://doi.org/10.5194/cp-14-857-2018

Parsons, B., Richter, F.M., 1980. A relation between the driving force and geoid anomaly associated with mid-ocean ridges. Earth Planet. Sci. Lett. 51, 445–450. https://doi.org/10.1016/0012-821X(80)90223-X

Pesaresi, M., Melchiorri, M., Siragusa, A., Kemper, T., 2016. Atlas of the Human Planet. https://doi.org/10.2760/19837

Phinney, E.J., Mann, P., Coffin, M.F., Shipley, T.H., 2004. Sequence stratigraphy, structural style, and age of deformation of the Malaita accretionary prism (Solomon arc–Ontong Java Plateau convergent zone). Tectonophysics 389, 221–246. https://doi.org/10.1016/j.tecto.2003.10.025

Piccolo, A., Kaus, B.J.P., White, R.W., Palin, R.M., Reuber, G.S., 2020. Plume — Lid interactions during the Archean and implications for the generation of early continental terranes. Gondwana Res. 88, 150–168. https://doi.org/10.1016/j.gr.2020.06.024

Platt, J.P., Behr, W.M., 2011. Grainsize evolution in ductile shear zones: Implications for strain localization and the strength of the lithosphere. J. Struct. Geol. 33, 537–550. https://doi.org/10.1016/j.jsg.2011.01.018

Prigent, C., Warren, J.M., Kohli, A.H., Teyssier, C., 2020. Fracture-mediated deep seawater flow and mantle hydration on oceanic transform faults. Earth Planet. Sci. Lett. 532, 115988. https://doi.org/10.1016/j.epsl.2019.115988

Pusok, A.E., Kaus, B.J.P., Popov, A.A., 2018a. The effect of rheological approximations in 3-D numerical simulations of subduction and collision. Tectonophysics 746. https://doi.org/10.1016/j.tecto.2018.04.017

Pusok, A.E., Kaus, B.J.P., Popov, A.A., 2018b. The effect of rheological approximations in 3-D numerical simulations of subduction and collision. Tectonophysics 746, 296–311. https://doi.org/10.1016/j.tecto.2018.04.017

Pysklywec, R.N., 2001. Evolution of subducting mantle lithosphere at a continental plate boundary. Geophys. Res. Lett. 28, 4399–4402. https://doi.org/10.1029/2001GL013567

Quenette, S., Moresi, L., Sunter, P.D., Appelbe, B.F., 2007. Explaining StGermain: An aspect oriented environment for building extensible computational mechanics modeling software. Proc. - 21st Int. Parallel Distrib. Process. Symp. IPDPS 2007; Abstr. CD-ROM. https://doi.org/10.1109/IPDPS.2007.370400

Ranalli, G., 1997. Rheology and deep tectonics. Ann. Di Geofis. https://doi.org/10.4401/ag-3893

Reagan, M.K., Heaton, D.E., Schmitz, M.D., Pearce, J.A., Shervais, J.W., Koppers, A.A.P.,

2019. Forearc ages reveal extensive short-lived and rapid seafloor spreading following subduction initiation. Earth Planet. Sci. Lett. 506, 520–529. https://doi.org/10.1016/j.epsl.2018.11.020

Regenauer-Lieb, K., Yuen, D.A., Branlund, J., 2001. The initiation of subduction: Criticality by addition of water? Science (80-.). 294, 578–580. https://doi.org/10.1126/science.1063891

Reuber, G.S., Kaus, B.J.P., Popov, A.A., Baumann, T.S., 2018. Unraveling the Physics of the Yellowstone Magmatic System Using Geodynamic Simulations. Front. Earth Sci. 6, 117. https://doi.org/10.3389/feart.2018.00117

Rey, P.F., Coltice, N., Flament, N., 2014. Spreading continents kick-started plate tectonics. Nature 513, 405–8. https://doi.org/10.1038/nature13728

Reynard, B., 2013. Serpentine in active subduction zones. Lithos 178, 171–185. https://doi.org/10.1016/j.lithos.2012.10.012

Riel, N., Capitanio, F.A., Velic, M., 2017. Numerical modeling of stress and topography coupling during subduction: Inferences on global vs. regional observables interpretation. Tectonophysics. https://doi.org/10.1016/j.tecto.2017.07.023

Salerno, V.M., Capitanio, F.A., Farrington, R.J., Riel, N., 2016. The role of long-term rifting history on modes of continental lithosphere extension. J. Geophys. Res. Solid Earth 121, 8917–8940. https://doi.org/10.1002/2016JB013005

Sandiford, D., Moresi, L., 2019. Improving subduction interface implementation in dynamic numerical models. https://doi.org/10.5194/se-2019-11

Schellart, W.P., 2017a. Andean mountain building and magmatic arc migration driven by subduction-induced whole mantle flow. Nat. Commun. 8, 1–13. https://doi.org/10.1038/s41467-017-01847-z

Schellart, W.P., 2017b. A geodynamic model of subduction evolution and slab detachment to explain Australian plate acceleration and deceleration during the latest Cretaceous-early Cenozoic. Lithosphere 9. https://doi.org/10.1130/L675.1

Schellart, W.P., 2009. Evolution of the slab bending radius and the bending dissipation in three-dimensional subduction models with a variable slab to upper mantle viscosity ratio. Earth Planet. Sci. Lett. 288, 309–319. https://doi.org/10.1016/j.epsl.2009.09.034

Schellart, W.P., 2008. Overriding plate shortening and extension above subduction zones: A parametric study to explain formation of the Andes Mountains. Bull. Geol. Soc. Am. 120, 1441–1454. https://doi.org/10.1130/B26360.1

Schellart, W.P., 2004a. Kinematics of subduction and subduction-induced flow in the upper mantle. J. Geophys. Res. B Solid Earth 109, 1–19. https://doi.org/10.1029/2004JB002970

Schellart, W.P., 2004b. Quantifying the net slab pull force as a driving mechanism for plate tectonics. Geophys. Res. Lett. 31, n/a-n/a. https://doi.org/10.1029/2004GL019528

Schellart, W.P., Chen, Z., Strak, V., Duarte, J.C., Rosas, F.M., 2019. Pacific subduction control on Asian continental deformation including Tibetan extension and eastward extrusion tectonics. Nat. Commun. 10, 4480. https://doi.org/10.1038/s41467-019-12337-9

Schellart, W.P., Freeman, J., Stegman, D.R., Moresi, L., May, D., 2007. Evolution and diversity of subduction zones controlled by slab width. Nature 446, 308–311. https://doi.org/10.1038/nature05615

Schellart, W.P., Lister, G.S., 2005. The role of the East Asian active margin in widespread extensional and strike-slip deformation in East Asia. J. Geol. Soc. London. 162, 959–972. https://doi.org/10.1144/0016-764904-112

Schellart, W.P., Lister, G.S., Jessell, M.W., 2002. Analogue modelling of asymmetrical back-arc extension. J. Virtual Explor. 7. https://doi.org/10.3809/jvirtex.2002.0026

Schellart, W.P., Lister, G.S., Toy, V.G., 2006. A Late Cretaceous and Cenozoic reconstruction of the Southwest Pacific region: Tectonics controlled by subduction and slab rollback processes. Earth-Science Rev. 76, 191–233. https://doi.org/10.1016/J.EARSCIREV.2006.01.002

Schellart, W.P., Moresi, L., 2013. A new driving mechanism for backarc extension and backarc shortening through slab sinking induced toroidal and poloidal mantle flow: Results from dynamic subduction models with an overriding plate. J. Geophys. Res. Solid Earth 118,

3221–3248. https://doi.org/10.1002/jgrb.50173

Schellart, W.P., Rawlinson, N., 2013. Global correlations between maximum magnitudes of subduction zone interface thrust earthquakes and physical parameters of subduction zones. Phys. Earth Planet. Inter. 225, 41–67. https://doi.org/10.1016/j.pepi.2013.10.001

Schmeling, H., Babeyko, A.Y., Enns, A., Faccenna, C., Funiciello, F., Gerya, T., Golabek, G.J., Grigull, S., Kaus, B.J.P., Morra, G., Schmalholz, S.M., van Hunen, J., 2008. A benchmark comparison of spontaneous subduction models-Towards a free surface. Phys. Earth Planet. Inter. 171, 198–223. https://doi.org/10.1016/j.pepi.2008.06.028

Scholz, C.H., 2019. The Mechanics of Earthquakes and Faulting. Cambridge University Press. https://doi.org/10.1017/9781316681473

Searle, R.C., Escartín, J., 2004. The rheology and morphology of oceanic lithosphere and mid-ocean ridges, Geophysical Monograph Series. https://doi.org/10.1029/148GM03

Sharples, W., Moresi, L.N., Velic, M., Jadamec, M.A., May, D.A., 2016. Simulating faults and plate boundaries with a transversely isotropic plasticity model. Phys. Earth Planet. Inter. 252, 77–90. https://doi.org/10.1016/j.pepi.2015.11.007

Simpson, G., 2017. Practical Finite Element Modeling in Earth Science Using Matlab, Practical Finite Element Modeling in Earth Science Using Matlab. https://doi.org/10.1002/9781119248644

Spitz, R., Bauville, A., Epard, J.-L., Kaus, B., Popov, A., Schmalholz, S., 2019. Control of 3D tectonic inheritance on fold-and-thrust belts: insights from 3D numerical models and application to the Helvetic nappe system. Solid Earth Discuss. 1–39. https://doi.org/10.5194/se-2019-173

Spitz, R., Schmalholz, S.M., Kaus, B.J.P., Popov, A.A., 2020. Quantification and visualization of finite strain in 3D viscous numerical models of folding and overthrusting. J. Struct. Geol. 131, 103945. https://doi.org/10.1016/j.jsg.2019.103945

Stegman, D.R., Farrington, R., Capitanio, F.A., 2010. A regime diagram for subduction styles from 3-D numerical models of free subduction. Tectonophysics 483, 29–45. https://doi.org/10.1016/J.TECTO.2009.08.041

Stegman, D.R., Freeman, J., Schellart, W.P., Moresi, L., May, D., 2006. Influence of trench width on subduction hinge retreat rates in 3-D models of slab rollback. Geochemistry, Geophys. Geosystems 7, n/a-n/a. https://doi.org/10.1029/2005GC001056

Stern, C.R., 2011. Subduction erosion: Rates, mechanisms, and its role in arc magmatism and the evolution of the continental crust and mantle. Gondwana Res. 20, 284–308. https://doi.org/10.1016/j.gr.2011.03.006

Stern, R.J., 2004. Subduction initiation: Spontaneous and induced. Earth Planet. Sci. Lett. 226, 275–292. https://doi.org/10.1016/j.epsl.2004.08.007

Stern, R.J., 2002. Subduction zones. Rev. Geophys. 40, 1012. https://doi.org/10.1029/2001RG000108

Stern, R.J., Dumitru, T.A., 2019. Eocene initiation of the Cascadia subduction zone: A second example of plume-induced subduction initiation? Geosphere 15, 659–681. https://doi.org/10.1130/GES02050.1

Stern, R.J., Gerya, T., 2018. Subduction initiation in nature and models: A review. Tectonophysics. https://doi.org/10.1016/j.tecto.2017.10.014

Strak, V., Schellart, W.P., 2016. Control of slab width on subduction-induced upper mantle flow and associated upwellings: Insights from analog models. J. Geophys. Res. Solid Earth 121, 4641–4654. https://doi.org/10.1002/2015JB012545

Tackley, P.J., 2000. Self-consistent generation of tectonic plates in time-dependent, three-dimensional mantle convection simulations 2. Strain weakening and asthenosphere. Geochemistry, Geophys. Geosystems 1, n/a-n/a. https://doi.org/10.1029/2000GC000043

Tao, W.C., O'connell, R.J., 1992. Ablative subduction: A two-sided alternative to the conventional subduction model. J. Geophys. Res. 97, 8877. https://doi.org/10.1029/91JB02422

Tetreault, J.L., Buiter, S.J.H., 2014. Future accreted terranes: A compilation of island arcs, oceanic plateaus, submarine ridges, seamounts, and continental fragments. Solid Earth 5, 1243–1275. https://doi.org/10.5194/se-5-1243-2014

Tetreault, J.L., Buiter, S.J.H., 2012. Geodynamic models of terrane accretion: Testing the fate of island arcs, oceanic plateaus, and continental fragments in subduction zones. J. Geophys. Res. Solid Earth 117, 1–23. https://doi.org/10.1029/2012JB009316

Thielmann, M., Kaus, B.J.P., 2012. Shear heating induced lithospheric-scale localization: Does it result in subduction? Earth Planet. Sci. Lett. 359–360, 1–13. https://doi.org/10.1016/j.epsl.2012.10.002

Toussaint, G., Burov, E., Jolivet, L., 2004. Continental plate collision: Unstable vs. stable slab dynamics. Geology 32, 33–36. https://doi.org/10.1130/G19883.1

Turcotte, D.L., Schubert, G., 2002. Geodynamics, Second Edi. ed. Cambridge University Press. https://doi.org/10.1017/CBO9780511807442

Ueda, K., Gerya, T., Sobolev, S. V., 2008. Subduction initiation by thermal-chemical plumes: Numerical studies. Phys. Earth Planet. Inter. 171, 296–312. https://doi.org/10.1016/j.pepi.2008.06.032

Ulvrova, M.M., Coltice, N., Williams, S., Tackley, P.J., 2019. Where does subduction initiate and cease? A global scale perspective. Earth Planet. Sci. Lett. 528, 115836. https://doi.org/10.1016/j.epsl.2019.115836

Uyeda, S., Ben-Avraham, Z., 1972. Origin and development of the Philippine Sea. Nature 238, 37. https://doi.org/10.1038/physci240176a0

Vargas, C.A., Mann, P., 2013. Tearing and breaking off of subducted slabs as the result of collision of the panama arc-indenter with Northwestern South America. Bull. Seismol. Soc. Am. 103, 2025–2046. https://doi.org/10.1785/0120120328

Vlaar, N.J., Wortel, M.J.R., 1976. Lithospheric aging, instability and subduction. Tectonophysics 32, 331–351. https://doi.org/10.1016/0040-1951(76)90068-8

Vogt, K., Willingshofer, E., Matenco, L., Sokoutis, D., Gerya, T., Cloetingh, S., 2018. The role of lateral strength contrasts in orogenesis: A 2D numerical study. Tectonophysics 746, 549–561. https://doi.org/10.1016/j.tecto.2017.08.010

Wang, K., 2021. If Not Brittle : Ductile , Plastic , or Viscous ?

https://doi.org/10.1785/0220200242.Introduction

Wells, R.E., Blakely, R.J., Sugiyama, Y., Scholl, D.W., Dinterman, P.A., 2003. Basin-centered asperities in great subduction zone earthquakes: A link between slip, subsidence, and subduction erosion? J. Geophys. Res. Solid Earth 108. https://doi.org/10.1029/2002JB002072

Whattam, S.A., Stern, R.J., 2015. Late Cretaceous plume-induced subduction initiation along the southern margin of the Caribbean and NW South America: The first documented example with implications for the onset of plate tectonics. Gondwana Res. 27, 38–63. https://doi.org/10.1016/j.gr.2014.07.011

White, W.M., 2013. Geochemistry. Wiley.

Wilson, J.T., 1966. Did the Atlantic Close and then Re-Open? Nature 211, 676–681. https://doi.org/10.1038/211676a0

Wright, J.E., Wyld, S.J., 2011. Late Cretaceous subduction initiation on the eastern margin of the Caribbean-Colombian Oceanic Plateau: One Great Arc of the Caribbean (?). Geosphere 7, 468–493. https://doi.org/10.1130/GES00577.1

Yang, H., Moresi, L.N., Quigley, M., 2020. Fault spacing in continental strike-slip shear zones. Earth Planet. Sci. Lett. 530, 115906. https://doi.org/10.1016/j.epsl.2019.115906

Yang, J., Kaus, B.J.P., Li, Y., Leloup, P.H., Popov, A.A., Lu, G., Wang, K., Zhao, L., 2020. Lower Crustal Rheology Controls the Development of Large Offset Strike-Slip Faults During the Himalayan-Tibetan Orogeny. Geophys. Res. Lett. 47. https://doi.org/10.1029/2020GL089435

Yang, T., Moresi, L., Zhao, D., Sandiford, D., Whittaker, J., 2018. Cenozoic lithospheric deformation in Northeast Asia and the rapidly-aging Pacific Plate. Earth Planet. Sci. Lett. 492, 1–11. https://doi.org/10.1016/j.epsl.2018.03.057

Zelst, I. Van, Crameri, F., Pusok, A.E., Glerum, A., Dannberg, J., 2021. 101 Geodynamic modelling: How to design, carry out, and interpret numerical studies. Solid Earth Discuss. [preprint]. https://doi.org/https://doi.org/10.5194/se-2021-14

Zhang, S., Leng, W., 2021. Subduction Polarity Reversal: Induced or Spontaneous? Geophys. Res. Lett. 48, 1–11. https://doi.org/10.1029/2021GL093201

Zhao, D., 2004. Global tomographic images of mantle plumes and subducting slabs: Insight into deep Earth dynamics. Phys. Earth Planet. Inter. 146, 3–34. https://doi.org/10.1016/j.pepi.2003.07.032

Zhong, X., Li, Z., 2019. Forced Subduction Initiation at Passive Continental Margins: Velocity-Driven Versus Stress-Driven. Geophys. Res. Lett. 46, 11054–11064. https://doi.org/10.1029/2019GL084022

Zhou, X., Li, Z.H., Gerya, T. V., Stern, R.J., Xu, Z., Zhang, J., 2018. Subduction initiation dynamics along a transform fault control trench curvature and ophiolite ages. Geology 46. https://doi.org/10.1130/G40154.1

Appendix A. Underworld scripts

The following section contains all the UW1 scripts referenced in Chapter 2 of this thesis.

The codes can be downloaded from https://github.com/jaime-almeida/basic-uw-scripts-.

Appendix B. LaMEM scripts

The following section contains all the LaMEM scripts referenced in Chapter 2 of this thesis.

These files can be downloaded from https://github.com/jaime-almeida/basic-lamem-inputs.

Instructions for generating a LaMEM partitioning file:

To create this file, simply type the following line of code in your terminal in the folder which contains your *.dat file:

mpiexec -n *number_of_cores* /path/to/your/lamem/executable -ParamFile *input.dat* -mode save_grid

The number of cores depends on the size/complexity of the model, and the LaMEM executable path depends on the directory in which it was installed.

Appendix C. geoProc code

The following section contains the source code for the *geoProc* library. The codes can be found at https://github.com/jaime-almeida/geoProc.

Appendix D. Supplementary videos for Chapter 4

The videos for Chapter 4 can be found attached to the present document.

Appendix E. Supplementary videos for Chapter 5

The videos for Chapter 5 can be found attached to the present document.

Appendix F. Research collaborations

During this PhD, my technical and scientific development allowed me to collaborate, as a co-author, on the development and publication of other works. This section lists these works, as well as what my contribution was in each of them.

Co-authorship paper #1 (published):

Gomes, A.S., Rosas, F.M., Duarte, J.C., Schellart, W.P., *Almeida, J.,* Tomás, R., Strak, V., 2019. Analogue modelling of brittle shear zone propagation across upper crustal morpho-rheological heterogeneities. J. Struct. Geol. 126, 175–197. https://doi.org/10.1016/j.jsg.2019.06.004

Abstract:

Crustal shearing of pre-tectonic weak bodies (e.g. salt pillows, igneous pockets) associated with basement strike-slip fault systems is common in nature. Yet the structural pattern arising from the interference between a brittle shear zone and such weak rheological heterogeneities is still not fully explained. In the present work, different sand-box analogue modelling experiments were carried out to better understand, not only the shear zone perturbation effect caused by a strictly rheologic (viscous-weak) anomaly, but also the one arising from a combined morphological perturbation (i.e. traverse topographic crest). Obtained results show that the development of different shear zone deformation patterns is in each case essentially determined by the interplay between: (i) ductile wrenching strain accommodation in the (viscous) weak body; and (ii) coincidence vs. mismatch between main brittle-viscous rheological boundaries and (crest-related) topographic steps. Comparison of the experimentally obtained results with complying natural examples is further discussed, and essentially focused on the NE Atlantic tectono-magmatic interference between the Gloria transform fault and the Tore-Madeira submarine ridge.

My contribution:

In analogue modelling studies, it is fundamental to understand how the rheology of each material helps to accommodate or dissipate the deformation. Due to my background on geodynamic modelling, I was able to provide insight on the quantification of this parameter, aiding to the discussion on the paper.

Co-authorship paper #2 (under review):

Oliveira, M. E., Gomes, A. S., Rosas, F. M., Duarte, J. C., França, G. S., *Almeida, J.*, Fuck, R. A, 2021. Double-rift nucleation above inherited crustal weaknesses: insights from 2D numerical models, Tectonophysics, under review.

Abstract:

Weak mechanical anisotropies inherited from previous tectonic cycles are known to work as nucleating rifting-seeds during subsequent continental rift evolution. However, during rift-to-drift evolution the common occurrence of double-rifting, in which two main rift branches evolve before only one of them renders continental break-up, is still not fully understood. We thus carried out a numerical study to investigate the influence of pre-existent rifting-seeds in the nucleation, and potential tectonic interference, of early formed grabens during rifting of a continental crustal segment. We considered not only the influence of the number and distance at which the seeds are located, but also the potential mechanical control exerted by different archetypal ("Crème Brûlée" vs. "Jelly Sandwich") crustal rheological configurations. Our results show that none of these factors can by themselves alone explain the mechanics underlying the formation of early rifting geometries and ensuing crustal break-up configurations. It is thus only when their combined influence is considered that a coherent explanation for these diversified geometries and modes of evolution arises. Moreover, in view of this new insight, it becomes apparent that double rifting is what to expect when only a single rifting-seed is present in the crust, or even in the absence of any inherited weaknesses, providing a possible explanation for the ubiquity of this type of rifting pattern in nature.

My contribution:

Geodynamic insight and technical contribution towards the development of the presented numerical continental rifting models.

Co-authorship paper #3 (under review):

Duarte, J., Riel, N., Civiero, C., Silva, S., Rosas, F., Schellart, W., Custodio S., *Almeida, J.*, Terrinha, P., Ribeiro, A., pre-print. Evidence of oceanic plate delamination in the Northern Atlantic. Nature. https://doi.org/10.21203/rs.3.rs-690433/v1

Abstract:

The Earth's surface is constantly being recycled by plate tectonics. Subduction of oceanic lithosphere and delamination of continental lithosphere constitute the two most important mechanisms by which the Earth's lithosphere is recycled into the mantle. Delamination or detachment in continental regions typically occurs below mountain belts due to a weight excess of overthickened lithospheric mantle, which detaches from overlying lighter crust, aided by the existence of weak layers within the continental lithosphere. Oceanic lithosphere is classically pictured as a rigid plate with a strong core that does not allow for delamination to occur. Here, we propose that active delamination of oceanic lithosphere occurs offshore Southwest Iberia. The process is assisted by the existence of a lithospheric serpentinized layer that allows the lower part of the lithosphere to decouple from the overlying crust. Tomography images reveal a sub-lithospheric high-velocity anomaly below this region, which we interpret as a delaminating block of old oceanic lithosphere. We present numerical models showing that for a geological setting mimicking offshore Southwest Iberia delamination of oceanic lithosphere is possible and may herald subduction initiation, which is a long-unsolved problem in the theory of plate tectonics. We further propose that such oceanic delamination is responsible for the highest-magnitude earthquakes in Europe, including the M8.5-8.7 Great Lisbon Earthquake of 1755 and the M7.9 San Vincente earthquake of 1969. In particular, our numerical models, in combination with calculations on seismic potential, provide a solution for the instrumentally recorded 1969 event below the flat Horseshoe abyssal plain, away from mapped tectonics faults. Delamination of old oceanic lithosphere near passive margins constitutes a new class of subduction initiation mechanisms, with fundamental implications for the dynamics of the Wilson cycle.

My contribution:

Geodynamic insight and technical contribution towards the development of the presented numerical subduction zone initiation models.

Co-authorship paper #4 (published):

Cartaxo, A.L., *Almeida, J.*, Gualda, E. J., Marsal, M., Loza-Alvarez, P., Brito, C., Isidro, I. A. (2020) A computational diffusion model to study antibody transport within reconstructed tumor microenvironments. BMC Bioinformatics 21, 529. https://doi.org/10.1186/s12859-020-03854-2

Abstract:

Antibodies revolutionized cancer treatment over the past decades. Despite their successfully application, there are still challenges to overcome to improve efficacy, such as the heterogeneous distribution of antibodies within tumors. Tumor microenvironment features, such as the distribution of tumor and other cell types and the composition of the extracellular matrix may work together to hinder antibodies from reaching the target tumor cells. To understand these interactions, we propose a framework combining in vitro and in silico models. We took advantage of in vitro cancer models previously developed by our group, consisting of tumor cells and fibroblasts co-cultured in 3D within alginate capsules, for reconstruction of tumor microenvironment features.

My contribution:

Technical contribution on the coding of a 2D diffusion model for the transport of antibodies within tumours.